Impact of climate change on the hydrology of High Mountain Asia

Effecten van klimaatverandering op de hydrologie in de hooggebergten van Azië

(met een samenvatting in het Nederlands)

PROEFSCHRIFT

ter verkrijging van de graad van doctor aan de Universiteit Utrecht
op gezag van de rector magnificus, prof. dr. G.J. van der Zwaan,
ingevolge het besluit van het college voor promoties in het openbaar te verdedigen
op vrijdag 27 mei 2016 des middags te 4.15 uur

door

Arthur Friedrich Lutz

geboren op 1 maart 1985 te Stuttgart, Duitsland

Promotor:
Prof. dr. ir. M.F.P. Bierkens

Copromotor:
Dr. W.W. Immerzeel

Impact of climate change on the hydrology of High Mountain Asia

Promotor
Prof. dr. ir. M.F.P. Bierkens

Copromotor
Dr. W.W. Immerzeel

Examination committee
Prof. dr. M.R. van den Broeke – Utrecht University
Prof. dr. G. Kaser – University of Innsbruck
Prof. dr. ir. E.J. Moors – VU University Amsterdam
Prof. dr. ir. R. Uijlenhoet – Wageningen University
Dr. A.B. Shrestha – International Centre for Integrated Mountain Development, Kathmandu

ISBN 978-90-6266-423-8

Published by Faculty of Geosciences, Universiteit Utrecht, The Netherlands, in:
Utrecht Studies in Earth Sciences (USES), ISSN 2211-4335

Typesetting: Jolanda Lutz, Arthur Lutz, Margot Stoete
Cover photo by Niko Wanders, taken in 2014 in Langtang National Park, Nepal.

Printed in the Netherlands by Ridderprint BV, Ridderkerk.

Utrecht Studies in Earth Sciences 104

Impact of climate change on the hydrology of High Mountain Asia

Arthur Lutz

Utrecht 2016

Utrecht Studies in Earth Sciences

Over every mountain there is a path,
although it may not be seen from the valley.

—Theodore Roethke

Contents

Acknowledgements

Over the past four years I have been working towards the completion of this thesis. The project started in 2012, when Walter and Marc suggested to extend my work at FutureWater into a PhD research. Since then the project progressed steadily, sometimes surprisingly quickly, and sometimes slower than expected (or hoped). Now in the end I am proud of the final result and achievement. Completing this thesis certainly wasn't a job that I could have done on my own. Many people have contributed to this work or supported me in one way or the other and deserve credit for that.

First of all I want to thank Walter, my colleague at FutureWater and copromotor at Utrecht University. Dear Walter, thank you so much for all your support and encouragement during the past four years. Since we started working together on mountain hydrology projects you have been an example to me right away. Your eye for scientific quality combined with your high efficiency have helped me tremendously to bring this thesis to its current form. It surely was a privilege to have you as my supervisor and to navigate in your slipstream. Equally important, you are a great person and I enjoy working with you a lot. If I have to mention one highlight it would be the great joined experience of the fieldwork in Langtang. I look forward to more teamwork and fun in the future! Next I want to thank my second supervisor and promotor Marc. Dear Marc, although you did not see me around very often, I am very grateful for your suggestions, reviewing and commenting. You always came up with smart stuff when I didn't see the way forward and your contributions certainly helped to get the papers to a higher level.

Writing this thesis would not have been possible without the support of FutureWater and its scientific director Peter Droogers. Dear Peter, thank you for giving me the opportunity to combine my work at FutureWater with a PhD research. Your practical point of view certainly helped me to keep moving forward efficiently. I think the way we work in FutureWater towards practical but at the same time high-quality solutions is the right way to go and I look forward to more nice projects in the future. A big thanks also to my other (former) colleagues at FutureWater: Gé, Gijs, Froukje, Jaïrus, Johannes, Martijn, Sergio and Wilco: Thanks for the pleasant, uncomplicated collaboration and fun at the office. Thanks also to my carpool buddies Gijs and Ruben for making the daily commute from Utrecht to Wageningen and back bearable.

Further, I certainly want to thank the people at the Intergovernmental Centre for Integrated Mountain Development (ICIMOD) in Kathmandu, as much of the work presented in this thesis came forth through assignments commissioned by ICIMOD. In particular I want to thank Arun Shrestha. Dear Arun-ji, thank you for the very pleasant cooperation during the past years and for sharing your vast knowledge on water issues in the Hindu Kush-Himalayan region. Thank you also for being part of my examination committee and making the long journey from Nepal to attend my defense! The list of people to thank at ICIMOD is much longer and I hereby want to thank them all for their collaboration and for making me feel very welcome every time I visited Nepal.

Thanks also to the many other people I met in the region for sharing their humour, food, knowledge and views on the water issues in High Mountain Asia and its river basins, and for introducing me to their cultures and backgrounds.

A great thanks is also awarded to the co-authors (other than mentioned above) who contributed to the papers that make up this thesis. Herbert, Hester, Flip, Francesca, Andreas and Philip, thank you for your valuable contributions!

Thanks also to colleagues at the Department of Physical Geography, many of whom I have known since I started studying in Utrecht back in 2003. I was not often present in the good old Zonneveldvleugel, but certainly enjoyed the easy-going working atmosphere whenever I was there. Special thanks to Tjalling for the walks during lunch breaks, Juul for helping out with any practical issues, and Niko for being a very quiet tent-companion during the fieldwork in Langtang.

The various organisations (not mentioned above) who financially supported parts of the work presented in this thesis are acknowledged as well: Asian Development Bank, the UK Department for International Development, Canadian International Development Research Centre, Norwegian Ministry of Foreign Affairs and the Swedish International Development Cooperation Agency.

Writing a PhD thesis as an on-the-side project within a reasonable timeframe inevitably meant that time had to be found regularly in the evenings and weekends; timeslots that are normally reserved to spend with loved ones. I must say that I am happy that, despite many periods of neglect from my side, I did not lose any friends (or my wife) during the last four years ☺. I want to thank all my dear friends who I love to spend time with, be it for running, cycling or walking in the outdoors, culinary pleasures, house and techno parties, playing games, drinking beer/coffee/tea, or hanging out in any other way. In addition to people already mentioned, in particular I want to mention Anouk & Ferry, Evert, Hilke & Rik, Marije & Menno, Mark, Opa Gill, Renske & Maarten, and the Upperfist collective –Hinse, Johan, Sander, Stefan, Tom–: thank you for your support, showing (or faking) interest for my work and for who you are! Thanks to my siblings Jolanda, Marianne, Bernd and their spouses for their support and special thanks to Jolanda for assisting with typesetting of the thesis. Dear mum and dad, thank you for your love, support and overall stimulation to take up challenges in education, work and science! And certainly also for jumping in for me in taking care of Lars regularly during the last year. The same goes for my in-laws: Thank you Tiny, Noël, Floor and Joeri!

The final paragraph is reserved for a vote of thanks to the two most important people in my life. Dear Lars, you are the most awesome and most inspiring little monkey in the world. Your epic smile spreads instant happiness and reminds me every single day to enjoy every moment to the fullest. I truly look forward to every day that you will be in my life! Dear Miriam, you have always been my top priority and in the foreground of this project our relationship grew stronger, we got married and started our little family. Nevertheless, this (sometimes crazy) undertaking certainly took a large toll from you. It was only because of your support and patience that I could neglect my duties as a boyfriend, husband and dad from time to time to get this thing done. Thank you so much for all your love, support and patience, and for all the fun we have together. Let's not forget that I also want to thank you for reviewing and commenting on most of my papers and helping me to wrap things up. Now that this project is finished, my full focus will stay on our happy family project. I love you!

Utrecht, 17 April 2016

Chapter 1

Introduction

1.1 Mountains and the hydrological cycle

1.1.1 The hydrological cycle

For human life and life in general, the hydrological cycle can be considered as the most important recycling system of matter on Earth, since water is an essential and widely used substance in every living organism. In today's society human beings use water directly to sustain their bodies and to sanitize themselves, their goods and their homes. The bulk of water is used indirectly for the production of agricultural products, raw materials and goods. In the hydrological cycle, water is transported between different reservoirs of water, such as oceans, lakes, rivers, groundwater storages, and also snow packs and glaciers. The fluxes of water between the different reservoirs are driven by a variety of physical processes, like for example the transpiration of water by plants to the atmosphere or the precipitation of water from the atmosphere to the Earth's surface (Figure 1.1).

The oceans, covering 71% of the Earth's surface form the largest reservoir of water, holding over 97% of the total amount of water on the planet [*Chahine*, 1992]. Only about 2.5% of the water on

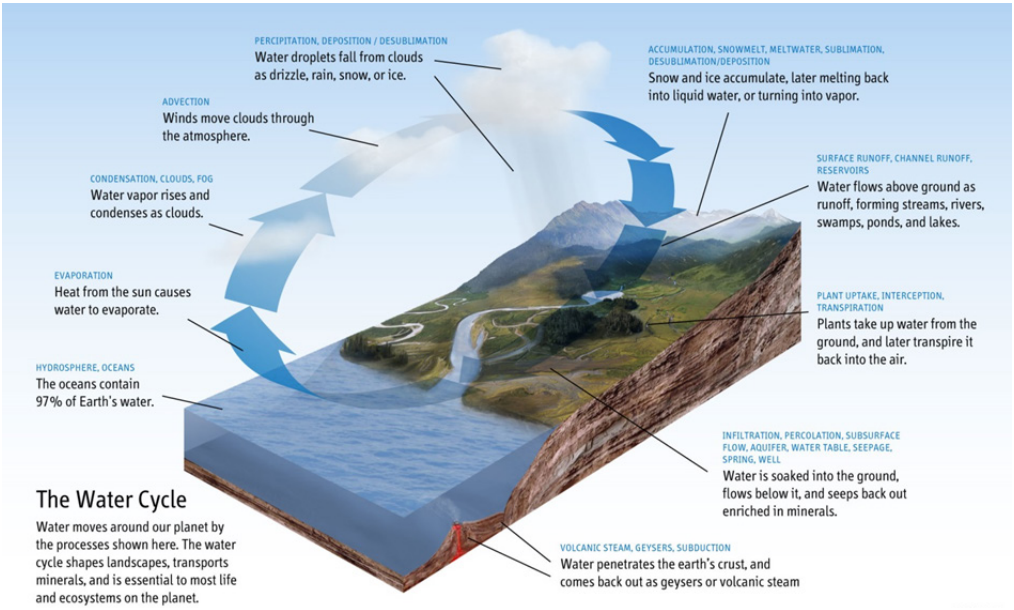

Figure 1.1: Schematic representation of the hydrological cycle. By Ehud Tal, licensed under Creative Commons (CC BY NC SA).

Earth is fresh water, of which the majority is stored as ice or as deep groundwater [*Oki and Shinjiro*, 2006]. Related to the different reservoir sizes and magnitude of fluxes into and out of the reservoir, also the average residence time of a water molecule differs strongly per reservoir. For example, the mean residential time of water in a natural river is about 2.5 weeks and a water molecule stays for ~10 days in the atmosphere [*Oki and Shinjiro*, 2006]. Water molecules in the oceans stay there on average for more than 3000 years, whereas groundwater residence times can be up to 10000 years. The average residence time of a water molecule in the Antarctic ice sheet is 12000 years, but the ice at the base of some parts of the ice sheet can be millions of years old [*Fischer et al.*, 2013]. Water resides in glaciers for shorter timescales than it does in ice sheets, often about 20-100 years, depending on the size and flow velocity of a glacier [*Marshak and Prothero*, 2008].

1.1.2 Mountains as water towers

Mountains form natural barriers in the landscape, and moving air masses in the atmosphere are lifted when passing a mountain range. When lifted, the air is cooled and because of that the amount of moisture that can be stored in the air decreases, resulting in precipitation of water. As a result, precipitation rates are particularly high in mountain ranges and thus mountain ranges are important sources of water [*Viviroli et al.*, 2003; *Kaser et al.*, 2010]. Liquid water flows downstream directly or is stored for short periods of time near the surface, whereas water can be stored on seasonal scales as seasonal snow, or for longer periods of time when stored as firn, ice, permafrost or as groundwater. The fact that mountains are higher than their surroundings ultimately forces all of the water that is not taken back to the atmosphere by evaporation or sublimation, to move downstream by the gravitational force. In liquid state this can be as surface runoff, lateral flow through the soil or percolation to deeper groundwater. In solid state this can be through wind-induced transport, gravitational downslope transport of snow (avalanching), or through the downward flow of glacier ice.

The fact that mountain ranges in High Mountain Asia (HMA) are the highest on Earth combined with monsoon-dominated precipitation regimes (implying large amounts of precipitation), makes the amount of water generated in those mountain ranges particularly large [*Viviroli et al.*, 2003; *Bookhagen and Burbank*, 2010]. Because of its large areas and volumes of snow and glacier ice, HMA is also referred to as the "Asian Water Tower", or the "Third Pole". HMA does not only comprise the Himalayas, but also other mountain ranges such as the Tien Shan, Pamir, Hindu Kush, Karakoram, and the vast Tibetan Plateau. The focus of this thesis is on the the Tien Shan and Pamir mountain ranges in the Amu Darya and Syr Darya basins, and the Hindu Kush, Karakoram and Himalayan ranges in the Indus, Ganges, Brahmaputra, Salween and Mekong river basins (Figure 1.2).

The importance of upstream water resources with respect to the total water resources differ per river basin and depend on the relative area of a basin located in mountainous parts, the amount of water stored as snow and ice, and the distribution of precipitation between the upstream part and downstream part of the basin. In HMA, the basins with the largest dependency on upstream water resources are the Indus and Amu Darya basins, which have very dry downstream climates, westerly-influenced precipitation regimes, and large glacier systems [*Immerzeel et al.*, 2010; *Immerzeel and Bierkens*, 2012; *Schaner et al.*, 2012].

HMA has a large volume of water stored as glacier ice. Different glacier inventories have been published in recent years, based on the mapping of glaciers from satellite imagery (Table 1.1). The largest glacier systems are in the Karakoram and Pamir mountain ranges. Differences between the glacier inventories stem from the use of imagery from different acquisition dates representing

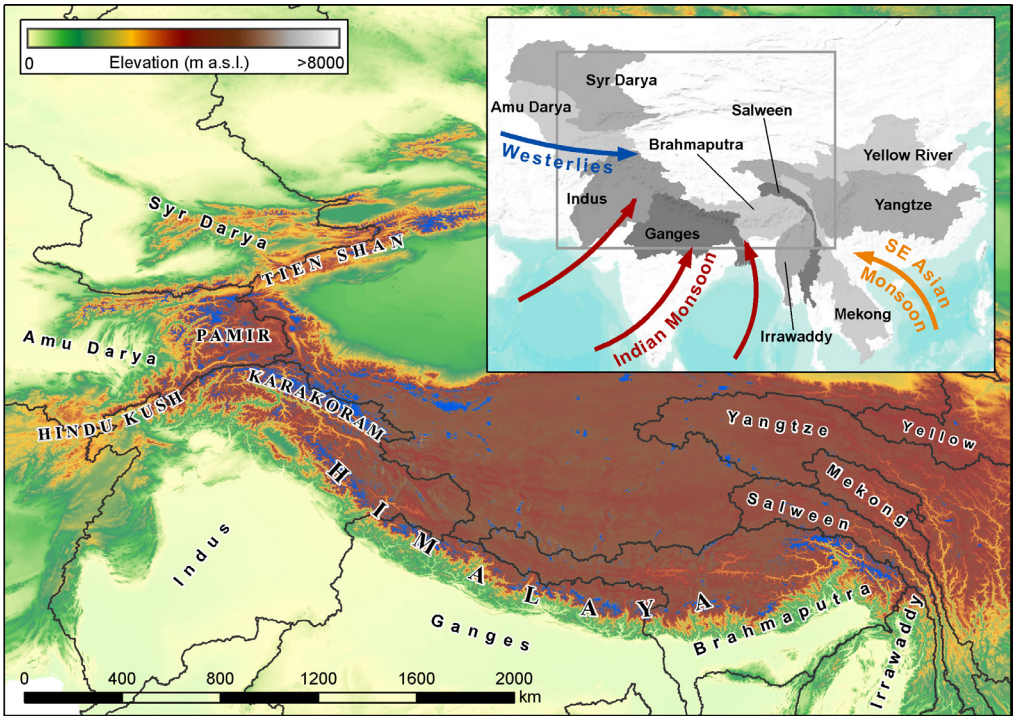

Figure 1.2: Map of the Asian mountain ranges, Tibetan Plateau and surroundings, showing parts of ten large river basins which have sources in High Mountain Asia. Glaciers (Randolph Glacier Inventory [*Pfeffer et al.*, 2014]) are indicated by the dark blue color. Elevation data is derived from the HydroSheds SRTM digital elevation model [*Lehner et al.*, 2008]. The inset shows the full extent of the ten river basins and the most important climatic systems.

a different status of glaciers and subjectivities in glacier area mapping, which is mostly manual digitization work [*Nuimura et al.*, 2015]. A significant proportion of the glaciers in the HMA region is covered by a layer of rock debris on their tongues [*Bajracharya and Shrestha*, 2011; *Scherler et al.*, 2011]. In the upper Indus basin ~18% of the glacier surface is debris-covered [*Khan et al.*, 2015a], whereas this is ~14% in the Ganges basin, and ~12% in the Brahmaputra basin [*Bajracharya and Shrestha*, 2011]. No large-scale estimates of the debris-covered glacier areas are available for the Pamir in the Amu Darya basin and the Salween and Mekong basins. Melting of glacier surfaces below a layer of debris can be either accelerated compared to debris-free surfaces if the debris layer is thin (a few centimeters), or dampened if the thickness is more than a threshold of 5 cm [Östrem, 1959; *Nicholson and Benn*, 2006; *Brock et al.*, 2010]. In the Pamir and Karakoram mountain ranges, large numbers of glaciers show periodical surging behavior, during which ice and debris are transported downslope at a rate of one to two orders of magnitude greater than during their phases of quiescence [*Hewitt*, 2007, 2011; *Quincey et al.*, 2011; *Sevestre and Benn*, 2015].

Ice volumes of glaciers are more difficult to obtain compared to glacier areas, because information of ice depth and bedrock topography is only available for a small selection of glaciers. Different widely used methods to estimate the ice volumes have been applied in the Karakoram and Himalayas, showing that the ice volume in the Karakoram is likely larger than the ice volume in the

Table 1.1: Glacier-covered areas in six different Asian river basins according to three different glacier inventories: Randolph Glacier Inventory (RGI) version 4.0 [*Pfeffer et al.*, 2014], ICIMOD glacier inventory [*Bajracharya and Shrestha*, 2011], and Glacier Area Mapping for Discharge from the Asian Mountains (GAMDAM) Glacier Inventory (GGI) [*Nuimura et al.*, 2015].

River basin	Glacier area (km^2)		
	GGI	ICIMOD	RGI 4.0
Amu Darya	2498	2566	3154 ± 256
Indus	23668	21193	26018 ± 1750
Ganges	7537	9012	10621 ± 824
Brahmaputra	9803	14020	17419 ± 1373
Salween	1318	1352	2198 ± 210
Mekong	225	235	586 ± 49

entire Himalayas (Figure 1.3) [*Frey et al.*, 2014]. The combined Indus, Ganges and Brahmaputra basins cover about 2.65 million km^2. Assuming the total ice volumes assessed by *Frey et al.* [2014] to cover all ice reserves in these basis, the ice volume can be compared to the long-term annual precipitation sum in these basins for 1978-2007, being 730 mm yr^{-1} [*Yatagai et al.*, 2012]. This indicates that the amount of water stored as ice in the mountains equals roughly 1.5 to 2.5 years of the combined basins' annual precipitation, based on the minimum and maximum estimate of the total ice volume (Figure 1.3).

Estimates of the snow cover and snow cover dynamics in HMA are mostly based on MODIS remotely sensed snow cover products [*Hall et al.*, 2002]. The Indus basin has the most extensive snow cover in HMA [*Immerzeel et al.*, 2009], and the snow cover follows distinct seasonal patterns, with maximum snow cover during winter, and minimum during summer [*Gurung et al.*, 2011]. However, for the Indus basin, the maximum in snow cover is observed in spring [*Immerzeel et al.*, 2009]. Since the inter-annual variability of precipitation in HMA is large, this also holds for the inter-annual variability of snow cover [*Immerzeel and Bierkens*, 2009]. Estimates of snow water equivalent are not available at the large scale and this remains challenging, since the snow depth cannot be assessed accurately by remote sensing products. Climate models might be more suitable to estimate snow water equivalent, but they generally have difficulties to simulate the observed snow cover accurately [*Ménégoz et al.*, 2013]. Furthermore, precipitation estimates provided by reanalysis, station observations, remote sensing and climate models have large discrepancies [*Ménégoz et al.*, 2013; *Immerzeel et al.*, 2015].

1.1.3 Downstream water demands

The water resources supplied by HMA are essential to hundreds of millions of people and future changes in both demand and supply may have large impacts for future water availability [*Immerzeel and Bierkens*, 2012; *Miller et al.*, 2012]. Whereas the analyses in this thesis focus on the supply side, this section briefly zooms to the demand side to illustrate the significance of HMA as a water resource for people living in the large Asian river basins. The river basins surrounding HMA have large populations, growing at high rates and with increasing demands for water and energy. The combined population of the ten large river basins with sources in HMA (Figure 1.2) is estimated at 1.3 billion people [*Shrestha et al.*, 2015] (~18% of the world's population [*UN*, 2015]). The combined population of the basins studied in this thesis (Syr Darya, Amu Darya, Indus, Ganges, Brahmaputra, Salween and Mekong) is estimated at 775 million people (~10% of the world's population

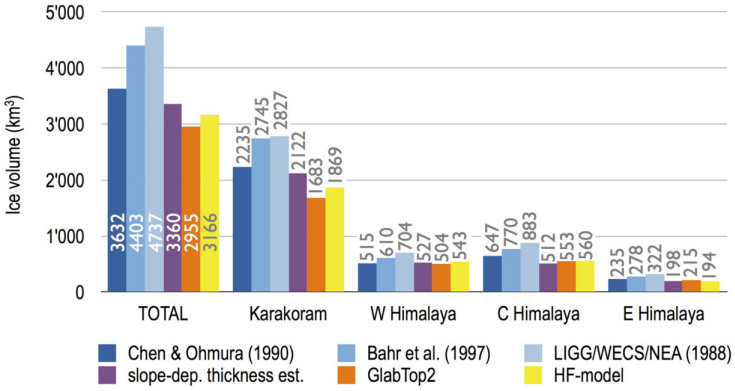

Figure 1.3: Estimates of ice volumes made with different methods. Source: [*Frey et al.*, 2014]

[*UN*, 2015]), of which 85% live in the Indus, Ganges and Brahmaputra basins. The populations of India, Pakistan, and Bangladesh, harbouring the major parts of the Indus, Ganges and Brahmaputra basins, are expected to grow by 30.1%, 63.9% and 25.6% respectively between 2015 and 2050 [*UN*, 2015].

The Indus basin has the world's largest irrigation scheme [*Jain et al.*, 2007]. The Punjab and Haryana regions are also called "bread baskets" and the West Bengal region is also called "rice bowl", because of their large (irrigated) agricultural productions. HMA has a large hydropower potential, which is largely unused. For example, Pakistan uses around 15% of its hydropower potential [*Mirza et al.*, 2008], whereas Nepal uses only 1.6% of its hydropower potential [*Surendra et al.*, 2011]. Despite the hydropower potential being not fully developed, large hydropower facilities are present in the region. For example, the Tarbela dam in the Indus river, has a storage capacity of 13.7 km^3 and an installed capacity of 3500 MW. The extensive amount of unused hydropower potential is being developed more rapidly in recent years [*Mirza et al.*, 2008], as the region faces energy-deficits since decades [*Molden et al.*, 2014]. The populations and life standards in the region are projected to increase further [*Qureshi*, 2011; *UN*, 2015]. The same holds for the areal of irrigated agriculture [*Fischer et al.*, 2005], and development of reservoirs for water storage and hydropower generation [*Siddiqi et al.*, 2012].

In the present time, the water resources in the areas surrounding HMA are already stressed. Parts of the Indus and Ganges groundwater reservoirs are among the most overstressed aquifers in the world [*Wada et al.*, 2010; *Gleeson et al.*, 2012; *Richey et al.*, 2015], indicating that water resources in this basin already depend largely on non-renewable sources of water. Within the 100 largest river basins worldwide, the Syr Darya, Amu Darya, Indus, Ganges and Brahmaputra are listed in the top 20 of most water-stressed river basins [*Gassert et al.*, 2013]. Even without bringing future climate change into the picture, increased water stress is expected for the future, considering the increasing water demand due to the expected increase in population, irrigated agriculture and energy consumption.

1.2 Mountains and climate change

1.2.1 Climate in High Mountain Asia

In general, the climate in the eastern part of the Himalayas is characterized by the East-Asian and Indian monsoon systems (Figure 1.2), causing the bulk of precipitation to occur from June to September. The precipitation intensity shows a strong north-south gradient caused by orographic effects [*Galewsky*, 2009]. Precipitation patterns in the Pamir, Hindu Kush and Karakoram ranges in the west are also characterized by westerly and southwesterly flows, causing the precipitation to be more evenly distributed over the year compared to the eastern parts [*Bookhagen and Burbank*, 2010] (Figure 1.4). In the Karakoram, up to two-thirds of the annual high-altitude precipitation occurs during the winter months [*Winiger et al.*, 2005; *Hewitt*, 2011]. About half of this winter precipitation is brought by western disturbances, being westerly-driven eastward propagating cyclones bringing sudden winter precipitation to the north-western parts of the Indian subcontinent [*Barlow et al.*, 2005]. The inter-annual variability in precipitation is higher for HMA than for the downstream parts of the river basins [*Immerzeel and Bierkens*, 2009].

Meteorological stations are relatively sparse in HMA because of the poor accessibility of the terrain. Especially precipitation can vary strongly over short horizontal distances due to orographic effects but high-altitude precipitation gauge networks are almost non-existent. If there are gauges, they are mostly located in the valley bottoms where precipitation amounts are smaller compared to higher altitudes. Besides, most gauges have difficulties capturing snowfall accurately. Direct snow-

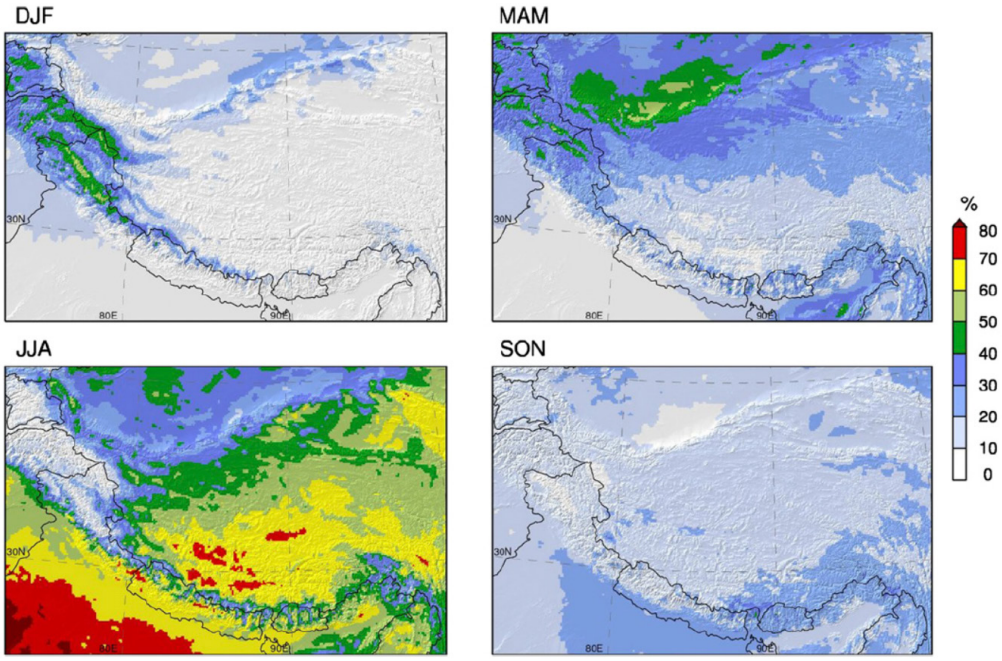

Figure 1.4: Percentage of the mean annual precipitation distributed over the periods December to February (DJF), March to May (MAM), June to August (JJA) and September to November (SON), as represented in the High Asia Reanalysis product. Source: [*Maussion et al.*, 2014]. ©American Meteorological Society. Used with permission.

accumulation measurements, using snow pillows, pits, and cores from accumulation zones are also scarce and usually only cover short periods. Precipitation predictions for the HMA region based on ground observations, which are not able to capture all the variations spatially, are therefore not very accurate and often replaced with or complemented by data from other approaches such as the use of remote sensing and reanalysis techniques to generate gridded climate products, to obtain more accurate predictions (Figure 1.5).

1.2.2 Observed climate change

Past trends in climate in HMA have been analyzed in multiple studies, of which key results are highlighted in this section. This is by no means a complete overview of the work done in this field, but serves to identify the main climatic trends observed in the region. *Palazzi et al.* [2013] analyzed trends in precipitation for different products, with records varying in length from 30 to 60 years, and ending around 2010. They found no statistically significant long-term trends for winter

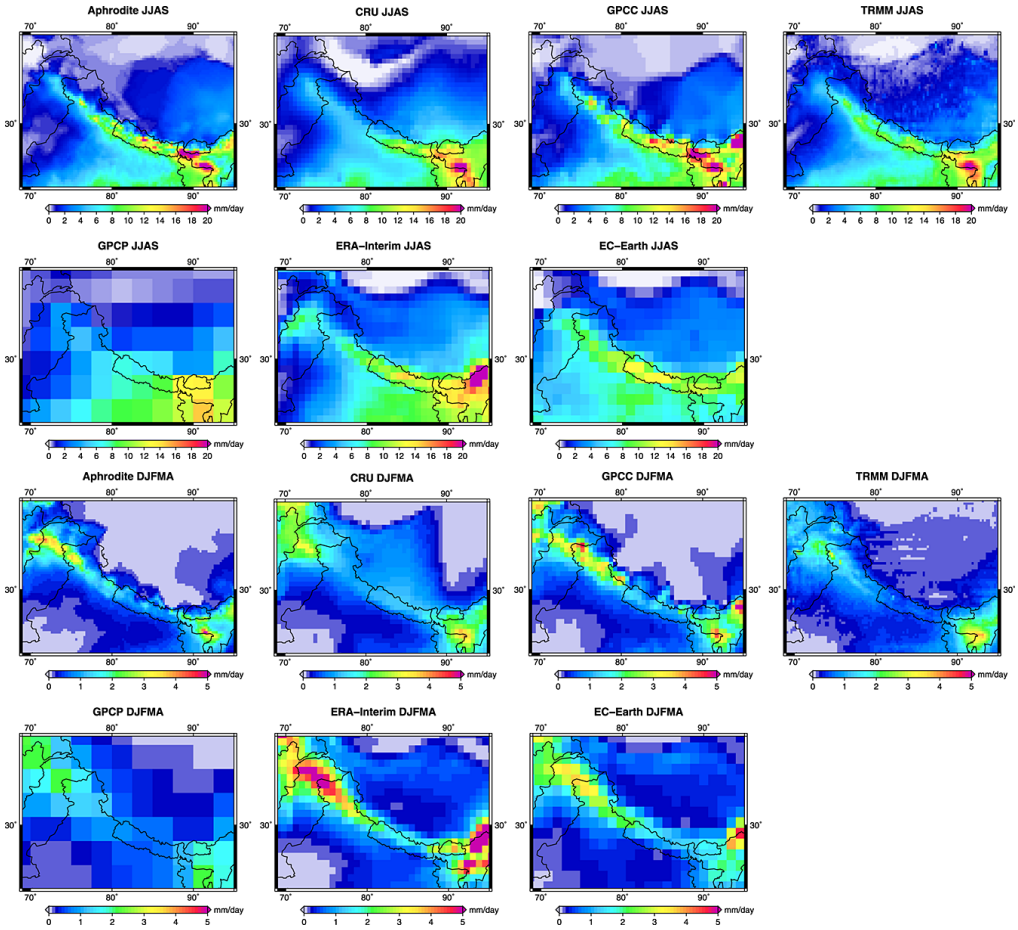

Figure 1.5: Multi-annual mean (1998-2007) of monsoon (JJAS) and winter (DJFMA) precipitation over the HMA region as represented by different datasets. Source: [*Palazzi et al.*, 2013]. Reprinted by permission from John Wiley and Sons. ©2012 American Geophysical Union.

precipitation averaged over the Hindu Kush-Himalayan area. Slightly increasing, though significant, trends in precipitation during the monsoon season were found for two out of nine products, whereas no significant trends were found in the seven other products. The trends show a very large spatial variability (Figure 1.6).

Trends in meteorological variables measured at ground stations were analysed in a number of studies, of which a few are mentioned here. *Fowler and Archer* [2006] analysed temperature records in the upper Indus basin for the period 1961-2000. They showed that winter mean and maximum temperatures increased significantly while mean and minimum summer temperatures declined consistently. The diurnal temperature range increased in all seasons. An analysis of precipitation records for the upper Indus basin by the same authors, showed significant increases in winter, summer and annual precipitation for several stations over the period 1961-1999 [*Archer and Fowler*, 2004]. *Khattak et al.* [2011] found stronger increasing trends in winter maximum temperature at higher elevations but no significant precipitation trends.

Studies in other areas also show warming temperature trends as for example on the Tibetan Plateau [*Liu and Chen*, 2000] and in the central Himalaya [*Shrestha et al.*, 1999]. The same authors also showed that for the central Himalaya no increasing trend in precipitation is observed, but that inter-annual variability is large [*Shrestha et al.*, 2000].

Studies worldwide show that recent increasing temperature trends are stronger for mountainous regions than for other land surfaces [*Rangwala and Miller*, 2012; *Pepin et al.*, 2015]. Such trends have been observed for the Himalayan region as well [*Bhutiyani et al.*, 2007; *Lu et al.*, 2010].

An analysis of the multi-annual variations in winter westerly disturbance (WWD) activity over the period 1971-2010 indicated enhanced strength and frequency of WWD and associated heavy precipitation events in the Karakoram and western Himalaya [*Cannon et al.*, 2014]. The central Himalaya, in contrast, experienced weakening influence of these disturbances and decreases in heavy winter precipitation.

To summarize the two preceding sections, it is clear that the climate in HMA is characterized by the monsoon bringing precipitation during the monsoon season (June-September) and westerly

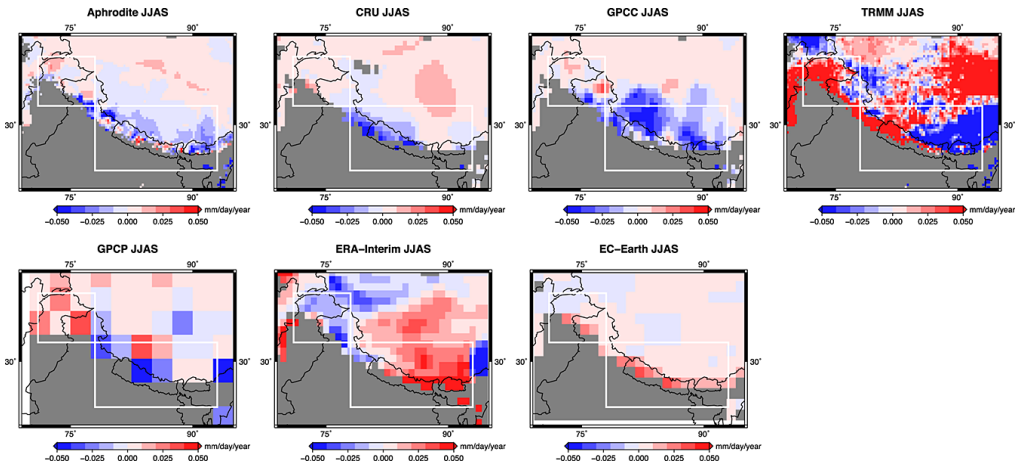

Figure 1.6: Spatial maps of summer (JJAS) precipitation trends for different products. Source: [*Palazzi et al.*, 2013]. Reprinted by permission from John Wiley and Sons. ©2012 American Geophysical Union.

systems bringing precipitation during winter. The monsoon influence decreases from southeast to northwest, whereas the westerly influence decreases from west to east. The conclusion can be drawn that the climate in HMA has been warming during recent decades, with steeper trends than in non-mountainous regions. Precipitation trends are mostly not significant, and interannual variability is large. Besides, the precipitation trends have large spatial and seasonal variability.

1.2.3 Observed changes in the cryosphere

1.2.3.1 Glacier changes

The evolution of glaciers in HMA is not homogeneous. The general tendency is that glaciers are retreating and losing mass, as shown by in situ mass balance measurements and results from different remote sensing studies [*Bolch et al.*, 2012; *Jacob et al.*, 2012; *Kääb et al.*, 2012; *Yao et al.*, 2012; *Gardelle et al.*, 2013; *Gardner et al.*, 2013; *Farinotti et al.*, 2015]. In situ measurements show that glaciers in the Brahmaputra basin are losing mass in the eastern Himalaya (Parlang Zangbo mountains, ~ -1.1 m w.e. yr^{-1}) and on the Tibetan Plateau (~ -0.4 to -0.55 m w.e. yr^{-1}) [*Yao et al.*, 2012]. The mass balances are also negative in the Ganges basin in Nepal (~ -0.76 m w.e. yr^{-1}) and in Himachal Pradesh (~ -0.91 m w.e. yr^{-1}) [*Yao et al.*, 2012], where part of the glaciers are in the Indus and part in the Ganges basin. In the Karakoram, located in the upper Indus basin, glacier mass balances are less negative or even positive, as shown by geodetic mass balance studies using remotely sensed digitial elevation models (DEMs) (+0.11±0.22 m w.e. yr^{-1}, Table 1.2) [*Gardelle et al.*, 2012]. These findings are also confirmed using IceSat and GRACE remote sensing data [*Kääb et al.*, 2012; *Gardner et al.*, 2013]. These anomalous observations are also known as the 'Karakoram anomaly' [*Hewitt*, 2005]. *Gardelle et al.* [2013] showed that the observed anomaly in the Karakoram extends to the Pamir mountain range, with an estimated average mass balance of +0.14±0.14 mm yr^{-1} from 2000 to 2009, and therefore suggest to revise the terminology of 'Karakoram anomaly' to 'Pamir-Karakoram anomaly'. Later research suggests that the center of the anomaly is located more eastwards over the Kunlun Shan mountains [*Kääb et al.*, 2015]. A review of debris-covered glacier changes in the HKH region shows a similar pattern, with mostly neutral mass balances in the Karakoram and negative mass balances in the other regions [*Scherler et al.*, 2011] (Figure 1.7). According to this analysis glaciers in the northern part of the Central Himalaya are losing mass at the highest rate.

Table 1.2: Glacier mass budget of nine sub-regions, as derived using the geodetic method, i.e. differencing of the SPOT5 DEM with acquisition date mentioned in the table and the SRTM DEM acquired in February 2000. Source: [*Gardelle et al.*, 2013].

Sub-region	Total glacier area (km^2)	Measured glacier area (%)	Acquisition date SPOT5 DEM	Mass balance (m w.e. yr^{-1})
Hengduan Shan	11584	12	24 Nov 2011	-0.33±0.14
Bhutan	4021	34	20 Dec 2010	-0.22±0.13
Everest	6226	23	4 Jan 2011	-0.26±0.14
West Nepal	6849	13	3 Jan 2011	-0.32±0.14
Spiti Lahaul	9043	23	20 Oct 2011	-0.45±0.14
Hindu Kush	6135	13	17-21 Oct 2008	-0.12±0.16
Karakoram East	19024	28	31 Oct 2010	+0.11±0.14
Karakoram West		30	3 Dec 2008	+0.09±0.18
Pamir	9369	34	29 Nov 2011	+0.14±0.14

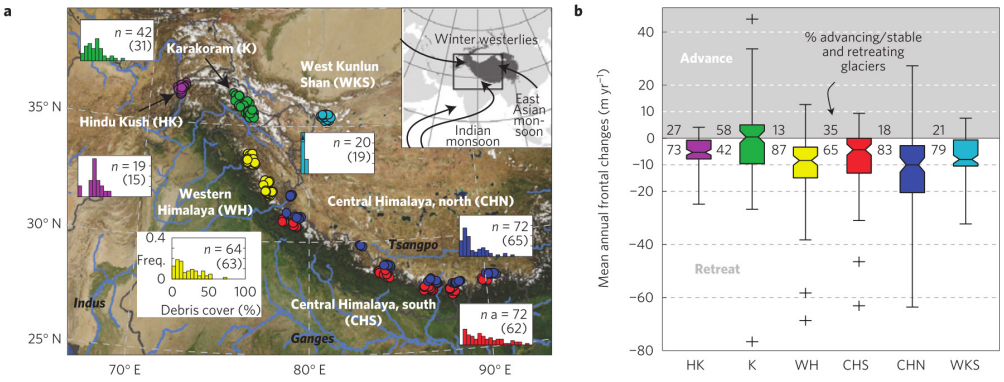

Figure 1.7: Regional distribution of debris-covered and stagnating glaciers. a) Location of glaciers (circles) grouped by region. Histograms give relative frequencies (y-axis, 0 – 40%) of debris cover (x-axis, 0 – 100% in 5% bins). Number of studied glaciers is given in upper-right corner, measured frontal changes in parentheses. Globe depicts location of subset and atmospheric transport directions. b) Regional distribution of mean annual frontal changes. Boxes give lower and upper quartiles and median (notches indicate 95%-confidence intervals). Whiskers extend 2.5 times the interquartile data range, crosses lie outside this range. Numbers left of boxes indicate percentage of advancing/stable (top) and retreating (bottom) glaciers. Reprinted by permission from Macmillan Publishers Ltd: Nature Geoscience [*Scherler et al.*, 2011], ©2011.

For the Tien Shan mountain range, *Farinotti et al.* [2015] used three different approaches to assess glacier changes. They used satellite gravimetry, laser altimetry, and glaciological modeling to estimate the total glacier mass change over the past 50 years. The three approaches yield consistent results and the authors estimate the overall decrease in total glacier area and mass from 1961 to 2012 to be 18±6% and 27±15%, respectively.

The estimates of ice volumes and areas in HMA discussed in section 1.1.2 indicate an average estimate of glacier area being ~9680 km^2 and an average estimate of ice volume being ~3650 km^3. This implies that the average ice thickness is roughly 375 m. Combining this with the observed mass balance trends discussed in this section, yields that a period roughly between 750 and 3750 years would be required to melt this amount of ice, assuming time-invariant glacier mass balances between -0.1 and -0.5 m w.e. yr^{-1}. This is however just a very rough and theoretical estimate for illustration purposes, since ice thicknesses and glacier mass balances are highly variable in space.

1.2.3.2 Snow cover

Snow cover monitoring on a regional scale has started only recently. With the availability of satellite data, near real-time spatial maps of snow cover have become available. However, long term trends in snow cover cannot be established, since these analyses cover a maximum of ten years. Most of the available studies are based on MODIS satellite products. They do not show clear general temporal changes in the snow covered area over the whole HMA region. There is a large inter-annual variation in snow cover and an increasing trend from west to east for HMA from 2000 until 2008 [*Immerzeel et al.*, 2009]. For the Indus basin, during winter a significant decreasing trend in snow cover is identified, but not for other seasons and not for other HMA river basins. A large scale study by ICIMOD also indicated large inter-annual and intra-annual variation in snow cover [*Gurung*

et al., 2011]. Their analysis of trends in snow cover during 2000-2010 did not yield statistically significant trends, but indicated increase in the western and eastern Hindu Kush-Himalayan region and decrease in the central parts. Studies by *Tahir et al.* [2011c, 2015] showed a stable or slight increase in snow cover in the Hunza basin (central Karakoram) and Astore basin (Western Himalayas) between 2000 and 2009, which may be the result of an increase in winter precipitation caused by westerly circulation. On the other hand, decreasing trends in snow cover for westerly-influenced subbasins of the Indus, including Hunza, and increasing trends for the more monsoon-influenced subbasins of the Indus were found [*Hasson et al.*, 2014]. A trend analysis of snow cover in the monsoon-dominated Sutlej basin in the Indus basin indicated a trend of snow cover reduction between 2000 and 2009 [*Mir et al.*, 2015]. A possible explanation of the contrasting trends found in different studies could be related to differences in processing of raw snow cover satellite images [*Hasson et al.*, 2014].

1.3 Climate modeling

1.3.1 Representative Concentration Pathways

Since the release of Intergovernmental Panel on Climate Change (IPCC)'s fifth Assessment Report, four representative concentration pathways (RCPs) have been defined as a basis for long-term and near-term climate modeling experiments in the climate modeling community [*van Vuuren et al.*, 2011b]. The four RCPs together span the range of radiative forcing values for the year 2100 as found in literature, from 2.6 to 8.5 Wm^{-2} (Table 1.3, Figure 1.8). Climate modelers use the time series of future radiative forcing from the four RCPs for their climate modeling experiments to produce climate scenarios. The development of the RCPs allowed climate modelers to proceed with experiments in parallel to the development of emission and socio-economic scenarios [*Moss et al.*, 2010]. The four selected RCPs were considered to be representative of the literature, and included

Table 1.3: Description and visualization of the four representative concentration pathways (RCPs). Source: [*van Vuuren et al.*, 2011b]

RCP	Description
RCP8.5	Rising radiative forcing pathway leading to 8.5 Wm^2 (~1370 ppm CO_2eq) by 2100
RCP6	Stabilization without overshoot pathway to 6 Wm^2 (~850 ppm CO_2eq) at stabilization after 2100
RCP4.5	Stabilization without overshoot pathway to 4.5 Wm^2 (~650 ppm CO_2eq) at stabilization after 2100
RCP2.6	Peak in radiative forcing at ~3 Wm2 (~490 ppm CO2eq) before 2100 and then decline (the selected pathway declines to 2.6 Wm2 by 2100

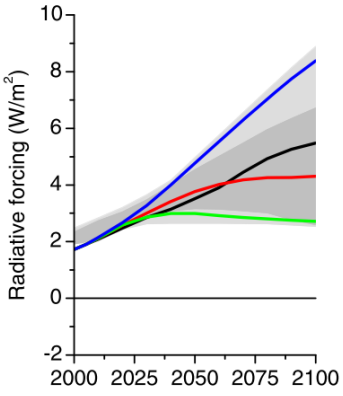

Figure 1.8: RCPs. blue: RCP8.5, black: RCP6, red: RCP4.5, green: RCP2.6. Source: [*van Vuuren et al.*, 2011b]

one mitigation scenario (RCP2.6), two medium stabilization scenarios (RCP4.5/RCP6) and one very high baseline emission scenario (RCP8.5) [*van Vuuren et al.*, 2011b].

Since the four RCPs are considered to be representative of radiative forcing that can be expected by 2100, each of them should theoretically be considered with equal probability to be included in climate change impact studies. However, in climate change impact studies there is usually a trade-off in how many RCPs and how many climate models can be included within the available time and resources, whilst at the same time having the ability of producing robust and reliable results.

Between 1996 and the release of the IPCC's fifth assessment report in 2013 [*IPCC*, 2013], the IPCC used a different set of future scenarios, combining main demographic, economic and technological driving forces with future greenhouse gas emissions. These scenarios were used in some of the literature cited in this thesis. An extensive description of this earlier generation of scenarios can be found in the IPCC's special report on emission scenarios [*IPCC*, 2000].

1.3.2 Types of climate models

Climate is modeled at different spatial scales. General Circulation Models (GCMs) are used to simulate global climate and operate at spatial resolutions ranging from ~100 km^2 to ~250 km^2. Regional Climate Models (RCMs) can be used to simulate regional climate at a typical resolution of ~10-50 km. Climate change information is usually required at a higher spatial resolution since applications like hydrological models, forced by the data from GCMs or RCMs, operate at higher resolutions, down to several meters. For example, the hydrological models used in the research described in this thesis operate at 1 km^2 spatial resolution.

The current state-of-the-art GCMs are organized in the fifth Coupled Model Intercomparison Project (CMIP5) archive [*Taylor et al.*, 2012], which was used as a basis by the IPCC for the generation of its fifth Assessment Report. A similar effort to organize the output from RCMs is the CORDEX framework [*Giorgi et al.*, 2009]. The earlier CMIP3 [*Meehl et al.*, 2007] archive is the main archive used for studies prior to the release of the CMIP5 archive.

1.3.3 Downscaling

Because of the discrepancy in spatial resolution, different downscaling techniques can be applied to overcome differences in resolution when climate models are used to force other models such as hydrological models. Downscaling techniques can be divided in two groups: dynamical downscaling and empirical-statistical downscaling [*Wilby and Wigley*, 1997].

1.3.3.1 Dynamical downscaling

Dynamical downscaling is the nesting of climate models of different spatial resolutions. A GCM, operating at spatial resolutions ranging from ~100 km^2 to ~250 km^2 usually provides the boundary conditions for a RCM that has a nested domain within the GCM domain, and operates at a resolution of ~10-50 km^2. Higher resolutions can be reached when a finer resolution RCM or a high-resolution numerical weather prediction model (which needs to be non-hydrostatic in mountainous areas) is nested within the RCM domain. The RCM then in turn provides the boundary conditions for the finer resolution RCM. On finer scales, Large Eddy Simulation (LES) models can be deployed, which can include atmospheric turbulence in the simulations. Because of the high spatial resolution of RCMs, computational resources are a limiting factor for the temporal and spatial coverage of the simulation [*Fowler et al.*, 2007].

1.3.3.2 Empirical-statistical downscaling

In most climate types, but especially in climate types with large spatial variation, such as the climate in mountainous regions, the GCM or RCM resolution is not sufficient to satisfactory simulate the climate, because climatic variables vary strongly over short distances due to orographic effects. Many processes such as local circulation patterns leading to hydrological extreme events cannot be resolved by GCMs [*Christensen and Christensen*, 2002]. Besides a gap in resolution, GCMs and RCMs exhibit biases with respect to observed climate data. To try to overcome these two problems, additional empirical-statistical downscaling and error correction techniques are required to account for the scale differences between GCMs/RCMs and hydrological models, and to correct for systematic biases between GCMs/RCMs and local-scale observations (Figure 1.9). Empirical-statistical methods are based on statistical relationships between large-scale predictors (climate model data) and local-scale observations [*Wilby and Wigley*, 1997; *Fowler et al.*, 2007; *Maraun et al.*, 2010]. Advantages of statistical downscaling methods include the possibility to provide point-scale climatic variables derived from GCM scale climate model output, the ability to directly incorporate observed data, and the computational efficiency compared to dynamical downscaling. Important disadvantages on the other hand, include the requirement of a sufficiently long and reliable observed historical data series for calibration and the assumption that the statistical relationship

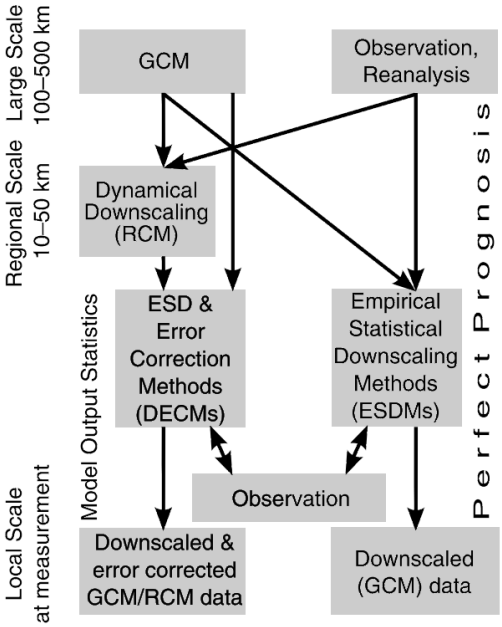

Figure 1.9: Scheme of different statistical downscaling approaches. Traditional empirical-statistical downscaling (right pathway) calibrates the statistical transfer function between large-scale observation/reanalysis data and local-scale observations. Empirical-statistical downscaling and error correction methods (DECMs) (left pathway) are calibrated on RCM or GCM data and local observations, account for downscaling as well as model errors. Adapted from [Themeßl et al., 2011a]. Reprinted by permission from John Wiley and Sons. ©2010 Royal Meteorological Society.

between the large-scale data and the local-scale data stays constant in the future [*Wilby and Wigley*, 1997; *Fowler et al.*, 2007].

Maraun et al. [2010] categorize statistical downscaling methods into 'perfect prognosis (PP)', which include regression models and weather typing schemes, 'model output statistics (MOS)', and 'weather generators (WG)'. Here the categorization by *Maraun et al.* [2010] is followed to summarize the different approaches for statistical downscaling.

Perfect Prognosis statistical downscaling approaches (or traditional empirical-statistical downscaling methods [*Themeßl et al.*, 2011b]) establish links between observed large-scale predictors and observed local-scale predictands. Often, the large-scale observations are replaced by data from reanalysis products. As predictors, variables with high predictive power to predict the variable of interest should be used. These can include various predictors representing the atmospheric circulation, humidity and temperature [*Maraun et al.*, 2010]. Different statistical models can be used to represent the statistical relationships between the large-scale observations and the local-scale observations. These include regression models, which can be linear models, more complex generalized linear models, generalized additive models, vector generalized linear models, or non-linear regression models [*Maraun et al.*, 2010]. Weather type based downscaling is based on the relation of different weather classes to local climate. Climate change can then be estimated by evaluating the change in frequency of the weather classes in the climate model [*Fowler et al.*, 2007].

In Model Output Statistics (MOS) approaches, the statistical relationship between predictors and predicted values is established by using simulated predictor values instead of observed values [*Maraun et al.*, 2010]. MOS combines a downscaling and an error correction step [*Themeßl et al.*, 2011a]. The predictors can be simulated time series or properties of the distributions of climatic variables. The predicted values can be local-scale time series or local-scale distributions of the variable of interest. MOS is mostly used for RCM downscaling, while MOS application for GCM downscaling is still limited [*Eden et al.*, 2012; *Eden and Widmann*, 2014]. Multiple post-processing methods, termed empirical-statistical downscaling and error correction methods (DECMs, Figure 1.9), are based on the MOS approach [*Themeßl et al.*, 2011a]. The most basic MOS approach is the simple delta change or perturbation method [*Prudhomme et al.*, 2002; *Kay et al.*, 2008], which downscales climate models to local scale using change factors. Differences between a future and control GCM run are superimposed on a local-scale baseline observation dataset. Because of the simplicity of this method, a large number of climate models can be downscaled, facilitating the possibility to use a large ensemble of possible future climates in climate change impact studies [*Wilby and Wigley*, 1997]. The major shortcoming of this method is the fact that only changes in the mean, minima and maxima of climatic variables are considered [*Fowler et al.*, 2007], making this less suitable to assess changes in the distribution's tails, i.e. the extreme weather events. Another method with a slightly different concept is the scaling method or direct approach [*Widmann and Bretherton*, 2003; *Lenderink et al.*, 2007]. In this approach the future precipitation is determined as the simulated future precipitation scaled to the ratio of the mean observed and mean control run precipitation.

The Advanced Delta Change (ADC) approach [*van Pelt et al.*, 2012], built on work by *Leander and Buishand* [2007] and *Shabalova et al.* [2003], has the advantage over the classical delta change method that not only changes in the mean are considered, but also the changes in extremes, thus making a non-linear transformation of climate signals derived from climate models. Besides, changes in multi-day precipitation events are also modeled. The approach has been successfully applied in the Rhine basin in Europe [*van Pelt et al.*, 2012]. Multiple succesful applications of the

Leander and Buishand [2007] approach were also demonstrated for the Rhine basin [*Hurkmans et al.*, 2010, *Terink et al., 2010*]. To test the usefulness of the initial non-linear bias-correction approach developed by *Leander and Buishand* [2007] in complex, orographically influenced climate systems, it was used to bias-correct RCM temperature and precipitation for the upper Rhone basin in Switzerland [*Bordoy and Burlando*, 2013]. The authors concluded that the method is able to dramatically reduce the RCM errors for both air temperature and precipitation and that the method could be used successfully for correcting future projections. However, they also observed that an undesired effect of the technique developed by *Leander and Buishand* [2007] was that it generated extreme precipitation values which considerably exceeded the range of the observations.

Quantile mapping [*Boe et al.*, 2007; *Deque*, 2007; *Themeßl et al.*, 2011b] is based on the principle of comparing distributions of a climatic variable in a dataset of historical observations and climate model control run and defining an error function to correct for biases for each quantile in the distribution. This error function is applied to a future climate model run to correct future climate data. The approach can be based on empirical or fitted probability distributions [*Piani et al.*, 2010; *Themeßl et al.*, 2011a]. New extremes can be simulated by linear extrapolation of the error function outside the range of the distribution in the calibration period [*Themeßl et al.*, 2011a].

Weather generators are stochastic models generating random sequences of weather variables, with statistical properties resembling observed weather [*Maraun et al.*, 2010]. They are most commonly used to simulate weather at point locations. Attempts to generate continuous spatial precipitation fields have only recently been extended for downscaling [*Maraun et al.*, 2010].

1.3.4 Future climate change in High Mountain Asia

Given the importance of HMA's water resources for the downstream areas, future changes in the climate may have large impacts on the water resources in HMA and its downstream areas [*Barnett et al.*, 2005; *Rees and Collins*, 2006; *Immerzeel et al.*, 2010]. This section summarizes the main findings considering future climate change in the region. Projections of 32 GCMs from the CMIP5 model ensemble, were analysed for the Hindu Kush-Karakoram and the Himalaya where RCP4.5 and RCP8.5 were considered [*Palazzi et al.*, 2014] (Figure 1.10). The CMIP5 models predicted wetter future conditions in the Himalaya during the monsoon season, with precipitation gradually increasing until the end of the century. For the Hindu Kush-Karakoram, wetter summer conditions were also projected for RCP8.5, whereas in both regions no significant change in winter precipitation was observable. The authors emphasize that no single model performs significantly better than the others, and the projections vary to a large degree.

Six statistically downscaled GCMs project accelerated seasonal increases in temperature and precipitation in the Brahmaputra basin for the period 2000 to 2100, with largest changes on the Tibetan Plateau and smallest changes on the Brahmaputra floodplain [*Immerzeel*, 2008].

An analysis of PRECIS RCM data for the A1B scenario in the Indus basin, until the end of the century, indicated a potential increase in winter precipitation in the upper Indus basin, whereas decreasing winter precipitation is projected for the lower Indus basin [*Rajbhandari et al.*, 2014]. The projected change in monsoon precipitation is highly variable. Greater warming is projected for the upper basin than for the lower basin, indicating that the observed elevation-dependent warming is likely to continue in the future. Furthermore a slightly greater increase in minimum air temperature than maximum air temperature is projected. A stronger warming of winter temperatures is projected, compared to other seasons. All three simulations indicated that changes in precipitation are more uncertain than temperature change.

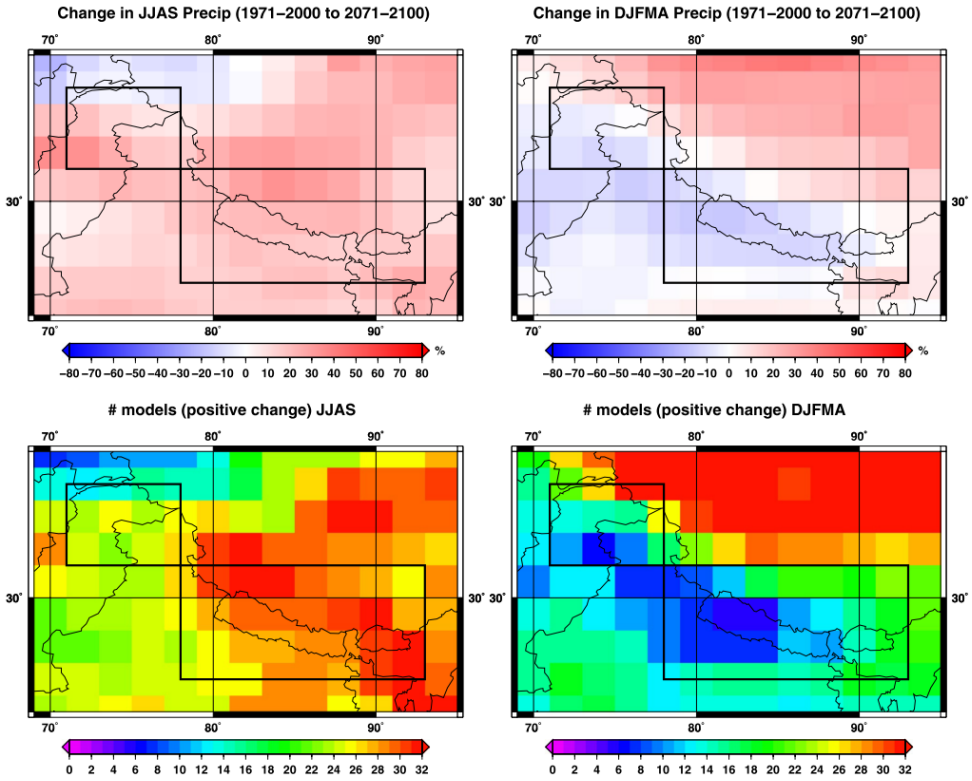

Figure 1.10: Projected percentage precipitation change in 2071–2100 (RCP 8.5 scenario) relative to 1971–2000 in summer (top left) and winter (top right) for the multi-model-mean of the CMIP5 ensemble. Number of models (out of 32) showing, in each 2˚×2˚ pixel, a positive precipitation change (bottom left and right) [*Palazzi et al.,* 2014].

Sharmila et al. [2015] analyzed future projections of Indian summer monsoon variability in CMIP5 GCMs for RCP8.5. The authors first filtered the CMIP5 ensemble for models simulating the monsoon satisfactory over a historical period. Subsequently changes in future monsoon dynamics were assessed for the five remaining models which were considered to provide satisfactory simulations of the monsoon. The projections of these five models are consistent and are summarized as follows:

- The Indian summer monsoon is very sensitive to global warming.
- Summer monsoon mean rainfall is likely to increase moderately.
- Higher rainfall intensity is likely over the core monsoon zone.
- A decreasing number of wet days is likely.
- The monsoon season lengthens due to later cessation.
- Larger inter-annual variability in monsoon intensity is likely.

Earlier projections for summer monsoon climate over India using a RCM and IPCC SRES scenarios already indicated an expected increase in summer monsoon precipitation by 9-16%

in the 2080s compared to the 1970s. Besides, the number of rainy days was projected to decrease accompanied by increasing rainfall intensity on wet days [*Krishna Kumar et al.*, 2011].

There are multiple studies on climate change (and the effects thereof) in smaller areas within HMA. A study using downscaled RCM output for the northern part of the upper Indus basin projected year-round increases in precipitation between 1961-1990 and 2071-2100 (+18% annual mean change) with increased intensity in the wettest months February, March and April (+27% seasonal mean) [*Forsythe et al.*, 2014]. In addition, year-round increases in mean temperature around +4.8 °C were projected. The authors emphasize that the year-round uniformity in temperature increase is in contrast to the asymmetrical recent trend in observations. Furthermore the authors emphasize that this study can be seen as exploratory because only one pair of simulations, from a single RCM driven by one GCM only was used, whereas the use of an ensemble of GCMs or RCMs would provide more information about a range of possible climatic futures in the upper Indus basin.

Downscaled climate change scenarios for the Langtang (upper Ganges) and Baltoro (upper Indus) catchments, using the Quantile Mapping downscaling approach [*Themeßl et al.*, 2011b], showed that a consistent temperature increase is expected in both catchments until the end of the 21st century [*Immerzeel et al.*, 2013]. A stronger increase in precipitation is projected for the Langtang catchment than for the Baltoro catchment, with a larger uncertainty of precipitation projections in Baltoro due to the large variability in GCM results over the Indus basin. For the Hunza basin in the upper Indus basin, *Ragettli et al.* [2013] also found a consistent temperature increase until 2050, based on three downscaled GCMs. Two GCMs indicated an increase in precipitation whereas the third indicated a decrease.

From these highlighted studies it is clear that changes are imminent and that some projected trends are consistent across different studies. It is very likely that the observed, exceptionally strong, warming trend continues for HMA in the future. Furthermore it is likely that the diurnal temperature range increases and that extremely high and low temperatures become more frequent. It is also likely that the amount of precipitation increases and intensifies, especially for the monsoon season. Inter-annual variation and the frequency and magnitude of extremely high precipitation events and dry spells are also likely to increase. However, a large degree of uncertainty remains, as the climatic projections by different climate models vary significantly. Furthermore there is a large gap in scale between the climate models and the scale at which processes are simulated in hydrological models, requiring additional downscaling and bias-correction before climate models can be used to force hydrological models.

1.3.5 Challenges

Given the large, and still growing, number of climate models available that can be used in a climate change impact study, the selection of a representative ensemble of climate models is one of the challenges when conducting such a study. The number of GCMs available for climate change projections is increasing rapidly. For example, the CMIP3 archive [*Meehl et al.*, 2007], which was used for the 4th IPCC Assessment Report [*IPCC*, 2007] contains outputs from 25 different GCMs, whereas the CMIP5 archive [*Taylor et al.*, 2012], which was used for the 5th IPCC Assessment Report [*IPCC*, 2013], contains outputs from 61 different GCMs. These GCMs often have multiple ensemble members resulting in an even larger number of available model runs. Besides, the spread in projections is large as demonstrated in section 1.3.4. Considering the large number of available climate models and constraints in the available computational and human resources, detailed climate change impact studies, such as described in this thesis, cannot include all projections.

In practice, rather one climate model or a small ensemble of climate models is selected for the assessment. Despite the importance of using an ensemble that is representative for the region of interest and shows the full uncertainty range, the selection of models to be included in the ensemble is not straightforward, and can be based on multiple criteria. Often climate models are selected based on their skill to simulate the present and near-past climate [e.g. *Pierce et al.*, 2009; *Biemans et al.*, 2013]. Another approach is the so-called envelope approach, where an ensemble of models covering a wide range of projections for one or more climatological variables of interest is selected from the pool of available models. This approach aims at covering all possible futures as projected by the entire pool of climate models. The decision on which variables are considered depends on the character and goals of the climate change impact assessment. The major drawback of envelope-based approaches is that the models' skill to simulate climate are not considered, since all available climate model runs are considered to have equal plausibility and only changes in the annual means are criteria for selection. On the other hand, selecting only models with a high skill in simulating present and past climate may lead to omission of possible futures. These two contrasting methods to select a climate model ensemble will result in different ensembles, with different mean projections and different uncertainties in the climate change projection. This in turn lead to different projections from the models forced by the future climate data. The uncertainty originating from the spread in climate models' projections is considered to be a large source of uncertainty in climate change impact studies, i.e.: this uncertainty is often larger than model parameter uncertainties, uncertainty stemming from natural variability and structural uncertainties in hydrological models [*Minville et al.*, 2008; *Finger et al.*, 2012]. Therefore, the selection of climate models is a crucial step when conducting a climate change impact study. To summarize in one sentence, selecting a representative ensemble of climate models is not straightforward, but imposes a major challenge.

Besides selecting a representative ensemble of climate models, another main challenge is the downscaling and bias-correction of climate models to higher spatial resolutions that make them suitable to force hydrological models. In this regard especially the downscaling in relation the representation of changes in extremes and seasonal shifts is challenging. Considering the large scale of the research described in this thesis, combined with high spatial resolution that is required to capture spatial variation in mountainous climate sufficiently, applying dynamical downscaling is not feasible for the research described in this thesis. Besides, a recent study that analyzed the uncertainty of the CORDEX South Asia regional climate models showed that the RCMs exhibit large uncertainties in both temperature and precipitation, that they exhibit a large cold bias and that they are unable to reproduce observed warming trends [*Mishra*, 2015]. Furthermore, the GCMs providing the boundary conditions for the RCMs performed better in simulating winter climate than the RCMs. For these reasons, empirical-statistical downscaling of GCMs may be the better option, but the downscaling method to use should be chosen with care, and should be able to include changes in precipitation extremes. Since the availability of a long-term historical climate dataset with sufficient quality is a prerequisite to apply empirical-statistical downscaling methods, this is a challenge as well in the poorly monitored HMA region.

1.4 Hydrological modeling

The hydrological properties and future hydrological changes of single catchments or entire river basins are typically assessed with hydrological models. Hydrological models are simplified representations of components of the hydrological cycle. Many hydrological models are used

and depending on the model's purpose they are based on different concepts and level of detail included. The simpler hydrological models are empirical models. These models are largely based on observed relationships rather than based on simulated physical processes. Usually they are based on the relationship between precipitation and discharge. These models are often lumped, treating a complete watershed as a homogeneous whole. On the other side are the more complex, physically-based models. These models have detailed, descriptions of physical processes, and often need a large number of input variables. They can include energy-balance modeling besides water balance modeling. Physically-based models are often distributed, dividing a watershed into elementary units like grid cells and calculating flows between them. There is a large transition zone between the empirical and physically-based models in terms of the detail of representation of physical processes. Models in the transition zone are often referred to as conceptual models. Similarly there is also a transition in spatial discretization between lumped models and distributed models. The models in the transition zone are often categorized as semi-distributed, dividing a watershed in different areas or subbasins.

1.4.1 Hydrological modeling in mountains

In hydrological models of mountainous environments, the inclusion of routines for snow melt and glacier melt is of key importance. Multiple hydrological models have been applied in HMA and here the most important ones are highlighted. Probably the most widely applied hydrological model in mountainous catchments is the semi-distributed Snowmelt Runoff Model (SRM) [*Martinec and Rango*, 1986]. In the SRM model the catchment is subdivided into elevation zones. For each zone, air temperature is extrapolated from a station elevation to the hypsometric mean elevation of the zone using a temperature lapse rate. Depending on the temperature, precipitation will fall as rain or snow in each of the zones and discharge from snow melt is calculated with a degree-day approach. Discharge from the elevation zones is added together before routing. Applications of this simplified approach in HMA include climate change impact assessments at different spatial scales [*Immerzeel et al.*, 2010; *Tahir et al.*, 2011a].

Another model frequently used is the semi-distributed Hydrologiska Byråns Vatten-balansavdelning (HBV) model [*Bergström*, 1992], which is suitable for catchment-scale applications. HBV is a conceptual model that handles both rainfall and snowfall and models accumulation and melt from a snow pack. The model also includes a routine for glacier melt. Snow melt and glacier melt are calculated with a degree-day approach that includes different degree-day factors for north-facing and south-facing slopes [*Konz and Seibert*, 2010]. Applications of the HBV model in HMA are restricted to catchment scale. Applications have been published for catchments in the Karakoram [*Akhtar et al.*, 2008, 2009] and Central Himalaya [*Konz et al.*, 2007].

A spatially distributed physically-based model for application at catchment scale has been applied in the Langtang and Baltoro watersheds [*Immerzeel et al.*, 2011, 2013]. The model has specific focus on cryospheric processes by including basal sliding of ice [*Weertman*, 1957], and avalanching of snow [*Bernhardt and Schulz*, 2010]. Glacier melt and snow melt are simulated using a degree-day modeling approach, incorporating the aspect of a grid cell.

The Topographic Kinematic Wave Approximation and Integration (TOPKAPI) model is a spatially distributed physically-based model that is suitable for applications at catchment scale [*Liu and Todini*, 2002]. Glacier and snow melt are calculated using an enhanced temperature index approach, taking incoming shortwave radiation and albedo into account besides air temperature. The model can be applied at an hourly time step. Applications in HMA include the Hunza basin in

the Karakoram [*Pellicciotti et al.*, 2012; *Ragettli et al.*, 2013] and Langtang catchment in the Central Himalayas [*Ragettli et al.*, 2015].

The Spatial Processes in Hydrology (SPHY) model [*Terink et al.*, 2015], is a physically-based, distributed model specifically designed for large-scale applications in mountainous areas under data-scarce conditions. This model uses degree-day modeling approaches to calculate melt. The SPHY model is used in the studies described in chapter 4 and chapter 5 of this thesis.

1.4.2 Representation of cryospheric processes in models

A number of hydrological modeling exercises have been conducted in HMA, with varying ways of representing the hydrological processes. Cryospheric processes play important roles in the regional hydrology, but can be simulated in different ways. A simple approach to estimate glacier melt is an ice ablation gradient model, such as applied in the Langtang catchment [*Racoviteanu et al.*, 2013]. In ablation gradient models, a gradient of increasing glacier melt with lowering altitude starting at zero melt at the equilibrium line altitude (ELA) is assumed, based on field measurements. Different ablation gradients can be adopted for debris-free glaciers and debris-covered glaciers. In other approaches glacier and snow melt is often simulated using a degree-day approach [*Hock*, 2003], based on the relation between air temperature and the amount of melt. A calibrated amount of melt water per positive degree of air temperature is assumed. The advantage of this method is that it can be applied in most cases, because air temperature data is mostly available and relatively easy to interpolate to spatial fields. Enhanced degree-day models are also used to integrate more variables such as radiation, aspect or albedo in the model [*Kustas et al.*, 1994; *Pellicciotti et al.*, 2005; *Heynen et al.*, 2013]. Glacier and snow melt can be simulated more accurately using models that include the energy balance, which however has large data requirements and can be applied to a limited modeling extent. Since the amount of snow transported downslope through avalanching can be substantial, it is also simulated in some models [*Bernhardt and Schulz*, 2010; *Immerzeel et al.*, 2013; *Ragettli et al.*, 2015]. Because the cryospheric processes are important in the river basins of HMA, the quality of results generated with the models largely depends on the representation of the relevant processes in those basins. The complexity of models can increase with increased spatial and temporal resolution and data availability. This means that the modeling extent largely determines how complex a model can be. Larger modeling extents allow for lower spatial resolutions of modeling, as the choice for modeling resolution is typically a trade-off between desired resolution and feasibility in terms of human and computation resources. To simulate changes in glaciers, ideally a simulation of changes in glacier geometry due to ice flow is included. This can be done by combining glacier mass balance models with two or three dimensional ice flow dynamics, [e.g. *Huss et al.*, 2007; *Jouvet et al.*, 2008], but these are computationally demanding, require detailed knowledge of glacier bed geometry and ice thickness distribution and a high spatial resolution. *Immerzeel et al.* [2013] use Weertman's sliding law [*Weertman*, 1957] to simulate basal sliding of ice, but this also requires modeling at a high spatial resolution. Therefore, applications of these types of models are limited to the catchment scale. In large-scale models, changes of future glacier changes can be included as scenarios of hypothetical glacier change [*Immerzeel et al.*, 2010]. At the intermediate scale, mass balance models combined with volume-area scaling [*Bahr et al.*, 1997] have been applied outside HMA [*Stahl et al.*, 2008].

1.4.3 Limitations at large river basin scale and data scarcity

While mass balance modeling is rather straightforward to implement and approaches of different complexity can be used (from simple degree-day to energy-balance models for the calculation of

ablation; see previous paragraph), changes in glacier geometry due to ice flow are more complex to include. At the same time, changes in glacier geometry have to be considered in regions where glacier melt makes a significant contribution to total runoff. Ideally, these should be simulated with mass balance models combined with two or three dimensional ice flow dynamics. However, these are computationally demanding and require detailed knowledge of glacier bed geometry and ice thickness distribution. Other approaches have been developed in which ice is transported from the accumulation zone to the ablation zone through basal sliding or creep [e.g. *Immerzeel et al.*, 2011, 2013b], but, like models of full ice flow dynamics, this approach is only applicable for small catchments as it requires modeling at high spatial resolution. In several hydrological models glaciers are treated as static entities that generate melt water and the glacier extent is modified for the future by making crude assumptions on the ice mass balance [e.g. *Immerzeel et al.*, 2010] or by imposing hypothetical glacier scenarios [e.g. *Singh and Bengtsson*, 2004; *Rees and Collins*, 2006; *Singh et al.*, 2006; *Finger et al.*, 2012]. A commonly used alternative method is to use volume-area scaling relationships [e.g. *van de Wal and Wild*, 2001; *Möller and Schneider*, 2010; *Radić and Hock*, 2011]. A parameterization of future glacier evolution has been developed for individual glacier systems [*Huss et al.*, 2010]. Although this approach can be applied to any area, it requires recalibration based on repeated DEMs for different glacier types. Several global scale models that simulate glacier mass balances have been developed [e.g. *Hirabayashi et al.*, 2010; *Radić and Hock*, 2011], but limited approaches to assess glacier evolution at the large river basin scale are available. Only few studies of glacier changes at basin scale have been conducted [*Prasch*, 2010; *Weber et al.*, 2010; *Prasch et al.*, 2013], all using the same modeling approach. This approach uses an energy-balance model for the calculation of melt and therefore requires additional atmospheric input besides air temperature.

1.4.4 Challenges

Forthcoming from the previous paragraph, the robust simulation of glacier responses to climate variations at the large river basin scale and under data-scarce conditions can be identified as a major challenge for the generation of robust climate change impact projections for the hydrology in HMA. Another major challenge is to use a hydrological modeling approach that can cover a large spatial scale, but includes sufficient detail to simulate the hydrology of HMA.

1.5 Research questions and thesis outline

In the preceding sections of this chapter major challenges were identified that should be overcome to obtain robust projections of climate change impacts for the hydrology in High Mountain Asia. In summary, these challenges are:

- Selection of representative ensembles of climate models as basis for climate change projections.
- Downscaling of climate models to make them suitable to force a high-resolution hydrological model while including future changes in precipitation extremes.
- Robust simulation of glacier responses to climate variations at large river basin scale and under data-scarce conditions.
- Developing hydrological modeling approaches at the river basin scale with sufficient detail to simulate the hydrology of HMA, and able to operate under data scarcity.

In the light of these challenges, the importance of the water resources provided by the high mountains in Asia, and the large, still poorly quantified, impact climate change may have on the hydrology of this region, the main research question I try to answer in this thesis is:

- *What are the impacts of climate change on the hydrology in High Mountain Asia?*

I will focus in particular on changes in overall water availability, seasonal shifts in runoff generation and changes in the frequency and magnitude of hydrological extremes.

Given the challenges described in this chapter, the following specific research questions are formulated, which together answer the main research question:

- *How can we select an ensemble of climate models that represents the uncertainty in the future's climate?*

- *How can we use climate change projections to assess changes in mountainous climate including seasonal changes and changes in extremes?*

- *How can we make robust simulations of future glacio-hydrological changes under data-scarce conditions at the large river basin scale?*

Answers to those research questions are pursued in the subsequent chapters of this thesis. Chapter 2 describes an innovative approach for selecting a representative ensemble of General Circulation Models from a larger inventory of climate models. The approach combines selection based on the entire range of changes in air temperature and precipitation as projected by the total inventory of climate models, selection based on the range of projected changes in temperature and precipitation extremes and selection based on climate models' skill in simulating historical climate. In chapter 3 a novel regionalized glacier mass balance model is presented, which is specifically developed to estimate changes in future glacier extent for inclusion in large-scale hydrological models. Chapter 4 describes the application of a large-scale, high-resolution cryospheric-hydrological model to quantify the impacts of climate change for water availability in the upper Indus, Ganges, Brahmaputra, Salween and Mekong river basins until 2050. In chapter 5, the hydrological model is applied to Asia's climate change hotspot; the upper Indus basin [*Immerzeel and Bierkens*, 2012]. Hydrological projections are generated for the entire 21st century. The analysis of the results focuses on changes in sources of runoff, seasonality and hydrological extremes. In chapter 6 the findings of the research are synthesized, including discussions on uncertainty, limitations and future research priorities. The major conclusions and their implications for water management in the region are discussed as well. Chapters 2 to 4 are based on published peer-reviewed scientific journal publications. Chapter 5 is based on a manuscript which is under review for publication in a peer-reviewed scientific journal.

Chapter 2

Selecting a representative ensemble of climate models

Based on: *Lutz, A.F., H.W. ter Maat, H. Biemans, A.B. Shrestha, P. Wester, and W.W. Immerzeel (in press), Selecting representative climate models for climate change impact studies: an advanced envelope-based selection approach, International Journal of Climatology.*

Abstract

Climate change impact studies depend on projections of future climate provided by climate models. The number of climate models is large and increasing, yet limitations in computational capacity make it necessary to compromise the number of climate models that can be included in a climate change impact study. The selection of climate models is not straightforward and can be done following different methods. Usually the selection is either based on the entire range of changes in climatic variables as projected by the total ensemble of available climate models, or on the skill of climate models to simulate past climate. Here we combine these approaches in a three-step sequential climate model selection procedure: 1) initial selection of climate models based on the range of projected changes in climatic means, 2) refined selection based on the range of projected changes in climatic extremes, and 3) final selection based on the climate model skill to simulate past climate. This procedure is illustrated for a study area covering the Indus, Ganges and Brahmaputra river basins. Subsequently the changes in climate between 1971-2000 and 2071-2100 are analysed, showing that the future climate projections in this area are highly uncertain, but that changes are imminent.

2.1 Introduction

Climate change impact studies depend on projections of future climate provided by climate models. Due to their coarse spatial resolution, outputs from General Circulation Models (GCMs) are usually directly downscaled to higher resolution using empirical-statistical downscaling methods, or used as boundary conditions for Regional Climate Models (RCMs), with their outputs being downscaled to higher resolution subsequently. The downscaled outputs are then used to assess future climatic changes and to drive other sector-specific models for climate change impact studies. Outcomes from these studies are used by policymakers to support decisions on climate change adaptation measures.

The number of GCMs available for climate change projections is increasing rapidly. For example, the CMIP3 archive [*Meehl et al.*, 2007], which was used for the 4th IPCC Assessment Report [*IPCC*, 2007] contains outputs from 25 different GCMs, whereas the CMIP5 archive [*Taylor et al.*, 2012],

which was used for the 5th IPCC Assessment Report [*IPCC*, 2013], contains outputs from 61 different GCMs. These GCMs often have multiple ensemble members resulting in an even larger number of available model runs.

Despite improvements in the CMIP5 models compared to CMIP3 in terms of process representation [e.g. *Blázquez and Nuñez*, 2013; *Sperber et al.*, 2013], uncertainty about the future climate remains large [e.g. *Knutti and Sedláček*, 2012], and locally even increases with the larger number of models available [e.g. *Joetzjer et al.*, 2013; *Lutz et al.*, 2013]. Considering the large number of available climate models and constraints in the available computational and human resources, detailed climate change impact studies cannot include all projections. In practice, rather one climate model or a small ensemble of climate models is selected for the assessment. Despite the importance of using an ensemble that is representative for the region of interest and shows the full uncertainty range, the selection of models to be included in the ensemble is not straightforward, and can be based on multiple criteria.

Often climate models are selected based on their skill to simulate the present and near-past climate [e.g. *Biemans et al.*, 2013; *Pierce et al.*, 2009]. Here we refer to this approach as the past-performance approach. Another approach is the so-called envelope approach, where an ensemble of models covering a wide range of projections for one or more climatological variables of interest is selected from the pool of available models. This approach aims at covering all possible futures as projected by the entire pool of climate models. Some approaches consider only the changes in mean air temperature and total annual precipitation [e.g. *Immerzeel et al.*, 2013; *Sorg et al.*, 2014; *Warszawski et al.*, 2014], whereas other approaches consider more climatological variables using cluster analysis algorithms [e.g. *Cannon*, 2014; *Houle et al.*, 2012]. Another approach uses criteria for model independence to generate a representative selection of models from a larger ensemble, where the ensemble of selected models has characteristics that reflect the larger ensemble [*Evans et al.*, 2013].

The decision on which variables are considered depends on the character and goals of the climate change impact assessment. For example a study on future hydrological floods will be most interested in changes of extremely high precipitation events, whereas a study on the impacts of climate change for the exploitation of ski slopes in a mountainous area will most likely consider changes in winter temperature and winter precipitation. The major drawback of envelope-based approaches is that the models' skill to simulate climate are not considered, since all available climate model runs are considered to have equal plausibility and only changes in the annual means are criteria for selection. On the other hand, selecting only models with a high skill in simulating present and past climate may lead to omission of possible futures. These two contrasting methods to select a climate model ensemble will result in different ensembles, with different mean projections and different uncertainties in the climate change projection.

The uncertainty originating from the spread in climate models' projections is considered to be a large source of uncertainty in climate change impact studies, e.g.: this uncertainty is often larger than model parameter uncertainties, uncertainty stemming from natural variability and structural uncertainties in hydrological models [*Minville et al.*, 2008; *Finger et al.*, 2012]. Therefore, the selection of climate models is a crucial step when conducting a climate change impact study.

Here we present an approach to select climate models combining the envelope approach and the past-performance approach. Our goal is to select an ensemble consisting of a manageable number of climate model runs, which still represents all possible futures in terms of future mean air temperature and annual precipitation sums, as well as future changes in climatic extremes. The climate in our study area is complex with mountainous climate types and monsoon dynamics

playing important roles. Because these are often poorly simulated by climate models [*Sperber et al.*, 2013], in addition, we aim at selecting only models that have sufficient skill in simulating the present day climate in our study area.

2.2 Study area and data

We illustrate our approach for a study area covering the Indus, Ganges and Brahmaputra river basins, ranging from their sources in the Hindu Kush-Himalayan mountains and Tibetan Plateau to their mouths in the Arabian Sea and Bay of Bengal respectively (Figure 2.1). This region is considered a climate change 'hotspot' [*De Souza et al.*, 2015; *Nepal and Shrestha*, 2015]. The ensemble of climate models selected using the approach described here, will be downscaled to assess future climate changes at different scales and force hydrological and crop growth models in later stages of the research.

We use the RCP4.5 and RCP8.5 model runs available in March 2013 in the CMIP5 repository [*Taylor et al.*, 2012] as the initial pool of climate models from which our ensemble of models can be selected. For RCP4.5 the total number of model runs available is 94, whereas 69 model runs are available for RCP8.5. For analysis of the projected changes in climatic extremes, we use the database presented in *Sillmann et al.* [2013a] and *Sillmann et al.* [2013b]. This database includes projected changes in the climatic indices as defined by the CCI/CLIVAR/JCOMM Expert Team on Climate Change Detection and Indices (ETCCDI, [*Peterson*, 2005]), for CMIP5 models. To evaluate the model performance of individual GCM runs we use the Watch Forcing Data ERA-Interim (WFDEI) dataset [*Weedon et al.*, 2014], which has been generated using the same methodology as the widely used WATCH Forcing Data [*Weedon et al.*, 2011] by making use of the ERA-Interim reanalysis data

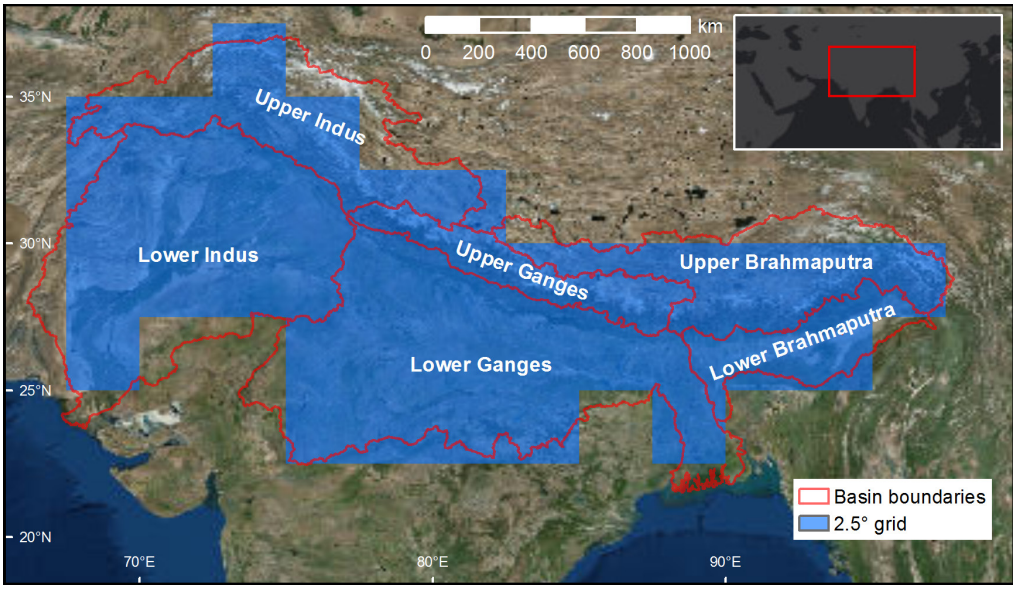

Figure 2.1: Study area comprising the Indus, Ganges, and Brahmaputra river basins. The 2.5° x 2.5°grid used for most steps in the selection procedure is shown in blue.

[*Dee et al.*, 2011]. We use the precipitation data in WFDEI which is bias-corrected to the GPCC precipitation climatology [*Schneider et al.*, 2013].

2.3 Methods

For the selection of GCM runs, the envelope-based approach and the past-performance approach are integrated in a three-step selection procedure (Figure 2.2). The initial selection of climate models is based on the projected average annual changes in the mean temperature and precipitation sum. Subsequently, this selection is refined based on changes in extremes of precipitation and temperature. Ultimately, the final selection is based on validation of the remaining models' past performance to the WFDEI climatic reference product [*Weedon et al.*, 2014].

2.3.1 Selection of Representative Concentration Pathways

In the climate modeling community, generally four representative concentration pathways (RCPs) are used as a basis for long-term and near-term climate modeling experiments. The four selected RCPs are considered to be representative of the scientific literature, and include one mitigation scenario (RCP2.6), two medium stabilization scenarios (RCP4.5/RCP6) and one very high baseline emission scenario (RCP8.5) [*van Vuuren et al.*, 2011b]. RCP2.6 is representative of the low end of the scenario literature in terms of emissions and radiative forcing [*van Vuuren et al.*, 2011a]. Often

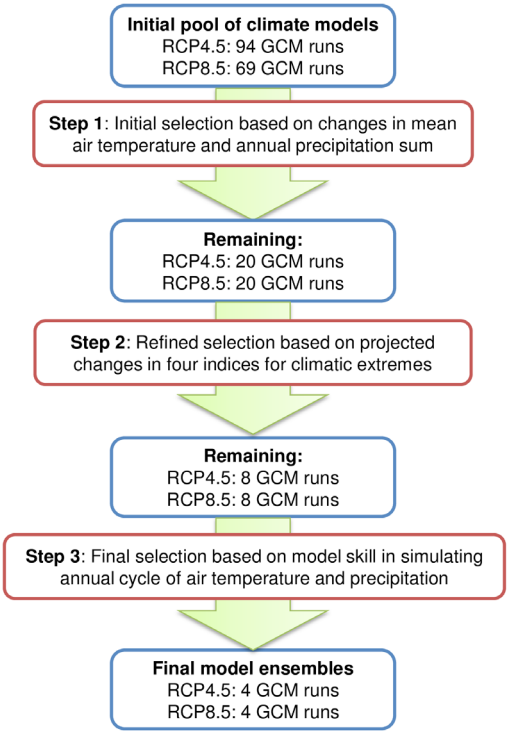

Figure 2.2: Flow-diagram showing the steps taken during the climate model selection procedure.

these scenarios show negative emissions from energy use in the second half of the 21st century. The scenario is shown to be technically feasible, but one of the key assumptions is the full participation of all countries in the world in the short run, including broadening participation beyond OECD countries, and commitment of important OECD countries [*van Vuuren et al.*, 2010]. As robust, realistic climate change scenarios need to be developed to facilitate the planning of adaptation measures we choose not to include RCP2.6 for the climate model ensemble. This leaves the choice between two medium stabilization scenarios (RCP4.5 and RCP6) and one very high baseline emission scenario (RCP8.5). The best choice in that case is to include RCP4.5 and RCP8.5, thus including one medium stabilization scenario and the high emission scenario, and covering the entire range of radiative forcing resulting from RCP4.5, RCP6 and RCP8.5. Although we decided to include only RCP4.5 and RCP8.5, the approach presented here can evidently be applied to model ensembles for the other RCPs as well.

2.3.2 Initial selection (step 1): changes in climatic means

The initial selection is based on the range of projections of changes in mean air temperature (ΔT) and annual precipitation sum (ΔP), between 1971-2000 and 2071-2100, averaged over all 2.5° x 2.5° grid cells included in the model domain (Figure 2.1). This calculation was done using the KNMI Climate Explorer (http://climexp.knmi.nl). For the model runs included in RCP4.5 and RCP8.5 separately, the 10th and 90th percentile values for ΔT and ΔP are determined, after resampling all GCM data to the same 2.5° x 2.5° grid. These values represent the four corners of the spectrum of projections for temperature and precipitation change. The 10th percentile value for ΔT and 10th percentile value for ΔP are in the "cold, dry" corner of the spectrum. The 10th percentile value for ΔT and 90th percentile value for ΔP are in the "cold, wet" corner of the spectrum. The 90th percentile value for ΔT and 10th percentile value for ΔP are in the "warm, dry" corner of the spectrum. The 90th percentile value for ΔT and 90th percentile value for ΔP are in the "warm, wet" corner of the spectrum. The 10th and 90th percentile values are chosen rather than the minimum and maximum projections to avoid selecting outliers, cf. other studies [e.g. *Immerzeel et al.*, 2013; *Sorg et al.*, 2014]. The proximity of the model runs to the 10th and 90th percentile values is derived from the model runs' percentile rank scores corresponding to their projections for ΔT and ΔP with respect to the entire range of projections in the entire ensemble:

$$D_{P_i^T,P_i^P} = \sqrt{\left(\left(\left|P_i^T - P_j^T\right|\right)^2 + \left(\left|P_i^P - P_j^P\right|\right)^2\right)} \qquad (2.1)$$

where $D_{P_i^T,P_i^P}$ is the distance of a model (j)'s ΔT and ΔP (P_j^T and P_j^P respectively) to the corner (i)'s 10th and/or 90th percentile score of ΔT and ΔP for the entire ensemble (P_i^T and P_i^P respectively). For each corner the five models with the lowest values for D and data available at a daily time step are selected from the ensemble. We select only models that have data available at a daily time step because this is a requirement for an empirical-statistical downscaling method to be applied to the GCM runs in a later stage. Nonetheless, model runs with data available at larger time steps are included in the initial pool of available model runs used to calculate the model runs' percentile scores, to have a complete representation of all projected possible futures. The initial selection results in 5 model runs x 4 corners = 20 model runs for each RCP.

For GCMs with ensemble members with different initial conditions available (denoted with rxixpx behind the GCM's name), all members are included in the ensemble that is subjected to the initial selection step. The inclusion of all initial condition ensemble members will lead to a different definition of the 10th and 90th percentile values, than when only one initial condition ensemble

member per GCM is included. We chose to include all initial condition ensemble members because each of them leads to a different future and there is no way to determine which of the initial condition ensemble members should be preferred over others.

2.3.3 Refined selection (step 2): changes in climatic extremes

The number of model runs remaining after the initial selection process is further reduced during the refined selection step. In this step, the model runs are evaluated for their projected changes in climatic extremes. We evaluate the changes in climatic extremes for air temperature and precipitation, by considering the changes in two ETCCDI indices [*Peterson*, 2005] (Table 2.1) for both air temperature and precipitation. For characterization of changes in air temperature extremes we analyse changes in the warm spell duration index (WSDI) and the cold spell duration index (CSDI). For characterization of changes in precipitation extremes we consider the precipitation due to extremely wet days (R99pTOT) and the number of consecutive dry days (CDD). Since the climate model ensemble will be used to force hydrological and crop growth models, we have chosen to analyse changes in R99pTOT and CDD as obvious indicators of precipitation extremes leading to associated hydrological extremes whereas CDD is an important indicator for dry spells affecting crop growth. WSDI is also an indicator for situations where crops may face water stress due to increased evapotranspiration during warm spells. Changes in WSDI and CSDI both have effects on the cryospheric processes (snow- and ice melt/accumulation), which are important in the upstream parts of our study area. The changes in these indices between 2071-2100 with respect to 1971-2000 are calculated from the database constructed by *Sillmann et al.* [2013a; 2013b]. Not all GCM runs used for the initial selection are included in this database. For those runs the ETCCDI indices were calculated using the same procedures as *Sillmann et al.* [2013a; 2013b] used in their study. The indices are calculated from the daily model output, for each individual year in the future period (2071-2100) and reference period (1971-2000), for the individual 2.5° x 2.5° grid cells covering the study area (Figure 2.1). For both periods, the indices are then averaged over the period of thirty years. The changes in the indices are then calculated as a percentual change for the future period with respect to the reference period. Subsequently these changes in the indices are averaged over the 2.5° x 2.5° grid cells covering the study area.

For each model selected during the initial selection, the most relevant index for air temperature and the most relevant index for precipitation are considered. For example, for the models in the warm, wet corner, WSDI indicating warm spells and R99pTOT indicating extreme precipitation events are considered. CDD and CSDI are not considered in that case, but they are considered for models in the dry and cold corners respectively. For the five models initially selected for each corner, the two relevant indices are both ranked and given scores 1 to 5. For example in the warm,

Table 2.1: Description of ETCCDI indices leading the refined selection step.

Meteorological variable	ETCCDI index	Index description
Precipitation	R99pTOT	precipitation due to extremely wet days (> 99th percentile)
Precipitation	CDD	consecutive dry days: maximum length of dry spell (P < 1 mm)
Air temperature	WSDI	warm spell duration index: count of days in a span of at least six days where TX > 90th percentile (TXij is the daily Tmax on day i in period j)
Air temperature	CSDI	Cold spell duration index: count of days in a span of at least six days where TN < 10th percentile (TNij is the daily Tmin on day i in period j

wet corner the model with the largest increase in R99pTOT scores 5 points for that index whereas the model with the smallest increase in R99pTOT scores 1 point for that index. Similarly, the model with the largest increase in WSDI scores 5 points for that index and the model with the smallest increase in WSDI scores 1 point for that index. Both scores are then averaged to obtain a final score. Based on that final score, the two models with the highest scores are selected. Thus for each corner the number of models is reduced from five to two models. For each RCP 4 corners x 2 models = 8 models are selected, which are validated to the climatic reference product in the next step.

2.3.4 Final selection (step 3): past performance

The models remaining after the refined selection are subjected to a validation to the Watch Forcing Data ERA-Interim (WFDEI) dataset [*Weedon et al.*, 2014]. The selected models are compared to the WFDEI for six subdomains (upstream Indus, upstream Ganges, upstream Brahmaputra, downstream Indus, downstream Ganges, downstream Brahmaputra, Figure 2.1). The skill assessment is done for the period 1980-2004, and skill scores are calculated for each model, taking into account all monthly values in this dataset spanning 25 years. Criteria to assess each model's ability to simulate the reference climate are comparisons between the model simulation and WFDEI for monthly average mean air temperature and monthly precipitation sums. The validation is done per subdomain (Figure 2.1) to analyse differences in model performance between the different river basins and between the mountainous upstream parts and downstream parts of the basins, and to avoid compensations of overestimations and underestimations in the entire domain.

To assess the performance of the selected GCM runs, skill scores are derived based on earlier work by *Perkins et al.* [2007], *Sanchez et al.* [2009] and *Kjellström et al.* [2010]. The calculation of temperature and precipitation skills are different. For the calculation of the skill score of temperature the approach by *Perkins et al.* [2007] is used. A metric was developed which "calculates the cumulative minimum value of two distributions of each binned value, thereby measuring the common area between two PDFs":

$$S_{score} = \sum_{1}^{n} \text{minimum}(Z_{GCM}, Z_{OBS}) \tag{2.2}$$

where n is the number of bins used to calculate the Probability Density Function (PDF) for a subdomain, Z_{GCM} is the frequency of values in a given bin from the model, and Z_{OBS} is the frequency of values in a given bin from the observed data. The number of bins used is 100. If a model simulates the observed frequencies perfectly, the skill score (S_{score}) will equal one, which is the total sum of the probability at each bin center in a given PDF.

The skill score of precipitation is based on the work of *Sanchez et al.* [2009], which consists of a collection of five skill score functions taking into account different aspects of the behavior of precipitation. These skill score functions are listed here for our case of comparing GCM data to the WFDEI dataset:

$$f_1 = 1 - \left(\frac{|A_{GCM} - A_{WFDEI}|}{2 \cdot A_{WFDEI}} \right)^{0.5} \tag{2.3}$$

$$f_2 = 1 - \left(\frac{|A^+_{GCM} - A^+_{WFDEI}|}{2 \cdot A^+_{WFDEI}} \right)^{0.5} \tag{2.4}$$

$$f_3 = 1 - \left(\frac{|A^-_{GCM} - A^-_{WFDEI}|}{2 \cdot A^-_{WFDEI}} \right)^{0.5} \quad (2.5)$$

$$f_4 = 1 - \left(\frac{|\overline{P_{GCM}} - \overline{P_{WFDEI}}|}{2 \cdot P_{WFDEI}} \right)^{0.5} \quad (2.6)$$

$$f_5 = 1 - \left(\frac{|\sigma_{GCM} - \sigma_{WFDEI}|}{2 \cdot \sigma_{WFDEI}} \right)^{0.5} \quad (2.7)$$

where A_{GCM} and A_{WFDEI} are the areas below the cumulative distribution functions of the GCMs and WFDEI respectively. Similarly, A^+ and A^- are the areas right and left of the 50th percentile. P is the mean annual precipitation over the total area and σ is the standard deviation of the probability distribution function. The distribution as a whole is taken into account through the total area below the density function (f_1, Eq. (2.3)) and the mean (f_4, Eq. (2.6)). High and low precipitation amounts are taken into account by analyzing the amounts above the 50th percentile limit (f_2, Eq. (2.4)) and the amounts below the 50th percentile limit (f_3, Eq. (2.5)) respectively. The shape of the distribution is considered through the variance (f_5, Eq. (2.7)). The five skill scores are multiplied to yield a total skill score for precipitation. The skill scores for temperature and precipitation are calculated for the control period for the six subdomains separately. Following *Perkins et al.* [2007] the average is taken from the skill scores for both temperature and precipitation and these scores are ranked per subdomain. Subsequently, the rankings of the subdomains are summed for each model run which then results in a ranking for the entire study area, further referred to as general ranking.

The analysis until here is based on the general performance of the model. However, one of the main meteorological phenomena in our study area is the Asian monsoon. Most GCMs have difficulty in simulating the right amount of precipitation and most of them underestimate the precipitation in the monsoon period [*Sperber et al.*, 2013]. The correct representation of monsoonal precipitation is key for hydrological impact studies in this region and an additional skill score specifically designed to quantify the capability of the GCM to simulate the monsoon is introduced. This skill score consists of the absolute bias in precipitation of the GCM for the complete monsoon period (June – September). The highest ranked GCM has the smallest absolute bias and the lowest ranked GCM the largest absolute bias. Finally, the two rankings (general ranking and monsoon ranking) are combined and weighted to reach a final ranking. The weight of the general ranking is 3 and the weight of the monsoonal ranking is 1. Based on this final ranking, the selection from step 2 (two model runs in each corner) is reduced to one model in each corner, forming the final ensemble of climate models.

2.4 Results

2.4.1 Selection of models

2.4.1.1 Initial selection (step 1): changes in climatic means

The initial selection is made based on the projected changes in mean air temperature (ΔT) and annual precipitation sums (ΔP) between 2071-2100 and 1971-2000 thus indicating the projected change during 100 years (Figure 2.3, Tables A1 and A2). For each GCM run, the distance to the 10th and 90th percentile values in the corners is calculated as described in section 2.3.2, and the five models that have daily output available and are located closest to these corners are selected

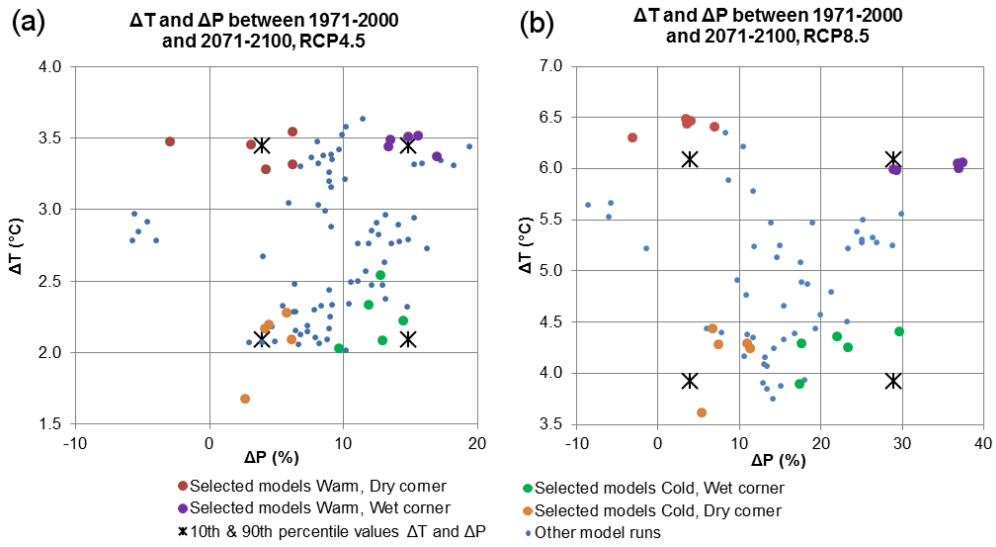

Figure 2.3: Projected changes in mean air temperature (ΔT) and annual precipitation sum (ΔP) between 2071-2100 and 1971-2000 for all included RCP4.5 (a) and RCP8.5 (b) GCM runs. Black crosses indicate the 10th and 90th percentile values for ΔT and ΔP. The model runs selected for step 2 are indicated with colors.

(Figure 2.3). The range in the projections for ΔT and ΔP is much larger for the RCP8.5 model pool than for the RCP4.5 model pool. ΔT ranges from 1.7 °C to 3.6 °C and ΔP ranges from -5.7% to +19.4% for RCP4.5, whereas for RCP8.5 these ranges are 3.6 °C to 6.5 °C and -8.5% to +37.4% respectively. This difference in the ranges of projections is also obvious from the differing degree of clustering in the scatterplots (Figure 2.3). Note that the values are averaged for all 2.5° x 2.5° grid cells in the study area, thus spatial heterogeneity is not considered. The proximity of selected models to the 10th and 90th percentile values can differ substantially. For example, the selected models in the warm, wet corner for RCP4.5 are all relatively close to the 90th percentile values for ΔT and ΔP, whereas some of the selected models in the cold, wet corner have a considerable distance from the 10th and 90th percentile values for ΔT and ΔP. This is partly due to the relatively small number of models with daily output available in this corner of the model pool. In the cold, wet corner for RCP8.5, all models have considerable distance to the 10th and 90th percentile values of ΔT and ΔP.

2.4.1.2 Refined selection (step 2): changes in climatic extremes

For the models remaining after the initial selection, the changes in four ETCCDI indices between 1971-2000 and 2071-2100 are calculated. For each corner, the two models that have the highest combined scores for the changes in the relevant temperature and precipitation indices are selected (models marked yellow in Figure 2.4). This process of calculating a combined score based on ranking can lead to the situation that models with the largest change in one of the ETCCDI indices are not selected. For example, in the warm, dry corner for RCP4.5, the IPSL-CM5A-MR_r1i1p1 and IPSL-CM5A-LR_r2i1p1 models are not selected, although they project the largest changes in CDD and WSDI respectively.

When looking at the combination of changes in mean air temperature, precipitation sums and changes in the ETCCDI indices (Figure 2.5), it is clear that in general the models projecting large

RCP	Projection	model	ΔR99P (%)	ΔCDD (%)	ΔWSDI (%)	ΔCSDI (%)	ΔT (°C)	ΔP (%)	T index rank	P index rank	Combined score
RCP4.5	Warm, dry	CMCC-CM_r1i1p1	98.3	10.5	1162.5	-97.1	3.3	4.2	4	4	4.0
		CMCC-CMS_r1i1p1	56.9	14.3	938.2	-98.4	3.5	-2.9	2	5	3.5
		IPSL-CM5A-LR_r2i1p1	72.2	4.8	886.1	-96.3	3.4	3.1	1	3	2.0
		IPSL-CM5A-LR_r3i1p1	72.9	3.8	961.0	-96.0	3.3	6.2	3	2	2.5
		IPSL-CM5A-MR_r1i1p1	75.6	1.4	1472.0	-99.7	3.5	6.2	5	1	3.0
	Warm, wet	CanESM2_r1i1p1	107.0	-10.0	633.9	-96.7	3.4	17.0	1	4	2.5
		CSIRO-Mk3-6-0_r3i1p1	57.8	-7.5	1600.8	-94.8	3.4	13.3	4	1	2.5
		CSIRO-Mk3-6-0_r4i1p1	109.3	-9.6	1530.3	-95.4	3.5	15.6	2	5	3.5
		CSIRO-Mk3-6-0_r5i1p1	87.7	-3.8	1634.4	-96.9	3.5	14.8	5	3	4.0
		CSIRO-Mk3-6-0_r6i1p1	69.1	-7.8	1563.8	-96.5	3.5	13.5	3	2	2.5
	Cold, wet	bcc-csm1-1_r1i1p1	104.7	-5.6	490.2	-88.8	2.2	14.5	2	4	3.0
		BNU-ESM_r1i1p1	140.3	-6.7	729.3	-85.9	2.5	12.7	3	5	4.0
		CCSM4_r2i1p1	66.9	-2.9	531.9	-84.8	2.0	9.7	4	3	3.5
		CNRM-CM5_r1i1p1	41.9	-0.7	454.2	-90.6	2.3	11.9	1	2	1.5
		IPSL-CM5B-LR_r1i1p1	35.1	-11.8	424.3	-80.7	2.1	12.9	5	1	3.0
	Cold, dry	bcc-csm1-1-m_r1i1p1	46.1	-2.3	569.3	-87.4	2.3	5.8	2	1	1.5
		CCSM4_r6i1p1	45.8	5.6	809.9	-88.2	2.2	4.5	1	5	3.0
		CESM1-BGC_r1i1p1	57.9	4.3	696.0	-85.6	2.1	6.1	3	4	3.5
		GISS-E2-R_r6i1p1	47.8	-2.2	764.7	-81.0	2.2	4.1	4	2	3.0
		inmcm4_r1i1p1	10.5	2.9	347.5	-63.4	1.7	2.7	5	3	4.0
RCP8.5	Warm, dry	CMCC-CMS_r1i1p1	140.2	24.1	1855.1	-99.4	6.3	-3.1	5	5	5.0
		IPSL-CM5A-LR_r1i1p1	125.4	3.3	1627.4	-99.3	6.5	3.5	2	1	1.5
		IPSL-CM5A-LR_r2i1p1	145.7	9.3	1346.7	-99.7	6.5	4.1	1	3	2.0
		IPSL-CM5A-LR_r3i1p1	143.9	6.4	1679.0	-99.7	6.4	6.9	4	2	3.0
		IPSL-CM5A-LR_r4i1p1	140.8	13.7	1651.8	-99.5	6.4	3.6	3	4	3.5
	Warm, wet	CanESM2_r1i1p1	219.0	-17.7	1378.5	-99.6	6.0	28.9	2	2	2.0
		CanESM2_r2i1p1	227.4	-15.2	1623.6	-99.8	6.1	36.9	5	3	4.0
		CanESM2_r3i1p1	295.5	-11.7	1426.1	-100.0	6.1	37.4	3	5	4.0
		CanESM2_r4i1p1	192.9	-12.6	1460.6	-100.0	6.0	29.4	4	1	2.5
		CanESM2_r5i1p1	261.7	-10.1	1242.2	-99.8	6.0	37.0	1	4	2.5
	Cold, wet	bcc-csm1-1_r1i1p1	220.6	-9.6	1215.6	-97.1	4.4	29.7	5	5	5.0
		CNRM-CM5_r1i1p1	75.6	-3.4	884.7	-99.3	3.9	17.4	2	1	1.5
		IPSL-CM5B-LR_r1i1p1	88.4	-16.7	897.8	-97.1	4.2	23.4	4	2	3.0
		MIROC5_r1i1p1	145.3	-12.4	1337.8	-99.8	4.3	17.7	1	3	2.0
		MRI-CGCM3_r1i1p1	157.0	-12.6	1452.5	-97.4	4.4	22.1	3	4	3.5
	Cold, dry	CCSM4_r1i1p1	112.5	7.9	1451.4	-99.7	4.3	11.0	1	4	2.5
		CCSM4_r6i1p1	102.8	5.0	1858.5	-98.3	4.2	11.4	4	1	2.5
		EC-EARTH_r2i1p1	161.6	9.2	1984.5	-99.3	4.4	6.8	2	5	3.5
		EC-EARTH_r9i1p1	175.7	5.5	1994.2	-98.9	4.3	7.4	3	2	2.5
		inmcm4_r1i1p1	30.3	5.6	905.6	-89.6	3.6	5.4	5	3	4.0

Figure 2.4: GCM runs analysed during the refined selection step. Models selected for step 3 are indicated with yellow color.

changes in the means, also project large changes in extremes. For example, for RCP4.5, the models projecting the largest increases in mean air temperature also show the largest increases in warm spells and the largest decreases in cold spells (Figure 2.5, panel a). For RCP8.5 this correlation is less marked (Figure 2.5, panel c). For precipitation, in both RCPs all models project increases in extremely high precipitation events, even the models that project decreasing total precipitation (Figure 2.5, panel b and c). Increases in dry spells (CDD) are projected by models that project

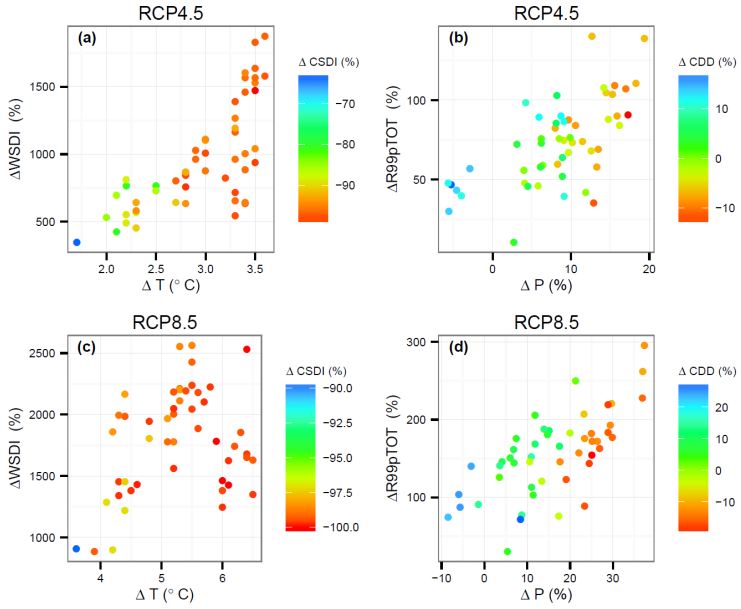

Figure 2.5: Projected changes in mean air temperature (ΔT), warm spell duration index (ΔWSDI), cold spell duration index (ΔCSDI) between 2071-2100 and 1971-2000 for RCP4.5 (a) and RCP8.5 (c). Projected changes in annual precipitation sum (ΔP), precipitation due to extremely wet days (ΔR99pTOT), consecutive dry days (ΔCDD) between 2071-2100 and 1971-2000 for RCP4.5 (b) and RCP8.5 (d).

moderate increases in total precipitation (up to around +10% and +20% for RCP4.5 and RCP8.5 respectively). The generally observed relationship that models projecting a larger increase in total precipitation also project a larger increase in precipitation due to extremely wet days and the strongest decrease in dry periods holds for both RCPs.

The selection of five models in each corner during the initial selection step, may lead to omission of the GCM runs with the largest projected changes in extremes. This is because projected changes in extremes are only considered in the refined selection step, i.e.: we consider the changes in mean air temperature and annual precipitation sum as leading criterion in our selection approach. The observation that the GCM runs located near the tails of the distribution of projected changes in the mean are generally also located near the tails of the distribution of projected changes in extremes (Figure 2.5), supports our sequence of selection steps.

2.4.1.3 Final selection (step 3): past performance

The final selection of models is based on a validation of model performance to the Watch Forcing Data ERA-Interim (WFDEI) dataset. Table 2.2 lists the calculated skill scores for the GCM runs remaining from step 2. The score ranking (Table 2.3) results in selecting the GCM runs for the final ensemble (Table 2.4). Note that this way of selecting GCM runs will omit GCM runs which have good skill for certain subdomains, like for example EC-EARTH_r2i1p1 for the Upper Ganges. The GCM runs which were preselected for the warm, wet corner are the models which perform less in simulating the present climate. For the warm, wet corner in the RCP4.5 scenario the selected

Table 2.2: Skill scores for GCM runs remaining after step 2. Skill scores are calculated for precipitation and air temperature for six subdomains separately. LI=Lower Indus, UI=Upper Indus, LB=Lower Brahmaputra, UB=Upper Brahmaputra, UG=Upper Ganges, LG=Lower Ganges. Note that GCM runs "CMCC-CMS_r1i1p1" and "inmcm4_r1i1p1" are selected in step 2 for both RCP4.5 and RCP8.5, but listed only once in the table.

GCM runs	Precipitation skill scores						Mean air temperature skill scores					
	LI	UI	LB	UB	LG	UG	LI	UI	LB	UB	LG	UG
CMCC-CM_r1i1p1	0.07	0.10	0.24	0.00	0.09	0.14	0.59	0.54	0.65	0.38	0.65	0.64
CMCC-CMS_r1i1p1	0.12	0.06	0.24	0.01	0.15	0.37	0.61	0.53	0.55	0.65	0.57	0.58
CSIRO-Mk3-6-0_r4i1p1	0.02	0.09	0.19	0.41	0.06	0.07	0.50	0.57	0.41	0.62	0.51	0.61
CSIRO-Mk3-6-0_r5i1p1	0.02	0.12	0.17	0.29	0.06	0.06	0.50	0.55	0.40	0.64	0.49	0.56
BNU-ESM_r1i1p1	0.32	0.15	0.10	0.04	0.23	0.29	0.60	0.53	0.40	0.57	0.60	0.43
CCSM4_r2i1p1	0.06	0.07	0.20	0.02	0.27	0.02	0.72	0.49	0.55	0.47	0.65	0.62
CESM1-BGC_r1i1p1	0.07	0.08	0.23	0.02	0.26	0.03	0.75	0.50	0.59	0.50	0.66	0.63
inmcm4_r1i1p1	0.14	0.36	0.15	0.37	0.24	0.21	0.52	0.45	0.27	0.41	0.51	0.59
IPSL-CM5A-LR_r4i1p1	0.06	0.10	0.05	0.29	0.07	0.41	0.61	0.58	0.69	0.43	0.61	0.66
CanESM2_r2i1p1	0.08	0.16	0.13	0.19	0.16	0.11	0.50	0.51	0.33	0.52	0.59	0.54
CanESM2_r3i1p1	0.14	0.16	0.13	0.20	0.11	0.12	0.55	0.46	0.32	0.52	0.63	0.58
bcc-csm1-1_r1i1p1	0.06	0.57	0.12	0.25	0.08	0.09	0.61	0.56	0.43	0.52	0.56	0.52
MRI-CGCM3_r1i1p1	0.04	0.26	0.05	0.10	0.03	0.16	0.48	0.45	0.59	0.41	0.50	0.57
EC-EARTH_r2i1p1	0.01	0.27	0.14	0.20	0.10	0.63	0.51	0.39	0.36	0.47	0.40	0.45

GCM ranked only 10th in the overall final ranking. This may be indicative that such a future is less probable. Another striking feature is that the same two models (inmcm4_r1i1p1 and CMCC-CMS_r1i1p1) are selected for both RCP4.5 and RCP8.5.

Figure 2.6 and Figure 2.7 show the monthly average of mean air temperature and monthly average of precipitation respectively for each subdomain, for all models that were selected during step 2. As could be expected, a large difference between all models is witnessed. Figure 2.6 shows that all GCMs show a cold bias in wintertime for the Upper Indus. Some models also have difficulties in simulating the annual precipitation cycle (Figure 2.7). Especially in the upper Indus, the models diverge in the simulation of the annual cycle. Mountainous climate is less densely monitored, leading to larger errors in mountainous areas in reference climate datasets, such as WFDEI. The larger biases between the simulation models and WFDEI over the mountainous areas may be partly attributed to this. The spread between the climate models is large but there is reasonable agreement for most of the subdomains. The mean and annual cycle are reasonably captured. Most GCM runs underestimate the precipitation in the lower subdomains. The analysis on the annual cycles indicates that the selected models are correctly selected. The large observed biases emphasize the necessity of applying downscaling and bias-correction methods before the GCM outputs can be used in an impact study.

Table 2.3: Ranking of the GCM runs for the six subdomains (LI: Lower Indus, UI: Upper Indus, LB: Lower Brahmaputra, UB: Upper Brahmaputra, LG: Lower Ganges, UG: Upper Ganges)

RCP	Projection	GCM run	Rank per subdomain						Total	General Rank	Monsoon Rank	Final Rank
			LI	UI	LB	UB	LG	UG				
RCP4.5	Warm, dry	CMCC-CM_r1i1p1	8	10	1	14	7	5	45	**7**	**7**	**6**
		CMCC-CMS_r1i1p1	4	12	3	9	8	3	39	**5**	**4**	**4**
	Warm, wet	CSIRO-Mk3-6-0_r4i1p1	14	8	7	1	11	9	50	**10**	**8**	**10**
		CSIRO-Mk3-6-0_r5i1p1	13	7	8	2	12	13	55	**14**	**9**	**14**
	Cold, wet	BNU-ESM_r1i1p1	1	4	10	10	3	7	35	**2**	**3**	**1**
		CCSM4_r2i1p1	3	14	4	13	2	11	47	**8**	**13**	**9**
	Cold, dry	CESM1-BGC_r1i1p1	2	13	2	11	1	10	39	**5**	**10**	**5**
		inmcm4_r1i1p1	9	2	14	3	4	4	36	**3**	**2**	**2**
RCP8.5	Warm, dry	IPSL-CM5A-LR_r4i1p1	6	5	5	6	9	2	33	**1**	**12**	**3**
		CMCC-CMS_r1i1p1	4	12	3	9	8	3	39	**5**	**4**	**4**
	Warm, wet	CanESM2_r2i1p1	10	6	12	7	5	12	52	**12**	**5**	**12**
		CanESM2_r3i1p1	5	11	13	5	6	8	48	**9**	**6**	**8**
	Cold, wet	bcc-csm1-1_r1i1p1	7	1	9	4	10	14	45	**7**	**11**	**7**
		MRI-CGCM3_r1i1p1	12	3	6	12	13	6	52	**12**	**14**	**13**
	Cold, dry	EC-EARTH_r2i1p1	11	9	11	8	14	1	54	**13**	**1**	**11**
		inmcm4_r1i1p1	9	2	14	3	4	4	36	**3**	**2**	**2**

Table 2.4: Final selected ensemble of GCM runs with projected changes in mean air temperature, precipitation and ETCCDI indices between 1971-2000 and 2071-2100 averaged over the study area.

RCP	Projection	GCM run	ΔT (°C)	ΔP (%)	ΔWSDI (%)	ΔCSDI (%)	ΔR99P (%)	ΔCDD (%)
RCP4.5	cold,wet	BNU-ESM_r1i1p1	2.5	12.7	729.3	-85.9	140.3	-6.7
	cold,dry	inmcm4_r1i1p1	1.7	2.7	347.5	-63.4	10.5	2.9
	warm, dry	CMCC-CMS_r1i1p1	3.5	-2.9	938.2	-98.4	56.9	14.3
	warm, wet	CSIRO-Mk3-6-0_r4i1p1	3.5	15.6	1530.3	-95.4	109.3	-9.6
RCP8.5	cold, dry	inmcm4_r1i1p1	3.6	5.4	905.6	-89.6	30.3	5.6
	warm, dry	CMCC-CMS_r1i1p1	6.3	-3.1	1855.1	-99.4	140.2	24.1
	cold, wet	bcc-csm1-1_r1i1p1	4.4	29.7	1215.6	-97.1	220.6	-9.6
	warm, wet	CanESM2_r3i1p1	6.1	37.4	1426.1	-100.0	295.5	-11.7

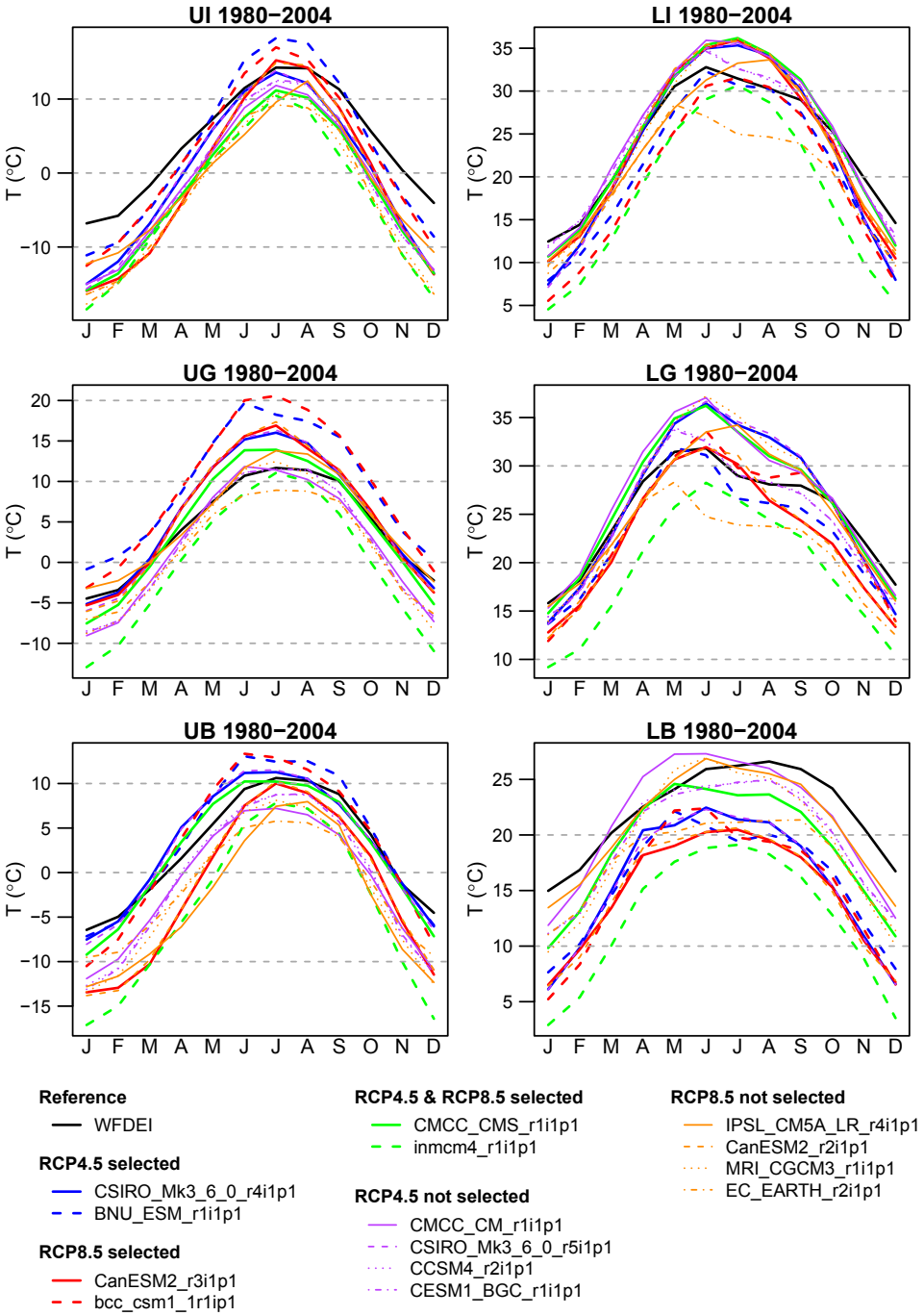

Figure 2.6: Average annual cycles of temperature for WFDEI and GCM runs per subdomain (UI=Upper Indus, LI=Lower Indus, UG=Upper Ganges, LG=Lower Ganges, UB=Upper Brahmaputra, LB=Lower Brahmaputra).

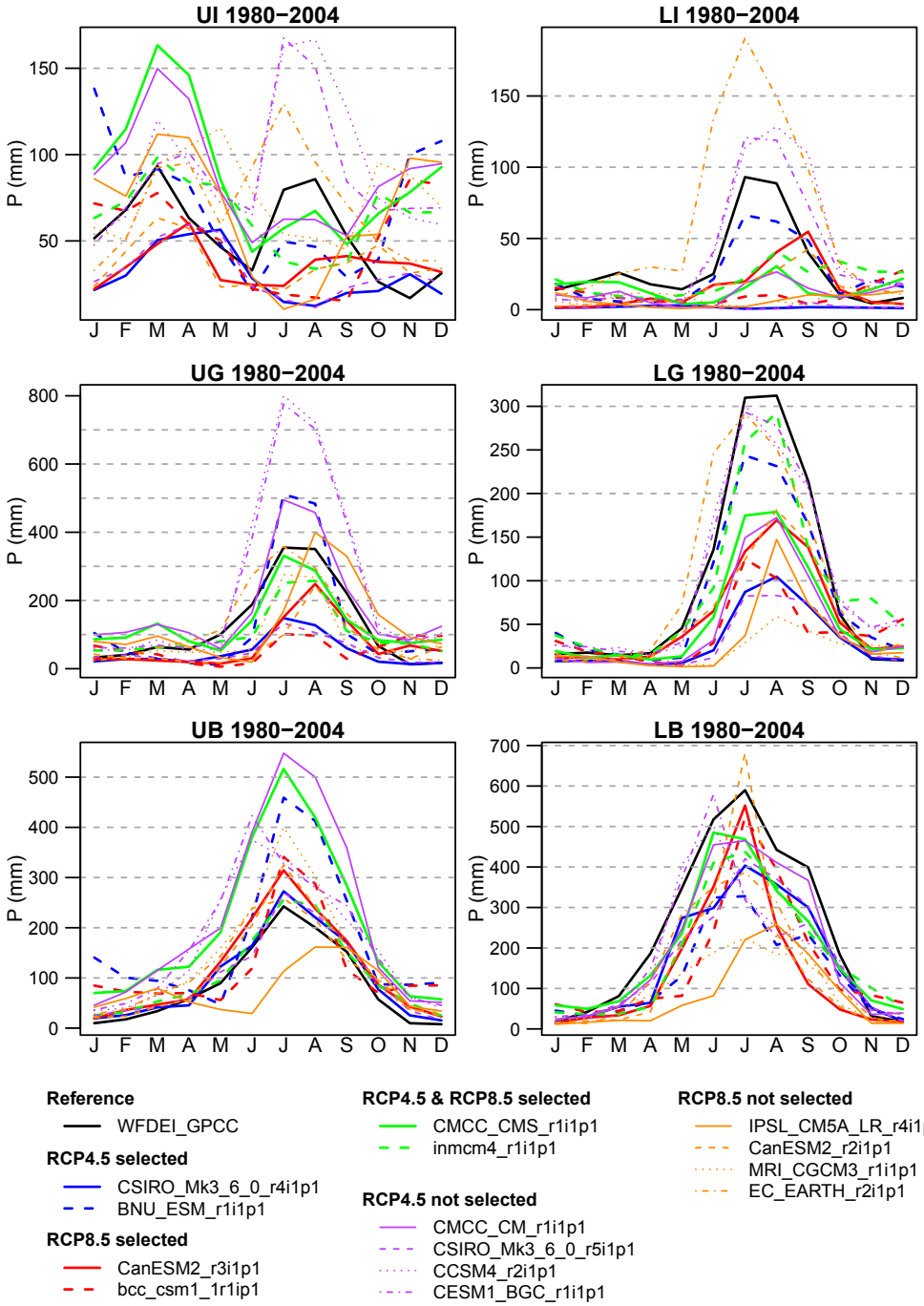

Figure 2.7: Average annual cycles of precipitation for WFDEI and GCM runs per subdomain (UI=Upper Indus, LI=Lower Indus, UG=Upper Ganges, LG=Lower Ganges, UB=Upper Brahmaputra, LB=Lower Brahmaputra).

2.4.2 Future climate in the Indus, Ganges and Brahmaputra basins

Averaged over the basins, according to the selected ensembles of GCM runs, mean air temperature increases by 1.7 to 3.5 °C for RCP4.5 and 3.6 to 6.3 °C for RCP8.5 between 1971-2000 and 2071-2100 (Table 2.4). However, there is large spatial variability within the study area (Figure 2.8). The largest increases in mean air temperature are projected for the upstream mountainous parts of the river basins, whilst the lowest increases are projected for the most downstream parts of the basins. The difference in projected temperature increase between the mountainous upstream and lower downstream parts of the river basin is several degrees. This elevation-dependent warming is in line with what was found in historical temperature records [*Rangwala and Miller*, 2012; *Pepin et al.*, 2015]. Our analysis shows that the observed elevation-dependent warming may become more pronounced in the future. The uncertainty within the ensemble is in general slightly larger for the downstream basins compared to the upstream basins for RCP4.5, although the opposite is observed for the Brahmaputra basin. For RCP8.5, the largest uncertainty in the projections is observed for the upstream basins.

For precipitation, in RCP4.5 the largest increases are projected for the eastern part of the lower Indus and the western part of the lower Ganges (Figure 2.8). At the same time, the uncertainty in the projections within the ensemble is also largest for this region. The RCP8.5 ensemble shows the largest increases in precipitation in the lower Brahmaputra basin, with the largest uncertainty in the projection also in that region. The uncertainty in model projections is spatially more uniform for the RCP8.5 ensemble than for the RCP4.5 ensemble. Note that for both RCPs the strongest decrease in precipitation is projected for the western part of the Indus basin. Traversing the Indus basin from west to east, the projected precipitation decrease changes to precipitation increase. These differences in projected precipitation changes may well be related to the contrasts in climate between the western Indus basin, with strong climatic influence from westerly systems, and the eastern Indus basin, which has a monsoon-dominated climate [*Bookhagen and Burbank*, 2010; *Maussion et al.*, 2014].

In addition to large spatial variability, seasonal variability in the climate change projections is large as well (Figure 2.9). The projected change in temperature shows a significant seasonal pattern for both RCPs. Averaged over the study area, both ensembles project the largest temperature increases for the drier winter months, and smallest temperature increase for the wet summer months. For both RCPs the uncertainty in projections is larger for the winter months, compared to the monsoon season (June-September). The uncertainty in model projections for temperature is larger for the RCP8.5 ensemble than for the RCP4.5 ensemble.

The intra-annual projections of precipitation change show some remarkable features (Figure 2.9). For the RCP4.5 ensemble, in general precipitation increases are projected for the monsoon season. Especially for July and August the spread between the projections is extremely large (for July ranging from almost no increase to 225% increase). For January the mean projection indicates decreasing precipitation, for February unchanged precipitation and slight precipitation increase for March and April. For May and June only small changes are projected. The uncertainty in the projections however is large here as well. Remarkable is also the strong projected precipitation increase in December, with an extremely large uncertainty in the projections. For RCP8.5, the intra-annual patterns in precipitation change are quite similar. Remarkable is the observation that the extremely large model spread as observed for July, August and December in the RCP4.5 ensemble, does not occur for any month in the RCP8.5 ensemble. Still, large uncertainty is observed for most months in the RCP8.5 ensemble, with both positive and negative projections of precipitation change for 10 out of 12 months.

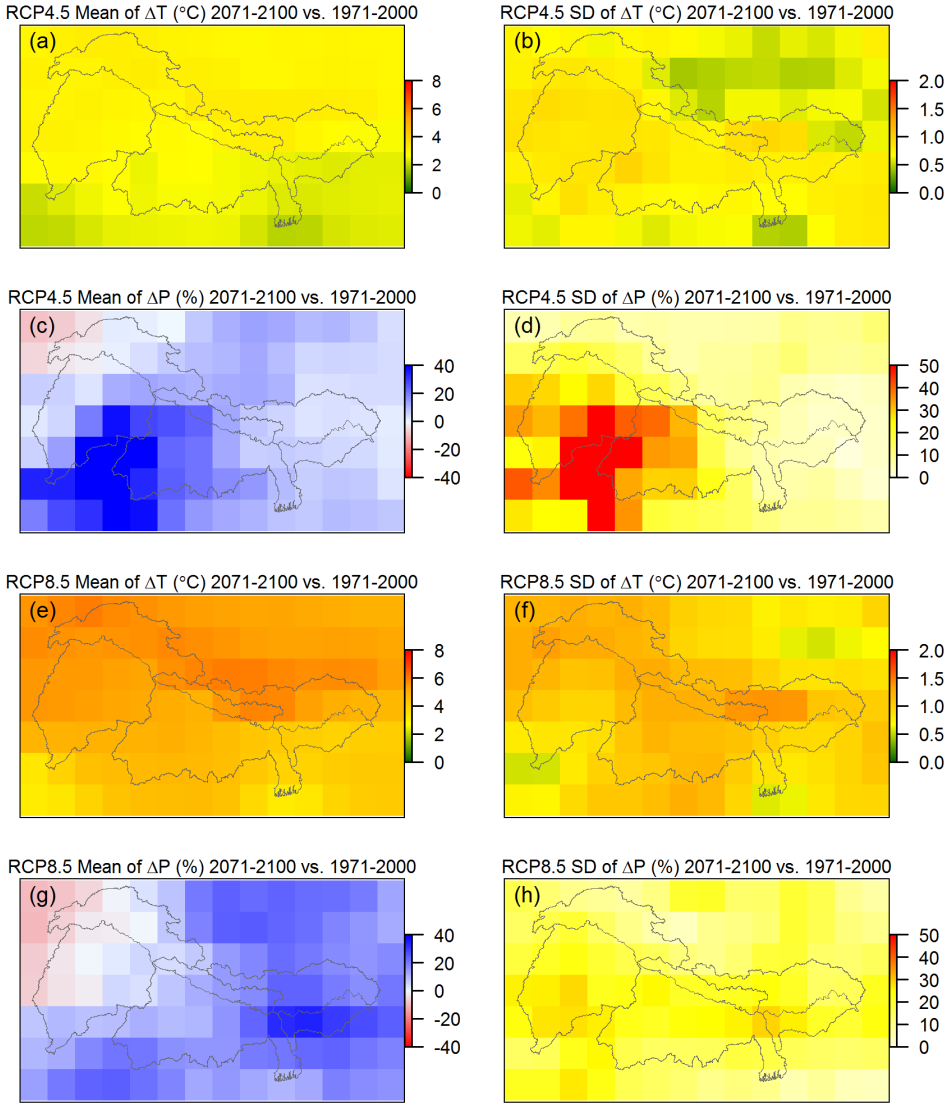

Figure 2.8: Projected changes between 1971-2000 and 2071-2100 in mean air temperature and annual precipitation sum in the Indus, Ganges and Brahmaputra basins. Upper panels show results for RCP4.5 model ensemble and lower panels show results for RCP8.5 model ensemble. Left panels show the mean of the model ensemble and right panels show the standard deviation of the model ensemble. Grey lines indicate upper and lower basin boundaries.

Regarding the projected changes in extremes, the wettest, driest, warmest, and coldest projections for the two ensembles are analyzed (Figure 2.10). For RCP4.5, the model with the largest projected increase in precipitation shows the largest increase in extreme precipitation events in the Ganges basin and the eastern part of the lower Indus basin. Decreases in precipitation due to extremely wet days are projected for the western part of the Indus basin. This also holds for the model with the

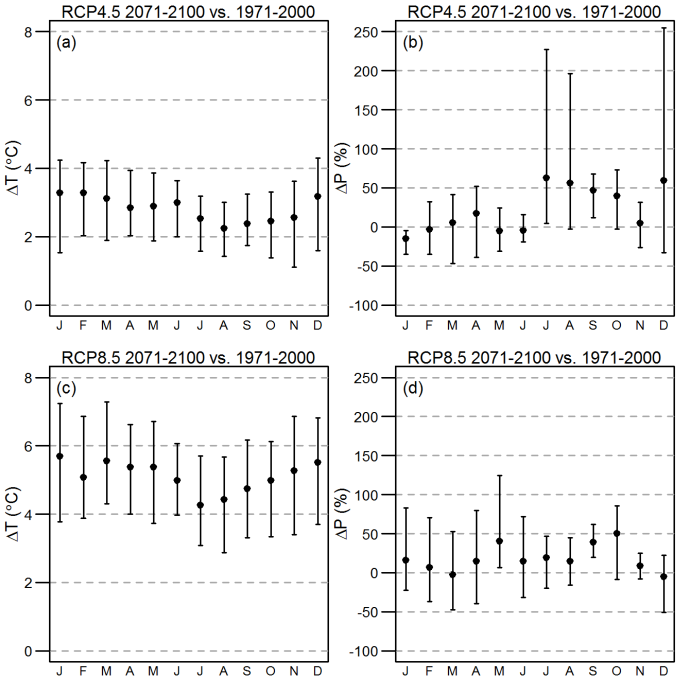

Figure 2.9: Study-area averaged monthly projected changes in temperature and precipitation between 1971-2000 and 2071-2100. Dots indicate model ensemble mean projection and whiskers indicate the range of projections according to the model ensemble.

largest projected increase in precipitation for RCP8.5. The western part of the Lower Indus basin is an area where a decreasing precipitation trend is projected (Figure 2.8). The largest increase in precipitation due to extremely wet days is projected in the Brahmaputra basin, according to this GCM run. An increase in dry spells is projected for almost the entire study area for both the RCP4.5 and RCP8.5 model ensemble. The strongest increases in dry spells are projected for the lower Ganges and upper Brahmaputra basins for both RCPs.

The duration of warm spells according to the warmest members in both ensembles increases for the entire study area. For both RCP4.5 and RCP8.5 the increase is strongest for the lower Indus basin. The duration of cold spells on the other hand, according to the coldest members in both ensembles, decreases for the entire study area. For RCP4.5, the decrease is smallest in the upper Indus and western part of the lower Indus basin, whereas strongest decreases are projected for the upper Brahmaputra basin. For RCP8.5, some grid cells even show a decrease in CSDI of 100%, meaning no period of at least six days in a row with the daily minimum temperature smaller than the 10th percentile temperature occurs during 2071-2100.

2.5 Discussion

Although our method aims to combine the strengths of envelope-based and past performance based selection of GCMs for impact studies a few limitations remain.

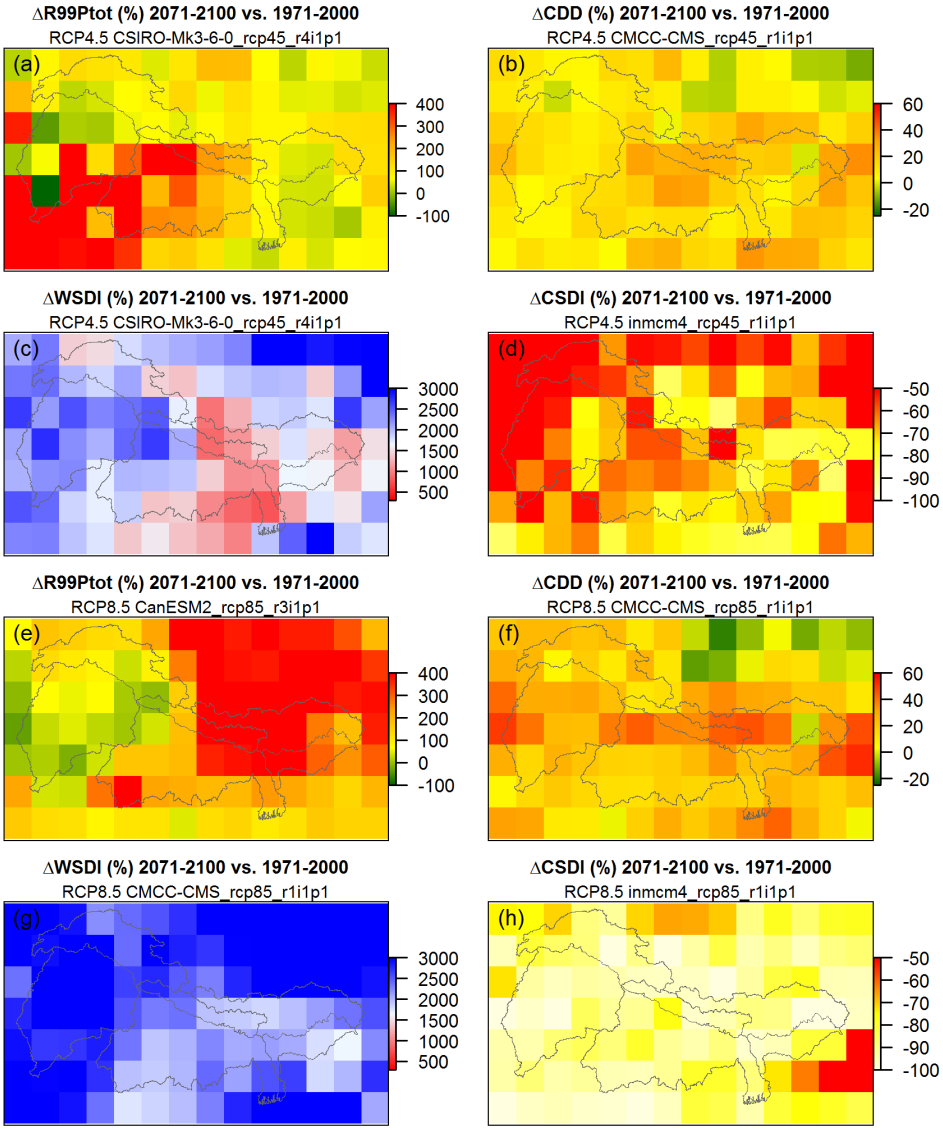

Figure 2.10: Projected changes in ETCCDI indices between 1971-2000 and 2071-2100 for RCP4.5 (a-d) and RCP 8.5 (e-h). Changes in the corresponding index are shown for the wettest (a,e), driest (b,f), warmest (c,g) and coldest (d,h) members in the 4-model ensembles.

The first issue is related to the scale of the application. During the first selection step projected changes are averaged over the entire area and this may dilute the spatial variation in projected changes. The same scaling issues apply to selection based on the changes in the extremes in the second step of our approach. This is not unique to our approach, but holds for most studies that cover a large spatial domain. A potential solution is to divide the study area into multiple parts and apply the selection approach to each part independently. However, the drawback of this approach is

the introduction of physical inconsistencies and erroneous boundary effects in the climate forcing at the transition from one GCM to another.

The second limitation relates to the fact that the envelope of changes in means is leading in the selection approach. This may result in a reduction in the range of projections of changes in climatic extremes in the ensemble. The same holds for the final step, when model runs are selected based on their skill in simulating past climate. Because the selection based on skill is introduced in the last step, with less GCM runs available to select from than before step 1 and step 2, the selected models do not necessarily have the best skill in simulating past climate. This indicates that the sequence of selection, or weighting of different criteria, is not fixed and may be subject to changes, depending on the type of climate change impact study. Another approach combining skill and envelope is introduced by *McSweeney et al.* [2012]. For a study area in Vietnam the researchers first eliminate model runs that do not have sufficient skill in simulating the monsoon, given its importance for their study area, before assessing the range of projections provided by the remaining models. In our approach we choose the range in projected climate change to be leading over the historical performance to ensure including all possible futures as projected by the CMIP5 multi-model ensemble, which is desirable for planning of adaptation strategies. Previous analyses of CMIP5 GCMs' skills to simulate the precipitation patterns in our study area, which are largely dominated by monsoon dynamics, showed that CMIP5 GCMs have poor skills in simulating the important features of the precipitation dynamics in our study area [*Sperber et al.*, 2013; *Palazzi et al.*, 2014; *Sperber and Annamalai*, 2014]. Since no single model or group of models clearly stands out in performance for our study area, this constitutes another reason to prefer to include all possible futures. To show how the chosen ordering of selection steps affects the model skill of the selected ensembles, we test how the model skill of selected models compares to model skill in the total model ensembles. Figure 2.11 shows how the biases in air temperature and precipitation in the ensembles of model runs remaining after selection step 2 correspond to the biases in the total model ensembles for winter season, monsoon season and at annual scale. Although the distributions differ slightly and especially for the winter season, the distributions of the selected models and total model ensembles are generally in the same magnitude, indicating that the skills of the selected models are comparable to the skills of the models in the entire ensemble. Thus we conclude that there is no significant bias towards models with poorer skills in the selected model ensembles.

Third, the weighting of different skill scores introduces a degree of subjectivity. In our approach of testing a model's past-performance we assign more weight to the model's skill in simulating the entire annual cycle of precipitation and temperature than to its skill in simulating the monsoon. Furthermore we assign equal weight to the indicators for precipitation extremes and temperature extremes in calculating model scores in step 2 of our approach. We have chosen to assign larger weight to the model's skill to simulate the entire annual cycle of precipitation and temperature and equal weight to air temperature and precipitation extremes because cryospheric processes in the upstream parts of the basins are important for the hydrological regimes of these basins [*Schaner et al.*, 2012; *Lutz et al.*, 2014]. Changes in these cryospheric processes are driven by the combined effect of changes in precipitation and temperature. In each of these issues, the weighting could be adjusted for other studies, depending on which climatic variables are more important in each particular case.

Finally, our approach assumes independency of all model runs, whereas some models share identical model code or use the same forcing and validation data, leading to model interdependency [*Jun et al.*, 2008; *Masson and Knutti*, 2011; *Knutti et al.*, 2013]. In our case where we include multiple initial condition ensemble members of the same GCM, this interdependency is particularly large.

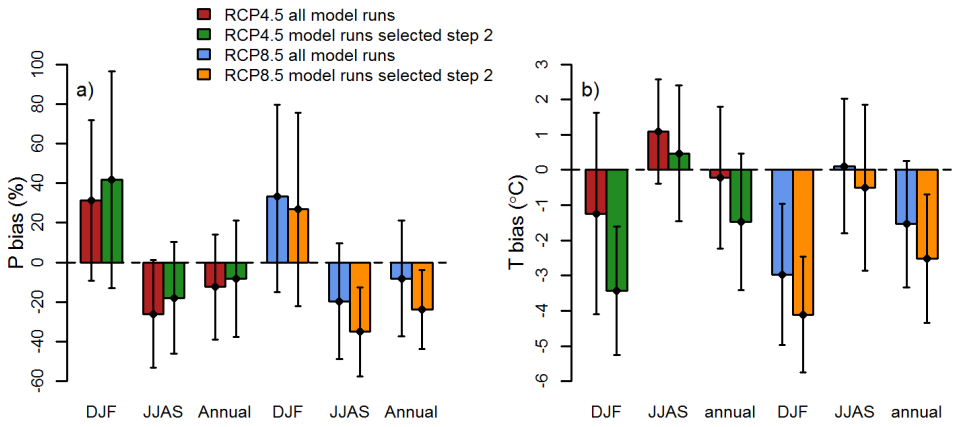

Figure 2.11: Comparison of GCM biases in all model runs and model runs remaining after selection step 2. Biases are calculated using monthly data for 1980-2004 with respect to WFDEI data [*Weedon et al.*, 2014], for precipitation (a) and mean air temperature (b). Biases are calculated for the winter season (DJF), monsoon season (JJAS) and annually. Bars indicate the ensemble mean biases and whiskers indicate the standard deviations of the ensemble's biases.

The approach as described here could be expanded by considering weighting metrics for the degree of CMIP5 model interdependencies [e.g. *Sanderson et al.*, 2015a, 2015b].

The use of GCMs for climate change impact studies is common practice, although the usefulness of this approach has recently been questioned [*Kundzewicz and Stakhiv*, 2010; *Bakker*, 2015]. As also demonstrated in this study, the biases between GCM simulations and observations are large, and many GCMs lack the skill to simulate important regional climatic features, such as the Asian monsoon in our case [*Sperber et al.*, 2013]. Dynamic and empirical-statistical downscaling and bias-correction methods may help to reduce the biases, but cannot completely bridge them [*Pielke and Wilby*, 2012]. This stresses that the currently available climate change projections must be used with caution when defining climate change adaptation policies.

2.6 Conclusions

The selection of climate models for climate change impact studies is not straightforward, while at the same time it is a crucial step when conducting such a study. The approach we introduce in this study seeks the optimal balance between ensuring that the selected GCMs represent changes in average and extreme climatic conditions well, but at the same time have reasonable skill in simulating the past climate, with a particular focus on the monsoon dynamics.

The ensembles of selected GCM runs for RCP4.5 and RCP8.5 show that the uncertainty of future climate in this region is very large. Projections of mean air temperature indicate an increase ranging from 1.7 °C to 6.3 °C between 1971-2000 and 2071-2100, averaged over the three river basins, with stronger warming at higher altitudes. The uncertainty in future precipitation is larger, with area-averaged projections ranging from -3.1% to +37.4%. All GCM runs included in the selected ensembles project increases in warm spells and decreases in cold spells. Besides, all selected GCM runs project increases in extremely high precipitation events, even the GCM runs

that project decreases in annual precipitation sum. Model runs projecting decrease in precipitation project increasing dry spells, and model runs projecting strong increases in precipitation project a reduction of dry spells. However, an increase in dry spells is projected by the model runs that project a minor increase in precipitation. These numbers are averages over the entire Indus, Ganges and Brahmaputra river basins. Spatial variability as well as seasonal variability, in terms of the mean projections and the uncertainty in the projections, are very large. This means that the future climate of the region remains very uncertain, which may compromise defining adequate adaptation policies.

Chapter 3

Simulating future glacier extent at the large river basin scale

Based on: *Lutz, A.F., W.W. Immerzeel, A. Gobiet, F. Pellicciotti, and M.F.P. Bierkens (2013), Comparison of climate change signals in CMIP3 and CMIP5 multi-model ensembles and implications for Central Asian glaciers, Hydrology and Earth System Sciences, Vol. 17, pp. 3661 – 3677.*

Abstract

Central Asian water resources largely depend on melt water generated in the Pamir and Tien Shan mountain ranges. To estimate future water availability in this region, it is necessary to use climate projections to estimate the future glacier extent and volume. In this study, we evaluate the impact of uncertainty in climate change projections on the future glacier extent in the Amu and Syr Darya river basins. To this end we use the latest climate change projections generated for the upcoming IPCC report (CMIP5) and, for comparison, projections used in the fourth IPCC assessment (CMIP3). With these projections we force a regionalized glacier mass balance model, and estimate changes in the basins' glacier extent as a function of the glacier size distribution in the basins and projected temperature and precipitation. This glacier mass balance model is specifically developed for implementation in large-scale hydrological models, where the spatial resolution does not allow for simulating individual glaciers and data scarcity is an issue. Although the CMIP5 ensemble results in greater regional warming than the CMIP3 ensemble and the range in projections for temperature as well as precipitation is wider for the CMIP5 than for the CMIP3, the spread in projections of future glacier extent in Central Asia is similar for both ensembles. This is because differences in temperature rise are small during periods of maximum melt (Jul-Sep) while differences in precipitation change are small during the period of maximum accumulation (Oct-Feb). However, the model uncertainty due to parameter uncertainty is high, and has roughly the same importance as uncertainty in the climate projections. Uncertainty about the size of the decline in glacier extent remains large, making estimates of future Central Asian glacier evolution and downstream water availability uncertain.

3.1 Introduction

The fate of Asian glaciers under climate change has been the topic of a heated scientific debate [*Cogley et al.*, 2010; *Immerzeel et al.*, 2010; *Kargel et al.*, 2011; *Bolch et al.*, 2012; *Sorg et al.*, 2012]. A main reason for this is the lack of systematic cryospheric observations and the absence of robust methods that can assess glacier evolution under climate change at the large river basin scale

[*Unger-Shayesteh et al.*, 2013]. Downstream water availability in several large Asian rivers is highly sensitive to changes in snow and glacier extent [*Immerzeel and Bierkens*, 2012], and large populations depend on the water generated upstream. This dependence is likely to increase as irrigated areas further expand under population growth [*Wada et al.*, 2011].

To assess future changes in high mountain hydrology, glacio-hydrological models forced by climate scenarios are used. Future glacier extent is a combined result of the glacier mass balance and ice-flow dynamics. While mass balance modeling is rather straightforward to implement and approaches of different complexity can be used (from simple degree-day to energy-balance models for calculation of ablation), changes in glacier geometry due to ice flow are more complex to include. At the same time, changes in glacier geometry have to be considered in regions where glacier melt makes a significant contribution to total runoff. Ideally, these should be simulated with mass balance models combined with two or three dimensional ice flow dynamics [e.g. *Huss et al.*, 2007; *Jouvet et al.*, 2008], but these are computationally demanding and require detailed knowledge of glacier bed geometry and ice thickness distribution. Other approaches have been developed in which ice is transported from the accumulation zone to the ablation zone through basal sliding or creep [e.g. *Immerzeel et al.*, 2011, 2013], but, like models of ice flow dynamics, this approach is only applicable for small catchments as it requires modeling at high spatial resolution. In several hydrological models glaciers are treated as static entities that generate melt water and the glacier extent is modified for the future by making crude assumptions on the ice mass balance [e.g. *Immerzeel et al.*, 2010] or by imposing hypothetical glacier scenarios [e.g. *Singh and Bengtsson*, 2004; *Rees and Collins*, 2006; *Singh et al.*, 2006; *Finger et al.*, 2012]. A commonly used alternative method is to use volume-area scaling relationships [e.g. *van de Wal and Wild, 2001; Möller and Schneider*, 2010; *Radić and Hock*, 2011].

A parameterization of future glacier evolution has been developed for individual glacier systems [*Huss et al.*, 2010]. Although this approach can be applied to any area, it requires recalibration based on repeated Digital Elevation Models (DEMs) for different glacier types. Several global scale models that simulate glacier mass balances have been developed [e.g. *Hirabayashi et al.*, 2010; *Radić and Hock*, 2011], but limited approaches to assess glacier evolution at the large river basin scale are available. To our knowledge only few studies of glacier changes at basin scale have been conducted [*Prasch, 2010; Weber et al., 2010; Prasch et al.*, 2012], all using the same modeling approach. This approach uses an energy-balance model for the calculation of melt and therefore requires additional atmospheric input besides air temperature. Thus, there is a strong need for an approach that can be applied at the large river basin scale, requires a minimum of data inputs which are readily available and which generalises changes in glacier extent over large areas without the need to model individual glaciers. At the same time this approach has to yield a reliable estimate of future glacier extent at the large river basin scale.

Models to estimate future ice areas and volumes are commonly forced by air temperature and precipitation provided by General Circulation Models (GCMs) which are downscaled to the study region. However, there is large spread in the GCM projections [Hawkins and Sutton, 2009, 2010; Radić and Clarke, 2011]. This large spread is especially true for precipitation in Asia [*Immerzeel et al.*, 2010]. There is growing agreement that impact studies should be forced by an ensemble of GCMs outputs [*Hawkins and Sutton*, 2009, 2010]. While this has been done for North America [e.g. *Radić and Clarke*, 2011; *Zhang et al.*, 2011], river basins originating in the European Alps [e.g. *Huss*, 2011; *Farinotti et al.*, 2012], for river basins worldwide [e.g. *Nohara et al.*, 2006], or for selected glaciers [e.g. *Giesen and Oerlemans*, 2010], no detailed assessments are available for Central Asia. *Hawkins and Sutton* [2009, 2010] identified three main sources of uncertainty in future climate

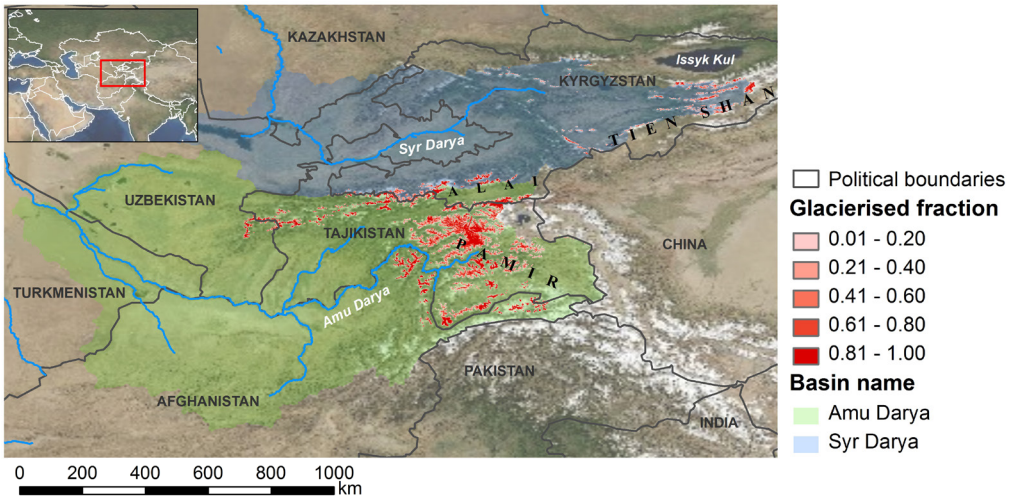

Figure 3.1. Upstream parts of the Amu and Syr Darya river basins (in green and pale blue, respectively), the main river system (blue lines), the initial glacierized fraction per 1 km grid cell (red shades) and political boundaries (black lines).

projections: i) model uncertainty due to the structural differences among GCMs, by which different models produce different projections for the same radiative forcing; ii) scenarios uncertainty due to different radiative forcing; and iii) uncertainty due to the natural climate variability. They showed that the first source of uncertainty is the larger throughout the century for both temperature and precipitation. It seems therefore imperative to take it into account in impact studies of glacier changes.

The aim of this study is to quantify the impact of uncertainty in climate change projections on the future glacier extent in the Amu Darya and Syr Darya river basins; two melt-water influenced rivers which provide the most important water sources in the Central Asian region. Therefore we analyse the differences in uncertainty range between the latest climate change projections provided by the fifth Coupled Model Intercomparison Project (CMIP5) generated for the fifth assessment report of the Intergovernmental Panel on Climate Change (IPCC), and climate change projections used for the fourth IPCC assessment report (CMIP3). These projections for the climate from 2008 to 2050 are analysed at a monthly scale, and the results are used to force a glacier model simulating the future response of glaciers and changes in glacier geometry at the basin scale. We quantify the uncertainty in glacier projections as a result of the range in the climate change projections, and show how this uncertainty differs between the CMIP3 and CMIP5 ensembles. Moreover, the sensitivity of the presented approach to the model parameters is separately addressed, and the approach is validated.

3.2 Study area

The sources of the Amu Darya and Syr Darya rivers are located in the Pamir and Tien Shan mountains respectively (Figure 3.1), and both rivers drain into the Aral Sea. Water allocation is a highly sensitive topic in the region. The upstream countries (Kyrgyzstan and Tajikistan) use water

mainly for hydropower production during winter, whereas the downstream countries (Uzbekistan, Turkmenistan and Kazakhstan) utilize water for irrigation during summer where around 22 million people depend on irrigated agriculture [*Siegfried et al.*, 2012]. Glacier melt provides an important source of water in both basins, given the dry and warm climate downstream [*Kaser et al.*, 2010; *Sorg et al.*, 2012]. The total glacierized area is 10,289 km^2 (1.3% of total 799,261 km^2 basin area) in the Amu Darya basin and 1596 km^2 (0.14% of total 1,117,625 km^2 basin area) in the Syr Darya basin, as calculated from the Randolph Glacier Inventory version 2.0 [*Arendt et al.*, 2012b], which for Central Asia is a compilation of data acquired between 1960 and 2010. Significant reductions in area and volume have been reported for the Tien Shan [*Khromova et al.*, 2003; *Aizen et al.*, 2007a, 2007b; *Bolch*, 2007; *Narama et al.*, 2010; *Siegfried et al.*, 2012] and Pamir mountains [*Khromova et al.*, 2006] during the last decades.

3.3 Data

3.3.1 Digital elevation models

In this study two DEMs are used. Both are based on the Shuttle Radar Topographic Mission (SRTM) DEM at a nominal resolution of 90 m. For the downscaling of GCMs, this DEM is resampled to 1 km resolution. From here on, this DEM will be referred to as the 1 km DEM, and 1 km will also be the spatial resolution of the glacier model. For sub-grid calculations, the SRTM DEM at 90 m resolution is used. This DEM is referred to as the 90 m DEM.

3.3.2 Climate data

A dataset of precipitation and temperature spanning thirty years (1978-2007) is used as reference for the climate change assessment. For this period, we use the Asian Precipitation Highly-Resolved Observational Data Integration Towards Evaluation of Water Resources (APHRODITE, [*Yatagai et al.*, 2012]) dataset for precipitation and Princeton's Global Meteorological Forcing Dataset (PGMFD, [*Sheffield et al.*, 2006]) for temperature. APHRODITE is a long-term continental-scale daily precipitation product based on a dense network of rain gauges, with spatial resolution of 0.25˚ (≈18-30 km in the studied area). The PGMFD was constructed by combining a suite of global observation-based datasets with the National Centers for Environmental Prediction – National Center for Atmospheric Research (NCEP – NCAR) reanalysis and it has a daily resolution and a spatial scale of 0.5˚ (≈36-60 km in the studied area). Daily precipitation data are bilinearly interpolated to 1 km resolution from the APHRODITE 0.25˚ gridded precipitation dataset grid cell centers. Gridded daily average near-surface air temperature data at 1 km resolution are obtained by bilinear interpolation from grid cell centers in the PGMFD 0.5˚ gridded temperature dataset, which are subsequently corrected for elevation using the 1 km DEM and a vertical temperature lapse rate (Table 3.1).

3.3.3 Climate change projections

We use the set of global climate change simulations which is used as basis for the upcoming fifth assessment report of the Intergovernmental Panel on Climate Change (IPCC), the CMIP5 multi-model ensemble [*Taylor et al.*, 2012]. All simulations which were available online in the PCMDI database (http://cmip-pcmdi.llnl.gov/cmip5/) earlier than 15 December 2011 are included in the analysis. In order to compare the CMIP5 multi-model ensemble to the previous generation of global

Table 3.1: Model parameters used in the glacier model. DDF_{CI} and DDF_{DC} were calibrated in a related study [Immerzeel et al., 2012a], MB_{OBS} is taken from [*WGMS*, 2011].

Parameter	Parameter description	Value
T_{lapse}	Temperature lapse rate	-0.0068 °C m^{-1}
$CorT$	Temperature correction	-3.48 °C
DDF_{CI}	Degree-day factor debris-free glaciers	7.94 mm °C^{-1} day^{-1}
DDF_{DC}	Degree-day factor debris-covered glaciers	3.97 mm °C^{-1} day^{-1}
MB_{OBS}	Average of observed mass balance, (WGMS, 2011), see Table 3.2	-0.47 m w.e. year^{-1}

climate change simulations, the CMIP3 multi-model ensemble [*Meehl et al.*, 2007], which is the basis of the fourth IPCC assessment report, is also analysed.

3.3.4 Glaciers

Glacier covered areas in the Amu and Syr Darya river basins are extracted from the Randolph Glacier Inventory version 2.0 (RGI 2.0) dataset [*Arendt et al.*, 2012b]. We updated the RGI 2.0 with more recently mapped glacier outlines (outlines provided by T. Bolch). The updates include outlines for the large glacier systems in the Fedchenko glacier region, which are not available in RGI 2.0 as well as more accurate outlines for numerous other glaciers in the Pamir and Tien Shan mountain ranges. We assume this compiled dataset of glacier extent to represent the glacier extent at the end of the reference period (2007), and to form the starting point for the future simulations of glacier extent.

From this dataset, the size distribution of glaciers is extracted (Figure 3.2). In the Amu Darya and Syr Darya river basins combined, 50% of the total glacier area consists of glaciers with a surface area smaller than 25 km^2 and 11% of the glacier area consists of glaciers smaller than 1 km^2. The

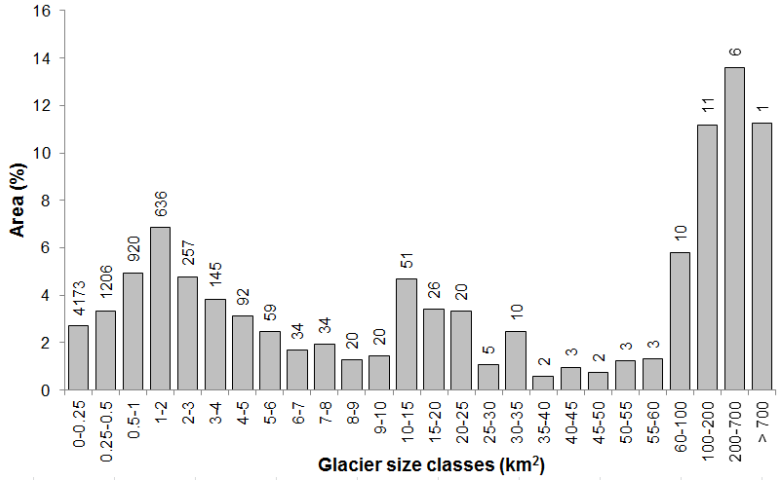

Figure 3.2. Distribution of glacier area over glacier size classes for the two basins combined. The numbers on top of the bins represent the number of glaciers in the particular size class.

median glacier size in the basin is 0.21 km^2. From this distribution 26 different glacier size classes are defined and used for further analysis (Figure 3.2).

The dataset with glacier extents is also used for the calculation of an initial fractional glacier cover per 1 km grid cell, to be used as starting point for the glacier model simulations. Each 1 km grid cell of the 1 km DEM is assigned a fractional glacier cover varying from 0 (no glacier cover) to 1 (entirely covered with glaciers) (Figure 3.1).

For model calibration, the average of the observed annual mass balance in the region's mountains is used, which is approximately -0.47 m water equivalent (w.e.) per year between 1978 and 2007, based on five glaciers with mass balance records in the region [*WGMS*, 2011] (Table 3.2).

3.4 Methods

3.4.1 Downscaling of GCM output

Downscaling of the GCMs outputs is necessary due to the large scale discrepancy between the climate models (operated on grids of 100 km grid distance or more) and the glacier model (operating on the 1 km scale). Since in our study, the major focus is on uncertainty stemming from the climate simulations, we include as many climate simulations as possible. We consider the CMIP3 and CMIP5 simulations based on all available emission scenarios: SRES B1, A1B, and A2 [*IPCC*, 2000] in the case of CMIP3, and rcp2.6, rcp4.5, rcp6.0, and rcp8.5 [*Meinshausen et al.*, 2011] in the case of CMIP5. Since it is difficult to associate probabilities to the emission scenarios, we do not use any prior assumption and give the same weight to all scenarios. We therefore calculate percentiles for all GCM realizations according to the inverse number of GCM realizations per scenario. We extract the grid cells of the climate models over the study region and analyse projected annual and monthly temperature and precipitation averaged over the period 2021 – 2050 and compare it to the period 1961 – 1990. Hence, the climate change signals refer to the changes during 60 years. We do this for the simulations in both ensembles. The range of temperature and precipitation projections is shown in Figure 3.3 for both ensembles.

We derive the 10th (Q10), 25th (Q25), 50th (Q50), 75th (Q75) and 90th (Q90) percentile values of the changes in precipitation and temperature for each month for the entire CMIP3 and CMIP5

Table 3.2: Observed mass balance data since for 1978-2007 for five glaciers in the study area (WGMS, 2011).

Glacier name	Mountain range	Latitude	Longitude	Mass balance (1978-2007)
		(decimal degrees)	(decimal degrees)	(mm w.e. y^{-1})
Abramov	Pamir – Alai	39.63	71.60	-538
Golubin	Tien Shan	42.47	74.50	-349
Kara Batkak	Tien Shan	42.10	78.30	-523
Tuyuksuyskiy	Tien Shan	43.05	77.08	-514
Urumqi	Tien Shan	43.08	86.82	-419
Average				-469
Standard deviation				82

ensemble. We compute a transient "delta change" value for 1961-2050 by linearly interpolating the changes between 1961-1990 and 2021-2050. This is done for every percentile and every month. For each simulated year in 2008-2050 we select a random year from the 1x1 km reference period climate dataset (1978-2007) and we superimpose the basin-averaged monthly temperature and precipitation change values to construct a transient time series from 2008 to 2050. These time series are then used as meteorological forcing for the glacier model, which is run with all the combinations of the percentile values of changes in precipitation and temperature. This well established "delta change" approach [*Arnell*, 1999; *Kay et al.*, 2008] removes large parts of climate models biases, which cancel out in the climate change signals. We have selected the delta change method as it allows us to include a large number of climate scenarios.

3.4.2 Glacier model

The method used in this study to estimate the glacier evolution is an approach with minimum data requirements. We use a mass balance model with parameterization of glacier area changes and subsequent aggregation of regional glacier characteristics. The model estimates the fractional glacier cover (G_F) for each 1 km grid cell at a monthly time step from 2008 until 2050. The model requires monthly average temperature and monthly precipitation sums, terrain elevation data, the initial fractional glacier cover for each 1 km grid cell and the distribution of glaciers over terrain elevation and glacier size classes as data input (section 3.3). Figure 3.4 provides a schematic representation of the modeling steps. First, one basin scale hypsometric curve is derived for the study area, which describes the distribution of glacierized area over the terrain elevation. Subsequently we calculate a monthly basin scale specific glacier mass balance. We do this by specifying the accumulation area

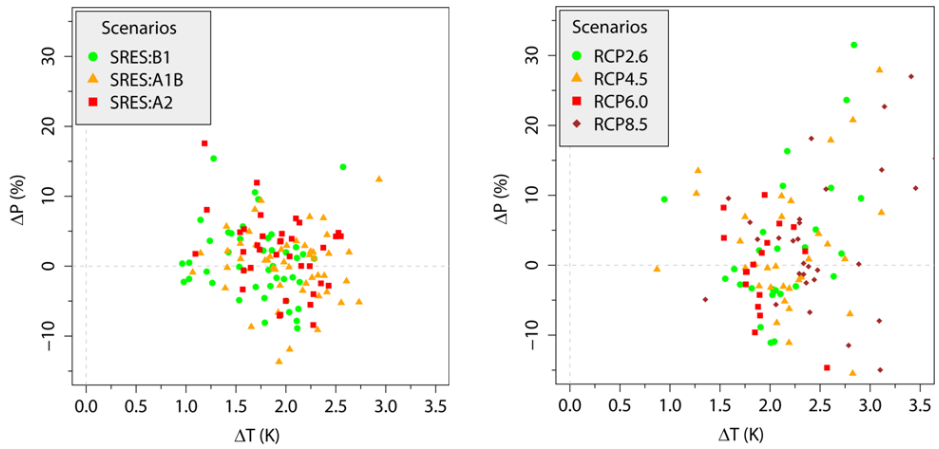

Figure 3.3. Range of projected changes (2021-2050 relative to 1961-1990) in yearly average temperature and precipitation in the upstream areas of the Amu and Syr Darya river basins. The left panel shows model runs used for the fourth assessment report of the IPCC (AR4) for three different emission scenarios (A1B (53 runs), A2 (36 runs), B1 (44 runs)). The right panel shows model runs that will be used for the fifth assessment report (AR5, all simulations available before 15 December 2011 are included) for four representative concentration pathways (RCP2.6 (26 runs), RCP4.5 (32 runs), RCP6.0 (17 runs), RCP8.5 (29 runs)). The plotted values are means over the values assigned to the grid cells of the climate models over the study region.

and ablation area using a monthly basin scale 0 °C isotherm and the basin scale hypsometric curve. The model is calibrated against the average of the observed mass balance in the basins during the climatic reference period. For the future, the basin scale mass balance is used to derive an annually updated area for the glaciers in each glacier size class by volume-area scaling [*Bahr et al.*, 1997]. The changes in area are aggregated for all glaciers in all size classes to obtain the basin scale changes in glacier area and construct a basin scale area depletion curve. Finally the basin scale area depletion curve can be used to calculate an updated fractional glacier cover per 1 km grid cell from 2008 until 2050.

3.4.2.1 Basin scale hypsometric curve

To generalize the hypsometry of the glaciers in the basins, we construct a basin scale hypsometric curve from the initial fractional glacier cover in the 1 km grid cells. To this end we need to derive the median elevation of the fractional glacier cover (H_{GLAC}) in a 1 km grid cell. First we use the 90 m DEM to calculate the average terrain altitude (H_{AVG}), standard deviation of the terrain altitude (H_{SD}), and maximum terrain altitude (H_{MAX}) within each 1 km grid cell at the 90 m subgrid. We then derive H_{GLAC} for each grid cell based on the distribution of terrain elevation and G_F, assuming that within a 1 km grid cell the distribution of ice follows the terrain elevation distribution and glaciers occupy the highest (coldest) end of the terrain elevation distribution.

Figure 3.5 shows schematically how H_{GLAC} can be determined from H_{AVG}, H_{SD} and G_F. It shows the terrain elevation distribution within a 1 km grid cell and the part of the terrain elevation distribution occupied by glacier ice. If we assume the terrain elevation distribution to be approximately normal, then we can estimate the median elevation of the fractional glacier cover as:

$$H_{GLAC} = min\left(H_{AVG} + H_{SD} \cdot F_N^{-1}\left(1 - \frac{G_F}{2}\right); H_{MAX}\right) \qquad \text{for } G_F > 0 \tag{3.1}$$

where $F_N^{-1}\left(1-\frac{G_F}{2}\right)$ is the $1-\frac{G_F}{2}$ quantile of the standard normal distribution and H_{MAX} is the maximum terrain elevation within the 1 km grid cell. H_{GLAC} is limited by H_{MAX} because the median elevation of the fractional glacier cover can not be higher than the maximum terrain elevation in the 1 km grid cell. If for example H_{AVG} = 4000 m a.s.l., H_{SD} = 200 m and G_F = 0.4, then H_{GLAC} = 4168 m a.s.l. When G_F = 1, the entire cell is covered with ice and thus Eq. (3.1) yields $H_{GLAC} = H_{AVG}$.

We sort the data for H_{GLAC} from low to high values for all grid cells with $G_F > 0$, with each value assigned a weight according to its fractional glacier cover as part of the total glacier area (i.e. the sum of G_F for all grid cells), to derive one basin scale hypsometric curve (Figure 3.6), representative for the average glacier altitude distribution in the study area. We construct the hypsometric curve using the initial fractional glacier cover and distribution of terrain elevation in a 1 km grid cell instead of computing it directly from the glacier outlines and 90 m DEM for consistency with the calculation of the updated fractional glacier cover at the end of each time step during the simulation (section 3.4.2.5).

3.4.2.2 Basin scale 0 °C isotherm and accumulation area ratio

Once the basin scale hypsometric curve is obtained, we want to use it to calculate a basin scale monthly mass balance. The idea is to determine the basin scale 0 °C isotherm for each month and combine it with the basin scale hypsometric curve to determine the basin scale accumulation area ratio, which in turn can be used to calculate the ablation and accumulation for each month and for the glaciers in each glacier size class.

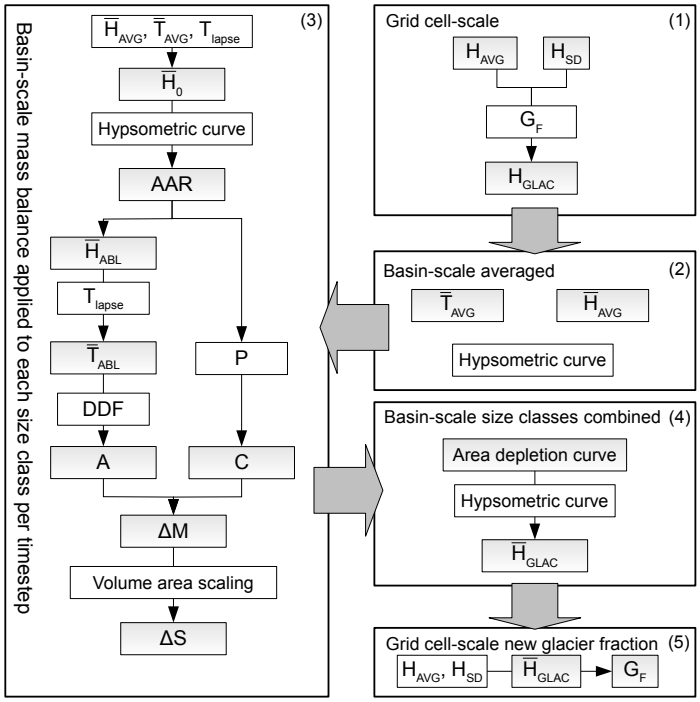

Figure 3.4. Schematic representation of glacier modeling steps. First calculations are made at the 1 km grid cell scale (1). Using the grid cell's mean terrain elevation (H_{AVG}) in combination with the standard deviation of terrain elevation within the grid cell (H_{SD}) and the fractional glacier cover of the grid cell (G_F), the median elevation of the part of the grid cell that is covered by ice can be determined (H_{GLAC}). Basin scale averaged temperature and elevation for grid cells with glaciers ($\overline{T}_{AVG}$ and $\overline{H}_{AVG}$) are calculated (2). Values of H_{GLAC} for all grid cells from step 1 are used to construct a basin scale hypsometric curve. Basin scale mass balance calculations are done for all glaciers in 26 glacier size classes with a monthly time step (3). Using $\overline{H}_{AVG}$, $\overline{T}_{AVG}$ and a temperature lapse rate (T_{lapse}) the basin scale 0 °C isotherm can be determined ($\overline{H}_0$). By combining $\overline{H}_0$ with the hypsometric curve the accumulation area ratio (*AAR*) can be calculated. With the *AAR* the amount of ablation (*A*) and accumulation (*C*) can be derived. A representative temperature for the ablation zone ($\overline{T}_{ABL}$) is calculated at the mean elevation of the ablation zone ($\overline{H}_{ABL}$). A degree-day factor (*DDF*) is used to calculate the actual ablation. The accumulation consists of the precipitation (*P*) over the accumulation zone. Using *A* and *C* a monthly mass balance (Δ*M*) is calculated. Applying volume-area scaling in October each year an updated glacier area is calculated for the glaciers in each size class and the change in area can be tracked (Δ*S*). With the result from step 3 a basin scale area depletion curve is constructed to derive an updated basin scale median elevation of the glacierized part of the basins ($\overline{H}_{GLAC}$) for each month (4). With $\overline{H}_{GLAC}$ and the elevation distribution within a grid cell (mean terrain elevation (H_{AVG}) and standard deviation of elevation (H_{SD})), the basin scale model output is downscaled to the grid cell scale for each month, to provide an updated fractional glacier cover (G_F) per grid cell (5).

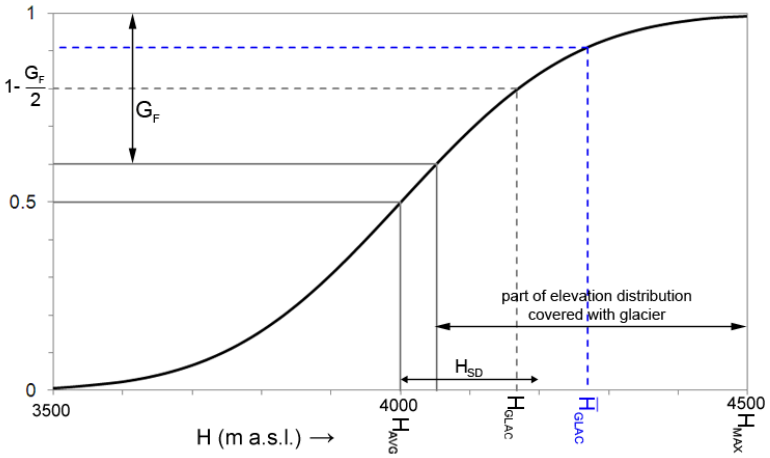

Figure 3.5. Distribution of terrain elevation within a 1 km grid cell. H_{AVG} is the mean terrain elevation in a 1 km grid cell. H_{SD} is the standard deviation of the terrain elevation distribution. G_F is the fractional glacier cover for a 1 km grid cell. H_{GLAC} is the obtained median elevation for the part of the grid cell covered with ice. In this figure G_F = 0.4, H_{AVG} = 4000 m a.s.l. and H_{SD} = 200 m. Eq. (3.1) yields H_{GLAC} = 4168 m a.s.l. During the simulation an updated value for G_F is calculated using $\overline{H}_{GLAC}$ and Eq. (3.10). In this example $\overline{H}_{GLAC}$ = 4270 m a.s.l. With H_{AVG} = 4000 m a.s.l. and H_{SD} = 200 m for this grid cell, Eq. (3.10), yields G_F = 0.18.

To determine the altitude of the basin scale 0 ˚C isotherm, we calculate the basin scale mean elevation ($\overline{H}_{AVG}$) and the monthly basin scale average temperature ($\overline{T}_{AVG}$). Then, using $\overline{H}_{AVG}$ and $\overline{T}_{AVG}$, we derive the altitude of the basin scale 0 °C isotherm ($\overline{H}_0$) for each month:

$$\overline{H}_0 = \overline{H}_{AVG} - \overline{T}_{AVG} \cdot T_{lapse}^{-1} \tag{3.2}$$

where T_{lapse} is a temperature lapse rate (°C m^{-1}), which is the mean of the saturated and dry adiabatic lapse rates (Table 3.1).

$\overline{H}_0$ is calculated for each month and combined with the basin scale hypsometric curve to calculate the basin scale accumulation area ratio (*AAR*) for each month. The value for AAR is looked up in the upper horizontal axis of Figure 3.6 for the corresponding value of $\overline{H}_0$ on the vertical axis. For example, in Figure 3.6, $\overline{H}_0$ = 4800 m a.s.l. and the associated *AAR* = 43% as derived from the basin scale hypsometric curve. The next step is to use the monthly *AAR* to scale the ablation area and accumulation area for each month, to calculate month specific accumulation and ablation.

3.4.2.3 Basin scale mass balance

For each month, a specific mass balance (ΔM [m w.e. y^{-1}]) is determined at basin scale:

$$\Delta M = C - A \tag{3.3}$$

where C (m) is the monthly accumulation and A (m) is the monthly ablation. The monthly accumulation at basin scale is calculated as:

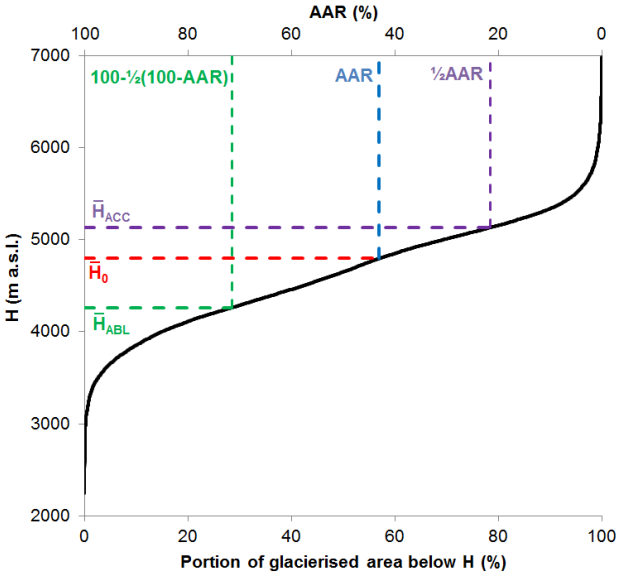

Figure 3.6: Mean basin scale hypsometric curve (black line) for elevation (H) and glacierized area of both basins. The blue dashed line indicates how the accumulation area ratio (AAR) is derived using the basin scale 0 °C isotherm ($\overline{H}_0$, red dashed line) and the hypsometric curve. In this example $\overline{H}_0$= 4800 m a.s.l. and the associated AAR = 43%. The median elevation of the accumulation area ($\overline{H}_{ACC}$) is indicated by the purple dashed line and the median elevation of the ablation area ($\overline{H}_{ABL}$) is indicated by the green dashed line.

$$C = P \cdot AAR \qquad \text{for } \overline{T}_{ACC} < 2\ ^{\circ}\text{C} \tag{3.4}$$

where P is the monthly precipitation sum over the glacierized area in the basins (m) and $\overline{T}_{ACC}$ is the basin scale average temperature representative for the accumulation zone. $\overline{T}_{ACC}$ can be derived from the median elevation of the accumulation zone at basin scale ($\overline{H}_{ACC}$), which is derived from the hypsometric curve (Figure 3.6). For example in Figure 3.6, $\overline{H}_0$ = 4800 m a.s.l. and AAR = 43%. Thus the upper 43% of the glacier area is located in the accumulation zone. The median elevation of this zone ($\overline{H}_{ACC}$) is 0.5 · 43% = 21.5% on the AAR-axis. Deriving $\overline{H}_{ACC}$ from the hypsometric curve yields $\overline{H}_{ACC}$ = 5133 m a.s.l. We calculate the temperature for the accumulation zone ($\overline{T}_{ACC}$) according to:

$$\overline{T}_{ACC} = \overline{T}_{AVG} + (\overline{H}_{ACC} - \overline{H}_{AVG}) \cdot T_{lapse} \tag{3.5}$$

Accumulation occurs when $\overline{T}_{ACC}$ is below 2 °C as stated in Eq. (3.4), in which case all precipitation over the accumulation zone is assumed to be solid.

The monthly ablation (A [m]) is calculated as:

$$A = \overline{T}^{+}_{ABL} \cdot DDF \cdot d \cdot (1 - AAR) \tag{3.6}$$

where $\overline{T}^{+}_{ABL}$ is the positive (set to zero when negative) basin scale monthly average temperature representative for the ablation zone (see derivation below), DDF is a composite degree-day factor (mm w.e. °C^{-1}day^{-1}) calculated as the weighted mean of two distinct values referring to debris free

and debris-covered ice (Table 3.1). Weighting is performed according to the fraction of debris free glaciers (85%) and debris-covered glaciers (15%). This ratio is based on observations in the western Tien Shan [*Wang et al.*, 2011]. The number of days in the month is *d*, and *AAR* is the accumulation area ratio. The degree-day factors for debris free glaciers and debris-covered glaciers were calibrated in a related hydrological study for the same river basins [*Immerzeel et al.*, 2012a].

To calculate $\overline{T}_{ABL}$ we derive the median elevation of the ablation zone at basin scale ($\overline{H}_{ABL}$) using the hypsometric curve and the *AAR*. For example in Figure 3.6, $\overline{H}_0$ = 4800 m a.s.l. and *AAR* = 43%. Thus the lower 57% of the glacier area is part of the ablation zone. The median elevation of this zone ($\overline{H}_{ABL}$) is 100% – 0.5 · (100% – *AAR*) = 71.5% on the *AAR*-axis. Deriving $\overline{H}_{ABL}$ in the hypsometric curve yields $\overline{H}_{ABL}$ = 4261 m a.s.l.

We calculate the temperature for the ablation zone ($\overline{T}_{ABL}$) according to:

$$\overline{T}_{ABL} = \overline{T}_{AVG} + (\overline{H}_{AVG} - \overline{H}_{ABL}) \cdot T_{lapse} \tag{3.7}$$

For each month a specific mass balance is calculated at basin scale as specified in Eq. (3.3).

3.4.2.4 Updating glacier area for glaciers in each size class

An intitial mean ice thickness is determined for the glaciers in each size class using volume-area scaling [*Bahr et al.*, 1997]. Volume-area scaling is based on physical arguments [*Bahr et al.*, 1997] and has been extensively used [e.g. *Farinotti et al.*, 2009; *Radić and Hock*, 2010; *Grinsted*, 2013]. The volume-area scaling can be expressed as a relation between the mean glacier thickness (*h* [m]) and glacier area (*A* [m^2]) [*Radić and Hock*, 2010; *Huss and Farinotti*, 2012]:

$$h = c \cdot A^{\gamma-1} \tag{3.8}$$

where *c* and γ are scaling parameters. We use the same scaling parameters as *Radić and Hock* [2010] use for mountain glaciers (*c* = 0.2055, γ = 1.375). With this relation we derive an initial mean ice thickness for the glaciers in each size class. This thickness is updated every month (t) for the glaciers in each size class (i) with the basin scale specific mass balance (section 3.4.2.3):

$$h_{i,t} = \max(h_{i,t-1} + \Delta M; 0) \tag{3.9}$$

To simulate future glacier extent, we force the model with the downscaled temperature and precipitation projections described in section 3.3.3 for 2008 until 2050 at a monthly time step. Each year at the beginning of a new glaciological year (in this study on October 1st), we use the inverse of Eq. (3.8) to calculate the new glacier area for each size class from the updated ice thickness. By aggregating the results for all glaciers in all size classes, the percentual change in total glacierised area in the basins from 2008 to 2050 with respect to 2007 is determined (Figure 3.7). An area depletion curve can be fitted through the time series of percentual changes in glacier area (Figure 3.7). By looking up the H values on the vertical axis in Figure 3.6 that correspond to the values of the area depletion curve for each time step on the upper horizontal axis, a time series of updated basin scale median elevation of the glacierized part of the basins ($\overline{H}_{GLAC}$) (Figure 3.7) is constructed, which can later be used to downscale the basin scale averaged changes in glacier area to monthly updated fractional glacier cover for each 1 km grid cell. For example in Figure 3.7, on 1 January 2040 the glacierized area is 52.0% of the glacierized area in 2007 as can be derived from the area depletion

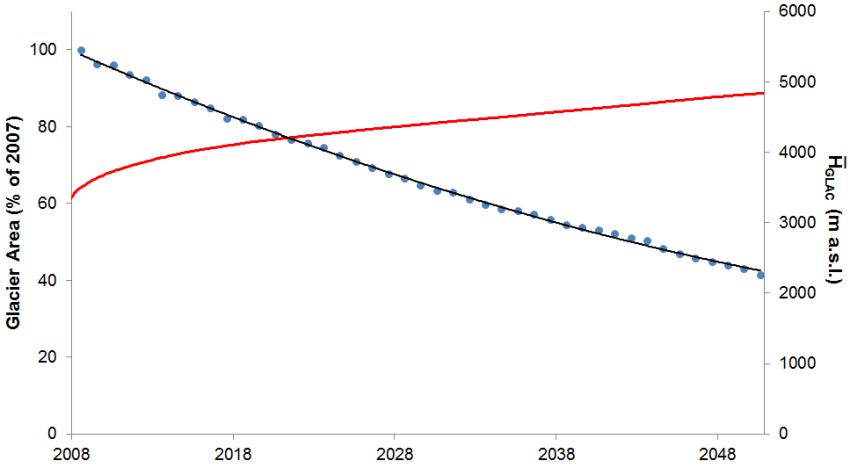

Figure 3.7. Relative change in glacier area aggregated for all glaciers at the beginning of October for each projected year (blue dots), fitted area depletion curve (black line), and basin scale median elevation of the glacierized part of the basins ($\overline{H}_{GLAC}$) (red line). In this figure the glacier area change, fitted area depletion curve and median elevation of the glacierized part of the basins are for the CMIP5 average projection (ΔT Q50, ΔP Q50), for the Amu and Syr Darya basins combined.

curve. Using the fractional glacier cover value 0.520 (=52.0%) in the lower horizontal axis in Figure 3.6 yields 4586 m a.s.l. for $\overline{H}_{GLAC}$ from the hypsometric curve.

3.4.2.5 Updating fractional glacier cover per grid cell

To create monthly maps of glacier extent, we update the fractional glacier cover (G_F) for each grid cell for each month from 2008 until 2050 using $\overline{H}_{GLAC}$ and the distribution of terrain elevation within a 1 km grid cell. Assuming that the glacier distribution follows the distribution of terrain elevation, and that the latter can be described by a normal distribution, we calculate G_F for a 1 km grid cell using the cumulative standard normal curve function:

$$G_F = min\left(2 \cdot \left(1 - F_N\left(\frac{\overline{H}_{GLAC} - H_{AVG}}{H_{SD}}\right)\right); 1\right) \tag{3.10}$$

For example in Figure 3.5, when $\overline{H}_{GLAC}$ = 4270 m a.s.l. and a given grid cell has H_{AVG} = 4000 m a.s.l. and H_{SD} = 200 m, then G_F = 0.18. If $\overline{H}_{GLAC}$ moves up, G_F decreases. G_F has an upper limit of 1, as the fractional glacier cover can not exceed this value. Thus, when $\overline{H}_{GLAC} \leq H_{AVG}$, G_F = 1.

3.4.2.6 Calibration

We calibrate the model for the reference period (1978-2007). Based on the average of the observed mass balance in the region during the reference period (Section 3.3.4, Table 3.2) the model is calibrated by correcting the monthly mean temperature for the reference period with a temperature correction (*CorT*) (Table 3.1), which is added to the temperature forcing. With the calibrated *CorT*, the model produces the same mass balance for the reference period as the average of the observed mass balance in the basins (MB_{OBS},Table 3.1). The *CorT* parameter accounts for a combined effect

of errors in the forcing data, temperature differences within a 1 km grid cell, vertical and horizontal errors from interpolation in the reference period climate dataset (section 3.3.2) and errors from averaging over the two basins. The degree-day factors for debris free glaciers and debris-covered glaciers where calibrated for a related hydrological study for the same river basins (Table 3.1) [*Immerzeel et al.*, 2012a]. The degree-day factors are within the range of other studies reported in the region [*Mihalcea et al.*, 2006; *Zhang et al.*, 2006; *Hagg et al.*, 2008; *Immerzeel et al.*, 2010, 2012b]. In addition we take into account variation in degree-day factors in the uncertainty analysis described in section 3.5.3.

3.4.2.7 Validation

Since data scarcity in Central Asia makes it difficult to validate the model performance we validate the method for the Austrian Alps, where multiple glacier inventories and glacier mass balance time series for twelve glaciers are available. We use two glacier inventories, marking the starting point and endpoint of the simulation. A glacier inventory representative for the year 1969 [*Patzelt*, 1978] is used as starting point for the simulation. A second glacier inventory is made with data from 1996-2002 [*Eder et al.*, 2000; *Lambrecht and Kuhn*, 2007]. We assume this inventory to be representative for 1997, since 81% of the glacier area was mapped in 1997 and 1998. Thus, 1997 is the last year of the simulation. We force the model with daily air temperature and daily precipitation from the PGMFD [*Sheffield et al.*, 2006]. We use the same DEMs, the same degree-day factors and the same volume-area scaling coefficients as for the application in Central Asia. The average of the observed mass balance in the Austrian Alps is -0.37 m w.e. yr^{-1} between 1969 and 1997 based on mass balance records from twelve individual glaciers (WGMS, 2011). We calibrate the *CorT* parameter to this average of the observed mass balance yielding *CorT* = 0.76 °C and simulate the

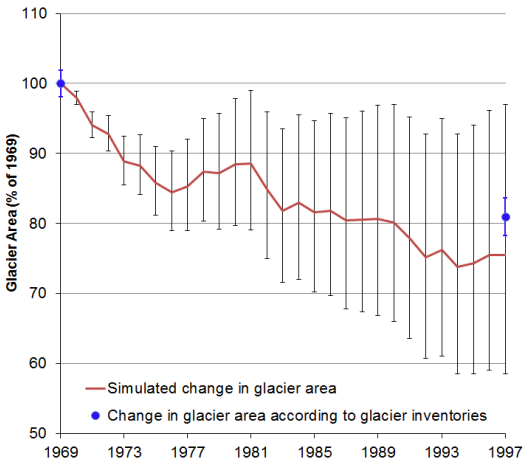

Figure 3.8. Simulated change in total glacier area in Austria in the European Alps between 1969 and 1997. The red line shows the simulation results when calibrated for the average of the observed mass balance during 1969-1997 in the area. Black error bars represent simulation results when calibrated for the average of the observed mass balance plus one standard deviation (positive error) and the average of the observed mass balance minus one standard deviation (negative error). Blue dots represent the observed differences in total glacier area according to glacier inventories and blue error bars indicate the error in the glacier inventories.

changes in glacier area until 1997. The simulated decrease in glacier area between 1969 and 1997 is 24.5%. Figure 3.8 shows the complete simulation of changes in glacier area from 1969 until 1997. The black error bars indicate simulation results when calibrated for the average of the observed mass balance plus one standard deviation (positive error) and the average of the observed mass balance minus one standard deviation (negative error). The observed decrease in glacier area according to the two glacier inventories equals 19.0% (Figure 3.8). The estimated error in the glacier inventories [*Lambrecht and Kuhn*, 2007] is displayed with the blue error bars. Considering the fact that our approach is a first order estimate of basin scale glacier area changes, the uncertainties in the methodology (as discussed in section 3.5.4) and uncertainties in the glacier outlines in the inventories, we conclude that the model performs satisfactory.

3.5 Results and Discussion

3.5.1 Future climate

All results stated are for the Amu Darya and Syr Darya basins combined and the climate change signals refer to the changes during 60 years (change between 1961 – 1990 and 2021 – 2050). Both the CMIP3 and CMIP5 ensembles show large variation in temperature and precipitation changes between models and between emission scenarios (Figure 3.9). On average, temperature is expected to rise by about 2 °C and precipitation to remain nearly constant. The uncertainty in temperature

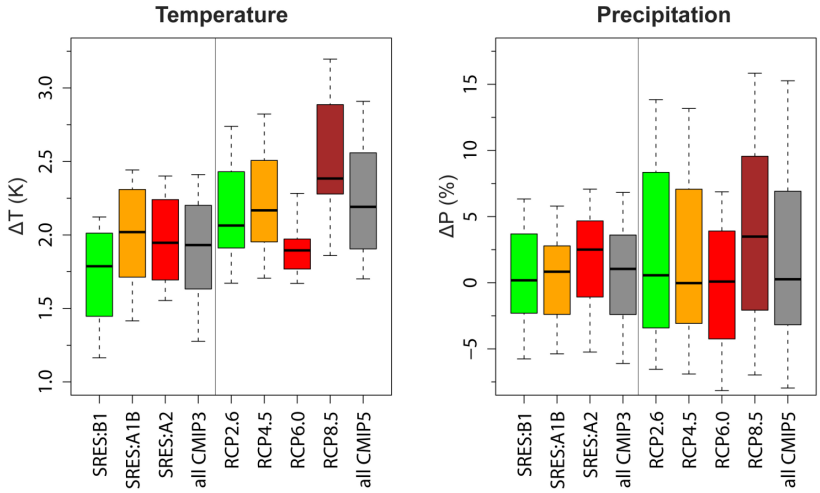

Figure 3.9. Box-whisker plots for projected changes in temperature (left) and precipitation (right) for three AR4 SRES emission scenarios and four AR5 representative concentration pathways extracted from the CMIP3 (SRES) and CMIP5 (RCP) databases. The A1B (53 GCM runs), A2 (36 runs) and B1 (44 runs) AR4 scenarios are used and the RCP2.6 (26 runs), RCP4.5 (32 runs), RCP6.0 (17 runs) and RCP8.5 (29 runs) AR5 scenarios are used. The values are mean delta change values for GCM grid cells covering the study area and represent the change over 60 years (1961-1990 to 2021-2050). The boxes represent the range from Q25 to Q75, divided by the median value (Q50). The whiskers represent the range between Q10 and Q25 (at the lower end of the distributions) and the range between Q75 and Q90 (at the higher end of the distributions).

projections (ΔT), expressed as the 90th and 10th percentiles, is estimated to range from 1.3 °C to 2.4 °C in the CMIP3 ensemble and from 1.7 °C to 2.9 °C in the CMIP5 ensemble (Figure 3.9, left panel). For precipitation projections (ΔP) the 90th and 10th percentiles range from -6% to +7% in the CMIP3 ensemble and from -8% to +15% in the CMIP5 ensemble (Figure 3.9, right panel). Though the climate projections of both ensembles mainly cluster around the same values (about 2 °C and 0%, for temperature and precipitation, respectively), the new CMIP5 ensemble includes the possibility of more extreme climate change. There are several "warmer" simulations (up to +3.5 °C) and many of those are also extreme in precipitation change (Figure 3.9). Note that this observation not only holds across scenarios, but also between GCM runs within a given scenario, e.g. RCP 2.6, 6.0 and 8.5 show similar extremes in temperature and precipitation. The CMIP5 ensemble also shows a larger average warming than CMIP3 (Figure 3.9, left panel). In addition, the variation between scenarios is also larger for CMIP5 for both precipitation and temperature (Figure 3.9).

Looking at the projections on a monthly scale (Figure 3.10), mean projections for temperature (ΔT, Q50) in July to September do not differ much between the two ensembles, although the range in temperature projections is higher for the CMIP5 ensemble compared to the CMIP3 ensemble (Figure 3.10, upper panel). However, mean temperature projections for October to May are higher for the CMIP5 ensemble compared to the CMIP3 ensemble. The spread in precipitation projections is generally larger for the CMIP5 ensemble compared to the CMIP3 ensemble (Figure 3.10, lower panel). Especially for March to September the mean projections for precipitation (ΔP, Q50) are higher for the CMIP5 ensemble compared to the CMIP3 ensemble, while little differences in mean projections for precipitation are observed for October to February.

As we choose to include as many climate projections as possible in our study we do not use particular GCMs but apply the quantile approach as described in section 3.4.1. A disadvantage of this approach is that systematic changes in the daily variability are not included. However since our glacier model is forced with monthly data we accept this for the benefit of including as many climate projections as possible.

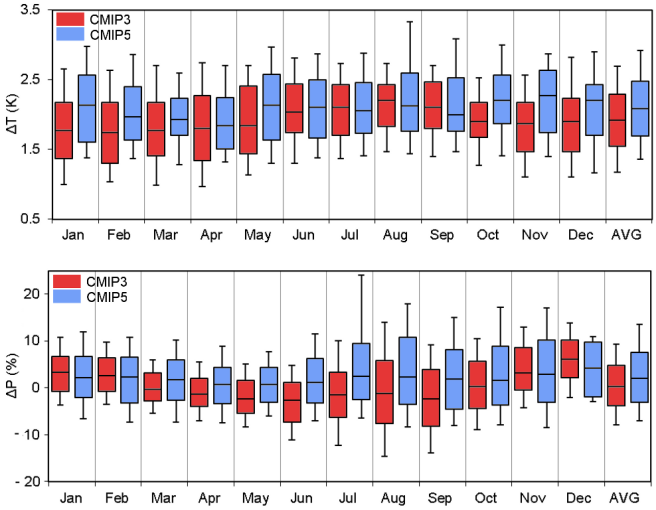

Figure 3.10. Box-whisker plots for projected changes per month in temperature (upper panel) and precipitation (lower panel) for the CMIP3 ensemble (red) and CMIP5 ensemble (blue). The definition of the boxplots is as in Figure 3.9.

3.5.2 Implications of climate change for Central Asian glaciers

We force the glacier model with all quantile combinations of the downscaled temperature and precipitation as analysed on a monthly basis (monthly delta change values) and obtain the basin scale cumulative mass balance for the simulated period (2007-2050). Figure 3.11 shows the cumulative mass balance for the average projection (ΔT Q50, ΔP Q50), for the very warm and very dry (ΔT Q90, ΔP Q10) case, for the very cold and very wet (ΔT Q10, ΔP Q90) case, for the very warm and very wet case (ΔT Q90, ΔP Q90) and for the very cold and very dry (ΔT Q10, ΔP Q10) case. The range of projections is higher for the CMIP5 (Figure 3.11, left panel) ensemble compared to CMIP3 (Figure 3.11, right panel). When forced with the CMIP3 ensemble the cumulative mass balance for 2007-2050 ranges from -32.3 m w.e. for the very cold, very wet case to -44.9 m w.e. in the very warm, very dry case. Forcing with the average projection yields -38.9 m w.e. When forced with the CMIP5 ensemble the range is from -32.2 m w.e. to -47.7 m w.e. for the very cold, very wet case and the very warm, very dry case, respectively. Forcing with the average projection yields a cumulative mass balance for 2008-2050 of -38.6 m w.e.

Figure 3.12, spanning the frequency space between the 10 and 90-percentiles for both temperature and precipitation, shows the percentual glacier retreat in 2050 for the CMIP3 and the CMIP5 case. Both cases show variability in future glacier extent. For the CMIP3 projections, a reduction in glacier area varying between 54.5% in 2050 when the model is forced by the ΔT Q10 and the ΔP Q90, and a reduction of 63.5% in 2050 when forced by the ΔT Q90 and ΔP Q10 is observed. By keeping ΔT constant at the Q50 level a 0.8% range in potential glacier retreat is found (from 59.0% to 59.8% decrease) over the full ΔP range for the CMIP3 case and a range of 6.7% is found (from 56.0% to 62.7% decrease) when ΔP is kept constant at the Q50 level. For the CMIP5 case this range is larger with a 1.1% range (from 59.1% to 60.2% decrease) when ΔT is kept constant at the Q50 level, and a 7.8% range (from 55.7% to 63.5% decrease) when ΔP is kept constant at the Q50 level. So, the range in temperature projections has a much larger impact on the predicted glacier extent as the range in precipitation projections.

The range for the CMIP5 based projection for glacier extent is slightly wider than for CMIP3. The ΔT Q10 and the ΔP Q90 combination results in a projected decrease of 54.4%, while the ΔT Q90 and the ΔP Q10 combination leads to a decrease of 65.1% (Figure 3.12). Although the mean

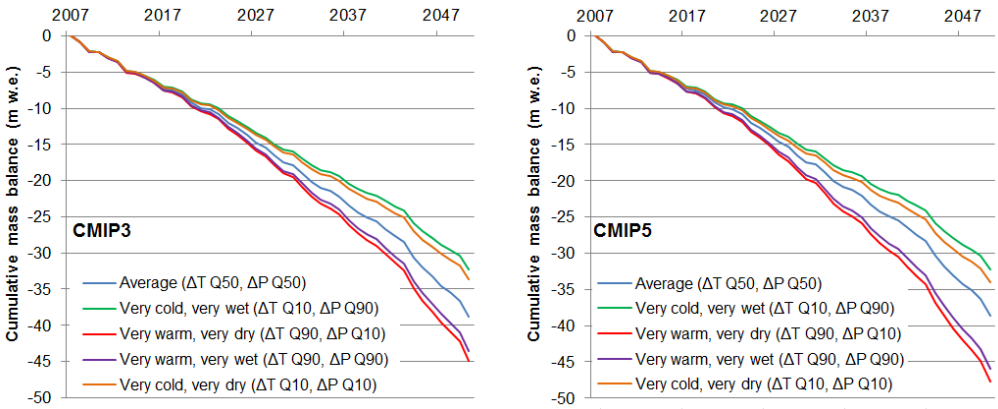

Figure 3.11: Basin scale cumulative glacier mass balance for the Amu Darya and Syr Darya river basins together for 2007-2050 based on the CMIP3 (left panel) and CMIP5 (right panel) model runs for the median and extreme values of temperature and precipitation change.

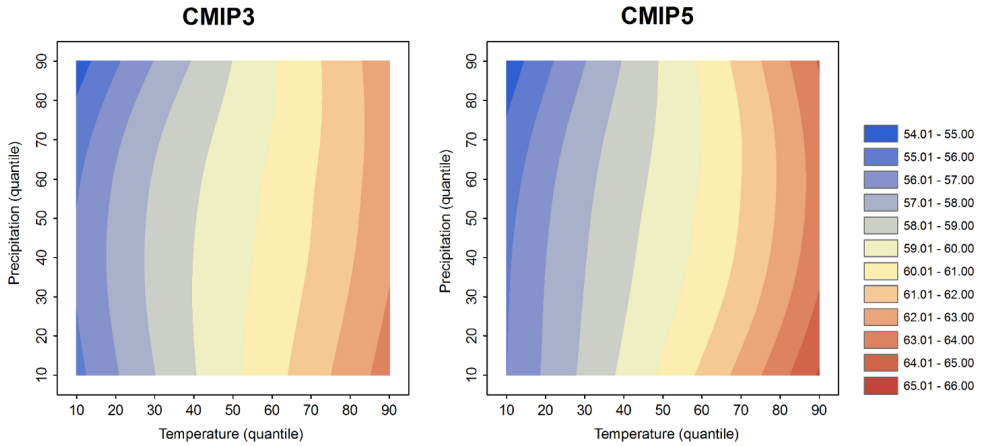

Figure 3.12. Percentual decrease (relative to 2007) in glacierized area by 2050 for the upstream parts of the Amu Darya and Syr Darya river basins together for the changes in temperature and precipitation for CMIP3 runs (left) and CMIP5 runs (right).

temperature projection on an annual basis is higher for the CMIP5 ensemble compared to the CMIP3 ensemble and the mean precipitation projections are almost similar, the projected decrease in glacier extent is practically the same (even 0.1% more decrease for the CMIP3 case). This can be explained by the fact that mean temperature projections (ΔT Q50) for July to September, when most of the melting takes place, are similar for CMIP3 and CMIP5 (Figure 3.10), and mean precipitation projections (ΔP Q50) are also similar for CMIP3 and CMIP5 during October to February when most accumulation takes place. From these results it is evident that it is important to assess climate change projections at the seasonal level rather than at the annual level, when making projections for future glacier extent.

Figure 3.13 shows the decrease in total glacier area in the Amu Darya and Syr Darya basins for the entire simulated period based on the CMIP3 (Figure 3.13, left panel) and CMIP5 (Figure 3.13, right panel) model runs. The range of glacier extent projections for the CMIP5 ensemble and the CMIP3 ensemble are very similar. The fact that the very cold, very dry projection is closer to the very cold, very wet projection than to the average projection for both ensembles again shows that the uncertainty in temperature projections has a much larger impact on the uncertainty in glacier extent than uncertainty in precipitation projections, and change in temperature is the main driver for future decrease in glacier extent in these areas.

Figure 3.14 shows, for the CMIP5 case, the projected glacier extent for 2050 for a selected area covering the large glacier systems in the central Pamir (Figure 3.14b) as compared with the initial glacier extent (Figure 3.14a). The three lower left panels (Figure 3.14c, e, g) show the projected fractional glacier cover per 1 km grid cell in 2050 for the average projection and the two most extreme projections (very cold, very wet and very warm, very dry). The right panels (Figure 3.14d, f, h) show the change in fractional glacier cover per 1 km grid cell with respect to the initial situation for these three cases. It can be clearly seen that the fractional glacier cover decreases strongest in the lowest glacierized parts, and that mainly the tongues in the valleys are affected. A similar figure shows a selected area in the Tien Shan (Figure 3.15). In the Tien Shan mountains the glaciers are smaller than in the central Pamir and many are located at lower elevations. As a result, in the Tien

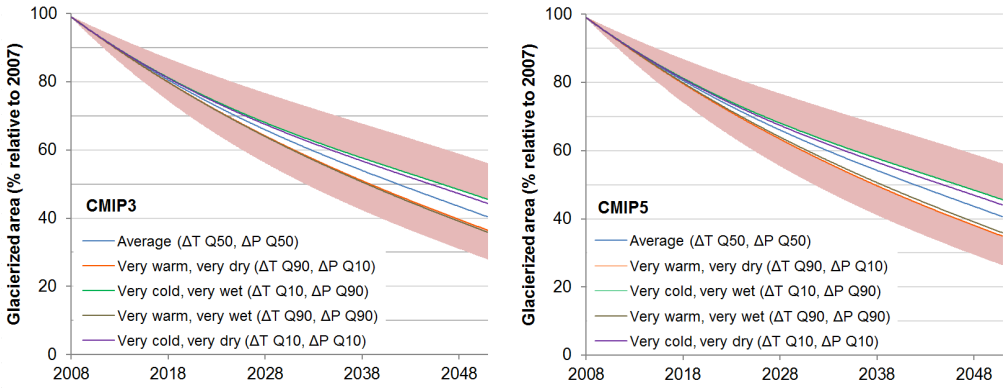

Figure 3.13. Decrease in total glacier area in the Amu Darya and Syr Darya basins combined for 2008-2050 based on the CMIP3 (left panel) and CMIP5 (right panel) model runs for the median and extreme values of temperature and precipitation change. The red error range added to the two most extreme cases is derived using an uncertainty analysis on model parameters and observed glacier mass balance information (see section 3.5.3).

Shan the impact of climate change will lead to a more rapid decrease in glacier extent than in the Pamir.

3.5.3 Parametric uncertainty analysis

Besides uncertainty in glacier extent as a result of the uncertainty in the climate change projections, the projected glacier changes are subject to other uncertainties. These include parametric uncertainty, uncertainty in present glacier extent and volume, uncertainty in the volume-area scaling, uncertainty in climate evolution, uncertainty in climatic forcing for the reference period, uncertainty in mass-balance time series and uncertainties stemming from simplifications and assumptions applied to the model. Since the mass balance model is based on an empirical approach requiring calibration we evaluate also, besides uncertainty in the climate change projections, how the uncertainties in the model parameters as well as uncertainty in the observed historical glacier mass balance translate in uncertainty in the future glacier extent by running the model for different sets of parameters and observed glacier mass balance. We assume the three critical model parameters (vertical temperature lapse rate (T_{lapse}), degree-day factor for clean ice glaciers (DDF_{CI}), degree-day factor for debris-covered glaciers (DDF_{DC})) to be three independent normally distributed (random) variables. The temperature correction (*CorT*) is recalibrated for each set of parameters. We use a mean DDF_{DC} = 3.97 mm $°C^{-1}$ d^{-1} and DDF_{CI} = 7.94 $°C^{-1}$ d^{-1} and both with σ = 1 $°C^{-1}$ d^{-1}. For T_{lapse} we use a mean -0.0068 °C m^{-1} and assume a standard deviation of 0.0012°C m^{-1}, which is based on the difference between the dry and saturated adiabatic lapse rate. The average of the observed glacier mass balance (MB_{OBS}) used is -0.47 m y^{-1} with a standard deviation of 0.082 m y^{-1} (Section 3.3.4, Table 3.2). For the observed mass balance we use an uncertainty range of two standard deviations. Based on these assumptions we sample 50 parameter sets and mass balance values. We then run a full simulation until 2050 with each of these 50 parameter-mass balance combinations (i.e. of T_{lapse}, DDF_{CI}, DDF_{DC}, MB_{OBS} and associated *CorT*, which is separately calibrated for each combination) and we estimate uncertainty by taking the standard deviation of

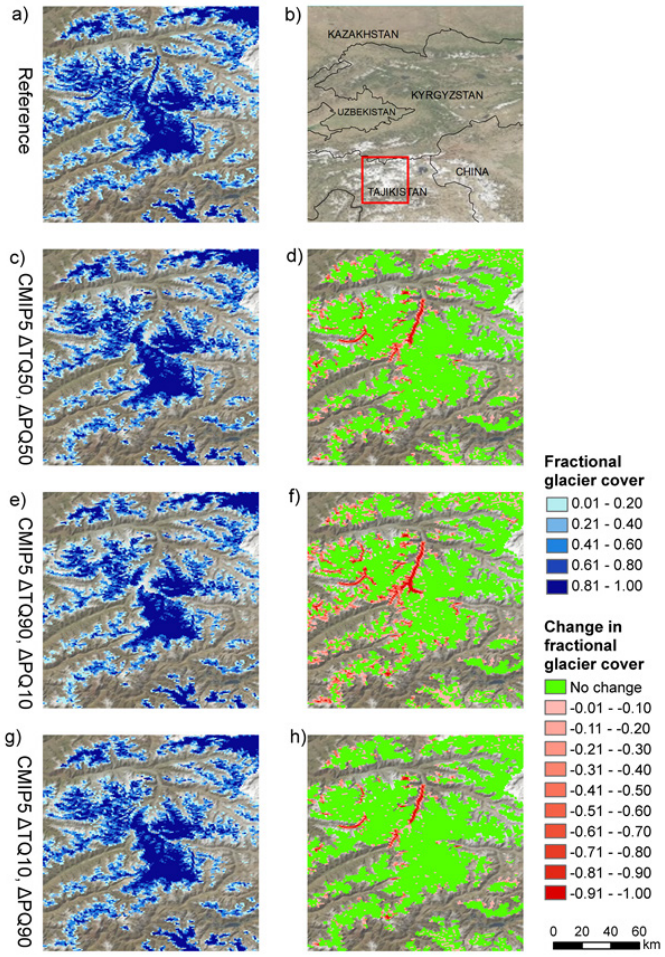

Figure 3.14. Projected fractional glacier cover in 2050 for the Fedchenko area in the Central Pamir. The square in the top right panel (b) represents the area enlarged in the other panels. Panel (a) shows the initial fractional glacier cover per 1 km grid cell. The three lower left panels show the simulated fractional glacier cover per 1 km grid cell in 2050 for the CMIP5 runs. Panel (c) shows the fractional glacier cover for the run with the 50th percentile (Q50) values of temperature and precipitation change. Panel (e) shows the projection with the strongest decrease in glacier cover, when the model is forced with the 90th percentile (Q90) for temperature change and 10th percentile (Q10) for precipitation change. Panel (g) shows the projection with the least decrease in glacier cover, when the model is forced with the 10th percentile (Q10) for temperature and 90th percentile (Q90) for precipitation change. The three lower right panels (d, f, h) show the change in fractional glacier cover per grid cell for the 2050 projections in the three lower left panels (c, e, g) with respect to the initial glacier cover (panel a).

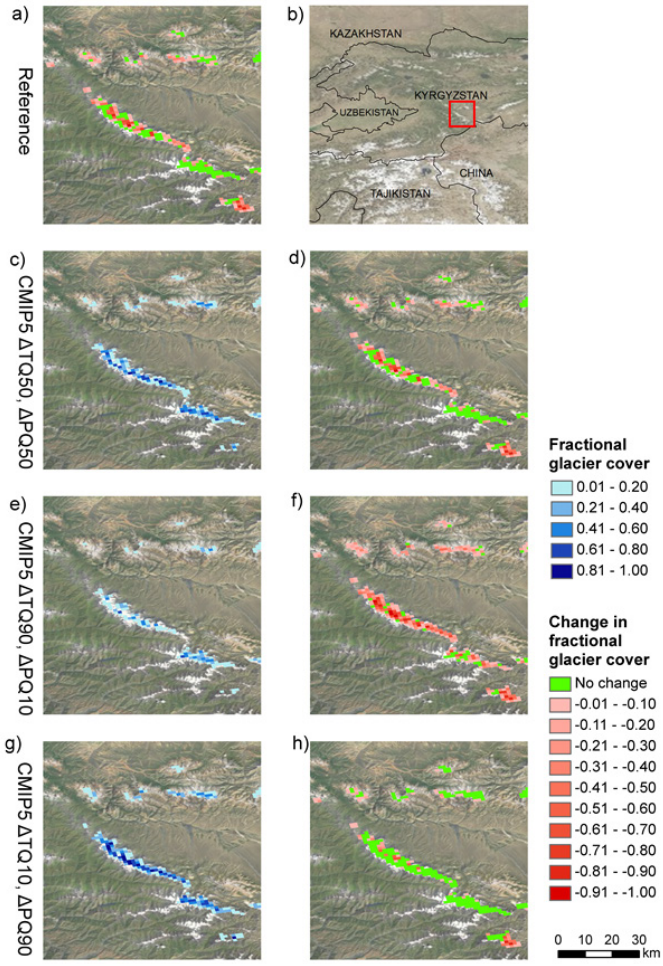

Figure 3.15. Projected fractional glacier cover in 2050 for a slected area in the Tien Shan mountains. The square in the top right panel (b) represents the area enlarged in the other panels. Panel (a) shows the initial fractional glacier cover per 1 km grid cell. The three lower left panels show the simulated fractional glacier cover per 1 km grid cell in 2050 for the CMIP5 runs. Panel (c) shows the fractional glacier cover for the run with the 50th percentile (Q50) values of temperature and precipitation change. Panel (e) shows the projection with the strongest decrease in glacier cover, when the model is forced with the 90th percentile (Q90) for temperature change and 10th percentile (Q10) for precipitation change. Panel (g) shows the projection with the least decrease in glacier cover, when the model is forced with the 10th percentile (Q10) for temperature and 90th percentile (Q90) for precipitation change. The three lower right panels (d, f, h) show the change in fractional glacier cover per grid cell for the 2050 projections in the three lower left panels (c, e, g) with respect to the initial glacier cover (panel a).

the 50 simulations [*Ragettli and Pellicciotti*, 2012]. This analysis allows to estimate the propagation of parameter uncertainty to uncertainty in the glacier model simulations.

The uncertainty resulting from model parameters is displayed for the very cold, very wet and the very warm, very dry cases in Figure 3.13. The effect of model parameter uncertainty leads to an additional uncertainty of ± 8.6% in total glacier extent in 2050 for both the CMIP5 and the CMIP3 case, showing that parameter uncertainty has roughly the same importance as uncertainty in the climate projections.

3.5.4 Limitations in the methodology

The advantage of low data requirements associated with the approach described in this paper of course comes with its limitations. We use volume-area scaling to estimate the initial ice volume based on the initial glacierized area and to translate new ice volumes to areas [*Bahr et al.*, 1997]. Approaches that use volume-area scaling are sensitive to the scaling parameters used [*Grinsted*, 2013], but have been largely used for large areas. Other methods based on ice physics and flux-balance principles have been suggested to estimate the initial ice volume [*Farinotti et al.*, 2009; *Huss and Farinotti*, 2012; *Paul and Linsbauer*, 2012], which could yield different results when applied in our modeling study.

We are interested in simulating the behavior of the glaciers as a result of climate perturbations at the basin scale. We do not model individual glaciers, and therefore we use an average of the observed mass balance for the five glaciers in calibration. This regionalization is justifiable over a longer period, but not at smaller time steps.

In our model setup, we construct one average hypsometric curve for the two river basins. This simplification constitutes a drawback as regional differences are neglected. To retain more regional differences a more accurate glacier modeling could be done by constructing different hypsometric curves for different (sub)basins, or theoretically for every grid cell. The same holds for basin scale averaged temperature and precipitation. As we use the initial hypsometric curve during the entire simulation, another improvement could be inclusion of regular recalculation of the hypsometric curve during the simulation based on the updated fractional glacier cover per grid cell.

Another area for improvement is the melt modeling. We now use a combined degree-day factor for debris free and debris-covered glaciers, which reflects the different behaviour of the two surfaces with melt decreasing under a thick debris cover [*Nicholson and Benn*, 2006; *Brock et al.*, 2010]. If the exact extent of both types of glaciers is available it would be recommendable to model the two types separately. However, melt modeling under debris-covered glaciers is not trivial as it crucially depends on debris thickness, which is not commonly available. Strong spatial variation is observed in the Alps as a result of the type and thickness of the debris layer. Improved models for melt under debris should be used that account for the effect of debris thickness [*Reid et al.*, 2012], provided that the thickness and characteristics of the debris layer are known. Apart from modeling melt under debris cover, melt modeling can be improved by including incoming solar radiation [e.g. *Pellicciotti et al.*, 2005], and considering other components of the energy balance. A general limitation of degree-day melt models is the necessity to calibrate the parameters for each case as the parameters are not transferable in time and space.

Given the limitations discussed above, we are aware that the glacier model used in this study is too coarse to reproduce the response of single glaciers and the complexity of processes involved. The model choice is imposed by the limited amount of data available and the large scale of our application. However, the model is suitable for our aim, i.e. to translate downscaled future climate scenarios into glacier response at the basin scale, and to assess how the spread and differences in

the future climate scenarios transform into differences in glacier response. Despite the fact that the simulated glacier response is subject to the uncertainties we discuss, the simulated trends are apparent. This study shows that parameter uncertainty and differences between GCMs should be taken into account and that the impact of climate change signals should take account of seasonal variation.

3.6 Conclusions

Both CMIP3 and CMIP5 climate change projections point towards a decline of glacier extent in Central Asia. Our results show that uncertainty about the range of this decline remains large. The range of projections for temperature and precipitation in the Central Asian region until 2050 for the CMIP5 ensemble is larger than for the CMIP3 ensemble and the median projection for CMIP5 models shows greater warming than for CMIP3 models. The CMIP5 ensemble shows higher projections for winter temperatures compared to CMIP3 while summer temperature projections are similar. On the other hand, the CMIP5 ensemble shows higher precipitation projections for the summer months compared to CMIP3 ensemble, while precipitation projections for the winter months are similar for both ensembles. As a result, the CMIP5 ensemble leads to a slightly wider range in projected glacier extent. For temperature and precipitation projections, the median projection shows a decrease in glacier extent between 2007 and 2050 of 59.4% for the CMIP5 ensemble compared to 59.6% in the CMIP3 case. The projected decrease in glacier extent ranges from 54.4% to 65.1% for the CMIP5 ensemble compared to 54.5% to 63.5% for the CMIP3 ensemble. Large spread is evident among models within both ensembles, in agreement with recent studies that have indicated that the differences among GCMs due to their structure and characteristics is the main source of uncertainty in future climate. Parametric uncertainty leads to additional uncertainty in the projections of future glacier extent, and has roughly the same importance as uncertainty in the climate projections. The mentioned ranges in projected glacier extent decrease demonstrate substantial uncertainty in climate change projections and associated glacier response for Central Asia. Furthermore it shows that it is imperative to use a representative selection of climate models and emission scenarios that span the entire range of possible future climates in climate change impact studies, to provide a complete picture of possible climate change impact. At the same time it shows that climate change signals should be analysed at a seasonal scale, when used to assess the response of glaciers to the changes in climate. The wide range in the projections implies an uncertain future for Central Asian glaciers.

Chapter 4

Modeling future changes in water availability resulting from climate change

Based on: *Lutz, A.F., W.W. Immerzeel, A.B. Shrestha, and M.F.P. Bierkens (2014), Consistent increase in High Asia's runoff due to increasing glacier melt and precipitation, Nature Climate Change, Vol. 4, pp. 587 – 592.*

Abstract

Rivers originating in the high mountains of Asia are among the most melt water dependent river systems on Earth, yet large human populations depend on their resources downstream. Across High Mountain Asia's river basins, there is large variation in the contribution of glacier and snow melt to total runoff, which is poorly quantified. The lack of understanding of the hydrological regimes of High Mountain Asia's rivers is one of the main sources of uncertainty in assessing the regional hydrological impacts of climate change. Here we use a large-scale, high-resolution, cryospheric-hydrological model to quantify the upstream hydrological regimes of the Indus, Ganges, Brahmaputra, Salween and Mekong rivers. Subsequently, we analyze the impacts of climate change for future water availability in these basins using the latest climate model ensemble. Despite large differences in runoff composition and regimes between basins and between rivers within basins, we project an increase in runoff at least until 2050, caused primarily by an increase in precipitation in the upper Ganges, Brahmaputra, Salween and Mekong basins and from accelerated melt in the upper Indus basin. These findings have immediate consequences for climate change policies where a transition towards coping with intra-annual shifts in water availability is desirable.

4.1 Introduction

Rivers originating in the high mountains of Asia are among the most melt water dependent river systems on Earth, yet large human populations depend on their resources downstream [*Schaner et al.*, 2012]. Across High Mountain Asia's river basins, there is large variation in the contribution of glacier and snow melt to total runoff [*Immerzeel and Bierkens*, 2012], which is poorly quantified. The lack of understanding of the hydrological regimes of High Mountain Asia's rivers is one of the main sources of uncertainty in assessing the regional hydrological impacts of climate change [*Miller et al.*, 2012].

In general, the climate in the eastern part of the Himalayas is characterized by the East-Asian and Indian monsoon systems, causing the bulk of precipitation to occur during June to September (Figure 4.1). The precipitation intensity shows a strong north-south gradient caused by orographic

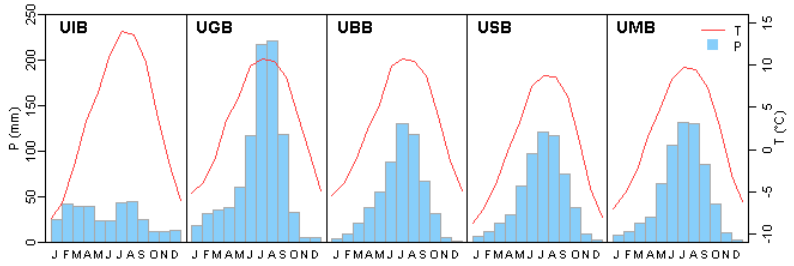

Figure 4.1: Monthly climatology for the five upstream river basins during the reference period (1998-2007). Plotted are mean air temperature (red line) as derived from the Princeton global meteorological forcing dataset [Sheffield et al., 2006] and basin-averaged precipitation sum (blue bars) as derived from APHRODITE [*Yatagai et al.*, 2012]). UIB=upper Indus basin, UGB=upper Ganges basin, UBB=upper Brahmaputra basin, USB=upper Salween basin, UMB=upper Mekong basin.

effects [*Galewsky*, 2009]. Precipitation patterns in the Hindu Kush and Karakoram ranges in the west are characterized by westerly and southwesterly flows, causing the precipitation to fall more equally distributed over the year (Figure 4.1) [*Bookhagen and Burbank*, 2010]. In the Karakoram up to two-thirds of the annual high-altitude precipitation occurs during the winter months [*Winiger et al.*, 2005; *Hewitt*, 2011]. In addition, basin hypsometry determines the ratio of solid and liquid precipitation within a basin. Solid precipitation can be stored long-term as perennial snow, and ice, or short-term as seasonal snow before turning into runoff by melting, while liquid precipitation runs off directly. Each of these runoff components can be further delayed by infiltration into the soil and recharge to groundwater. The magnitude of the contribution of each of these runoff components to the total runoff determines a basin's runoff composition and to a large extent also its response to climate variability and change.

Climate change impact assessments are characterized by large uncertainties stemming from large variation in climate change projections between different General Circulation Models (GCMs) [*Hawkins and Sutton*, 2010], large regional variation in climate projections and uncertainties in the associated response of the cryosphere [*Bolch et al.*, 2012; *Radić and Hock*, 2013]. In addition, the present day hydrological regime is not well understood, constituting a major source of uncertainty in the assessment of climate change impact for hydrology in High Mountain Asia. Thus, detailed and comprehensive assessments of the future water availability in the region are only possible once the current hydrological regime is better quantified [*Miller et al.*, 2012].

Although methods to quantify melt water contribution exist, high-resolution modeling studies focus on small scale watersheds [*Frenierre and Mark*, 2013]. High-resolution approaches that explicitly simulate ice dynamics, necessary to simulate the transient response to climate change, are even scarcer [*Immerzeel et al.*, 2013]. On the other hand, large-scale assessments in the region are often qualitative [*Archer*, 2003; *Immerzeel and Bierkens*, 2012] or include crude assumptions and simplifications to simulate the response of the cryosphere to climate change, which cannot be resolved at low resolution [*Immerzeel et al.*, 2010; *Kaser et al.*, 2010; *Schaner et al.*, 2012; *Siderius et al.*, 2013]. In this study we close this scale gap by implementing a large-scale modeling approach at such a resolution that allows accurate simulation of key hydro-cryospheric processes. Only by using a distributed hydrological modeling approach incorporating transient changes in climate,

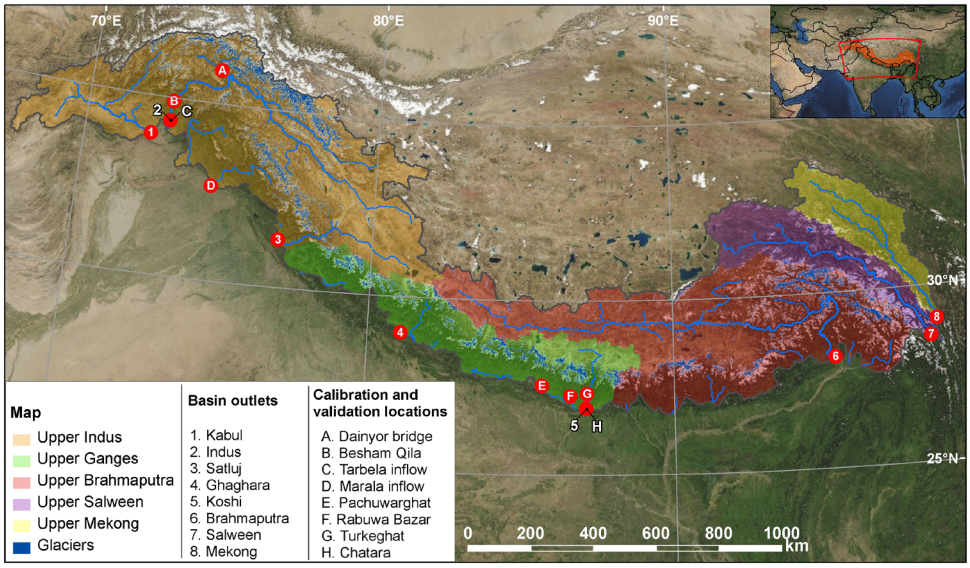

Figure 4.2: Map of the study area showing the outlet locations of major rivers and station locations used for model calibration and validation.

snow cover, glacier dynamics and runoff, appropriate adaptation and mitigation strategies can be developed [*Sorg et al.*, 2012].

Here we use a fully distributed, high-resolution cryospheric-hydrological model to assess upstream runoff composition in five major Asian river basins (Figure 4.2), and we demonstrate how runoff composition and total runoff volume are expected to change until 2050 by forcing this model with an ensemble of the latest GCM outputs.

4.2 Methods and Data

4.2.1 Cryospheric-hydrological model

We use the Spatial Processes in Hydrology (SPHY) model [*Terink et al.*, 2015], which is a high-resolution raster based, fully distributed cryospheric-hydrological model. The model is based on commonly applied hydrological models: Soil Water Assessment Tool [*Neitsch et al.*, 2011; *Arnold et al.*, 2012], Soil Water Atmosphere Plant model [van *Dam et al.*, 2008], Snowmelt Runoff Model [*Gómez-Landesa and Bleiweiss*, 2008] and PCRaster Global Water Balance model [*Bierkens and van Beek*, 2009; *Wada et al.*, 2010]. The model runs at 1x1 km spatial resolution with daily time steps and incorporates all major hydrological and cryospheric processes. The key model processes are outlined below.

The actual runoff which is calculated for each grid cell consists of four possible contributing factors: rainfall-runoff, snow melt, glacier melt, and baseflow. For each grid cell the total runoff generated per time step (Q_{TOT}) is calculated:

$$Q_{TOT} = Q_{GM} + Q_{SM} + Q_{RR} + Q_{BF} \quad (4.1)$$

where Q_{GM} is runoff from glacier melt, Q_{SM} is runoff from snow melt, Q_{RR} is rainfall-runoff and Q_{BF} is baseflow. To determine the contribution of each of the four components to the total runoff within a grid cell, a subgrid parameterization is used in which for each cell the fractional ice cover (G_F), ranging from 0 (no ice cover) to 1 (complete ice cover), is determined. For the remaining fraction of the grid cell the model maintains a dynamic snow storage and soil water storage. As the glacier-covered fraction can change over time, the size of the remaining fraction is adapted accordingly. A variable groundwater storage is maintained for the entire grid cell. Runoff from glacier melt is defined as all the melt generated in the glacierized cell fraction. Runoff from snow melt consists of the snow melt released from the snow storage. Rainfall-runoff consists of the surface runoff from rainfall and lateral flow released from the soil water storage. Baseflow is released from the groundwater storage. Each of these four runoff types is routed downstream using a digital elevation model (DEM) and a recession function.

A differentiation is made between debris free glaciers and debris-covered glaciers, based on altitude and slope. Glaciers at lower altitude tend to have more debris cover because of the cumulative accumulation of debris from higher grounds and glacier parts with a small slope have more debris cover compared to steep-sloped parts of the glacier. We use the same slope differentiation as observed in the European Alps [*Paul et al.*, 2004]. Although we acknowledge that local geology and geomorphology could control debris dynamics, we have constrained our classification to a slope and elevation threshold.

The daily melt from debris free glaciers (A_{CI},[mm we]) is calculated as:

$$A_{CI} = \max(T_{AVG}, 0) \cdot DDF_{CI} \cdot F_{CI} \tag{4.2}$$

where T_{AVG} is the average air temperature, DDF_{CI} is a degree-day factor for debris free glaciers (mm $°C^{-1}day^{-1}$) and F_{CI} is the fraction of debris free glaciers within the fractional glacier cover (G_F) of a grid cell. The daily melt from debris-covered glaciers (A_{DC}, [mm we]) is calculated in a similar way, but with a different degree-day factor:

$$A_{DC} = \max(T_{AVG}, 0) \cdot DDF_{DC} \cdot F_{DC} \tag{4.3}$$

where DDF_{DC} is a degree-day factor for debris-covered glaciers (mm $°C^{-1}day^{-1}$) and F_{DC} is the fraction of debris-covered glaciers within the fractional glacier cover (G_F) of a grid cell. The total glacier melt per grid cell (A_{GLAC},[mm we]) is then calculated by summing the melt from the debris-covered and debris-free glacier types and multiplying by the fractional glacier cover:

$$A_{GLAC} = (A_{CI} + A_{DC}) \cdot G_F \tag{4.4}$$

To model glacier changes at the large river basin scale, where hydrological models operate at a spatial resolution of 1x1 km or lower, parameterizations of future glacier changes become necessary [*Huss et al.*, 2010; *Lutz et al.*, 2013]. The future changes in fractional glacier cover are simulated according to a recently developed parameterization [*Lutz et al.*, 2013], where basin-scale changes in glacier extent are a function of the glacier size distribution in the basins and projections of temperature and precipitation. We calibrate this parameterization to regional mass balance trends [*Kääb et al.*, 2012].

A dynamic snow storage is simulated for each grid cell at a daily time step, based on the model presented by *Kokkonen et al.* [2006]. Similar as for glacier melt, a degree-day melt modeling

approach is used to calculate the snow melt. Besides the accumulation of snow to the snow storage, the process of refreezing of melt water within the existing snow storage is incorporated in the model.

Below the snow storage, a dynamic soil water storage is maintained to derive the amount of rainfall-runoff and infiltration to groundwater. The soil is split into a root zone layer and a subsoil layer as in SWAP [van *Dam et al.*, 2008]. Quantitative soil properties, estimated using pedotransfer functions [*Keshavarzi et al.*, 2010] and soil type, are used in the "van Genuchten model" to simulate soil water storage [*van Genuchten and Nielsen*, 1985]. Surface runoff is calculated as saturation excess runoff. For the root zone layer the actual evapotranspiration is calculated using the Modified Hargreaves reference evapotranspiration equation [*Droogers and Allen*, 2002] and a land use dependent crop coefficient. Lateral flow of water in the soil between cells, exchange of water between soil layers and the groundwater reservoir through percolation and capillary rise, as well as the release of baseflow from the groundwater reservoir, are calculated as in SWAT [*Neitsch et al.*, 2011].

4.2.2 Data sources

We use the 15 arc-second void-filled and hydrologically conditioned HydroSHEDS DEM [*Lehner et al.*, 2008], which is based on the SRTM DEM [*Farr et al.*, 2007]. This DEM is resampled to 1x1 km spatial resolution in UTM projection.

Glacier outlines are extracted from an updated version of the Randolph Glacier Inventory [*Arendt et al.*, 2012a], provided by ICIMOD [*Bajracharya and Shrestha*, 2011]. The outlines are recalculated to a fractional glacier cover per 1x1 km grid cell.

Land use characteristics are extracted from the MERIS Globcover product [*Defourny et al.*, 2007] and soil characteristics are derived from the Harmonized World Soil Database [*FAO/IIASA/ISRIC/ISSCAS/JRC*, 2012].

Records of observed discharge are provided by the Nepal Department of Hydrology and Meteorology, International Water Management Institute Pakistan, the Pakistan Water and Power Development Authority and the Pakistan Meteorological Department.

As meteorological forcing we use the Asian Precipitation Highly-Resolved Observational Data Integration Towards Evaluation of Water Resources (APHRODITE [*Yatagai et al.*, 2012]) dataset for precipitation and Princeton's Global Meteorological Forcing Dataset (PGMFD [*Sheffield et al.*, 2006]) for temperature. APHRODITE is a long-term continental-scale daily precipitation product based on a dense network of rain gauges, and the daily PGMFD was constructed by combining a suite of global observation-based datasets with the National Centers for Environmental Prediction – National Center for Atmospheric Research (NCEP – NCAR) reanalysis. Some caution is appropriate as the large-scale forcing datasets are (partly) based on ground observations. Ground observations in mountainous areas are sparse, especially in the studied region, and are mainly located in the valleys. In mountainous meteorology, vertical lapse rates are important characteristics of climatic variables as air temperature and especially precipitation. The vertical temperature lapse rate is largely dependent on the moisture content of the air and generally varies between the dry adiabatic lapse rate (-0.0098 °C m^{-1}) and the saturated adiabatic lapse rate (typically -0.005 °C m^{-1}, strongly dependent on the temperature). Thus, vertical temperature lapse rates tend to decrease with elevation as the air gets dryer with altitude [*Tahir et al.*, 2011a]. This may not be well represented in the ground station data as the stations are located in the valley bottoms. Precipitation also varies greatly over short horizontal distances in mountain areas and although APHRODITE is considered to be the best performing precipitation dataset for the Himalayas [*Andermann et al.*, 2011], strong

Table 4.1: Calibrated model parameters.

Parameter	Description	Units	Calibrated value
DDFci	Degree-day factor debris-free glaciers	mm °C day^{-1}	6.0
DDFdc	Degree-day factor debris-covered glaciers	mm °C day^{-1}	3.0
DDFs	Degree-day factor snow	mm °C day^{-1}	4.8
SnowSC	Water storage capacity of snow pack	mm mm^{-1}	0.5
PrecF	Multiplication factor for precipitation forcing	-	1.17
αGW	Baseflow recession constant	-	0.05
kx	Routing recession coefficient	-	0.959

vertical lapse rates have been reported, in particular in the Karakoram in the upper Indus basin [*Hewitt*, 2005, 2011; *Winiger et al.*, 2005]. An underestimate in precipitation may lead to problems in model calibration, by for example compensating the shortage of precipitation with increased melt [*Schaefli et al.*, 2005]. To correct for the inherent underestimation of precipitation and avoid correcting for this with wrong melt parameters, we use a single precipitation multiplication factor subject to calibration. We stress the importance of improvements in meteorological forcing data for mountainous terrain facing data scarcity.

We use the latest climate model ensemble generated for the fifth assessment report of the Intergovernmental Panel on Climate Change by the fifth phase of the Climate Model Intercomparison Project (CMIP5 [*Taylor et al.*, 2012]) as future climate forcing. We include two representative concentration pathways (RCPs): RCP4.5 and RCP8.5.

4.2.3 Modeling strategy

Initially the model is forced with the meteorological forcing data for 1998-2007 and model parameters (Table 4.1) are calibrated to daily observed discharge at three locations (locations C, G and H in Figure 4.2). These locations were chosen because they have complete, high quality flow records for the reference period, represent a variety of catchment sizes and represent both climatological regimes (the monsoon dominated eastern and southern Himalayas and the upper Indus basin where the climate is influenced by westerly streams in addition to the monsoon).

The model is calibrated against total flow, not individual flow components, at a daily time step for the complete 10-year period using the PEST parameter estimation software [*Doherty and Skahill*, 2006]. Averaged for the three locations the Nash-Sutcliffe criterion for model efficiency equals 0.79 and the Pearson correlation coefficient equals 0.93 on average (Figure 4.3). The model performance is validated independently versus complete 10-years discharge records at five locations (locations A, B, D, E and F in Figure 4.2). For the five validation locations the average Nash-Sutcliffe criterion for model efficiency equals 0.65 and the average Pearson correlation coefficient is 0.87 (Figure 4.3). We conclude that the model performs satisfactory given the large scale, complexity and heterogeneity of the modeled region and data scarcity. We use one parameter set for the entire domain, which inherently means some stations perform better than others. In the particular case of the upper Indus, another possible explanation could be uncertainty in air temperature forcing in the highest parts of the upper Indus basin, since especially in this area, the used forcing datasets are based on very sparse observations.

Besides validation to observed discharge, the model's runoff separation in different components is compared to findings in smaller scale modeling studies in the region (Table 4.2). Although the

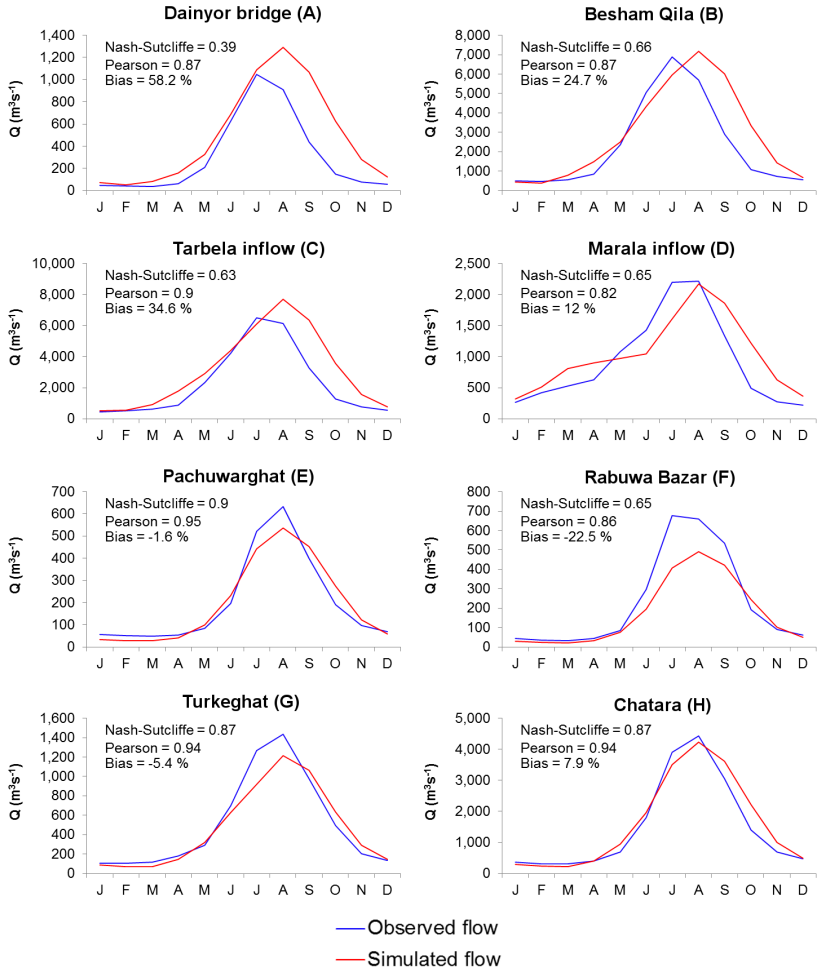

Figure 4.3: Average observed (blue line) and simulated (red line) annual hydrographs for 1998-2007 at calibration stations (C, G, H) and independent validation stations (A, B, D, E, F). The geographical locations of the stations are listed in Figure 4.2. Each plot lists the Nash-Sutcliffe criterion of model efficiency, Pearson correlation coefficient and bias.

comparison is evidently hampered by differences in scale and model concepts, it does provide further confidence in the models capability. For the Satluj subbasin in the upper Indus basin an average contribution of glacier and snow melt of 59% was found for 1986-1996 [*Singh and Jain*, 2002]. The remaining 41% were attributed to rain. In our results for 1998-2007, 48% of the runoff is glacier and snow melt, 39% is rainfall-runoff and 13% is baseflow. Hence the studies show reasonable agreement, especially considering that part of the baseflow originates from glacier and snow melt, which is not considered in the other study. In the Langtang watershed, compared to our study, *Immerzeel et al.* [2011] estimated very similar contributions using a high-resolution combined cryospheric hydrological model. Other estimates for the Langtang watershed by *Racoviteanu et al.* [2013] using a straightforward ice ablation model, which were validated using

Table 4.2: Comparison of results regarding runoff contributions in this study to other studies[1].

Site (river, location)	Reference	Period cited study	Contribution per component in cited study (%)				Contribution per component in this study for 1998-2007 (%)			
			Glacier melt	Snow melt	Rain runoff	Base flow	Glacier melt	Snow melt	Rain runoff	Base flow
Satluj, Bhakra Dam	Singh and Jain [2002]	1986-1996	59		41	-	27.6	20.8	38.6	13.0
Langtang Khola, Kyangjing	Immerzeel et al., [2011]	2001-2010	47.0	6.9	28.8	17.4	52.5	12.8	25.0	9.7
Langtang Khola, Kyangjing	Racoviteanu et al. [2013]	1988-2006	58.3	41.7			52.5	12.8	25.0	9.7
Dudh Koshi, Rabuwa Bazar	Racoviteanu et al. [2013]	1988-2006	7.4	92.6			18.8	4.8	64.8	11.6
Indus, Besham Qila	Mukhopadhyay and Khan, [2014]	1969-2010	70		30		67.3	17.6	7.1	8.0
Hunza, Dainyor bridge	Mukhopadhyay and Khan, [2014]	1966-2010	74		26		80.6	9.6	1.3	8.5
Gilgit, Gilgit	Mukhopadhyay and Khan, [2014]	1980-2010	68		32		54.2	26.0	12.3	7.5
Indus, Kachura	Mukhopadhyay and Khan, [2014]	1970-2010	71		29		72.7	15.1	4.1	8.2

[1]In the compared studies the separation in runoff contributors differs from our approach with differentiation of four components. Therefore values may represent multiple components as indicated by the number of columns covered in the table.

isotope analysis and mixing models, indicated 58.3% annual average contribution of glacier melt, matching also well with the 53% contribution we estimated for 1998-2007 in the same watershed. Further downstream, for the Dudh Koshi river, the ice ablation model by Racoviteanu et al. simulates 7.4% contribution by glacier melt, where in this study 18.8% was found. At this location the ice ablation model results were however not validated. The discrepancy in the model results may result from the high sensitivity of the ice ablation model to the chosen equilibrium line altitude (ELA) and ice ablation gradient as well as the difference in scale of the applications. *Mukhopadhyay and Khan* [2014] estimated long-term contributions of melt water to total runoff for multiple locations in the upper Indus basin, by separating annual hydrographs in different flow regimes, using linear smoothing and recursive digital filtering techniques. Comparing our results to what Mukhopadhyay and Khan found at four locations covering large parts of the upper Indus basin, shows that our estimates of melt water contribution are consistently somewhat higher than their results. Nevertheless, the estimates in the two studies match quite well, given the differences in time period, scales, and approach. Hence, we conclude that the used model is capable of simulating the magnitude and composition of runoff.

We use the CMIP5 multi-model ensemble [*Taylor et al.*, 2012], which is the set of global climate change simulations which is used as basis for the fifth assessment report of the Intergovernmental Panel on Climate Change (IPCC), as climate change forcing for our model. We analyzed the projected changes in average air temperature (°C) and precipitation (%) between 1961-1990 and 2021-2050 for all available CMIP5 simulations for two emission scenarios: RCP4.5 (43 model runs) and RCP8.5 (41 model runs). Based on these projected differences four combinations (dry and cold;

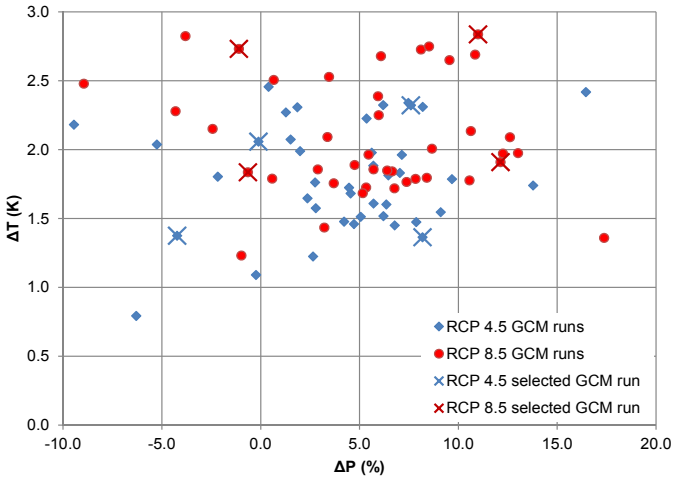

Figure 4.4: Projected changes of temperature and precipitation between 1961-1990 and 2021-2050 over the model domain for RCP4.5 (43 model runs, blue diamonds) and RCP8.5 (41 model runs, red dots). The selected model runs (marked with crosses) are located closest to the 10- and 90-percentiles of temperature change and precipitation change, and are used as climatic forcing in the hydrological model.

Table 4.3: Projected changes in temperature (ΔT) and precipitation (ΔP) averaged over the five basins for 2021-2050 with respect to 1961-1990.

RCP	Description	GCM	Ensemble	ΔT (°C)	ΔP (%)
RCP4.5	dry, cold	GISS-E2-R	r4i1p1	1.4	-4.2
	dry, warm	IPSL-CM5A-LR	r4i1p1	2.1	-0.1
	wet, cold	CCSM4	r5i1p1	1.4	8.2
	wet, warm	CanESM2	r4i1p1	2.3	7.6
RCP8.5	dry, cold	GFDL-ESM2G	r1i1p1	1.8	-0.7
	dry, warm	IPSL-CM5A-LR	r4i1p1	2.7	-1.1
	wet, cold	CSIRO-Mk3-6-0	r3i1p1	1.9	12.1
	wet, warm	CanESM2	r4i1p1	2.8	11.0

dry and warm; wet and cold; wet and warm) for each RCP were derived based on the 10th and 90th percentile values of the projected changes. The model runs closest to the percentile values were selected (Figure 4.4, Table 4.3).

Subsequently we apply the well-established "delta change" approach to generate time series of future air temperature and precipitation [*Arnell*, 1999; *Kay et al.*, 2008]. For each selected model we compute a transient "delta change" value by linearly interpolating the changes between 1961–1990 and 2021–2050 for the GCM grid cells at their nominal resolution. This is done for each month (Jan-Dec), to include possible seasonal differences in the GCM output. For each simulated year

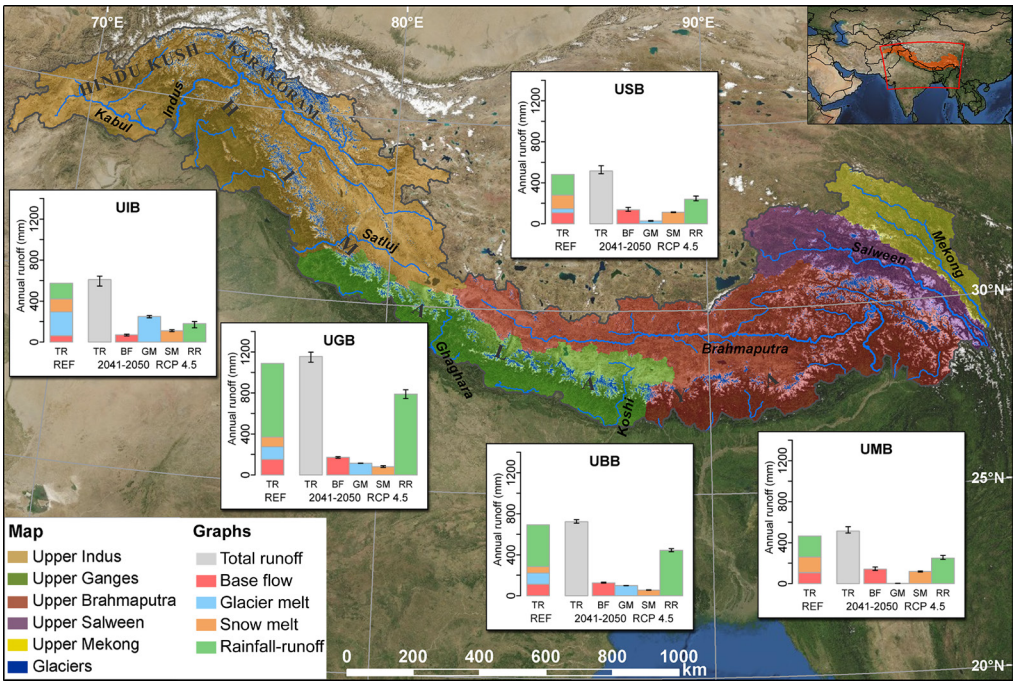

Figure 4.5: The upstream basins of Indus (UIB, brown), Ganges (UGB, green), Brahmaputra (UBB, red), Salween (USB, purple) and Mekong (UMB, yellow). Bar plots show the average annual runoff generation (TR) for the reference period (1998-2007, REF, first column). The second column shows the mean projected annual total runoff (TR) for the future (2041-2050 RCP4.5) when the model is forced with an ensemble of 4 GCMs. In the subsequent columns TR is split in four contributors (BF: baseflow, GM: glacier melt, SM: snow melt, RR: rainfall-runoff). Error bars indicate the spread in model outputs for the model forced by the ensemble of 4 GCMs.

in 2008–2050, we select a random year from the 1x1 km reference period climate dataset and we superimpose the monthly temperature and precipitation change grids to construct a transient time series from 2008 to 2050. These time series are then used as meteorological forcing for the SPHY model.

4.3 Results and Discussion

4.3.1 Hydrological regimes

In the upper Indus basin (UIB), stream flow is dominated by glacier melt water, contributing 40.6% of the total runoff (Figure 4.5, Table 4.4). Despite its larger relative glacierized area, glacier melt only contributes 11.5% of the total runoff generated in the upper Ganges basin (UGB). Due to the monsoon-dominated precipitation regime in the UGB, the runoff regime is rain dominated here (Figure 4.5, Table 4.4). The hydrological regime in the upper Brahmaputra basin (UBB) is comparable to the UGB, although the relative contribution of glacier melt and snow melt in the UBB are slightly larger compared to the UGB. This can be explained by the differences in hypsometry

Table 4.4: Basin characteristics.

Basin	Precipitation (mm yr^{-1})	Glacierized area (%)	Runoff (mm yr^{-1})	Contribution to total runoff (%)			
				Glacier melt	Snow melt	Rainfall-runoff	Base flow
Upper Indus	346	4.9	574	40.6	21.8	26.8	10.8
Upper Ganges	900	5.4	1088	11.5	8.6	66.0	13.9
Upper Brahmaputra	573	3.1	691	15.9	9.0	58.9	16.2
Upper Salween	595	1.3	480	8.3	27.5	42.0	22.2
Upper Mekong	642	0.2	464	0.9	32.5	43.9	22.8

Table 4.5: Basin hypsometry expressed as basin area distributed over four elevation classes

Basin	Basin area (%) in elevation class			
	< 3000 m a.s.l.	3001-4000 m a.s.l.	4001-5000 m a.s.l.	5001-6000 m a.s.l.
Upper Indus	30.0	15.7	31.9	21.8
Upper Ganges	41.0	11.6	26.3	19.7
Upper Brahmaputra	16.3	13.2	41.0	29.2
Upper Salween	0.9	6.2	67.5	25.4
Upper Mekong	0.3	10.2	80.1	9.3

of these basins (Table 4.5), with the UBB having a larger portion of its area at higher elevations, favoring solid precipitation in this basin. Rainfall-runoff is the dominant component in the upper Salween basin (USB) and upper Mekong basin (UMB). Notably, however, is the large contribution of seasonal snow melt in these basins, compared to the three other basins (Figure 4.5, Figure 4.6), since large parts of these basins are located on the Tibetan Plateau (Table 4.5).

At the outlets of the UIB, the contribution of glacier melt in the Indus River is much larger compared to the Kabul and Satluj Rivers (Figure 4.7). The snow dominated Kabul River's flow peaks during the spring months, while the glacier melt dominated Indus River peaks during summer, when glacier melt is at its maximum. The discharge in the Satluj River peaks during the summer months as well, but this is explained by a monsoon dominated rainfall regime in this basin (Figure 4.8), rather than by glacier melt. Hence, the Satluj discharge peak is directly related to the peak in rainfall during the monsoon, which is also the case for the UGB, UBB, USB and UMB (Figure 4.7). In the UBB, glacier melt is important for the most eastern tributaries (Figure 4.8), enhancing the flow peak at the upstream basin outlet during the summer months (Figure 4.7). The Salween and Mekong discharges peak during the monsoon-months, where flow composition is dominated by snow melt during the first months and dominated by rainfall-runoff during the last months of the monsoon season (Figure 4.7). The contribution of baseflow to the total flow varies from 11% in the UIB to 23% in the UMB (Figure 4.5).

4.3.2 Climate change scenarios

To estimate the impacts of climate change for the future hydrological regimes in the five basins, we force the model with the latest ensemble of climate models. While GCMs agree that, between the

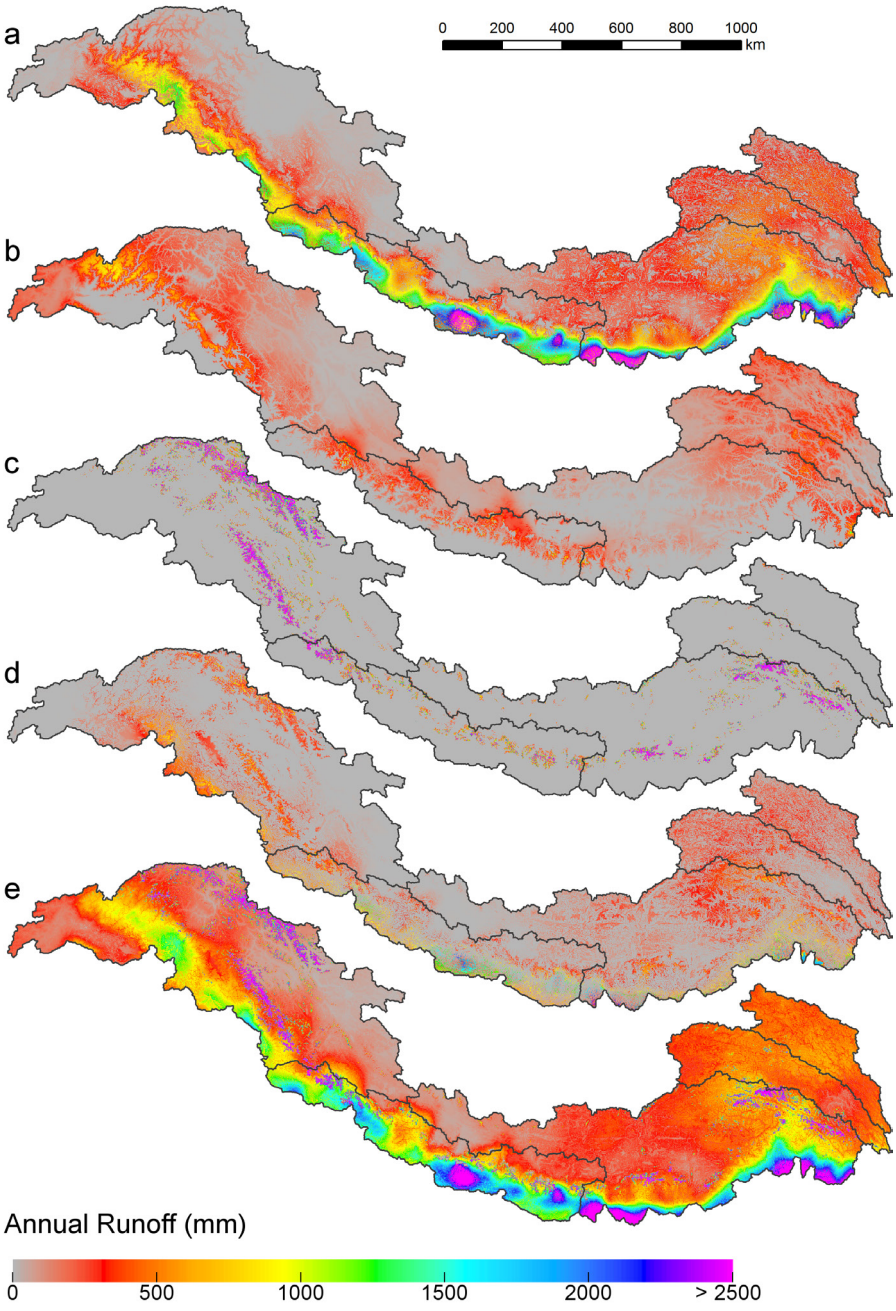

Figure 4.6: Annual runoff generated during the reference period (1998-2007) at 1x1 km model resolution. Upper panels show the runoff generated by each component: a) rainfall-runoff, b) snow melt, c) glacier melt, d) baseflow. Panel e shows the total runoff (e.g. the sum of the four components).

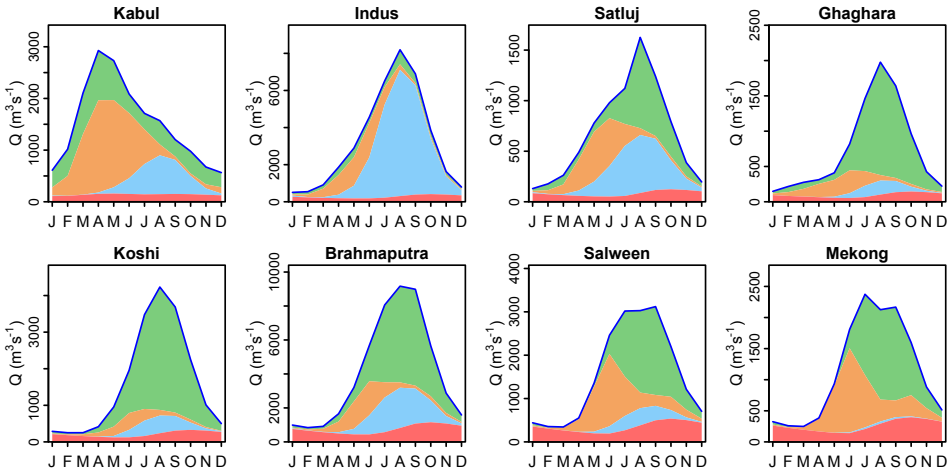

Figure 4.7: Average annual hydrographs for the reference period (1998-2007) at major river's outlets from the upstream domain (locations indicated in Figure 4.2). The blue line indicates the total discharge. The stream flow composition is indicated for four components: baseflow (red), glacier melt (blue), snow melt (orange), rainfall-runoff (green).

reference period (1998-2007) and 2050, temperatures will increase in the region by ~1 to 2.2 °C, and with roughly the same magnitude throughout the year, precipitation projections are uncertain. Averaged over the five basins, changes in precipitation of -3.5% to +9.5% are projected for the same period. This uncertainty range is even larger for individual basins and for specific seasons (Figure 4.9). On the whole, an increase in precipitation is projected for each basin except for the UIB, where projections of precipitation change show opposite signs.

4.3.3 Future glacier extent

For the river basins with significant contribution of glacier melt to total flow, the future evolution of the glacier cover is crucial. Observed glacier changes are not uniform in the region [*Hewitt*, 2011; *Bolch et al.*, 2012; *Yao et al.*, 2012; *Gardelle et al.*, 2013]. While glaciers are losing mass in most parts of the Himalayas, stability or even mass gain is observed in the Pamir and Karakoram ranges. Since the 1 km model resolution does not allow for explicit inclusion of ice flow, we use a parameterization of basin scale glacier changes [*Lutz et al.*, 2013] calibrated to regional mass balance trends [*Kääb et al.*, 2012], to simulate future glacier changes. As a result of increasing air temperatures, a decrease in glacier extent is projected for all basins for all ensemble members despite the projected precipitation increase in most ensemble members (Table 4.6). Our basin-scale estimates of future glacier changes are in good agreement with previous large-scale work [*Radić et al.*, 2014].

4.3.4 Future changes in hydrology

For all basins, the amount of glacier melt water contributing to the total flow does not change much at least until 2050 since the decrease in glacier area is compensated by an increase in melt rate (Figure 4.5, Figure 4.10, Table 4.7). For the UIB, increasing glacier melt water is projected by all ensemble members in both RCPs.

The future amount of snow melt in the UIB decreases slightly for all ensemble members in both RCPs, as the increasing temperatures and limited change in precipitation result in a shift towards

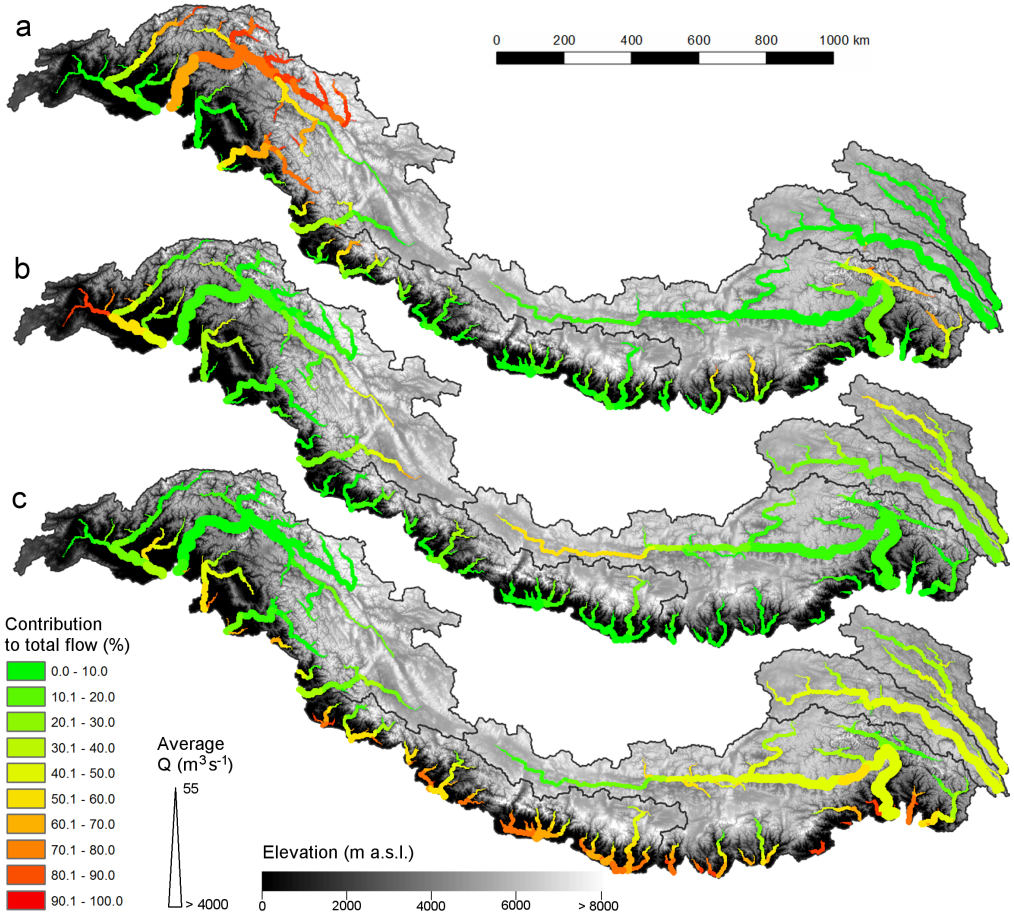

Figure 4.8: Contribution to total flow by glacier melt (a), snow melt (b) and rainfall-runoff (c) for major streams during the reference period (1998-2007). Line thickness indicates the average discharge during the reference period.

more liquid precipitation (Figure 4.5, Figure 4.10, Figure 4.9). Overall, for three out of four ensemble members in RCP4.5, the annual runoff generated in the UIB increases by 7-12% in 2041-2050 with respect to the reference period. Only for the dry and warm scenario a decrease (-5%) in runoff is projected (Figure 4.5) primarily resulting from a precipitation decrease (Figure 4.9). For RCP8.5 three ensemble members project a 2-8% increase in runoff while the dry and warm scenario projects a -5% decrease in runoff (Figure 4.10). The projected changes in the average annual hydrographs of the Kabul, Indus and Satluj Rivers reveal how different the responses to climate change are between rivers with different stream flow composition (Figure 4.11, Figure 4.12). For example, the flow in the Indus River is dominated by temperature driven glacier melt during summer, and the uncertainty in future flow is therefore relatively small as a result of small uncertainty in future temperature changes. The Kabul River on the other hand, has a much larger rainfall-runoff and snow component, leading to a larger uncertainty in future flow as a result of large uncertainties in future precipitation Figure 4.9, Figure 4.11, Figure 4.12).

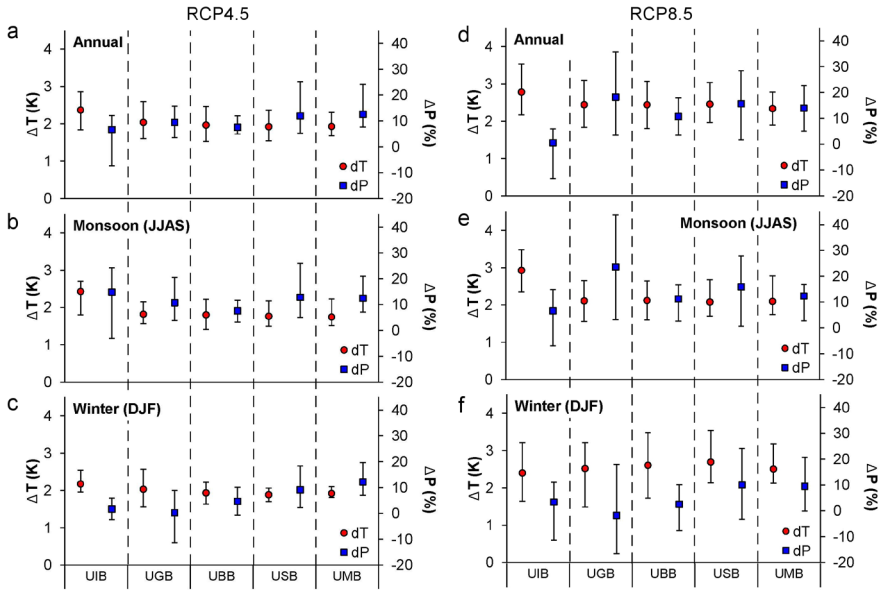

Figure 4.9: Projected changes in temperature (ΔT, red circles) and precipitation (ΔP, blue squares) for 2021-2050 with respect to 1961-1990 per basin for RCP4.5 (left panels) and RCP8.5 (right panels). Changes are shown on annual basis (a,d), for the monsoon period (b,e) and winter months (c,f). Red circles and blue squares indicate the mean projection for an ensemble of four GCMs. The error bars indicate the full range of projections for the 4 GCM-ensemble. UIB = upper Indus basin, UGB = upper Ganges basin, UBB = upper Brahmaputra basin, USB = upper Salween basin, UMB = upper Mekong basin.

Table 4.6: Simulated remaining glacier area (%) in 2050 with respect to 2007.

RCP	Description	GCM	Ensemble	Upper Indus	Upper Ganges	Upper Brahmaputra	Upper Salween	Upper Mekong
RCP4.5	dry, cold	GISS-E2-R	r4i1p1	79	64	69	56	61
	dry, warm	IPSL-CM5A-LR	r4i1p1	76	58	61	42	41
	wet, cold	CCSM4	r5i1p1	80	63	64	42	44
	wet, warm	CanESM2	r4i1p1	76	55	58	37	37
RCP8.5	dry, cold	GFDL-ESM2G	r1i1p1	76	59	61	40	41
	dry, warm	IPSL-CM5A-LR	r4i1p1	72	55	57	38	37
	wet, cold	CSIRO-Mk3-6-0	r3i1p1	77	63	64	42	42
	wet, warm	CanESM2	r4i1p1	73	52	55	33	32

Table 4.7: Simulated average annual runoff (mm) differentiated for each runoff component for the reference period (1998-2007) and future period (2041-2050). Values for the future period are the mean of the model output when forced with 4-GCM ensembles for RCP4.5 and RCP8.5 respectively.

Basin	Period	Total runoff	Glacier melt	Snow melt	Rainfall-runoff	Baseflow
Upper Indus	1998-2007	574	233	125	154	62
	2041-2050 RCP4.5	609	250	109	180	71
	2041-2050 RCP8.5	586	251	103	165	68
Upper Ganges	1998-2007	1088	125	94	718	151
	2041-2050 RCP4.5	1156	115	81	789	172
	2041-2050 RCP8.5	1238	116	74	862	185
Upper Brahmaputra	1998-2007	691	110	62	407	112
	2041-2050 RCP4.5	722	99	56	443	126
	2041-2050 RCP8.5	727	99	52	448	128
Upper Salween	1998-2007	480	40	132	202	107
	2041-2050 RCP4.5	516	27	112	240	137
	2041-2050 RCP8.5	523	25	107	248	144
Upper Mekong	1998-2007	464	4	151	204	106
	2041-2050 RCP4.5	513	3	119	250	142
	2041-2050 RCP8.5	511	3	113	252	143

For the rainfall-runoff dominated UGB the future hydrology largely depends on the precipitation projections. These projections have very large uncertainties, and large variation between the annually averaged and seasonal projections (Figure 4.9). Overall, all ensemble members in both RCPs project precipitation increases for the UGB during the monsoon, leading to increases in total annual runoff up to 10% for RCP4.5 and 27% for RCP8.5 respectively. The absolute amounts of glacier melt and snow melt do not change much, but their relative contributions decrease due to the increased rainfall-runoff. As a consequence, increased flows are observed during the discharge peak in the monsoon season, with large uncertainty in the magnitude of flow increase (Figure 4.11, Figure 4.12).

For the UBB, the uncertainty in the precipitation projections is small compared to the other basins, especially for RCP4.5 (Figure 4.9). An increase in precipitation up to 12% for RCP4.5 and up to 18% for RCP8.5 is projected, which in combination with rising temperatures leads to 3-8% increase in annual runoff for RCP4.5 and 1-13% increase for RCP8.5. This is also reflected in the Brahmaputra outlet's average annual hydrograph for 2041-2050 (Figure 4.11, Figure 4.12), where year round increases in flow are projected due to the consistent increase in precipitation. Notably, the projected increase in precipitation during the monsoon months is small compared to the neighboring UGB and USB, explaining the smaller increase in runoff during the monsoon season. The relative contribution of baseflow remains unchanged for the future scenarios and therefore baseflow changes proportional to the change in total runoff.

Given the similarities of the hydrological regimes and climate change projections in the USB and UMB, their hydrological responses are similar. Projected precipitation increases are fairly constant

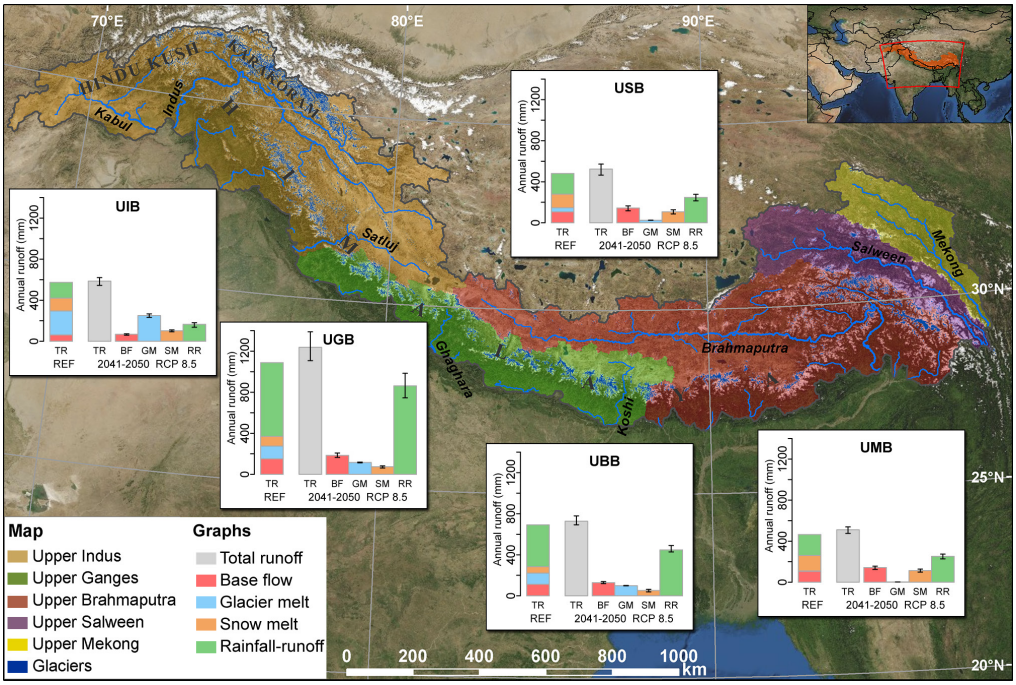

Figure 4.10: The upstream basins of Indus (brown), Ganges (green), Brahmaputra (red), Salween (purple) and Mekong (yellow). Glaciers are indicated as blue polygons (ICIMOD glacier inventory [*Bajracharya and Shrestha*, 2011]), major streams are indicated by blue lines (streams derived from HydroSHEDS [*Lehner et al.*, 2008]). Bar plots show the average annual runoff generation (TR) for the reference period (1998-2007, REF, first column). The second column shows the mean projected annual total runoff (TR) for the future (2041-2050 RCP8.5) when the hydrological model is forced with an ensemble of 4 GCMs. In the subsequent columns the projected annual total runoff is split in four contributors to total runoff (BF: baseflow, GM: glacier melt, SM: snow melt, RR: rainfall-runoff). For the projections the error bars indicate the spread in model outputs for the model forced by the ensemble of 4 GCMs. UIB = upper Indus basin, UGB = upper Ganges basin, UBB = upper Brahmaputra basin, USB = upper Salween basin, UMB = upper Mekong basin.

for all seasons and the uncertainty in precipitation projections is somewhat larger for the USB compared to the UMB (Figure 4.9). An associated increase in runoff is expected for all ensemble members (Figure 4.5, Figure 4.10). At the outlet of the upstream basins, increased flows are expected for August-May related to increased precipitation and a shift in snow melt peak to earlier spring, while decreasing flows are expected in June and July, related to the same shift (Figure 4.11, Figure 4.12). Furthermore, the snow melt peak decreases in magnitude as the ratio of liquid and solid precipitation shifts in favor of liquid precipitation in response to increased temperatures.

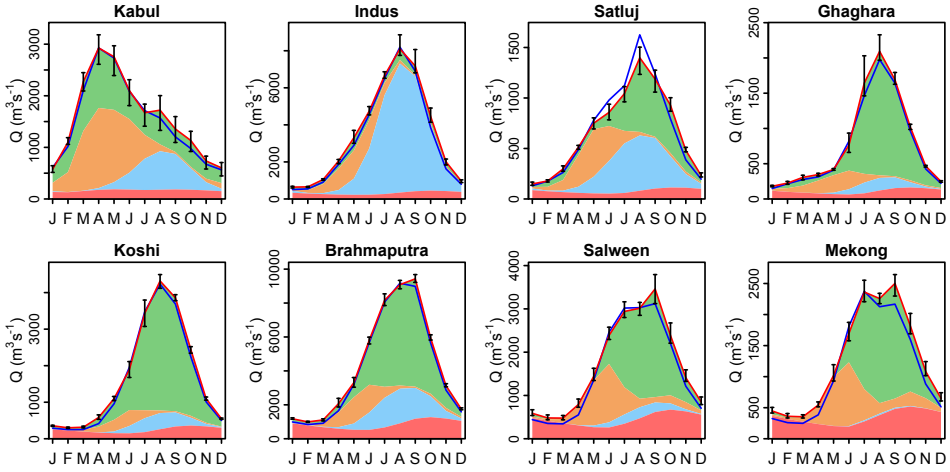

Figure 4.11: Average annual hydrographs for the future period (2041-2050, RCP4.5) at major river's outlets from the upstream domain (locations are indicated in Figure 4.2). Plots show the mean projected discharge when forced with the 4 GCM ensemble (red line) and the discharge for the reference period (1998-2007, blue line). For the future period the stream flow composition is indicated for four components: baseflow (red), glacier melt (blue), snow melt (orange), rainfall-runoff (green). The error bars indicate the spread in projections for the future period when forced with the ensemble of 4 GCMs.

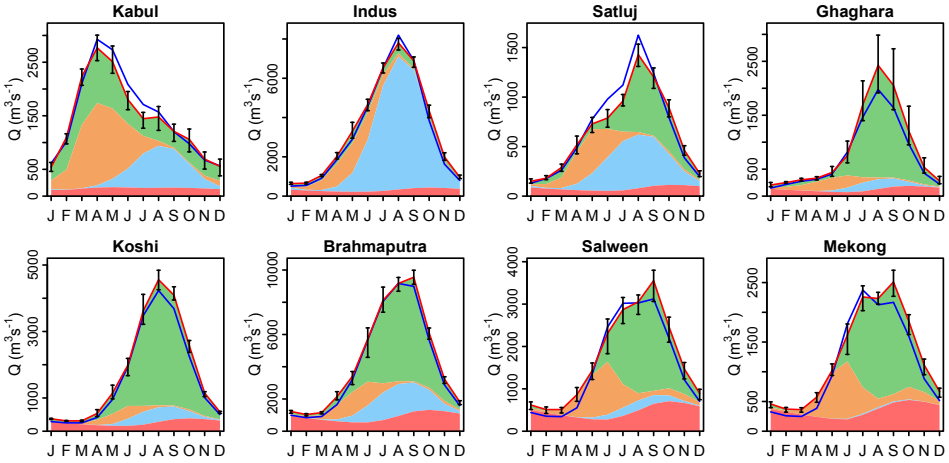

Figure 4.12: Average annual hydrographs for the future period (2041-2050, RCP8.5) at major river's outlets from the upstream domain (locations indicated in Figure 4.2). Plots show the mean projected discharge when forced with the 4 GCM ensemble (red line) and the discharge for the reference period (1998-2007, blue line). For the future period the stream flow composition is indicated for four components: baseflow (red), glacier melt (blue), snow melt (orange), rainfall-runoff (green). The error bars indicate the spread in projections for the future period when forced with the ensemble of 4 GCMs.

4.4 Conclusions

Previous work indicated future increases in runoff in two contrasting smaller catchments in the UIB and UGB [*Immerzeel et al.*, 2013]. Here we use a novel high-resolution cryospheric-hydrological modeling approach to show that these findings also hold at large scale, despite the large differences in hydrological regimes between basins and between rivers and tributaries within basins. In contrast to the UGB, UBB, USB and UMB, where the main driver of runoff increase is the projected increase in precipitation, the main driver in the UIB is accelerated melt. The contradictory precipitation projections for this basin make water availability in the UIB highly uncertain in the long run, requiring further research. Since a consistent increase in runoff is expected for these five basins at least until 2050, a change of focus to coping with extreme events and intra-annual shifts in water availability is desirable. Changes in the frequency of extreme events, which are not addressed in this study, may increase natural hazards, while intra-annual shifts in water availability can have major consequences for regional food security when flow peaks and growing seasons are not coinciding.

Chapter 5

Modeling future changes in hydrological sources, seasonal shifts and extremes in the upper Indus basin

Based on: *Lutz, A.F., W.W. Immerzeel, P.D.A. Kraaijenbrink, and A.B. Shrestha (under review), Climate change impacts on the upper Indus hydrology: sources, shifts and extremes. PLOS-ONE.*

Abstract

The Indus basin heavily depends on its upstream mountainous part for the downstream supply of water while downstream demands are high. Since downstream demands will likely continue to increase, accurate hydrological projections for the future supply are important. We use an ensemble of statistically downscaled CMIP5 General Circulation Model outputs for RCP4.5 and RCP8.5 to force a cryospheric-hydrological model and generate transient hydrological projections for the entire 21st century for the upper Indus basin. Three methodological advances are introduced: (i) A new precipitation dataset that corrects for the underestimation of high-altitude precipitation is used. (ii) The model is calibrated using data on river runoff, snow cover and geodetic glacier mass balance. (iii) An advanced statistical downscaling technique is used that accounts for changes in precipitation extremes. The analysis of the results focuses on changes in sources of runoff, seasonality and hydrological extremes. We conclude that the future of the upper Indus basin's water availability is highly uncertain in the long run, mainly due to the large spread in the future precipitation projections. Despite large uncertainties in the future climate and long-term water availability, basin-wide patterns and trends of seasonal shifts in water availability are consistent across climate change scenarios. Most prominent is the attenuation of the annual hydrograph and shift from summer peak flow towards the other seasons for most ensemble members. In addition there are distinct spatial patterns in the response that relate to monsoon influence and the importance of meltwater. Analysis of future hydrological extremes reveals that increases in intensity and frequency of extreme discharges are very likely for most of the upper Indus basin and most ensemble members.

5.1 Introduction

The water resources supplied by the upper Indus basin (UIB) are essential to millions of people and future changes in both demand and supply may have large impacts [*Immerzeel and Bierkens*, 2012]. The UIB provides water for the world's largest continuous irrigation scheme through several

large reservoirs (e.g. the Tarbela and Mangla dams, Figure 5.1), which depend for more than 50% of their annual inflow on snow and glacier melt water [*Immerzeel et al.*, 2010; *Lutz et al.*, 2014; *Mukhopadhyay and Khan*, 2014a, 2015a]. In combination with variable precipitation patterns, the intra-annual variation in streamflow is high [*Reggiani and Rientjes*, 2014] and so is the supply to the downstream areas. Water demands are high, primarily because of water consumption by irrigated agriculture [*Jain et al.*, 2007], and hydropower generation [*Mirza et al.*, 2008]. At the same time the downstream part of the basin is characterized by very dry conditions [*Wanders and Wada*, 2014], making it largely dependent on water supply from the upstream areas. The downstream demands exceed the supply and on an annual basis groundwater resources are depleted by an estimated 31 km^3 [*Cheema et al.*, 2014], which makes the Indus basin aquifer the most overstressed aquifer in the world [*Wada et al.*, 2010; *Gleeson et al.*, 2012; *Richey et al.*, 2015]. The strong dependence of river runoff on snow and glaciers in combination with a rapidly growing population and associated increase in water and energy demand make the Indus basin globally a climate change hotspot [*De Souza et al.*, 2015].

The climate of the UIB is complex and is the result of an intricate interaction between monsoon circulation, westerlies and the topography [*Hewitt*, 2011; *Scherler et al.*, 2011; *Mölg et al.*, 2013; *Maussion et al.*, 2014; *Mishra*, 2015]. The interaction between topography and precipitation manifests itself at various scales ranging from a synoptic scale of several hundreds of kilometers to an orographic meso-scale of less than 30 kilometers [*Barros et al.*, 2004]. Along the Himalayan arc the monsoon influence is largest but this influence decreases in north-western direction where mid-latitude westerlies become increasingly important, e.g. at the junction of the Karakoram,

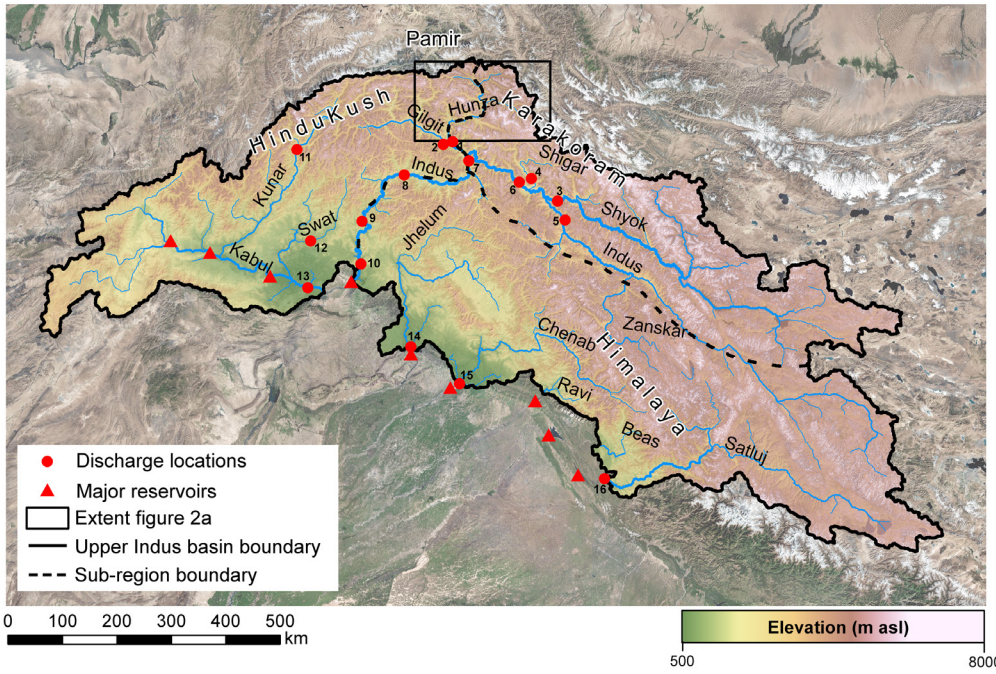

Figure 5.1: The upper Indus basin. The map shows the main rivers, mountain ranges, digital elevation model and locations of the main dams. Numbered red dots indicate stream flow locations

Pamir and Hindu Kush mountain ranges (Figure 5.1). Precipitation from the westerlies is highest in winter when low-pressure systems reach the western margin of the greater Himalaya. This supply of moisture reaches higher elevations than the summer monsoon, which might be related to the higher tropospheric extent of the westerly airflow [*Scherler et al.*, 2011].

Several studies investigated historical trends in precipitation and temperature in the UIB. Trend analysis on precipitation for 17 stations throughout the UIB showed statistically significant increasing trends in precipitation for several stations in annual, summer and winter precipitation between 1961 and 1990 [*Archer and Fowler*, 2004]. In a subsequent study by the same authors, trends in temperature between 1961 and 2000 were also assessed and it was found that (i) the diurnal temperature range is increasing consistently in all seasons, (ii) winter mean and maximum temperatures show significant increases and (iii) mean and minimum summer temperatures show a consistent declining trend [*Fowler and Archer*, 2006]. These findings were confirmed also for a more recent period (1980 – 2009) for roughly the same stations. In this study it was found that a few stations in the Karakoram and Gilgit regions (Figure 5.1) showed a significant increase in precipitation. Minimum temperatures are increasing throughout the year, except for summer, and maximum temperatures are increasing throughout all seasons [*Bocchiola and Diolaiuti*, 2013]. Trend analysis on the ERA40 reanalysis dataset for the Baltoro region in the Karakoram (Figure 5.1) showed negative summer temperature trends from 1958 until 1990 and a positive trend from 1991 to 2001 [*Quincey et al.*, 2009]. The authors also found an increasing trend in annual precipitation from 1970 to 1990 and a decreasing trend during the 1990s. This increase is attributed to trends in spring and summer. Trend analysis on several gridded precipitation products did not confirm these findings and although for several gridded products a negative precipitation trend was found for the Himalayan range, positive precipitation trends could not be confirmed for the Hindu Kush – Karakoram region [*Palazzi et al.*, 2013]. Studies on the winter westerly disturbances, being the major source of winter precipitation, indicate strong intra-seasonal variability and a trend of enhanced frequency and strength of these disturbances in the Karakoram and western Himalaya between 1979 and 2010, leading to increased heavy winter precipitation [*Cannon et al.*, 2014, 2015].

There is great debate on the response of glaciers in the UIB to climate change during the last decade. The glaciers in the Himalayan range are seemingly losing mass at rates similar to other mountainous regions in the world, however the glaciers in the Karakoram and Pamir mountain ranges have neutral mass balances on average and are characterized by a large number of surging glaciers [*Hewitt*, 2007; *Kääb et al.*, 2012, 2015; *Gardelle et al.*, 2013; *Gardner et al.*, 2013; *Quincey et al.*, 2015]. This so called Karakoram anomaly has not been explained, but a possible reason could be a combination of a decrease in summer temperatures and an increase in precipitation. However this is still speculative and requires further study and understanding of atmospheric processes leading to high-altitude precipitation. This hypothesis is supported by an increasing trend in snow cover that was found in the Hunza basin based on MODIS snow cover analysis [*Tahir et al.*, 2011b, 2015] and that the water balance of the UIB can be closed without large negative glacier mass balances [*Reggiani and Rientjes*, 2014]. On the other hand, decreasing trends in snow cover for the most westerly-influenced subbasins, including Hunza, and increasing trends for the more monsoon-influenced subbasins were found [*Hasson et al.*, 2014]. A trend analysis of snow cover in the monsoon-dominated Sutlej basin indicated a trend of snow cover reduction between 2000 and 2009 [*Mir et al.*, 2015]. *Kapnick et al.* [2014] conclude that the Karakoram is protected from reductions in annual snowfall under climatic warming because the seasonal cycle is dominated by non-monsoonal winter precipitation.

Rising temperatures in basins strongly depending on glacier melt are likely to result in an increase in stream flow in the near future and a decline in the far future. This is caused by the fact that the total amount of glacier melt is a tradeoff between increasing melt rates on one hand and reduced glacier areas on the other hand. The moment when the trend in glacier melt changes from positive to negative is highly variable [*Immerzeel et al.*, 2013; *Soncini et al.*, 2015]. *Reggiani and Rientjes* [2014] analyzed a 1961 to 2009 record of reservoir inflow at Tarbela, which is the largest reservoir on the main stem of the Indus river (Figure 5.1), and found a declining trend, although statistically insignificant. Further upstream trend analysis on streamflow records at different locations identified stable or declining trends in runoff too [*Tahir et al.*, 2011b; *Sharif et al.*, 2013; *Mukhopadhyay and Khan*, 2015b]. These studies are indicative that large parts of the UIB are (not yet) experiencing accelerated melt, which could indeed be partly attributed to the Karakoram anomaly. However, contrary to these findings, a recent study in the Shigar river basin [*Mukhopadhyay and Khan*, 2014b] reports rising river flows. However, the authors do not relate this to the existence of the Karakoram anomaly. Instead, they argue that an increase in runoff is possible under neutral glacier mass balance conditions as a result of increasing temperature and precipitation, i.e. the mass turnover of the glacier is increasing, yet the mass balance remains neutral.

Climate simulations are used to generate projections of future climate change in the UIB. Analysis of precipitation change signals in a large number of General Circulation Model (GCM) runs indicates that an increase in summer precipitation and on average no significant change in winter precipitation are likely [*Palazzi et al.*, 2014]. However, the spread in the precipitation changes from the GCM ensemble is large, because the complex UIB climate is difficult to simulate [*Turner and Annamalai*, 2012]. Analysis with regional climate models (RCM) reveals consistent warming until the end of the century with greater warming in the upper Indus than in the lower Indus. Precipitation projections show a non-uniform change with increases projected for the upper parts and decreases for the lower parts [*Rajbhandari et al.*, 2014; *Ali et al.*, 2015]. However care needs to be taken in using RCMs directly in impact studies. A recent study that analyzed the uncertainty of the CORDEX South Asia regional climate models showed that the RCMs exhibit large uncertainties in both temperature and precipitation, that they exhibit a large cold bias and that they are unable to reproduce observed warming trends [*Mishra*, 2015]. Empirical-statistical downscaling, which may be better suited under such complex conditions, is another approach to generate forcing for climate change impact models, where climate model output is statistically corrected using transfer functions with local observations during a historical period. Empirical-statistical downscaling of GCMs in the UIB based on an ensemble of selected GCMs showed a modest increase in precipitation and a consistent warming, which is stronger in the upper parts of the basin [*Immerzeel et al.*, 2013; *Lutz et al.*, 2014]. The application of a stochastic weather generator to downscale RCM data in the northern UIB lead to a projection of year-round increasing precipitation, with increased intensity during the wettest months and year-round uniformly increasing temperatures [*Forsythe et al.*, 2014].

Hydrological impact studies have been conducted for the UIB at various spatial scales and key assumptions in those studies relate to (i) the reference climate dataset being used, (ii) the future climate forcing and downscaling method, (iii) the type and complexity of the hydrological model, (iv) the treatment of glacier evolution in the future and (v) the calibration and validation strategy. *Immerzeel et al.* [2010] used a simple lumped model, statistically downscaled GCM data for the A1B emission scenario and hypothetical glacier retreat scenarios to project a modest decrease in average upper Indus flow around 2050. For the Baltoro catchment in the upper parts of the Shigar river basin (Figure 5.1) it was shown that river runoff will be on the rise throughout this century as a result of a persistent high glacier melt water yield in combination with a modest projected increase in

precipitation [*Immerzeel et al.*, 2013]. In this study a fully distributed glacio-hydrological model was used including a simple ice flow model. The model was calibrated using runoff and data on glacier extents and flow velocities and forced using an ensemble of empirical-statistically downscaled climate models. A recent study focusing on the Shigar river basin with a semi-distributed model also shows an increase in flow until the middle of the century and then a gradual decrease, but still higher than the control runs [*Soncini et al.*, 2015]. A large-scale distributed modeling study focusing on assessing climate change impacts in the upstream parts of five major Asian river basins shows a consistent increase in average water availability until 2050 [*Lutz et al.*, 2014]. Other studies covering the Indus upstream of Tarbela (Figure 5.1), but based on a limited number of climate models also project increasing flow throughout the 21st century [*Ali et al.*, 2015; *Khan et al.*, 2015b]. Projections of changes in hydrological extremes in the UIB are very limited [*Bocchiola et al.*, 2011], but are at the same time very much desired [*Lutz et al.*, 2014; *Nepal and Shrestha*, 2015; *Soncini et al.*, 2015].

In this study we systematically assess present day hydrology of the UIB and the impacts of climate change using a new fully distributed cyrospheric-hydrological model at a high spatial resolution (1 km^2) that includes all relevant components of the high altitude water balance [*Terink et al.*, 2015]. We introduce several novel components which may advance our understanding of the complex impact of climate change on the UIB hydrology:

- A new historical precipitation dataset [*Immerzeel et al.*, 2015] that corrects for the underestimation of high altitude precipitation is used.
- The model is calibrated on river runoff at several locations, MODIS based snow cover estimates and geodetic glacier mass balance data.
- An advanced statistical downscaling technique for climate change scenarios until 2100 is used that accounts for changes in precipitation extremes.
- The analysis is focusing on changes in sources of runoff, changes in seasonality and changes in hydrological extremes.

5.2 Methods

5.2.1 Cryospheric-hydrological model

We use the high-resolution, raster-based, fully distributed Spatial Processes in Hydrology (SPHY) cryospheric-hydrological model [*Terink et al.*, 2015], which was applied in a river basin-scale study on climate change impacts for water availability in five major Asian river basins before [*Lutz et al.*, 2014]. The model runs at 1 km^2 spatial resolution with a daily time step. The actual runoff, which is calculated for each grid cell, consists of four possible contributing factors: rainfall-runoff, snow melt, glacier melt, and baseflow. For each grid cell the total runoff generated per time step (Q_{TOT}) is calculated:

$$Q_{TOT} = Q_{GM} + Q_{SM} + Q_{RR} + Q_{BF} \quad (5.1)$$

where Q_{GM} is runoff from glacier melt, Q_{SM} is runoff from snow melt, Q_{RR} is rainfall-runoff and Q_{BF} is baseflow. To determine the contribution of each of the four components to the total runoff within a grid cell, a subgrid parameterization is used in which for each cell the fractional ice cover (G_F), ranging from 0 (no ice cover) to 1 (complete ice cover), is determined. Glacier melt is simulated using a degree-day modeling approach [*Hock*, 2003]. A differentiation in debris-covered and debris-free glaciers is made based on thresholds for elevation and terrain slope [*Paul et al.*, 2004], and

different degree-day factors are used for both glacier types (Table 5.2). For the remaining fraction of the grid cell, the model maintains a dynamic snow and soil water storage. The glacier fraction per grid cell is adapted dynamically in time. A variable groundwater storage is maintained for the entire grid cell. A part of the glacier melt generated in the glacierized cell fraction is treated as surface runoff and the remaining part is treated as groundwater recharge. Runoff from snow melt consists of the snow melt released from the snow storage, which is simulated using a degree-day modeling approach. Besides accumulation and melt, refreezing of snow melt and rain water within the snow storage is included in the model. Gravitational snow transport between grid cells is simulated with the SnowSlide routine [*Bernhardt and Schulz*, 2010]. Snow sublimation is estimated using a simple elevation-dependent potential sublimation function. We assume that the majority of sublimation comes from snowblown sublimation with highest wind speeds prevailing at higher elevations, and therefore potential sublimation is assumed to increase linearly with elevation above 3000 m a.s.l. by a calibrated factor. The actual sublimation is the potential sublimation limited by the snow storage present in the grid cell. Rainfall-runoff consists of the surface runoff from rainfall and lateral flow released from the soil water storage. Soil water processes are simulated for a topsoil and subsoil layer and processes simulated include evapotranspiration, infiltration, percolation, capillary rise, surface runoff and lateral flow. Baseflow is released from the groundwater storage. Each of these four runoff types is routed downstream using a digital elevation model (DEM) and a routing recession function. The model is described in detail by *Terink et al.* [2015].

5.2.2 Datasets

Meteorological observations from stations are sparse in the mountains, in particular in the upper Indus. Data mostly originates from valley stations which are not representative for high altitude precipitation. The few stations that are located at higher elevations are typically subject to undercatch in case of snow [*Cheema and Bastiaanssen*, 2012]. Therefore, meteorological datasets consistently seem to underestimate precipitation in the UIB [*Immerzeel et al.*, 2012b; *Palazzi et al.*, 2013]. As forcing for the SPHY-model we therefore use the precipitation dataset presented by *Immerzeel et al.* [2015], which uses the observation-based APHRODITE [*Yatagai et al.*, 2012] dataset as a basis. The raw precipitation data are corrected by using IceSat-derived zonal glacier mass balances [*Kääb et al.*, 2012] as a proxy to estimate high altitude precipitation. Details of the methodology and dataset are described by *Immerzeel et al.* [2015]. The correction factors that were found by *Immerzeel et al.* [2015] for 2003-2007 are applied to the daily APHRODITE data for 1971-2000 to generate a 30-year reference climate dataset at 1 km^2 spatial resolution and daily timestep. By using this dataset we aim to overcome the fundamental problem of underestimated precipitation in distributed modeling of high-mountain hydrology.

As digital elevation model (DEM) we use the 15 arc-second void-filled and hydrologically conditioned HydroSHEDS DEM [*Lehner et al.*, 2008], which is based on the SRTM DEM [*Farr et al.*, 2007]. This DEM is resampled to 1 km^2 spatial resolution. Glacier outlines are extracted from the Randolph Glacier Inventory [*Pfeffer et al.*, 2014], and they are recalculated to a fractional glacier cover per 1 km^2 grid cell. Land use characteristics are extracted from the MERIS Globcover product [*Defourny et al.*, 2007], and quantitative soil properties are derived from the Harmonized World Soil Database (HWSD, [*FAO/IIASA/ISRIC/ISSCAS/JRC*, 2012]) using pedotransfer functions [*Keshavarzi et al.*, 2010].

MODIS snow cover data [*Hall et al.*, 2002] and geodetic glacier mass balance data [*Bolch et al.*, 2016, in preparation] are used for model calibration. Discharge observations provided by the Pakistan Water and Power Development Authority (WAPDA) are used for model calibration and

validation. IceSat-derived zonal glacier mass balance data [*Kääb et al.*, 2012] are used for calibration of a basin-scale parameterization of glacier changes [*Lutz et al.*, 2013].

5.2.3 Calibration and validation

The model is calibrated using a systematic three-step approach to overcome equifinality problems [*Beven*, 2006; *Pellicciotti et al.*, 2012]. First, parameters related to glacier melt are calibrated using geodetic mass balance data for the Hunza basin (Figure 5.1, Figure 5.2a). The geodetic mass balance data indicates differences in glacier surface elevation, from differencing SRTM [*Farr et al.*, 2007] and ASTER [*Tachikawa et al.*, 2011] DEMs. The SRTM DEM was acquired in February 2000, but due to radar penetration it underestimates glacier elevations and is likely to be more representative of the elevation of glaciers at the end of the 1999 melt season [*Berthier et al.*, 2007]. The ASTER DEMs were collected in late September and early October 2008. The elevation differences are transformed to average annual glacier mass balances (m w.e. yr^{-1}) for 30 individual glaciers by using an average ice density of 850 kg m^{-3} [*Huss*, 2013]. The 30 individual glaciers only include glaciers with a surface area covering at least 5 km^2 (5 model grid cells) to avoid scale problems, and fractional glacier cover for the individual model grid cells are extracted from an updated version of the ICIMOD glacier inventory, which includes distinction of debris-free and debris-covered ice surfaces for the Hunza basin (courtesy of S.R. Bajracharya). Using the model temperature and precipitation forcing the glacier mass balances for the individual glaciers are simulated for October 1999 to September 2007. Melt is calculated with a degree-day approach for the grid cells with a fractional glacier cover. Accumulation is calculated as solid precipitation falling on the grid cells with fractional glacier cover and the adjacent grid cells with a slope steeper than 0.2 towards the glacier surface [*Immerzeel et al.*, 2015]. The simulated data does not coincide completely with the geodetic mass balance data because the forcing data is only available until 2007. The model parameters related to glacier melt (*DDFci*, *DDFdc*, see Table 5.2) are then optimized for agreement between the simulated and observed glacier mass balances and different melt parameters are used for debris-covered glaciers and debris-free glaciers.

Second, parameters related to snow storage and melt (*DDFs*, *SnowSC*, *Sm*, *ShdMin*, *SubPot*, see Table 5.2) are calibrated independently by comparing SPHY simulated snow cover and MODIS remotely sensed snow cover [*Hall et al.*, 2002]. Remotely sensed snow cover has proven to be useful to improve model calibration in areas with high snow cover [*Bookhagen and Burbank*, 2010; *Pellicciotti et al.*, 2012]. The same processed MOD10C2 dataset is used as by *Immerzeel et al.* [2009]. From the beginning of 2000 until halfway 2008 the snow cover imagery is averaged for 46 different periods of 8 days (5 days for the last period) to generate 46 different average snow cover maps. That means period 1 is the average snow cover for 1-8 January for 2000 until 2008, period 2 is the average snow cover for 9-16 January for 2000 until 2008, etc. Because the MODIS snow cover product is available at 0.05° x 0.05° spatial resolution, SPHY model snow cover output is averaged over 8 day periods, resampled and projected from 1 km^2 spatial resolution to the same time periods, resolution and geographic projection as the MODIS product. Parameters related to snow melt are optimised to minimize the difference between SPHY simulated snow cover and MODIS observed snow cover.

Third, after calibration of the model parameters related to glacier melt and snow melt, remaining parameters related to baseflow and routing (αGW, *kx*, see Table 5.2) are calibrated to observed discharge at two locations in the UIB. The selection of locations is primarily dictated by data availability and data access. Secondly the selection is made such that it is a representative subset of the UIB, with different climatic and hydrological regimes. Calibration is performed at a daily time step for the same periods for which stream flow records are available. Parameter optimization is

done using PEST parameter estimation software [*Doherty*, 2005]. The calibrated parameters are assumed to be spatially uniform, i.e. one set of parameters is calibrated and assumed to be applicable to the entire UIB.

The calibrated SPHY model is independently validated to observed discharge at two locations that are not used in model calibration.

5.2.4 GCM downscaling

We select two ensembles containing four GCM runs from the CMIP5 database [*Taylor et al.*, 2012]: one ensemble for the medium stabilization scenario RCP4.5 and one ensemble for the very high radiative forcing scenario RCP8.5. To include all possible futures and because for our study area there is no particular GCM performing best, and no GCM is able to simulate all aspects of the precipitation dynamics in the region satisfactory [*Sperber et al.*, 2013; *Palazzi et al.*, 2014; *Sperber and Annamalai*, 2014], we choose to use the entire range of projections available. For both ensembles we therefore select four GCM runs covering the entire spectrum of projected changes in temperature and precipitation, as projected by all the CMIP5 GCM runs with output available for that RCP (Table 5.1). We select the models closest to the 10^{th} and 90^{th} percentile values of the projections, to avoid the inclusion of outliers, similar as in other studies [*Immerzeel et al.*, 2013; *Lutz et al.*, 2014; *Sorg et al.*, 2014].

The selected GCM runs are statistically downscaled by applying the Advanced Delta Change (ADC) method [*van Pelt et al.*, 2012]. ADC has the advantage over the classical delta change method [*Arnell*, 1999; *Kay et al.*, 2008] that it is not based on changes in the mean, but changes in the entire precipitation distribution, including extreme precipitation, which is a prerequisite for the assessment of changes in hydrological extremes. This is achieved by applying a non-linear transformation to five-day sums of precipitation data. Five-day sums are considered because extreme discharge events usually depend on multiple days of extreme precipitation. The transformation parameters are determined from the GCM control and future runs. Because of the large difference in resolution between the historical dataset (1 km^2) and the GCM data (~1.0 to 2.5°), both datasets are interpolated to a common grid of 25 km^2 resolution. Because ADC focuses on increasing detail in the high end of the precipitation distributions, two different equations are used for the transformation of the observed 5-day precipitation sums, based on the 90% quantile.

Table 5.1: GCM runs included in the climate model ensemble used to force the hydrological model, and projected changes in temperature and precipitation between 2071-2100 and 1961-1990, averaged over the GCM grid cells covering the upper Indus basin.

RCP	Scenario	GCM	ΔT (°C)	ΔP (%)
RCP4.5	DRY, COLD	inmcm4_r1i1p1	2.1	-4.6
	DRY, WARM	IPSL-CM5A-LR_r3i1p1	4.3	-6.3
	WET, COLD	MRI-CGCM3_r1i1p1	2.5	10.5
	WET, WARM	CanESM2_r4i1p1	4.4	13.2
RCP8.5	DRY, COLD	MPI-ESM-LR_r1i1p1	6.0	-7.9
	DRY, WARM	IPSL-CM5A-LR_r3i1p1	8.0	-10.2
	WET, COLD	CSIRO-Mk3-6-0_r1i1p1	5.6	29.8
	WET, WARM	MIROC5_r3i1p1	6.7	31.0

This quantile is determined per calendar month over the entire reference period for every 25 km^2 grid cell. The two transformation equations are:

$$P^* = aP^b \; for \; P^O < P_{90}^O \tag{5.2}$$

$$P^* = \overline{E^F}/\overline{E^C} \cdot (P^O - P_{90}^O) + a(P_{90}^O)^b \; for \; P^O > P_{90}^O \tag{5.3}$$

where P^* represents the transformed 5-day sums, P the reference climate dataset 5-day sums, P_{90} the 90% quantile and a and b are the transformation coefficients. The superscripts ^{O}, ^{C} and ^{F} denote whether the variable represents respectively the reference climate time series (^{O}), the GCM control series (^{C}) or the GCM future series (^{F}). For 5-day precipitation sums that exceed the P_{90} of their month an excess value (E) is determined. The mean future excess ($\overline{E^F}$) and mean control excess ($\overline{E^C}$) in Eq. (5.3) are determined per calendar month over the entire future or control period for every 25 km^2 grid cell:

$$\overline{E^C} = \frac{\sum P^C - P_{90}^C}{n^C} \text{ and } \overline{E^F} = \frac{\sum P^F - P_{90}^F}{n^F} \tag{5.4}$$

The linear scaling of the transformed precipitation with the ratio of future and control excess in Eq. (5.3) expresses a change in the slope of the extreme value plot of the five-day maximum precipitation amounts [*van Pelt et al.*, 2012].

The transformation coefficients a and b are derived from the 60% and 90% quantiles by:

$$b = \frac{\log\{g_2 \cdot P_{90}^F / (g_1 \cdot P_{60}^F)\}}{\log\{g_2 \cdot P_{90}^C / (g_1 \cdot P_{60}^C)\}} \tag{5.5}$$

$$a = P_{60}^F / (P_{60}^C)^b \cdot g_1^{1-b} \tag{5.6}$$

Bias correction factors g_1 and g_2 account for systematic differences in P_{60} and P_{90} in the reference climate time series and GCM control series, and are determined by:

$$g_1 = P_{60}^O / P_{60}^C \tag{5.7}$$

and

$$g_2 = P_{90}^O / P_{90}^C \tag{5.8}$$

To reduce sampling variability in the transformation coefficients, the P_{60} and P_{90} are smoothed temporally by using a weighted mean with weights of 0.25, 0.5 and 0.25 on respectively the previous, current and next month. The mean excesses are smoothed temporally in a similar manner. The ADC-method is described in more detail in *van Pelt et al.* [2012b].

Because the variability in precipitation within a common grid cell in the UIB is much larger than in the Rhine basin, for which the ADC-method was originally developed, the a and b parameters are additionally capped to avoid unrealistically high transformed daily precipitation values, which can occur due to the non-linear transformation of the precipitation value. This is done by constraining the a parameter and associated b parameter as follows:

$$for \; b < 0.55, a = 6 \; and \; b = 0.55 \tag{5.9}$$

This constraining is based on the distribution of a and b parameter values observed in the transformation in the Rhine basin [*Kraaijenbrink*, 2013].

The transformation parameters are determined and five-day sums are transformed for each future period spanning 10 years, by using a moving 30-year window from the GCM future series centered around the 10 year future period under consideration. For example, in the calculation of the transformation parameters for 2061-2070, the GCM future series for 2051-2080 is used. For the last future ten-year period (2091-2100) the GCM future series for 2071-2100 is used, similar as for 2081-2090, because most GCM runs do not go beyond 2100. After transformation a change factor can be determined for each five-day sum, which can be subsequently used to transform the individual days that belong to that specific sum. The change factor R is determined as:

$$R = P^{*} / P \tag{5.10}$$

To generate a baseline daily time series spanning 100 years from 2001 to 2100 that can be subjected to the change factors, a series of 100 years of daily precipitation is randomly selected from the 1971-2000 reference climate dataset (P_d^O). The change factor (R) is used to transform the individual daily precipitation sums to future daily precipitation (P_d^F):

$$P_d^F = P_d^O \cdot R \tag{5.11}$$

Due to the non-linear transformation of precipitation, the mean climate change signal in the bias-corrected downscaled data is modified from the mean climate change signal in the raw GCM data. Such modification of the mean climate change signal is often observed in statistical bias-correction and downscaling methods and may be considered as an undesired deficiency of a bias-correction and downscaling method [*Hempel et al.*, 2013], although this is a current topic of discussion [*Ehret et al.*, 2012; *Maurer and Pierce*, 2014; *Gobiet et al.*, 2015]. We choose to correct for this effect and therefore the transformed daily precipitation values are scaled for each future ten year period at the grid cell level at monthly scale to the ratio of future and reference precipitation sum according to the raw GCM data as follows:

$$corP_d^F = P_d^F \cdot \left[\frac{P^F}{P^C} \cdot \frac{P^O}{P_d^F} \right]_m \tag{5.12}$$

with $corP_d^F$ being the final transformed daily precipitation value, P^F being the future precipitation sum in the GCM future run, P^C being the precipitation sum in the GCM control run, P^O being the precipitation sum in the reference dataset and P_d^F being the initially transformed precipitation (Eq. (5.11)).

The temperature transformation, in contrast to that of precipitation, is linear in nature and has the form [*van Pelt et al.*, 2012]:

$$T^{*} = \frac{\sigma^F}{\sigma^C}\left(T - \overline{T^O}\right) + \overline{T^O} + \overline{T^F} - \overline{T^C} \tag{5.13}$$

where T^{*} represents the transformed temperature; T the temperature in the reference climate dataset; $\overline{T^O}$, $\overline{T^C}$ and $\overline{T^F}$ the monthly mean of respectively the reference, GCM control and GCM future temperature; σ^C and σ^F the standard deviations of the daily GCM control and GCM future temperature calculated per calendar month. The temperature transformation is applied to daily temperature values directly. The same series of 100 years of randomly selected years from the

reference period as for precipitation is used for the transformation of air temperature data. The transformation is applied to mean, maximum and minimum air temperature separately (i.e.: T in Eq. (5.13) can be replaced by *Tmean*, *Tmax* or *Tmin*).

Each of the downscaled GCM scenarios is used to force the hydrological model with transient runs from 1 January 2001 until 31 December 2100.

5.2.5 Future glacier changes

Future glacier changes are simulated at large scale for the UIB divided in three sub-regions: one sub-region for each of the mountain ranges Hindu Kush, Karakoram and Himalaya (Figure 5.1). For each of these three regions a regionalized glacier mass balance model is used to estimate changes in the regional glacier extent as a function of the glacier size distribution in the sub-regions and the downscaled future climate data [*Lutz et al.*, 2013]. This glacier mass balance model is specifically developed for implementation in large-scale hydrological models, where the spatial resolution does not allow for the simulation of individual glaciers and data scarcity is an issue. The model is initially forced with the climatic forcing for the reference period and calibrated to sub-region-averaged glacier mass balance data derived from IceSat data [*Kääb et al.*, 2012], before it is used to calculate sub-region-scale glacier changes for each of the downscaled GCM ensemble members from 2001 until 2100. The Randolph Glacier Inventory [*Pfeffer et al.*, 2014] is assumed to be representative for the state of the glacier extent at the start of the future simulation in 2001.

5.3 Results and Discussion

5.3.1 Calibration and validation

After calibration of the degree-day factors of debris-covered and debris-free glaciers (Table 5.2) the area-weighted mean glacier mass balance (+0.11 m we yr^{-1}) matches very well with the observed area-weighted mean glacier mass balance (+0.12 m we yr^{-1}) (Figure 5.2b). The interquartile range is also similar. However, the total spread within the sample of 30 individual glaciers is larger in the simulation than in the observations. The larger spread in the simulation stems most probably from the quite coarse model resolution at 1 km^2. The calibrated values for the degree-day factors for debris-free and debris-covered glaciers (Table 5.2) fall well within the range of values derived in field experiments in the greater Hindu Kush-Himalayan region [*Zhang et al.*, 2006]. Given the large scale and the fact that we use a fixed parameter set for all glaciers we conclude that the calibrated parameters can be considered representative for the UIB.

Averaged over the UIB, the calibrated SPHY model simulates snow cover reasonably well (Figure 5.2c, d). The largest overestimates occur in the Karakoram range and the Himalayan range in the most southeastern part of the UIB. The largest underestimates occur in the Hindu Kush and mountain ranges to the south of the Karakoram. At the basin scale, there is also a slight overestimation of snow cover during most parts of the year (Figure 5.2d). Overestimates may well be related to the fact that snow redistribution by wind from one grid cell to another is not included in the SPHY model. Another explanation could be related to the simple approach used to estimate sublimation, whereas sublimation can potentially be an important component of the high-altitude water balance in the HKH region [*Wagnon et al.*, 2013]. Studies in other areas revealed that blowing snow sublimation plays a larger role than ground sublimation from the snow pack, and that sublimation losses can be in the order of tens of percents of the total snow accumulation, and up to ~90% on very windy ridges [*Strasser et al.*, 2008; *Lenaerts et al.*, 2010; *MacDonald et al.*, 2010].

Table 5.2: Critical model parameters and their calibrated values.

Parameter acronym	Description	Units	Calibrated value
DDFci[1]	Degree-day factor debris-free glaciers	mm °C day^{-1}	7.1
DDFdc[1]	Degree-day factor debris-covered glaciers	mm °C day^{-1}	3.0
DDFs[2]	Degree-day factor snow	mm °C day^{-1}	5.0
SnowSC[2]	Water storage capacity of snow pack	mm mm^{-1}	0.5
Sm[2]	Minimum slope for gravitational snow transport	m m^{-1}	0.2
ShdMin[2]	Minimum snow holding depth	mm	50
SubPot[2]	Potential sublimation function	mm day^{-1}	0.0015* (h -3000) (for h > 3000 m a.s.l.)
αGW[3]	Baseflow recession constant	-	0.005
kx[3]	Routing recession coefficient	-	0.9476

[1]Calibrated with geodetic mass balance data [Bolch et al., 2016, in preparation]
[2]Calibrated with MODIS snow cover data [Hall et al., 2002; Immerzeel et al., 2009]
[3]Calibrated with observed discharge records (Pakistan Water and Power Development Authority)

Table 5.3: Correlation of observed and simulated discharge at locations used for model calibration and validation.

ID in Fig. 5.1	Name	River	Calibration (C) or Validation (V)	Used period (observation interval)	Nash-Sutcliffe efficiency (-)	Pearson's coefficient of correlation (-)	Bias (%)
10	Tarbela Inflow	Indus	C	Apr 1976-Dec 2007 (10 days)	0.78	0.91	9.7
14	Mangla inflow	Jhelum	C	Apr 1976 – Dec 2007 (10 days)	0.84	0.93	-6.4
1	Dainyor Bridge	Hunza	V	1966-2004 (daily)	0.76	0.88	-2.8
15	Marala Inflow	Chenab	V	Apr 1976-Dec 2007 (10 days)	0.71	0.90	-23.1

Calibration to observed discharge shows that averaged over the two locations, the Nash-Sutcliffe efficiency [*Nash and Sutcliffe*, 1970] calculated at a daily time step equals 0.81, whereas Pearson's correlation coefficient equals 0.92 (Table 5.3). For the location at Tarbela, covering a large part of the Indus basin, there is a positive bias of 9.7% in the simulation. The bias is largest during the months with high contribution of snow melt to the discharge (Figure 5.3a), and is thus likely related to the overestimate of snow cover on the part of the Tibetan Plateau that is part of this catchment (Figure 5.2d), which in turn relates to the high precipitation forcing in spring. For the Jhelum basin upstream of Mangla reservoir, with large contribution of snow melt to the stream flow, the model simulates the seasonal patterns in stream flow well (Figure 5.3b).

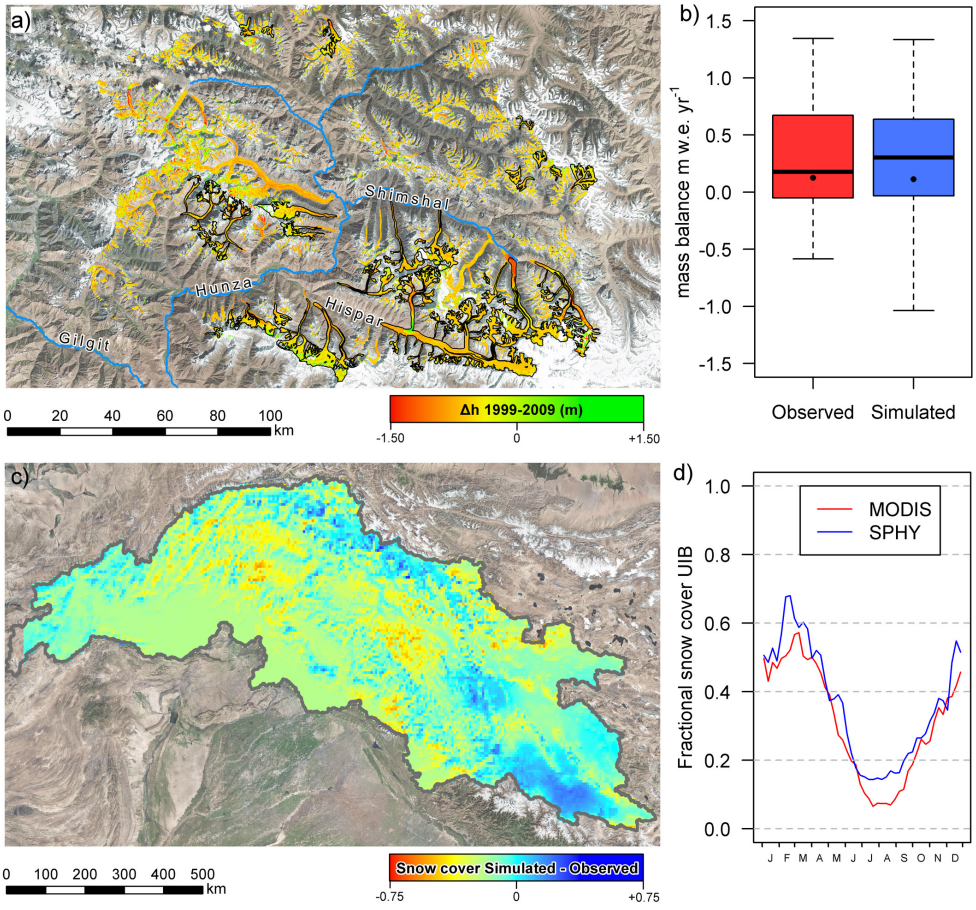

Figure 5.2: Calibration results for model parameters related to glacier melt and snow melt. a) Elevation difference on glaciers for 1999-2009 derived from DEM-differencing. Outlines of glaciers used for calibration are indicated black. b) Box plots showing the distribution of observed and simulated glacier mass balances for 30 individual glaciers indicated in the area in panel a. Black dots indicate the observed and simulated area-weighted mean mass balance of all considered glaciers. c) Average difference between SPHY simulated snow cover and MODIS observed snow cover. d) MODIS observed and SPHY simulated fractional snow cover averaged over the UIB and averaged for 2000-2007.

For the Hunza basin upstream of Dainyor bridge, which harbours the highest and most scarcely monitored part of the UIB and is used for model validation, simulated stream flow is slightly underestimated during the peak season in July and August, and overestimated during September and October (Figure 5.3c). During these months the stream flow is dominated by glacier melt, which is driven by air temperature. This suggests that the APHRODITE temperature fields may lack some accuracy for this area where observations are very scarce. Besides the model slightly underestimates snow cover in the northern part of the Hunza basin (Figure 5.2c), which may

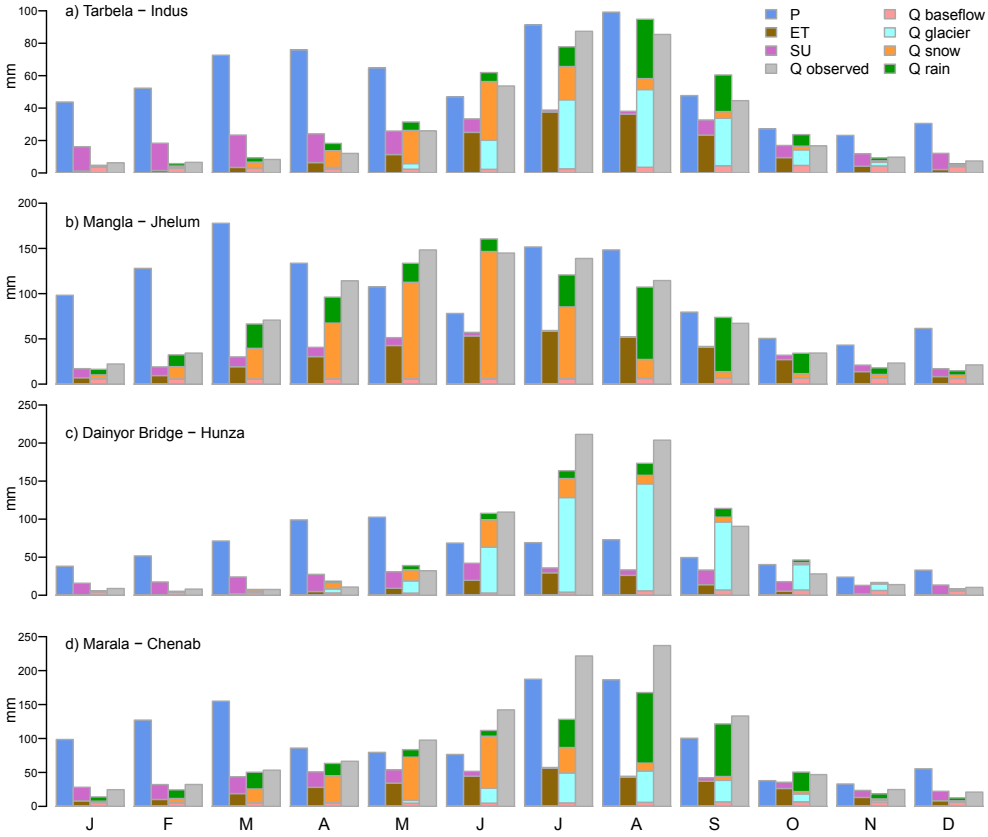

Figure 5.3: Monthly-averages of most important water balance terms and observed discharge for catchments used for calibration and validation (Table 5.3). Plots show precipitation (P), evapotranspiration (ET), sublimation (SU), observed discharge (Q_observed), baseflow (Q_baseflow), glacier melt (Q_glacier), snow melt (Q_snow) and rainfall-runoff (Q_rain).

contribute to the underestimate of the flow peak. For the Chenab basin, located to the southeast of the Jhelum basin, the model underestimates the flow during July and August, leading to a negative bias (Figure 5.3d). In this case the bias is most likely related to a shortage of precipitation in the forcing data, being 1222 mm yr^{-1} for the validation period whereas the observed discharge is only slightly lower (1100 mm yr^{-1}).

The annual water balance for 2003-2007, largely coinciding with the period covered by IceSat-derived glacier mass balances for three sub-zones in the UIB (Figure 5.1), is plausible for the Indus upstream of Besham Qila with precipitation input being 664 mm yr^{-1}, the negative glacier mass balance contributing 25 mm yr^{-1}, and evapotranspiration, sublimation and discharge being 174 mm yr^{-1}, 139 mm yr^{-1} and 367 mm yr^{-1}, respectively on the other side of the water balance. The gap in the water balance of 9 mm yr^{-1} is negligible and can be attributed to changes in storages in the soil, snow cover and groundwater. Given the complexity of high mountain hydrology, the scale of the application, the use of one parameter set for the entire basin, and large uncertainties in the meteorological model forcing, we conclude that the model performance is satisfactory for our purpose to estimate the impacts of climate change for the UIB's future hydrology.

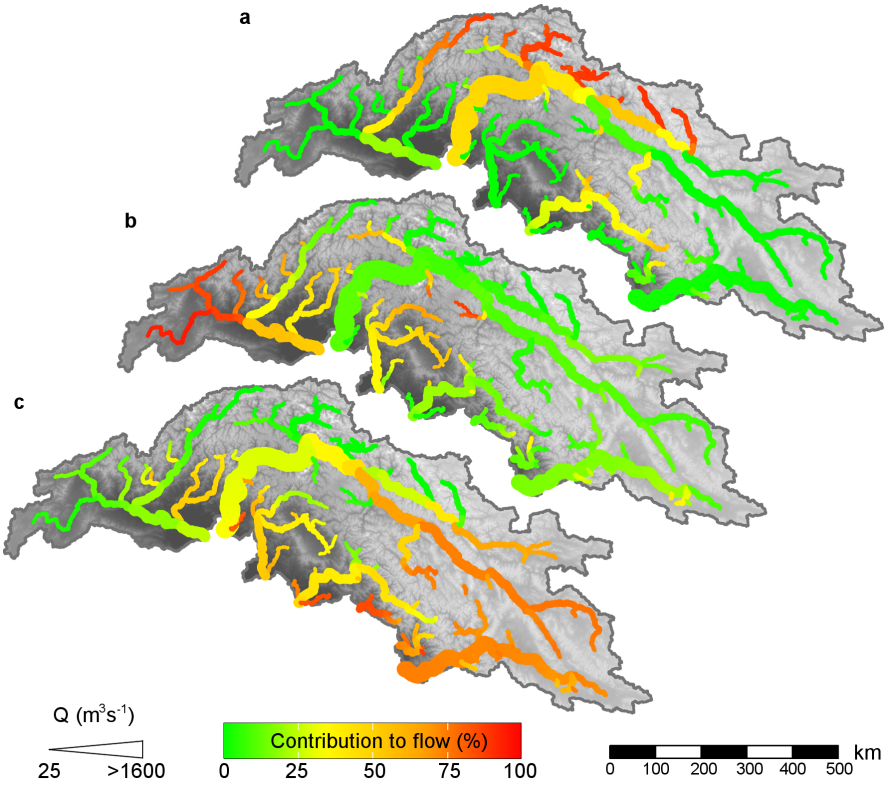

Figure 5.4: Streamflow composition in the upper Indus basin. Contributions of glacier melt (a), snow melt (b) and rainfall-runoff (c) to the total flow averaged over the reference period (1971-2000). The magnitude of streamflow is indicated by the symbol size.

5.3.2 Present day hydrology

The hydrological regimes during the reference period have a large spatial variation in the UIB (Figure 5.4). Strong south to north and east to west gradients are visible in the intensity of the rainfall-runoff generation, consistent with the intensity of the monsoon that comes in from the southeast during the monsoon season. In the monsoon-dominated Sutlej basin the contribution of rainfall to the total flow at the outlet is 74%, whereas this is 33% for the Indus at Tarbela. Snow melt has highest importance in the water coming from the Hindu Kush mountains in the Kabul basin, which receive large amounts of solid precipitation from westerly disturbances during the winter months. Glacier melt contribution is highest in the most glaciated Karakoram subbasins, like Hunza (85%) and Shigar (43%), and the upstream reaches of Kunar. This makes the Indus river the most melt-water dependent river leaving the UIB (55% glacier and snow melt at Tarbela). The lower-latitude Satluj, Beas, Ravi, Chenab and Jhelum rivers are dominated by input from rainfall, most of which falls during the monsoon season. The Jhelum river also has a substantial snow melt component (32%). Our estimates of stream flow composition match reasonably well with what others found based on a conceptual model [*Mukhopadhyay and Khan*, 2014a, 2015a]. The results from this study show a slight shift in runoff composition towards higher contribution

of snow melt and rainfall and lower contribution of glacier melt compared to our earlier findings [*Lutz et al.*, 2014]. This is because the current study is focused on the UIB only whereas the earlier study comprised the upstream basins of five Asian rivers, and most importantly because in the current study we use precipitation forcing that is corrected for the underestimate of high altitude precipitation, whereas this was not available at the time of the 2014 study. In the 2014 results, the shortage of precipitation input is compensated by higher glacier melt rates when calibrated only to observed stream flow, a common problem in the simulation of mountain hydrology [*Pellicciotti et al.*, 2012]. Associated to the large differences in the hydrological regimes between the tributaries are also differences in the intra-annual distribution of river discharge. Although the peak of glacier melt largely coincides with the peak in monsoonal rains, the snow melt peak occurs during spring. These contrasts in hydrological regimes of the different tributaries feeding the downstream basin may lead to different responses to future climate change.

5.3.3 Future climate

The downscaled GCM ensembles for RCP4.5 and RCP8.5 show that the future climate in the UIB is highly uncertain. Both ensembles indicate strong warming (Figure 5.5a,b), with significantly stronger warming for the parts of the basin with the highest elevation. The difference in warming can be up to ~1 °C (RCP4.5) and ~2 °C (RCP8.5) between the lowest and the highest areas in the UIB. This is well in line with presently observed elevation-dependent warming [*Rangwala and Miller*, 2012; *Pepin et al.*, 2015]. Comparing the average warming in the UIB (+2.1 to +8.0 °C between 1971-2000 and 2071-2100) to the global average (+1.8 to +4.4 between the same periods for the same RCPs [*Knutti and Sedláček*, 2012]), also demonstrates that the UIB is likely to warm stronger than other parts in the world. The uncertainty in warming is largest in the eastern and northern parts of the UIB. Seasonal differences in the temperature projections are limited. For both RCPs, strongest temperature increases are projected for January and June (Figure 5.5e,f). These projected temperature changes are well in line with what was found in other studies for the Indus basin [*Rajbhandari et al.*, 2014; *Ali et al.*, 2015], although the different scenarios and climate models used in those studies make a direct comparison difficult.

The precipitation projections are highly uncertain. The RCP4.5 mean projection shows clear contrasting trends of precipitation increase in the southeastern part and precipitation decrease in the northwestern part of the UIB (Figure 5.5c). This contrast is also observed for the RCP8.5 mean projection (Figure 5.5d), although the area with a projected increase in precipitation is larger. Besides, the precipitation increase is much higher for RCP8.5 than for RCP4.5, and the magnitude of precipitation decrease is smaller. The range of the precipitation projections however is very large. For both ensembles, for each geographical location there are both ensemble members that predict an increase and a decrease in precipitation. The ensemble range is much larger for RCP8.5 compared to RCP4.5 and can be up to 100% for the most downstream parts. The mean projected precipitation trend in the southeastern parts of the UIB suggest that monsoon intensity increases, and that the monsoon protrudes further to the northwest with increasing temperatures. Averaged over the UIB, significant seasonal patterns can be observed in the precipitation projections (Figure 5.5e,f). In general, although subject to a large uncertainty, the mean projection in both ensembles is indicating precipitation decrease during February-May and increase in October-January, with the increase being strongest in October. Especially the months October through January have very large uncertainties in RCP8.5. Despite this large uncertainty, an increase in precipitation is likely. Shifts in precipitation patterns originating from westerly disturbances are more difficult to interpret. The increasing precipitation during winter months combined with decreases during the

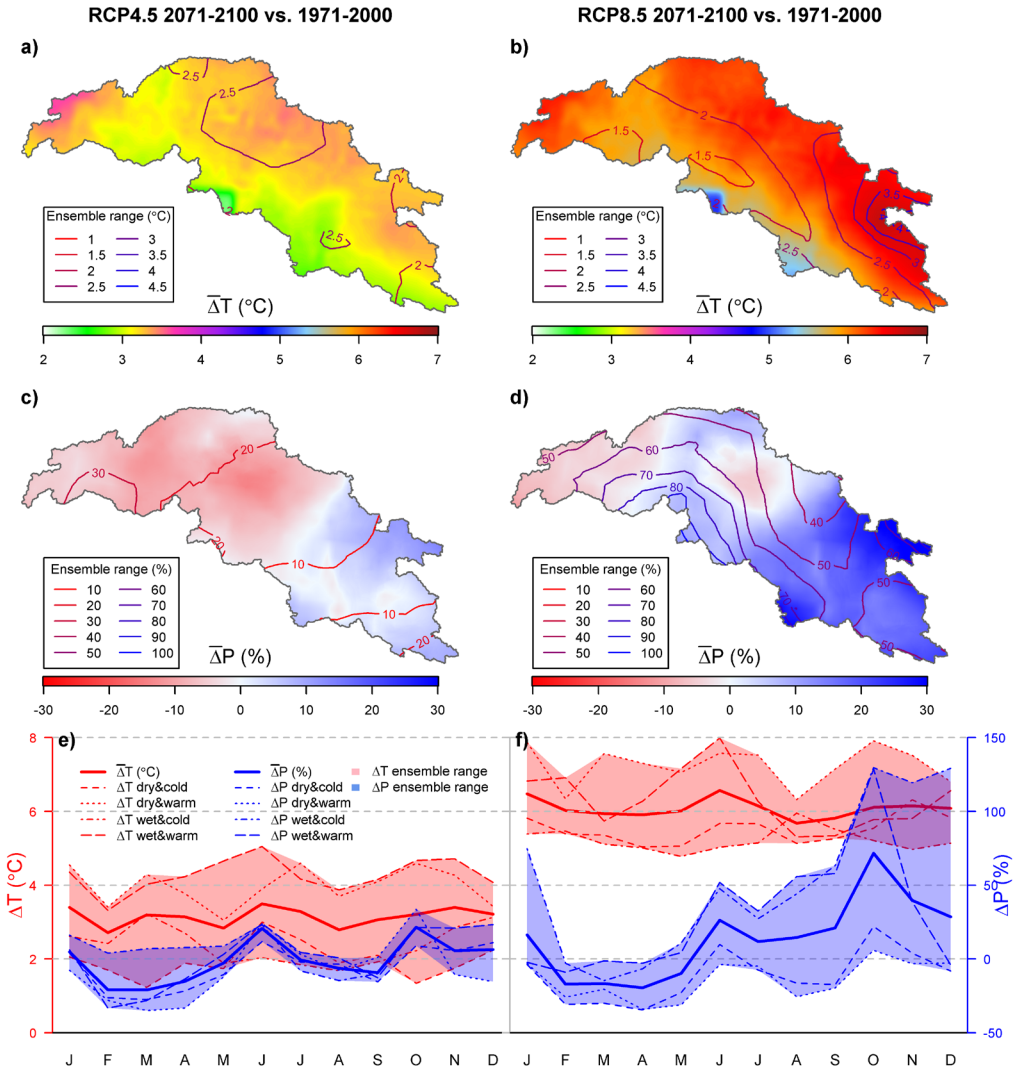

Figure 5.5: Projected changes in temperature and precipitation for 2071-2100 compared to 1971-2000. Projections are shown for the RCP4.5 (left panels) and RCP8.5 ensembles (right panels). a,b) Ensemble mean change in air temperature. Contour lines denote the ensemble range of projections. c,d) Ensemble mean change in annual precipitation sum. Contour lines denote the ensemble range of projections. e,f) Ensemble mean changes in air temperature and precipitation per month of the year. Shading denotes the ensemble range of projections.

early spring months could suggest that the westerly disturbances set in earlier, however the spatial pattern reveals mostly a precipitation decrease (on annual scale) in those areas where westerly disturbances are the main contributor to total precipitation. The trends, and large uncertainties of precipitation change we find in our ensembles are similar to what was found in an analysis of 32 CMIP5 GCMs over the Hindu Kush-Karakoram-Himalaya region [*Palazzi et al.*, 2014], and once

more demonstrate the need for improvement of climate simulations in this region, to lower the uncertainty in the future's climate.

5.3.4 Future glacier extent

The large uncertainty in the climate change scenarios translates in the projected changes in glacier extent (Table 5.4). Even though the wet scenarios project large increases in precipitation, glacier area decreases considerably during the 21st century throughout the basin, since the precipitation increases cannot compensate for the ample rises in temperature. Our projections are in the same order as projections made in recent other studies at large scale [*Radić et al.*, 2014; *Zhao et al.*, 2014].

5.3.5 Future hydrology

The uncertainty in UIB's future climate evidently also reflects in the projections of the future hydrology. Nevertheless, several remarkably consistent patterns of projected hydrological changes can be observed across the range of scenarios.

5.3.5.1 Stream flow composition

The contribution of glacier melt has decreased by the end of the century across all scenarios (Figure 5.6a,d,g,j). For RCP8.5 the decrease is strongest for the wet, warm scenario and smallest for the dry, cold scenario. The changes in snow melt contribution also show a consistent signal across scenarios, but with high spatial variation (Figure 5.6b,e,h,k). The strongest decreases are projected for the Hindu Kush mountain range consistent with the high warming rates. In the Karakoram and in the Zanskar subbasin, the contribution of snow melt increases in favor of glacier melt, since the glacier area is reduced but seasonal snow still provides a considerable amount of melt water. Although the strongest precipitation increases are projected for the winter months (Figure 5.5e,f), all year increases in temperature lead to a shift in the precipitation regime to more precipitation falling as rain instead of snow. For the ensemble means, averaged over the UIB the portion of the precipitation falling as rain changes from 58% during 1971-2000 to 66% during 2071-2100 for RCP4.5 and 75% for RCP8.5, consistent with earlier projections of changes in UIB snowfall [*Viste and Sorteberg*, 2015]. Remarkably, despite this shift in precipitation regime, snow melt contribution to total runoff increases or stays equal in most parts of the UIB except for the Kabul basin (Figure

Table 5.4: Projected remaining glacier area (%) in 2100 compared to the reference situation for three sub-regions in the upper Indus basin, when forced by the individual ensemble members.

RCP	Scenario	GCM run	Remaining glacier area (%) in 2100 compared to RGI		
			Himalaya	Hindu Kush	Karakoram
RCP4.5	DRY, COLD	inmcm4_r1i1p1	34.6	29.5	50.3
	DRY, WARM	IPSL-CM5A-LR_r3i1p1	17.7	12.3	27.1
	WET, COLD	MRI-CGCM3_r1i1p1	41.6	54.5	64.9
	WET, WARM	CanESM2_r4i1p1	15.4	8.0	26.1
RCP8.5	DRY, COLD	MPI-ESM-LR_r1i1p1	13.8	12.6	28.6
	DRY, WARM	IPSL-CM5A-LR_r3i1p1	9.5	7.7	13.6
	WET, COLD	CSIRO-Mk3-6-0_r1i1p1	15.2	12.9	30.9
	WET, WARM	MIROC5_r3i1p1	12.4	6.4	14.0

5.5b,e,h). This can be explained by the combined effect of increased evapotranspiration due to higher temperatures and increased water availability in the soil and a reduction of sublimation due to decreases in snow cover. For the western part of the Kabul basin the strongest increases in temperature are projected (Figure 5.5a,b), leading to a reduction in snow melt contribution and increase in rainfall-runoff contribution across scenarios. The RCP8.5 wet & warm scenario leads to largest increases in rainfall-runoff contribution (Figure 5.6l) and for this scenario the contribution of snow melt is mostly reduced (Figure 5.6k).

5.3.5.2 Water availability and intra-annual shifts

Changes in stream flow composition are also related to changing hydrological regimes in different times of the year (Figure 5.7). For most catchments (1-11) in the near future (2021-2050) for RCP4.5, flows show little changes during the high flow season and increase during autumn and especially spring. This is most likely due to an increase in autumn and winter precipitation (Figure 5.5e,f) and earlier onset of snow- and glacier melt. Despite the projected decrease in annual precipitation in most of the main Indus branch's basin (Figure 5.5c), annual-averaged water availability is unchanged for the locations in the Indus river (6-10), and increases slightly for the upstream subbasins of Hunza, Shigar and Shyok. For Hunza and Shigar this is most likely related to increased glacier melt, and for the Shyok basin upstream of Yogo it is a combination of precipitation increases for the mean of the scenarios (Figure 5.5c) and increased glacier melt. The

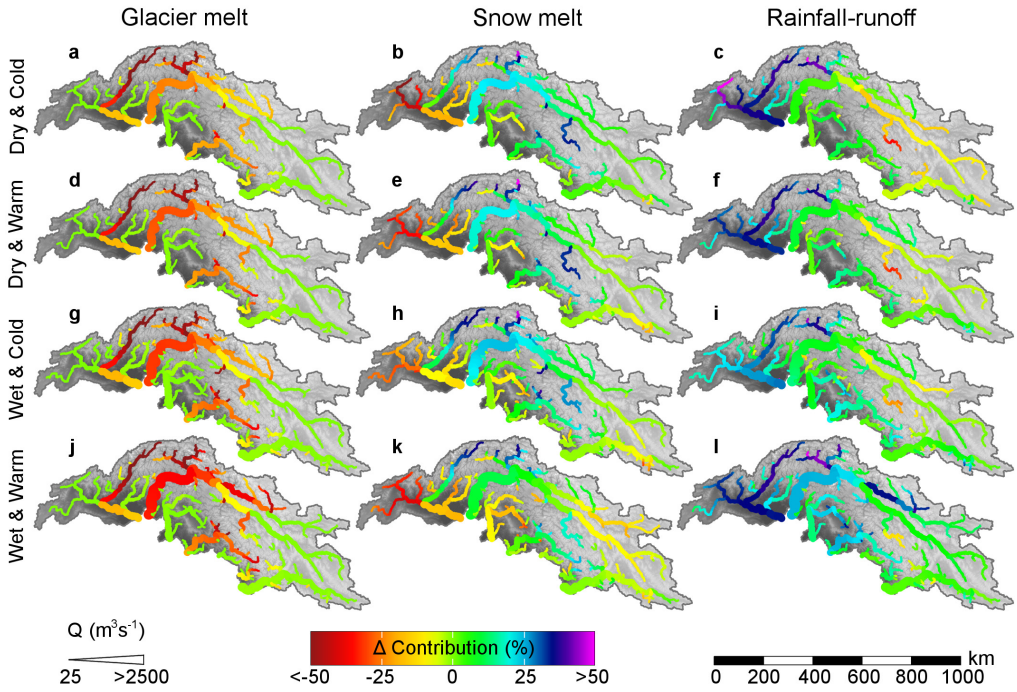

Figure 5.6: Changes in the contributions of individual components to the total flow for 2071-2100 compared to 1971-2000 for the cryospheric-hydrological model forced by the downscaled GCMs in the RCP8.5 ensemble. Changes are calculated as the contribution to stream flow in the future period (%) minus the contribution to stream flow in the reference period (%).

lower altitude subbasins (12-15) show a different pattern of seasonal shifts, with strong decreases in flow during June and July and often also for the spring months. Autumn and winter flows increase slightly, and annual-averaged water availability decreases slightly for these sub-basins. These basins have large rainfall-runoff and snow melt components, and decreases in precipitation during spring and the monsoon season combined with higher evapotranspiration rates, most likely cause runoff to decrease during those months, whereas precipitation increases during the winter months, cause increasing runoff during winter (Figure 5.5e). For the end of the century (2071-2100), the mean projection for RCP4.5 shows similar changes in intra-annual water distribution as for the near future, but much more pronounced. As glacier areas have reduced significantly by then, the amount of glacier melt water decreases substantially, causing reductions in discharge during the summer months. In addition, flows in the high flow season decline further by reduced precipitation during the monsoon season, and total water availability decreases for the entire UIB due to reduced precipitation in combination with increased evapotranspiration. Flows in spring tend to increase more strongly due to earlier onset of snow and glacier melt during these months. Only for the Satluj river, being the most rain-dominated river in the UIB, increases in water availability are projected for the far future according to the RCP4.5 ensemble mean since precipitation is projected to increase for this part of the UIB (Figure 5.5c).

In terms of total water availability, the RCP8.5 ensemble shows quite contrasting projections with increases in annual water availability in the near and far future. The patterns in the shifts

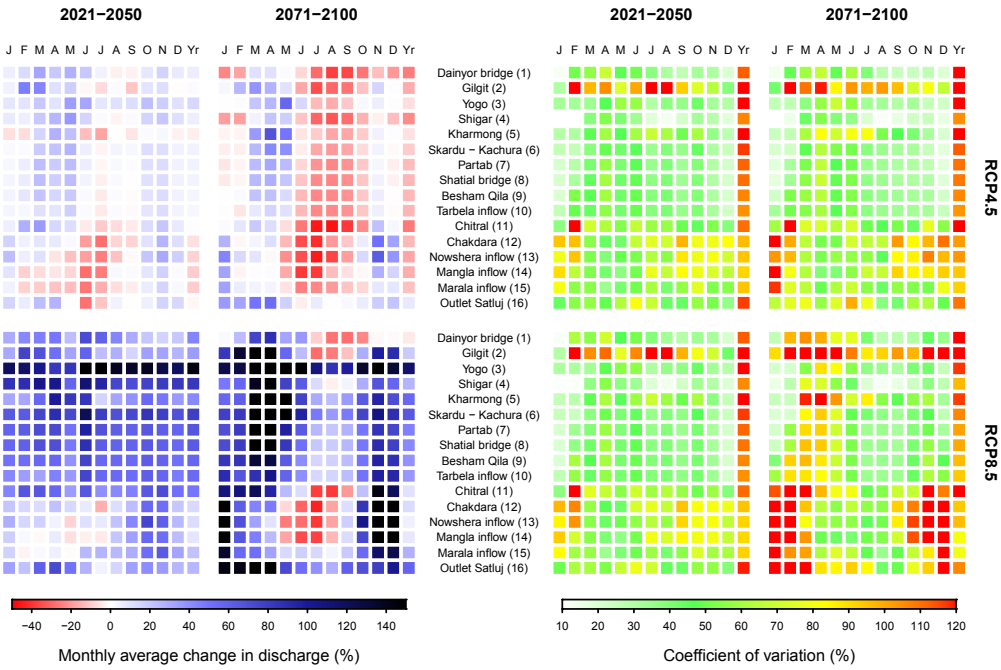

Figure 5.7: Ensemble mean monthly average changes in discharge at individual locations in the upper Indus basin (left) and coefficient of variation for the entire ensemble (right). Changes are shown for the near future (2021-2050) and the far future (2071-2100) compared to 1971-2000, for the RCP4.5 and RCP8.5 ensembles. Numbers in parentheses behind the location names refer to the locations in Figure 5.1.

in the ensemble mean projection however are consistent with RCP4.5, implying a transition to a more attenuated hydrograph. That flows increase during all parts of the year, including the high flow season, is most likely because precipitation is projected to increase for all seasons except spring and glacier melt rates in the near future increase stronger compared to RCP4.5 due to stronger temperature increase. Earlier onset of melt in spring causes runoff to increase during spring despite reduced precipitation input during this season. The projection for the far future shows that despite strong precipitation increases, the glacier melt dominated Chitral, Hunza, Gilgit and Shigar subbasins experience reductions in flow during the high flow season, since the glacier extent has decreased strongly by then (Table 5.4). The similar contrasting shifts between the high-altitude and lower altitude subbasins as for RCP4.5 can be observed. Besides, the contrast in the precipitation projections between the Kabul subbasin and the remaining part of the UIB (Figure 5.5d) are also visible in the projections of changes in total water availability. The remarkable strong year-round increase in flows in the near future as well as far future for the Shyok subbasin upstream of Yogo, can most likely be explained by the fact that projected precipitation increases are strongest in this subbasin (Figure 5.5d). Similarly strong year-round increases in flow for the rain-dominated Satluj river can be explained by strong precipitation increases in this subbasin.

Our results of intra-annual changes are in line with the projections made for the Shigar catchment [*Soncini et al.*, 2015]. There, the initial increase of summer flows is projected halfway through the century followed by a decline at the end of the century, that is accompanied by increasing flows in spring. *Ali et al.* [2015] project increasing flow in the UIB until the end of the 21st century, with more rapid increase during the first half of the century. The authors assessed changes for RCP4.5 and RCP8.5, and used one downscaled GCM and one RCM for their projections. They project stronger increase in winter flows compared to summer flows, consistent with our results. Similar results were found using the previous generation IPCC scenarios A2 and B2 for one RCM [*Khan et al.*, 2015b]. Accurate comparisons to the cited studies is however hampered by the use of different scenarios and climate models.

The patterns are consistent for both RCPs, but the uncertainty is large: for the combined RCP4.5 and RCP8.5 ensembles total water supply from the UIB in 2071-2100 changes by -15% to +60% with respect to 1971-2000. Large uncertainties in hydrological projections have also been found earlier for the Shigar catchment [*Immerzeel et al.*, 2013; *Soncini et al.*, 2015], and at larger scale [*Bliss et al.*, 2014]. Striking is the particularly large uncertainty observed for the Gilgit subbasin in both RCPs (Figure 5.7), which is most likely caused by a particularly large uncertainty in monsoon and autumn precipitation and summer air temperatures in both RCPs for this subbasin.

5.3.5.3 Hydrological extremes

Large changes in extreme discharges can be expected for most parts of the UIB (Figure 5.8). For most rivers, the highest water levels occur during the coinciding melting and monsoon season, and therefore the changes in return levels are largely determined by the projected climate changes during those months. However, the peak flows are also significantly determined by the meltwater from snow and glacier melt stemming from winter precipitation, forming a basic flow level during the melting and monsoon season which is exacerbated by runoff originating from extreme precipitation events.

Remarkably, the return levels for extreme discharges in the very upstream Hunza river with its highly glaciated basin increase for all scenarios, including the scenarios projecting overall dryer conditions. For the Hunza river with a large contribution of glacier melt, the decreases in glacier extent play a large role, lowering the continuous flow from glacier melt during the melting season.

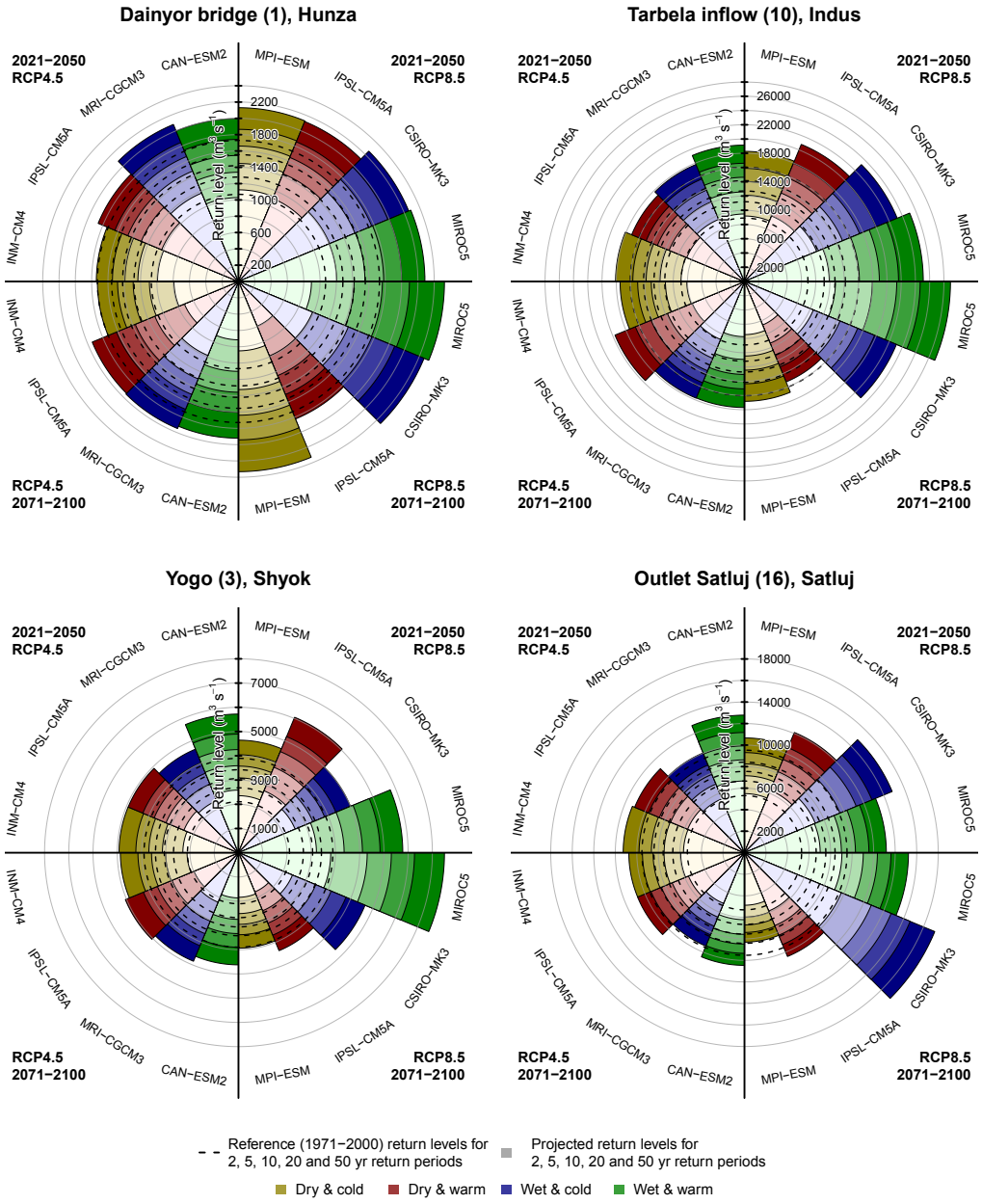

Figure 5.8: Return levels at four locations in the UIB for 2, 5, 10, 20, 50 years return periods for the hydrological model forced with the individual downscaled GCMs, for the near future (2021-2050) and the far future (2071-2100). Dashed lines indicate the corresponding return levels during the reference period (1971-2000). Return levels were obtained by fitting a Gumbel extreme value distribution [*Gumbel*, 1941] through the simulated annual flow maxima for the 30-year periods.

Nevertheless, even for the far future, when the contribution of glacier melt and the total flow has significantly decreased, the extremes in discharge are clearly increasing, due to increases in extreme precipitation, across scenarios. Earlier work in the Shigar subbasin to the east of Hunza also indicates that hydrological extremes may considerably increase until the end of the century [*Bocchiola et al.*, 2011; *Soncini et al.*, 2015].

The return levels for extreme discharges at Tarbela, where the main Indus branch leaves the UIB, increase for most scenarios as well, except the RCP8.5 dry & warm scenario, because precipitation events are projected to be more intense across the climate model ensemble. At Tarbela, the most extreme changes in return levels are projected for the RCP8.5 wet & warm scenario, with 100-years return level increasing by more than 100% between 1971-2000 and 2071-2100.

For the Shyok basin, return levels clearly increase most for the RCP8.5 wet & warm scenario, which also project the largest precipitation increases. Interestingly, the RCP4.5 wet & warm scenario projects stronger return level increases for the near future compared to the far future, despite increasing precipitation intensity. Since the Shyok river has a large glacier melt contribution, this is related to the lower continuous flow from glacier melt during the melting season in the far future.

At the outlet of the rainfall-runoff dominated Satluj basin the range of projected changes in return levels is largest. As this is the most rainfall-runoff dominated river, the discharge of this river is also most sensitive to changes in extreme precipitation. In addition, precipitation projections have large spread for this part of the UIB (Figure 5.5c,d), which may also imply a large spread in the projected precipitation extremes.

The model runs forced with the RCP8.5 MIROC5 and CSIRO-Mk3 GCMs clearly stand out from the other model runs for Satluj, Shyok, and the Indus at Tarbela, projecting the wettest future and strongest increases in precipitation intensity. Since the uncertainty in future climate is larger for the RCP8.5 ensemble compared to the RCP4.5 ensemble, it is not surprising that the range of the projected return levels is also larger for the RCP8.5 ensemble.

5.3.6 Uncertainty

This study sheds light on the propagation of uncertainty in the future climate for the future hydrology. We emphasize that the future climate in the upper Indus basin is highly uncertain as none of the current state-of-the art GCMs and RCMs satisfactory simulates the monsoon and westerly dynamics in the region [*Sperber et al.*, 2013; *Ramesh and Goswami*, 2014; *Mishra*, 2015], making the reliability of future scenarios questionable. We stress the importance of improvement in the representation of the complex climate in High Mountain Asia in order to be able to narrow down the uncertainty in future projections.

Besides the uncertainty within climate model ensembles and climate models themselves, additional uncertainties are introduced in the hydrological model forcing and other data, parameters, and representation of physical processes. Although we use climate model forcing that is corrected for the underestimate of high-altitude precipitation [*Immerzeel et al.*, 2015], these data can still have large biases. For example, the UIB-averaged corrected precipitation is estimated to be 913±323 mm yr^{-1} between 2003 and 2007. Further narrowing down of the uncertainty in historical precipitation data is a prerequisite for better estimates of future climate change impacts. Important data used in this study that also introduce uncertainty are the subregion-averaged glacier mass balance data derived from IceSat data [*Kääb et al.*, 2012], since they are used for the calibration of the large-scale glacier change parameterization.

Uncertainties are introduced by using a single set of calibrated model parameters for the entire domain, and parameters themselves have their own uncertainties, which are ideally all taken into

account [*Ragettli et al.*, 2013]. Currently no basin-wide map with distinction of debris-free and debris-covered glaciers is available for the UIB, and thus the differentiation of both glacier surface types is based on assumptions of elevation and slope constraints controlling the glacier surface type. A map with distinction of both glacier surface types would solve this key issue. Another key issue is the limited understanding of the role of sublimation in the high mountain water balance [*Strasser et al.*, 2008; *Wagnon et al.*, 2013].

5.4 Conclusions

In this study we use a distributed hydrological model which we force with the latest suite of climate models using an advanced statistical downscaling technique. This study stands out from previous work as for the first time shifts in seasonal water availability are assessed in combination with changes in hydrological extremes at basin scale for the upper Indus basin.

The main conclusion that can be drawn from this study is that the upper Indus basin faces a very uncertain future in terms of water availability in the long run. Projections of changes in water availability from the upper Indus basin at the end of the 21st century range from -15% to +60% with respect to 1971-2000. This uncertainty mainly stems from the large spread in the projections of precipitation change throughout the 21st century. Therefore, formulating adequate adaptation measures which take into account the uncertain future is of vital importance, thus requiring hydrological projections to be made based on an ensemble of climate models representing all possible futures.

Despite the large uncertainties in future climate and water availability, basin-wide patterns and trends of intra-annual shifts in water availability are consistent across climate change scenarios. These trends mainly consist of minor increases in summer flows combined with increased flows during other seasons in the near future (2021-2050) and decreases in summer flows combined with stronger increasing flows during the other seasons in the far future (2071-2100). Furthermore, increases in intensity and frequency of extreme discharges are found for most of the UIB and for most scenarios and models considered, implying increases in flooding events during the 21st century.

Population growth in combination with increasing standards of living and associated increases in energy and food production will continue to expand the downstream water and energy demand [*Qureshi*, 2011; *Siddiqi et al.*, 2012]. This implies a growing dependency on the uncertain future water resources, which calls for sound basin-wide adaptation strategies to be developed across sectors that take into account the changing demand and supply in the Indus basin as well as uncertainties therein.

Chapter 6

Synthesis

In Asia, water resources largely depend on water generated in the mountainous upstream parts of several large river basins, and millions of people depend on their waters downstream. Water demands are high, primarily because of water consumption by irrigated agriculture, and the water demand for hydropower generation. Future hydrological changes may have large environmental and societal impacts. The impacts of climate change for the water resources in the high mountains of Asia are poorly quantified. To contribute to the quantification of these impacts in High Mountain Asia (HMA) the main research question of this thesis is:

- *What are the impacts of climate change on the hydrology in High Mountain Asia?*

I identified major challenges hampering the quantification of these impacts at the large river basin scale, which I tried to overcome by answering the following questions:

- *How can we select an ensemble of climate models that represents the uncertainty in the future's climate?*
- *How can we use climate change projections to assess changes in mountainous climate including seasonal changes and changes in extremes?*
- *How can we make robust simulations of future glacio-hydrological changes under data-scarce conditions at the large river basin scale?*

In this chapter, the main findings of my research are synthesized, placed in a broader perspective and integrated. In addition, the uncertainties and limitations associated to the used methodologies and resulting projections are summarized. Finally, the implications of the findings and future research priorities are discussed. In section 6.4, where the main research question is discussed, I summarize the impacts of climate change on the hydrology in High Mountain Asia (HMA), as demonstrated by this study, and I speculate about the possible consequences of the findings.

6.1 Selecting a representative ensemble of climate models

Climate change impact studies depend on projections of future climate provided by climate models. The number of climate models is large and increasing, yet limitations in computational capacity make it (still) necessary to compromise the number of climate models that can be included in a climate change impact study. The selection of climate models however is a crucial step in any climate change impact assessment, since the assessment's outcome depends heavily on which

climate models are included. Selecting climate models is not straightforward and can be done following different methods. Usually the selection is either based on the entire range of changes in climatic variables as projected by the total ensemble of available climate models, or on the skill of climate models to simulate past climate. In chapter 2 a novel approach is presented where the aforementioned approaches are combined in a three-step sequential climate model selection procedure: 1) initial selection of climate models based on the range of projected changes in climatic means, 2) refined selection based on the range of projected changes in climatic extremes, and 3) final selection based on the climate model skill to simulate past climate. The aim of adopting this procedure is to end up with an ensemble of climate models that covers all possible futures in terms of changes in climatic means, extremes and including only climate models that show sufficient performance in simulating the observed climate in HMA. In chapter 2 I show that this selection procedure leads to a representative ensemble of climate models, covering the majority of the possible futures, without compromising model skill. This is a significant step forward with respect to other studies where model ensembles are selected based on only one of the mentioned criteria, or where no ensemble is used but just one or two climate models. Climate change impact studies that rely on such a very limited amount of climate models are less robust, since they cover only a limited part of the possible trajectories of future climate change. Adequate and robust climate change adaptation policies can only be formulated when climate change impact studies are based on an ensemble of climate models covering a broad range of possible futures.

Although the approach described in chapter 2 proves to be a robust way to establish such an ensemble, the design of the procedure is prone to a certain level of subjectivity. Each of these subjectivities can be a point of discussion where other well-argued choices could also have been made. First, different ordering of the selection steps will lead to different ensembles of selected models. The alternative choice to make the climate model's performance in simulating historical climate the leading criterion can be made, which can be justified given the complexity of the monsoon-dominated climate [*McSweeney et al.*, 2012]. Second, instead of excluding climate models in each selection step, scoring in each of the selection steps could be combined [*Cannon*, 2014], thereby avoiding removal of the models with best skill from the ensemble. Further attempts should be made to quantify model interdependency [*Knutti et al.*, 2013; *Sanderson et al.*, 2015a, 2015b] and include this aspect in the climate model selection procedure. In this study, multiple climate model runs with differing initial conditions were considered as individual model runs, thereby giving that particular model a larger probability of being selected over other models. Also, climate models from different institutes share parts of their code that represents physical processes, and are therefore not independent [*Knutti et al.*, 2013]. Another important issue in selecting climate models is related to spatial scale. In the approach described in chapter 2, but also in other approaches covering a large spatial domain, projected changes are averaged over the entire study area and this may dilute the spatial variation in projected changes. A potential solution is to divide the study area into multiple parts and apply the selection approach to each part independently. However, the drawback of this approach is the introduction of physical inconsistencies and erroneous boundary effects in the climate forcing at the transition from one General Circulation Model (GCM) to another. Therefore, if selecting climate models for multiple river basins at once, as done for the study described in chapter 2, the selection area should not be smaller than a physically confined river basin, keeping climate forcing physically consistent over such a system.

Recent research suggests that modified climate change signals in empirical-statistically downscaled data may be more realistic than the climate change signals carried by the raw data of the same GCM run [*Gobiet et al.*, 2015]. This would have ample consequences for the selection

procedure presented here and proper assessment of the spread in climate change projections would require empirical-statistical downscaling of all climate models prior to making the selection. At this moment this is not feasible computationally and timewise, but it might be in the future. It is however important to keep in mind that a climate model ensemble that is selected for a climate change impact study by any envelope-based approach, may turn out to be not as representative as thought.

6.2 Using climate change projections to assess changes in mountainous climate

A large scale gap exists between GCMs and hydrological models, which are forced by climate scenarios driven by GCMs. For large-scale studies, empirical-statistical downscaling methods are required to bridge the scale gap between a GCM and a hydrological model. In the research described in this thesis two different empirical-statistical downscaling techniques are used. In chapter 4, the delta change approach is used to downscale an ensemble of eight GCMs and generate climate change scenarios until 2050. In the delta change approach, climate change signals are estimated as the difference in mean air temperature and mean precipitation between the raw GCM data for the future and the raw GCM data for a historical control run. This approach was applied on a monthly scale and subsequently the change grids were superimposed on randomly selected years from historical climate dataset with high spatial and temporal resolution. The design of this approach allows including changes in the means of the temperature and precipitation distributions whereas changes in other parts of the distributions are corrected with the same factors as the mean. When used to generate climate change forcing for hydrological models, this approach is suitable to assess changes in overall future water availability, as described in chapter 4. In chapter 5, the more sophisticated Advanced Delta Change approach is used to downscale an ensemble of eight GCMs. The Advanced Delta Change approach allows for a non-linear transformation of climate change signals in the projected precipitation data. This approach focuses on proper transformation in the high tail of the precipitation distribution, i.e. the precipitation extremes. Therewith the basin-scale assessment presented in chapter 4 could be taken a step further and allowed the analysis of changes in hydrological extremes in the upper Indus basin as described in chapter 5. This study leads to the conclusion that the frequency and magnitude of extreme discharges is very likely to increase during the 21st century.

A main feature of empirical-statistical downscaling techniques is that they require high-resolution historical climate data with sufficient quality to derive accurate transfer functions between GCM-simulated climate and real climate. This remains challenging in the data-scarce HMA region. At smaller scales, improvement of present-climate forcing data can be achieved by making existing ground data more accessible, expanding existing field monitoring networks and initiating new measurement campaigns. The improved understanding of the dynamics of high-altitude precipitation has key importance in that respect. Progress has been made over the past years and the knowledge of HMA climates is growing. Work at smaller scales tremendously helps to improve our understanding of underlying processes and feedbacks. At the large scale however, we rely on regional and global datasets to be used as historical reference climate data. Bias-correction of these datasets, integrating information from different sources should have major priority. An example is the use of observed glacier mass balance data to correct precipitation estimates at large scale [*Immerzeel et al.*, 2015]. Such efforts should be further developed and data from stations,

remote sensing and weather models should be combined to improve climatic datasets in HMA. The venture of new satellite derived precipitation products, such as the recently established Global Precipitation Measurement Mission may help in better quantification of precipitation patterns in HMA at large scale.

There are many different statistical downscaling approaches and choosing the most appropriate method is challenging, especially for complex climate types like in HMA. *Themeßl et al.* [2011b] compared different empirical-statistical downscaling methods for precipitation in the Austrian Alps and found that the Quantile Mapping method has best performance in mountainous climate, particularly at high quantiles, which is promising for assessing future changes in extreme precipitation events. Another advantage of Quantile Mapping is that it can be applied to other climatic variables, including air temperature, as well. A catchment scale application of the Quantile Mapping approach to downscale GCM data to station level in HMA was successful [*Immerzeel et al.*, 2013], and applications of the method at large scale should be explored as well. The Advanced Delta Change approach applied in chapter 5 proved to be useful in assessing future changes in precipitation extremes, but its performance was not compared to other statistical downscaling techniques. Direct comparison to for example the Quantile Mapping method could provide more insight in its performance.

Another basic assumption of empirical-statistical downscaling methods is the assumed stationarity of biases between GCM data and observed data through time. How large the consequences of this assumption in terms of errors in the projections are remains unclear. Empirical-statistical downscaling methods often modify the climate change signal from the raw GCM data, i.e. climate change signals in the downscaled data differ from climate change signals in the raw GCM data. Often, this is regarded as an undesired consequence of an empirical-statistical downscaling method [*Hempel et al.*, 2013]. Other research suggests that the modification of the climate change signal is actually improvement of the climate change signal [*Maurer and Pierce*, 2014; *Gobiet et al.*, 2015]. This clearly needs further research as clarity about this issue is necessary to gain better understanding of the actual added value of empirical-statistical downscaling.

From the analysis in chapter 2 in this thesis and research by others it is clear that CMIP5 GCMs as well as state-of-the-art RCMs have poor skills in simulating the important features of the precipitation dynamics (monsoon and westerly systems) in HMA [*Sperber et al.*, 2013; *Palazzi et al.*, 2014; *Ramesh and Goswami*, 2014; *Sperber and Annamalai*, 2014; *Mishra*, 2015]. This is what leads to the large uncertainty in the future climate projections for HMA which in turn leads, to a large extent, to the large uncertainties in hydrological projections presented in this thesis. Dynamic and empirical-statistical downscaling and bias-correction methods may help to reduce the biases, but cannot completely bridge them [*Pielke and Wilby*, 2012]. This stresses that the currently available climate change projections must be used with caution when defining climate change adaptation policies.

To narrow down these uncertainties in HMA, priority should be on improvement of the climate models. Since computational capacities continue to increase, spatial resolution and representation of processes of climate models can and will improve in the future. Combined with increasing knowledge of the relevant climate dynamics, ultimately the climatic projections will get better. Knowledge gained in climate modeling efforts at smaller scales [e.g. *Collier and Immerzeel*, 2015], could be used to improve larger scale climate models. However, in the meantime we will have to deal with this uncertainty in the future climate and try to reduce the overall uncertainty by improving reference climate forcing data, representation of processes in glaciological and hydrological models, and other input data.

6.3 Simulating future glacio-hydrological changes under data scarcity at the large river basin scale

The research presented in this thesis constitutes a significant step forward in our understanding of the hydrological cycle in HMA and the impacts that climate change will have in this region throughout the 21st century. The thesis describes the first river basin scale study in High Mountain Asia that integrates:

- a new high-resolution, fully distributed cryospheric-hydrologic modeling approach, that can operate under data-scarce conditions,
- downscaled climate change scenarios based on representative ensembles of statistically downscaled General Circulation Models, allowing the assessment of changes in overall water availability, seasonal shifts and changes in the frequency and magnitude of hydrological extremes,
- a novel approach to estimate future glacier changes at the large river basin scale.

Integrating these components in an approach to quantify the impacts of climate change for high mountain hydrology clearly fills a scientific knowledge gap since the majority of climate change impact assessments in HMA is either conducted at the catchment scale [*Tahir et al.*, 2011a; *Immerzeel et al.*, 2013; *Ragettli et al.*, 2013; *Soncini et al.*, 2015], or based on simpler modeling approaches and crude assumptions on changes in future glacier cover [*Immerzeel et al.*, 2010]. Besides, previous large-scale studies only used a limited number of climate models. With the approach described in this thesis robust hydrological projections were generated for HMA.

Besides the selection of representative climate models and choosing suitable empirical-statistical downscaling methods, a key challenge is the simulation of future changes in glacier extent, which is not straightforward at large river basin scale because the spatial resolution of modeling (1 km^2 in this case) does not allow for the explicit simulation of ice flow. In chapter 3 a novel basin-scale parameterization of future glacier changes under data-scarce conditions is presented. This approach fills the gap between approaches that simulate glacier changes at catchment scale, including dynamics of ice flow [*Jouvet et al.*, 2008; *Immerzeel et al.*, 2013] and large-scale applications based on crude assumptions of hypothetical glacier changes [*Rees and Collins*, 2006; *Immerzeel et al.*, 2010]. The improved ability to simulate glacier changes at the basin scale is one of the key advances that allowed for improvement in hydrological projections for HMA, as described in chapter 4 and chapter 5.

Although the adoption of this novel method is a significant step forward, the design of the approach for data-scarce regions and large-scale applications does come with some limitations. As the approach heavily relies on volume-area scaling it is very sensitive to the value used for the multiplicative scaling parameter. Attempts to define different scaling parameters based on glacier size and region have been undertaken but yield a large range of outcomes [*Grinsted*, 2013]. Volume-are scaling has been widely applied [*Bahr et al.*, 2015], and many recent efforts for simulating future glacier evolution at large scale rely on it, at least for estimating initial ice volumes.

A future improvement that should be explored is better estimation of the spatial distribution of glacier changes within the river basin, since the current approach assesses climatic and glacier changes only at the basin scale. Applying the model to smaller groups of glaciers should be possible, now that spatially distributed geodetic mass balance data which can be used for model calibration become more widely available. The eventual goal is to be able to simulate the evolution of individual

glaciers satisfactory, but this will remain challenging given the mismatch in scale between meteorological forcing data and the actual climatology over individual glaciers. The models which simulate the evolution of individual glaciers [*Huss and Hock*, 2015; *Radić et al.*, 2014; *Marzeion et al.*, 2012], all require significant correction of forcing data through calibration parameters, and rely on sparse observed glacier mass balance data. However, the development of these approaches, in combination with the continuous improvement in global and regional datasets of glacier outlines and other properties, and mass balance data from multiple sources certainly leads to improved simulation of future glacier extent and application of these approaches or adopted versions thereof should be explored at river basin scale in HMA.

The use of a fully distributed cryospheric-hydrological model to simulate hydrology for five large Asian river basins (chapter 4) and the upper Indus basin (chapter 5) at high spatial resolution under data-scarce conditions, is unique and has led to more robust projections of climate change impact for hydrology in HMA than previous assessments. The study in five Asian river basins described in chapter 4 produced a set of water availability scenarios up to 2050, covering the majority of possible futures as projected by the current state-of-the-art climate models. It also produced new knowledge on the spatial distribution of relative contributions of snow- and glacier melt and rainfall to total flow in HMA. The study in the upper Indus basin, described in chapter 5 went a step further and in addition produced hydrological projections for the entire 21st century, and allowed for the assessment of changes in hydrological extremes. Besides, the quantification of the spatial distribution of relative contributions of snow melt and glacier melt and rainfall was further refined with respect to the study described in chapter 4 by using improved historical precipitation fields [*Immerzeel et al.*, 2015], and improved calibration of model parameters, by integrating data of geodetic glacier mass balance, remotely sensed snow cover, and observed discharge in the calibration procedure, in an attempt to overcome equifinality problems.

Although the presented approach is advanced, robust, and brought new insights, there are some points that require attention in the future. Besides historical meteorological forcing, which should be further improved as already stated in section 6.2, the modeling approach relies on other input data from regional and global datasets. Major improvements in the simulation of glacier melt can be reached when a better distinction of debris-covered and debris-free glaciers becomes available for HMA. However, even if such a mapping effort becomes available, it has to be kept in mind that our understanding of processes related to glacier melt under debris cover in particular is still limited, although it is advancing [e.g. *Collier et al.*, 2014; *Nicholson and Benn*, 2013]. Improvements in the soil and land use data can lead to improvements in the model performance. A better quantification of the contribution of glacier melt and snow melt to total stream flow can be made when seasonal snow melt from the glacier surface is included in the model. In the current version of the model all melt generated in the glacier-covered part of a grid-cell is defined as glacier melt, whereas the contribution of seasonal snow melt from the glacier surface is substantial in reality. Although a groundwater reservoir is simulated in the model, the processes related to this groundwater reservoir are largely based on assumptions. Paying more attention to improved representation of processes related to groundwater is justified, given that the role of groundwater for HMA's discharge may be larger than the role of snow melt and glacier melt in the central and Eastern Himalayas [*Andermann et al.*, 2012; *Bookhagen*, 2012].

One other important aspect that has come forward from the analyses in this thesis is the lack of understanding of the role of sublimation of snow and ice in the water balance of HMA. No published results on sublimation quantities in HMA are available, but research in other regions with high amounts of snow suggest that the amount of snow going back to the atmosphere can be in

the order of 10-50% of seasonal snowfall and up to 90% at mountain crests [*Pomeroy and Essery*, 1999; *Strasser et al.*, 2008; *MacDonald et al.*, 2010]. A study on Himalayan glaciers also suggests that sublimation fluxes may be high [*Wagnon et al.*, 2013]. The study in the upper Indus basin presented in chapter 5 estimates the sublimation flux to amount ~20% of the annual precipitation, with a simplified method to estimate sublimation, suggesting that this is indeed an important water balance component in HMA. Therefore, the quantification of this flux, as well as the development of approaches to simulate this flux under data-scarce conditions and at river basin scale should have high research priority.

The analysis of changes in the frequency and magnitude of extreme discharge events could form a first step to more detailed hazard and risk mapping in the region. As the analysis in chapter 5 shows that the frequency and magnitude of extreme precipitation and discharge events will most likely increase, this will lead to increases in hazards related to flooding events, glacier lake outburst floods (GLOFs) [*Fujita et al.*, 2009; *Komori et al.*, 2012; *Wang et al.*, 2015] and landslides [*Hewitt*, 1998; *Dahal et al.*, 2008; *Sharma and Kumar*, 2008]. Integrating large-scale projections of changes in extreme precipitation and discharge with risk and susceptibility mapping could lead to improved regional projections of changes in natural hazards.

6.4 Climate change impacts on the hydrology of High Mountain Asia

The presented basin-scale integration of representative downscaled climate change scenarios, with a novel approach to assess future changes in glacier extent, and a high-resolution cryospheric-hydrological model suitable for application under data-scarce conditions, produced robust climate change impact projections for the hydrology in HMA. The most important results show that further shrinkage of the glacier extent is likely for all of HMA, but that water availability is most probably secured for most of HMA at least until 2050. This is due to increased glacier melt in the upper Indus basin and increased precipitation in the upper Ganges, Brahmaputra, Salween and Mekong basins, but with large uncertainty ranges. Although no projections have been made for the second half of the century for the upper Ganges, Brahmaputra, Salween and Mekong river basins, water availability will most probably increase since most climate models project further increases in precipitation in these basins towards 2100 (chapter 2). For the upper Indus basin, projections until the end of the 21st century indicate that water availability in this basin is highly uncertain in the long run. Discharge in HMA peaks during the monsoon season (June-September) which coincides with the period of maximum melt. Analysis of seasonal shifts indicates that the distribution of water is likely to be more equal over the seasons in the future, with shifts towards the low flow season. Also for the seasonal shifts, uncertainty is large because of the large uncertainty in future climate. Analysis of changes in meteorological extremes and associated hydrological extremes indicates that the frequency and magnitude of extreme discharges is likely to increase for the majority of the upper Indus basin. Strongest increases are projected for the rivers with large contribution of rainfall to the flow. This suggests more frequent and more severe occurrence of flooding events in the future.

Although the scope of the research presented in this thesis is limited to the upstream parts of the large river basins studied, I will use this paragraph to speculate about the downstream consequences of the findings presented in this thesis. First of all, I want to emphasize that the consequences may affect hundreds of millions of people living in the downstream areas of Asia's large river basins, implying the importance of this study. One major, and positive, conclusion that can be drawn from this study is that the Asian water towers are likely to continue to fulfill their role for decades to

come. However, changes are imminent. Seasonal shifts in water availability towards the low flow seasons can be beneficial for agriculture, since with the increasing temperatures, growing seasons may be extended and periods of water deficit may shorten. On the other hand, if water availability is reduced during the current growing season, this may hamper the agricultural production. For the generation of hydropower, increases of discharge during the low-flow season are beneficial, allowing higher production levels. Increases in the frequency and magnitude of hydrological extremes however will likely lead to severe flooding, whereas many parts of the HMA region already face severe flooding in the present situation. Besides direct damage of flooding, an increase in extreme discharges also enhances sedimentation rates into hydropower structures and reservoirs, lowering their lifetimes and storage capacities. Even if the water supply from upstream does not lessen or even increase, the expected large increases in downstream demand will increase pressure on the already stressed water resources in Asian river basins. As changes are imminent, adaptation to these changes is of key importance. In this respect, the entire range of projections should be considered as possible futures, making the formulation of adequate and robust adaptation options an enormous challenge. For proper assessment of the speculations drawn here, basin-wide integrated approaches are needed, which combine projections of changes in upstream supply with projections of changes in downstream demand, across sectors and across seasons.

6.5 How are the projections generated in these studies used?

The results described in this thesis are based on outcomes of multiple applied research projects with strong focus on regional climate change adaptation. I feel confident that the most important conclusions drawn from these studies will find their way to regional decision and policy makers, in its present form or through other knowledge products. An excellent example is the Himalayan Climate and Water Atlas [*Shrestha et al.*, 2015], featuring many of the results described in chapter 4, which was presented at the COP Climate Summit in Paris, 2015. Besides, the large-scale work described in this thesis serves as a starting point for future catchment-scale studies on water availability and flood hazards in High Mountain Asia.

References

Aizen, V. B., V. A. Kuzmichenok, A. B. Surazakov, and E. M. Aizen (2007a), Glacier changes in the Tien Shan as determined from topographic and remotely sensed data, *Glob. Planet. Change*, *56*(3-4), 328 – 340, doi:10.1016/j.gloplacha.2006.07.016.

Aizen, V. B., E. M. Aizen, and V. A. Kuzmichonok (2007b), Glaciers and hydrological changes in the Tien Shan: simulation and prediction, *Environ. Res. Lett.*, *2*, 045019, doi:10.1088/1748-9326/2/4/045019.

Akhtar, M., N. Ahmad, and M. J. Booij (2008), The impact of climate change on the water resources of Hindukush – Karakorum – Himalaya region under different glacier coverage scenarios, *J. Hydrol.*, *355*(1-4), 148 – 163, doi:10.1016/j.jhydrol.2008.03.015.

Akhtar, M., N. Ahmad, and M. J. Booij (2009), Use of regional climate model simulations as input for hydrological models for the Hindukush-Karakorum-Himalaya region, *Hydrol. Earth Syst. Sci.*, *13*(7), 1075 – 1089, doi:10.5194/hess-13-1075-2009.

Ali, S., D. Li, F. Congbin, and F. Khan (2015), Twenty first century climatic and hydrological changes over Upper Indus Basin of Himalayan region of Pakistan, *Environ. Res. Lett.*, *10*(014007), doi:10.1088/1748-9326/10/1/014007.

Andermann, C., S. Bonnet, and R. Gloaguen (2011), Evaluation of precipitation data sets along the Himalayan front, *Geochemistry, Geophys. Geosystems*, *12*(7), 1 – 16, doi:10.1029/2011GC003513.

Andermann, C., L. Longuevergne, S. Bonnet, A. Crave, P. Davy, and R. Gloaguen (2012), Impact of transient groundwater storage on the discharge of Himalayan rivers, *Nat. Geosci.*, *5*(2), 127 – 132, doi:10.1038/ngeo1356.

Archer, D. (2003), Contrasting hydrological regimes in the upper Indus Basin, *J. Hydrol.*, *274*(1-4), 198 – 210, doi:10.1016/S0022-1694(02)00414-6.

Archer, D. R., and H. J. Fowler (2004), Spatial and temporal variations in precipitation in the Upper Indus Basin, global teleconnections and hydrological implications, *Hydrol. Earth Syst. Sci.*, *8*(1), 47 – 61, doi:10.5194/hess-8-47-2004.

Arendt, A. et al. (2012a), Randolph Glacier Inventory – A Dataset of Global Glacier Outlines: Version 3.2.,

Arendt, A. et al. (2012b), *Randolph Glacier Inventory [v2.0]: A Dataset of Global Glacier Outlines*, Boulder Colorado, USA.

Arnell, N. W. (1999), Climate change and global water resources, *Glob. Environ. Chang.*, *9*, S31 – S49.

Arnold, J. G. et al. (2012), SWAT: Model use, calibration, and validation, *Trans. ASABE*, *55*(4), 1491 – 1508.

Bahr, D. B., W. T. Pfeffer, and G. Kaser (2015), A review of volume-area scaling of glaciers, *Rev. Geophys., 53*, 95–140, doi:10.1002/2014RG000470.

Bahr, D. B., M. F. Meier, and S. D. Peckham (1997), The physical basis of glacier volume-area scaling, *J. Geophys. Res.*, *102*(B9), 20355 – 20362.

Bajracharya, S. R., and B. Shrestha (2011), *The status of glaciers in the Hindu Kush-Himalayan region.*, edited by S. R. Bajracharya and B. Shrestha, ICIMOD, ICIMOD.

Bakker, A. M. R. (2015), The Robustness of the Climate Modelling Paradigm. PhD thesis., Vrije Universiteit Amsterdam.

Barlow, M., M. Wheeler, B. Lyon, and H. Cullen (2005), Modulation of Daily Precipitation over East Africa by the Madden – Julian Oscillation, *Mon. Weather Rev.*, *133*, 3579 – 3594, doi:10.1175/JCLI-D-13-00693.1.

Barnett, T. P., J. C. Adam, and D. P. Lettenmaier (2005), Potential impacts of a warming climate on water availability in snow-dominated regions., *Nature*, *438*(7066), 303 – 309, doi:10.1038/nature04141.

Barros, A. P., G. Kim, E. Williams, and S. W. Nesbitt (2004), Probing orographic controls in the Himalayas during the monsoon using satellite imagery, *Nat. Hazards Earth Syst. Sci.*, *4*(1), 29 – 51, doi:10.5194/nhess-4-29-2004.

Bergström, S. (1992), *The HBV model: Its structure and applications.*

Bernhardt, M., and K. Schulz (2010), SnowSlide: A simple routine for calculating gravitational snow transport, *Geophys. Res. Lett.*, *37*(11), L11502, doi:10.1029/2010GL043086.

Berthier, E., Y. Arnaud, R. Kumar, S. Ahmad, P. Wagnon, and P. Chevallier (2007), Remote sensing estimates of glacier mass balances in the Himachal Pradesh (Western Himalaya, India), *Remote Sens. Environ.*, *108*(3), 327 – 338, doi:10.1016/j.rse.2006.11.017.

Beven, K. (2006), A manifesto for the equifinality thesis, *J. Hydrol.*, *320*(1-2), 18 – 36, doi:10.1016/j.jhydrol.2005.07.007.

Bhutiyani, M. R., V. S. Kale, and N. J. Pawar (2007), Long-term trends in maximum, minimum and mean annual air temperatures across the Northwestern Himalaya during the twentieth century, *Clim. Change*, *85*(1-2), 159 – 177, doi:10.1007/s10584-006-9196-1.

Biemans, H., L. H. Speelman, F. Ludwig, E. J. Moors, A J. Wiltshire, P. Kumar, D. Gerten, and P. Kabat (2013), Future water resources for food production in five South Asian river basins and potential for adaptation – A modeling study., *Sci. Total Environ.*, *468-469*, S117 – S131, doi:10.1016/j.scitotenv.2013.05.092.

Bierkens, M. F. P., and L. P. H. van Beek (2009), Seasonal Predictability of European Discharge: NAO and Hydrological Response Time, *J. Hydrometeorol.*, *10*(4), 953 – 968, doi:10.1175/2009JHM1034.1.

Blázquez, J., and M. N. Nuñez (2013), Analysis of uncertainties in future climate projections for South America: Comparison of WCRP-CMIP3 and WCRP-CMIP5 models, *Clim. Dyn.*, *41*(3-4), 1039 – 1056, doi:10.1007/s00382-012-1489-7.

Bliss, A., R. Hock, and V. Radić (2014), Global response of glacier runoff to twenty-first century climate change, *J. Geophys. Res. Earth Surf.*, *119*, 1 – 14, doi:10.1002/2013JF002931.

Bocchiola, D., and G. Diolaiuti (2013), Recent (1980-2009) evidence of climate change in the upper Karakoram, Pakistan, *Theor. Appl. Climatol.*, *113*(3-4), 611 – 641, doi:10.1007/s00704-012-0803-y.

Bocchiola, D., G. Diolaiuti, A. Soncini, C. Mihalcea, C. D'Agata, C. Mayer, A. Lambrecht, R. Rosso, and C. Smiraglia (2011), Prediction of future hydrological regimes in poorly gauged high altitude basins: the case study of the upper Indus, Pakistan, *Hydrol. Earth Syst. Sci.*, *15*(7), 2059 – 2075, doi:10.5194/hess-15-2059-2011.

Boe, J., L. Terray, F. Habets, and E. Martin (2007), Statistical and dynamical downscaling of the Seine basin climate for hydro-meteorological studies, *Int. J. Climatol.*, *27*, 1643 – 1655, doi:10.1002/joc.

Bolch, T. (2007), Climate change and glacier retreat in northern Tien Shan (Kazakhstan/Kyrgyzstan) using remote sensing data, *Glob. Planet. Change*, *56*(1-2), 1 – 12, doi:10.1016/j.gloplacha.2006.07.009.

Bolch, T. et al. (2012), The State and Fate of Himalayan Glaciers, *Science*, *336*, 310 – 314, doi:10.1126/science.1215828.

Bookhagen, B. (2012), Hydrology: Himalayan groundwater, *Nat. Geosci.*, *5*(2), 97 – 98, doi:10.1038/ngeo1366.

Bookhagen, B., and D. W. Burbank (2010), Toward a complete Himalayan hydrological budget: Spatiotemporal distribution of snowmelt and rainfall and their impact on river discharge, *J. Geophys. Res.*, *115*(F3), 1 – 25, doi:10.1029/2009JF001426.

Bordoy, R., and P. Burlando (2013), Bias Correction of Regional Climate Model Simulations in a Region of Complex Orography, *J. Appl. Meteorol. Climatol.*, *52*(1), 82 – 101, doi:10.1175/JAMC-D-11-0149.1.

Brock, B. W., C. Mihalcea, M. P. Kirkbride, G. Diolaiuti, M. E. J. Cutler, and C. Smiraglia (2010), Meteorology and surface energy fluxes in the 2005 – 2007 ablation seasons at the Miage debris-covered glacier, Mont Blanc Massif, Italian Alps, *J. Geophys. Res.*, *115*, D09106, doi:10.1029/2009JD013224.

Cannon, A. J. (2014), Selecting GCM Scenarios that Span the Range of Changes in a Multimodel Ensemble: Application to CMIP5 Climate Extremes Indices, *J. Clim.*, *28*, 1260 – 1267, doi:10.1175/JCLI-D-14-00636.1.

Cannon, F., L. M. V. Carvalho, C. Jones, and B. Bookhagen (2014), Multi-annual variations in winter westerly disturbance activity affecting the Himalaya, *Clim. Dyn.*, *44*(1-2), 441 – 455, doi:10.1007/s00382-014-2248-8.

Cannon, F., L. M. V. Carvalho, C. Jones, and J. Norris (2015), Winter westerly disturbance dynamics and precipitation in the western Himalaya and Karakoram: a wave-tracking approach, *Theor. Appl. Climatol.*, doi:10.1007/s00704-015-1489-8.

Chahine, M. T. (1992), The hydrological cycle and its influence on climate, *Nature*, *359*(373-380).

Cheema, M. J. M., and W. G. M. Bastiaanssen (2012), Local calibration of remotely sensed rainfall from the TRMM satellite for different periods and spatial scales in the Indus Basin, *Int. J. Remote Sens.*, *33*(8), 2603 – 2627, doi:10.1080/01431161.2011.617397.

Cheema, M. J. M., W. W. Immerzeel, and W. G. M. Bastiaanssen (2014), Spatial quantification of groundwater abstraction in the irrigated indus basin, *Groundwater*, *52*(1), 25 – 36, doi:10.1111/gwat.12027.

Chen, J. and A. Ohmura (1990), Estimation of Alpine glacier water resources and their change since the 1870s, IAHS Publications – Hydrology in Mountainous Regions, I – Hydrological Measurements; the water cycle, Proceedings of two Lausanne Symposia, August 1990, edited by: Lang, H. and Musy, A., IAHS Publ., 193, 127–135.

Christensen, J. H., and O. B. Christensen (2002), Severe summertime flooding in Europe, *Nature*, *421*(February), 805 – 806.

Cogley, J. G., J. S. Kargel, G. Kaser, and C. J. van der Veen (2010), Tracking the source of glacier misinformation, *Science, 327*(5965), 522 – 522.

Collier, E., L. I. Nicholson, B. W. Brock, F. Maussion, R. Essery, and A. B. G. Bush (2014), Representing moisture fluxes and phase changes in glacier debris cover using a reservoir approach, *Cryosph., 8*(4), 1429–1444, doi:10.5194/tc-8-1429-2014.

Collier, E., and W. W. Immerzeel (2015), High-resolution modeling of atmospheric dynamics in the Nepalese Himalaya, *J. Geophys. Res. Atmos.*, *120*, 9882–9896, doi:10.1002/2015JD023266.

Dahal, R. K., S. Hasegawa, A. Nonomura, M. Yamanaka, S. Dhakal, and P. Paudyal (2008), Predictive modelling of rainfall-induced landslide hazard in the Lesser Himalaya of Nepal based on weights-of-evidence, *Geomorphology*, *102*(3-4), 496 – 510, doi:10.1016/j.geomorph.2008.05.041.

Dam, J. C. van, P. Groenendijk, R. F. A. Hendriks, and J. G. Kroes (2008), Advances of modeling water flow in variably saturated soils with SWAP, *Vadose Zo. J.*, *7*(2), 640 – 653.

Dee, D. P. et al. (2011), The ERA-Interim reanalysis: configuration and performance of the data assimilation system, *Q. J. R. Meteorol. Soc.*, *137*(656), 553 – 597, doi:10.1002/qj.828.

Defourny, P., C. Vancutsem, P. Bicheron, C. Brockmann, F. Nino, L. Schouten, and M. Leroy (2007), GLOBCOVER: A 300 m global land cover product for 2005 using ENVISAT MERIS time series, in *Proceedings of ISPRS Commission VII Mid-Term Symposium: Remote Sensing: from Pixels to Processes, Enschede (NL) 8-11 May 2006*, pp. 8 – 11.

Deque, M. (2007), Frequency of precipitation and temperature extremes over France in an anthropogenic scenario: Model results and statistical correction according to observed values, *Glob. Planet. Change*, *57*(1-2), 16 – 26, doi:10.1016/j.gloplacha.2006.11.030.

Doherty, J. (2005), *PEST: Model Independent Parameter Estimation - Fifth Edition of User Manual*, Brisbane.

Doherty, J., and B. E. Skahill (2006), An advanced regularization methodology for use in watershed model calibration, *J. Hydrol.*, *327*(3-4), 564 – 577, doi:10.1016/j.jhydrol.2005.11.058.

Droogers, P., and R. G. Allen (2002), Estimating reference evapotranspiration under inaccurate data conditions, *Irrig. Drain. Syst.*, *16*, 33 – 45.

Eden, J. M., and M. Widmann (2014), Downscaling of GCM-Simulated Precipitation Using Model Output Statistics, *J. Clim.*, *27*(1), 312 – 324, doi:10.1175/JCLI-D-13-00063.1.

Eden, J. M., M. Widmann, D. Grawe, and S. Rast (2012), Skill, Correction, and Downscaling of GCM-Simulated Precipitation, *J. Clim.*, *25*(11), 3970 – 3984, doi:10.1175/JCLI-D-11-00254.1.

Eder, K., R. Würländer, and H. Rentsch (2000), Digital photogrammetry for the new glacier inventory of Austria, *Int. Arch. Photogramm. Remote Sensing.*, *XXXIII*(Part B4), 254 – 261.

Ehret, U., E. Zehe, V. Wulfmeyer, K. Warrach-Sagi, and J. Liebert (2012), Should we apply bias correction to global and regional climate model data? (HESS Opinions), *Hydrol. Earth Syst. Sci.*, *16*(9), 3391 – 3404, doi:10.5194/hess-16-3391-2012.

Evans, J. P., F. Ji, G. Abramowitz, and M. Ekström (2013), Optimally choosing small ensemble members to produce robust climate simulations, *Environ. Res. Lett.*, *8*(044050), 1 – 4, doi:10.1088/1748-9326/8/4/044050.

FAO/IIASA/ISRIC/ISSCAS/JRC (2012), *Harmonized World Soil Database (version 1.2)*., Rome, Italy and Laxenburg, Austria.

Farinotti, D., M. Huss, A. Bauder, and M. Funk (2009), An estimate of the glacier ice volume in the Swiss Alps, *Glob. Planet. Change*, *68*(3), 225 – 231, doi:10.1016/j.gloplacha.2009.05.004.

Farinotti, D., S. Usselmann, M. Huss, A. Bauder, and M. Funk (2012), Runoff evolution in the Swiss Alps: projections for selected high-alpine catchments based on ENSEMBLES scenarios, *Hydrol. Process.*, *26*(13), 1909 – 1924, doi:10.1002/hyp.8276.

Farinotti, D., L. Longuevergne, G. Moholdt, D. Duethmann, T. Mölg, T. Bolch, S. Vorogushyn, and A. Güntner (2015), Substantial glacier mass loss in the Tien Shan over the past 50 years, *Nat. Geosci.*, (9296), doi:10.1038/ngeo2513.

Farr, T. G. et al. (2007), The Shuttle Radar Topography Mission, *Rev. Geophys.*, *45*(RG2004).

Finger, D., G. Heinrich, A. Gobiet, and A. Bauder (2012), Projections of future water resources and their uncertainty in a glacierized catchment in the Swiss Alps and the subsequent effects on hydropower production during the 21st century, *Water Resour. Res.*, *48*(2), 1 – 20, doi:10.1029/2011WR010733.

Fischer, G., M. Shah, F. N. Tubiello, and H. van Velhuizen (2005), Socio-economic and climate change impacts on agriculture: an integrated assessment, 1990-2080, *Philos. Trans. R. Soc. B Biol. Sci.*, *360*(1463), 2067 – 2083, doi:10.1098/rstb.2005.1744.

Fischer, H. et al. (2013), Where to find 1.5 million yr old ice for the IPICS "Oldest-Ice" ice core, *Clim. Past*, *9*, 2489 – 2505, doi:10.5194/cp-9-2489-2013.

Forsythe, N., H. J. Fowler, S. Blenkinsop, A. Burton, C. G. Kilsby, D. R. Archer, C. Harpham, and M. Z. Hashmi (2014), Application of a stochastic weather generator to assess climate change impacts in a semi-arid climate: The Upper Indus Basin, *J. Hydrol.*, *517*, 1019 – 1034, doi:10.1016/j.jhydrol.2014.06.031.

Fowler, H. J., and D. R. Archer (2006), Conflicting Signals of Climatic Change in the Upper Indus Basin, *J. Clim.*, *19*(17), 4276 – 4293, doi:10.1175/JCLI3860.1.

Fowler, H. J., S. Blenkinsop, and C. Tebaldi (2007), Linking climate change modelling to impacts studies: recent advances in downscaling techniques for hydrological modelling, *Int. J. Climatol.*, (September), 1547 – 1578, doi:10.1002/joc.

Frenierre, J. La, and B. G. Mark (2013), A review of methods for estimating the contribution of glacial meltwater to total watershed discharge, *Prog. Phys. Geogr.*, 1 – 28, doi:10.1177/0309133313516161.

Frey, H., H. Machguth, M. Huss, C. Huggel, S. Bajracharya, T. Bolch, A. Kulkarni, A. Linsbauer, N. Salzmann, and M. Stoffel (2014), Estimating the volume of glaciers in the Himalayan-Karakoram region using different methods, *Cryosph.*, *8*(6), 2313 – 2333, doi:10.5194/tc-8-2313-2014.

Fujita, K., A. Sakai, T. Nuimura, S. Yamaguchi, and R. R. Sharma (2009), Recent changes in Imja Glacial Lake and its damming moraine in the Nepal Himalaya revealed by *in situ* surveys and multi-temporal ASTER imagery, *Environ. Res. Lett.*, *4*(4), 045205, doi:10.1088/1748-9326/4/4/045205.

Galewsky, J. (2009), Rain shadow development during the growth of mountain ranges: An atmospheric dynamics perspective, *J. Geophys. Res.*, *114*(F1), F01018, doi:10.1029/2008JF001085.

Gardelle, J., E. Berthier, Y. Arnaud, and A. Kääb (2013), Region-wide glacier mass balances over the Pamir-Karakoram-Himalaya during 1999 – 2011, *Cryosph.*, *7*(4), 1263 – 1286, doi:10.5194/tc-7-1263-2013.

Gardner, A. S. et al. (2013), A reconciled estimate of glacier contributions to sea level rise: 2003 to 2009., *Science*, *340*(6134), 852 – 85277, doi:10.1126/science.1234532.

Gassert, F., P. Reig, T. Luo, and A. Maddocks (2013), *A Weighted Aggregation of Spatially Distinct Hydrological Indicators*, Washington D.C.

van Genuchten, M. T., and D. R. Nielsen (1985), On describing and predicting the hydraulic properties of unsaturated soils, *Ann. Geophys.*, *3*(5), 615 – 628.

Giesen, R. H., and J. Oerlemans (2010), Response of the ice cap Hardangerjøkulen in southern Norway to the 20th and 21st century climates, *Cryosph.*, *4*(2), 191 – 213, doi:10.5194/tc-4-191-2010.

Giorgi, F., C. Jones, and G. R. Asrar (2009), Addressing climate information needs at the regional level: the CORDEX framework, *Bull. – World Meteorol. Organ.*, *58*(3), 175 – 183.

Gleeson, T., Y. Wada, M. F. P. Bierkens, and L. P. H. van Beek (2012), Water balance of global aquifers revealed by groundwater footprint, *Nature*, *488*(7410), 197 – 200, doi:10.1038/nature11295.

Gobiet, A., M. Suklitsch, and G. Heinrich (2015), The effect of empirical-statistical correction of intensity-dependent model errors on the temperature climate change signal, *Hydrol. Earth Syst. Sci.*, *19*, 4055 – 4066, doi:10.5194/hess-19-1-2015.

Gómez-Landesa, E., and M. P. Bleiweiss (2008), *Snowmelt Runoff Model (SRM) User's Manual*.

Grinsted, A. (2013), An estimate of global glacier volume, *Cryosph.*, *7*(1), 141 – 151, doi:10.5194/tc-7-141-2013.

Gumbel, E. J. (1941), The return period of flood flows, *Ann. Math. Stat.*, *12*(2), 163 – 190.

Gurung, D. R., A. Giriraj, K.S. Aung, B. Shrestha, and A. V. Kulkarni (2011), Snow-Cover Mapping and Monitoring in the Hindu Kush-Himalayas, ICIMOD, Kathmandu.

Hagg, W., C. Mayer, A. Lambrecht, and A. Helm (2008), Sub-Debris Melt Rates on Southern Inylchek Glacier, Central Tian Shan, *Geogr. Ann. Ser. A Phys. Geogr.*, *90*(1), 55 – 63, doi:10.1111/j.1468-0459.2008.00333.x.

Hall, D. K., G. A. Riggs, N. E. Digirolamo, and K. J. Bayr (2002), MODIS Snow-Cover Products, *Remote Sens. Environ.*, *83*, 88 – 89.

Hasson, S., V. Lucarini, M. R. Khan, M. Petitta, T. Bolch, and G. Gioli (2014), Early 21st century climatology of snow cover for the western river basins of the Indus River System, *Hydrol. Earth Syst. Sci.*, *18*, 4077 – 4100, doi:10.5194/hess-18-4077-2014.

Hawkins, E., and R. Sutton (2009), The Potential to Narrow Uncertainty in Regional Climate Predictions, *Bull. Am. Meteorol. Soc.*, *90*(8), 1095 – 1107, doi:10.1175/2009BAMS2607.1.

Hawkins, E., and R. Sutton (2010), The potential to narrow uncertainty in projections of regional precipitation change, *Clim. Dyn.*, *37*(1-2), 407 – 418, doi:10.1007/s00382-010-0810-6.

Hempel, S., K. Frieler, L. Warszawski, J. Schewe, and F. Piontek (2013), A trend-preserving bias correction – the ISI-MIP approach, *Earth Syst. Dyn.*, *4*(2), 219 – 236, doi:10.5194/esd-4-219-2013.

Hewitt, K. (1998), Catastrophic landslides and their effects on the Upper Indus streams, Karakoram Himalaya, northern Pakistan, *Geomorphology*, *26*(1-3), 47 – 80, doi:10.1016/S0169-555X(98)00051-8.

Hewitt, K. (2005), The Karakoram Anomaly? Glacier Expansion and the "Elevation Effect," Karakoram Himalaya, *Mt. Res. Dev.*, *25*(4), 332 – 340.

Hewitt, K. (2007), Tributary glacier surges: an exceptional concentration at Panmah Glacier, Karakoram Himalaya, *J. Glaciol.*, *53*(181), 181 – 188, doi:10.3189/172756507782202829.

Hewitt, K. (2011), Glacier Change, Concentration, and Elevation Effects in the Karakoram Himalaya, Upper Indus Basin, *Mt. Res. Dev.*, *31*(3), 188 – 200, doi:10.1659/MRD-JOURNAL-D-11-00020.1.

Heynen, M., F. Pellicciotti, and M. Carenzo (2013), Parameter sensitivity of a distributed enhanced temperature-index melt model, *Ann. Glaciol.*, *54*(63), 1 – 11, doi:10.3189/2013AoG63A537.

Hirabayashi, Y., P. Döll, and S. Kanae (2010), Global-scale modeling of glacier mass balances for water resources assessments: Glacier mass changes between 1948 and 2006, *J. Hydrol.*, *390*(3-4), 245 – 256, doi:10.1016/j.jhydrol.2010.07.001.

Hock, R. (2003), Temperature index melt modelling in mountain areas, *J. Hydrol.*, *282*(1-4), 104 – 115, doi:10.1016/S0022-1694(03)00257-9.

Houle, D., A. Bouffard, L. Duchesne, T. Logan, and R. Harvey (2012), Projections of future soil temperature and water content for three Southern Quebec forested sites, *J. Clim.*, *25*(21), 7690 – 7701, doi:10.1175/JCLI-D-11-00440.1.

Hurkmans, R. T. W. L., W. Terink, R. Uijlenhoet, P. J. J. F. Torfs, D. Jacob, and P. A. Troch (2010), Changes in Streamflow Dynamics in the Rhine Basin under Three High-Resolution Regional Climate Scenarios, *J. Clim.*, *23*(3),679 – 699,doi:10.1175/2009JCLI3066.1.

Huss, M. (2011), Present and future contribution of glacier storage change to runoff from macroscale drainage basins in Europe, *Water Resour. Res.*, *47*, W07511, doi:10.1029/2010WR010299.

Huss, M. (2013), Density assumptions for converting geodetic glacier volume change to mass change, *Cryosph.*, *7*(3), 877 – 887, doi:10.5194/tc-7-877-2013.

Huss, M., and D. Farinotti (2012), Distributed ice thickness and volume of all glaciers around the globe, *J. Geophys. Res.*, *117*(F04010), 10, doi:10.1029/2012JF002523.

Huss, M., and R. Hock (2015), A new model for global glacier change and sea-level rise, *Front. Earth Sci., 3*(September), 1–22, doi:10.3389/feart.2015.00054.

Huss, M., S. Sugiyama, A. Bauder, and M. Funk (2007), Retreat Scenarios of Unteraargletscher, Switzerland, Using a Combined Ice-Flow Mass-Balance Model, *Arctic, Antarct. Alp. Res.*, *39*(3), 422 – 431, doi:10.1657/1523-0430(06-036)[HUSS]2.0.CO;2.

Huss, M., G. Jouvet, D. Farinotti, and A. Bauder (2010), Future high-mountain hydrology: a new parameterization of glacier retreat, *Hydrol. Earth Syst. Sci.*, *14*(5), 815 – 829, doi:10.5194/hess-14-815-2010.

Immerzeel, W. W. (2008), Historical trends and future predictions of climate variability in the Brahmaputra basin, *Int. J. Climatol.*, *28*, 243 – 254, doi:10.1002/joc.

Immerzeel, W. W., and M. F. P. Bierkens (2009), Seasonal prediction of monsoon rainfall in three Asian river basins: the importance of snow cover on the Tibetan Plateau, *Int. J. Climatol.*, *30*, 1835 – 1842, doi:10.1002/joc.2033.

Immerzeel, W. W., and M. F. P. Bierkens (2012), Asia's water balance, *Nat. Geosci.*, *5*(12), 841 – 842, doi:10.1038/ngeo1643.

Immerzeel, W. W., P. Droogers, S. M. de Jong, and M. F. P. Bierkens (2009), Large-scale monitoring of snow cover and runoff simulation in Himalayan river basins using remote sensing, *Remote Sens. Environ.*, *113*(1), 40 – 49, doi:10.1016/j.rse.2008.08.010.

Immerzeel, W. W., L. P.. Van Beek, and M. F. P. Bierkens (2010), Climate change will affect the Asian water towers, *Science*, *328*(5984), 1382 – 5, doi:10.1126/science.1183188.

Immerzeel, W. W., L. P. H. van Beek, M. Konz, A. B. Shrestha, and M. F. P. Bierkens (2011), Hydrological response to climate change in a glacierized catchment in the Himalayas, *Clim. Change*, *110*, 721 – 736, doi:10.1007/s10584-011-0143-4.

Immerzeel, W. W., A. F. Lutz, and P. Droogers (2012a), *Climate Change Impacts on the Upstream Water Resources of the Amu and Syr Darya River Basins*, Wageningen, The Netherlands.

Immerzeel, W. W., F. Pellicciotti, and A. B. Shrestha (2012b), Glaciers as a Proxy to Quantify the Spatial Distribution of Precipitation in the Hunza Basin, *Mt. Res. Dev.*, *32*(1), 30 – 38, doi:10.1659/MRD-JOURNAL-D-11-00097.1.

Immerzeel, W. W., F. Pellicciotti, and M. F. P. Bierkens (2013), Rising river flows throughout the twenty-first century in two Himalayan glacierized watersheds, *Nat. Geosci.*, *6*, 742 – 745, doi:10.1038/ngeo1896.

Immerzeel, W. W., N. Wanders, A. F. Lutz, J. M. Shea, and M. F. P. Bierkens (2015), Reconciling high altitude precipitation with glacier mass balances and runoff, *Hydrol. Earth Syst. Sci.*, *12*, 4755 – 4784, doi:10.5194/hessd-12-4755-2015.

IPCC (2000), *Special report on emission scenarios*, edited by N. Nakicenovic and R. Swart, Cambridge University Press, Cambridge, UK.

IPCC (2007), *Climate change 2007: Synthesis Report. Contribution of Working Groups I, II and III to the Fourth Assessment Report of the Intergovernmental Panel on Climate Change*, edited by R. K. Pachauri and A. Reisinger, Geneva, Switzerland.

IPCC (2013), *Climate Change 2013: The Physical Science Basis. Contribution of Working Group I to the Fifth Assessment Report of the Intergovernmental Panel on Climate Change*, Cambridge, UK.

Jacob, T., J. Wahr, W. T. Pfeffer, and S. Swenson (2012), Recent contributions of glaciers and ice caps to sea level rise, *Nature*, 1 – 5, doi:10.1038/nature10847.

Jain, S. K., P. K. Agarwal, and V. P. Singh (2007), The Indus Basin, in *Hydrology and Water Resources of India*.

Joetzjer, E., H. Douville, C. Delire, and P. Ciais (2013), Present-day and future Amazonian precipitation in global climate models: CMIP5 versus CMIP3, *Clim. Dyn.*, *41*(11-12), 2921 – 2936, doi:10.1007/s00382-012-1644-1.

Jouvet, G., M. Picasso, J. Rappaz, and H. Blatter (2008), A new algorithm to simulate the dynamics of a glacier: theory and applications, *J. Glaciol.*, *54*(188), 801 – 811, doi:10.3189/002214308787780049.

Jun, M., R. Knutti, and D. W. Nychka (2008), Spatial Analysis to Quantify Numerical Model Bias and Dependence, *J. Am. Stat. Assoc.*, *103*(483), 934 – 947, doi:10.1198/016214507000001265.

Kääb, A., E. Berthier, C. Nuth, J. Gardelle, and Y. Arnaud (2012), Contrasting patterns of early twenty-first-century glacier mass change in the Himalayas, *Nature*, *488*(7412), 495 – 8, doi:10.1038/nature11324.

Kääb, A., D. Treichler, C. Nuth, and E. Berthier (2015), Brief Communication: Contending estimates of 2003-2008 glacier mass balance over the Pamir – Karakoram – Himalaya, *Cryosph.*, *9*(2), 557 – 564, doi:10.5194/tc-9-557-2015.

Kapnick, S. B., T. L. Delworth, M. Ashfaq, S. Malyshev, and P. C. D. Milly (2014), Snowfall less sensitive to warming in Karakoram than in Himalayas due to a unique seasonal cycle, *Nat. Geosci.*, (October), 1 – 7, doi:10.1038/ngeo2269.

Kargel, J. S., J. G. Cogley, G. J. Leonard, U. Haritashya, and A. Byers (2011), Himalayan glaciers: The big picture is a montage, *Proc. Natl. Acad. Sci. U. S. A.*, *108*(34), 14709 – 14710, doi:10.1073/pnas.1111663108.

Kaser, G., M. Grosshauser, and B. Marzeion (2010), Contribution potential of glaciers to water availability in different climate regimes., *Proc. Natl. Acad. Sci.*, *107*(47), 20223 – 20227, doi:10.1073/pnas.1008162107.

Kay, A. L., H. N. Davies, V. A. Bell, and R. G. Jones (2008), Comparison of uncertainty sources for climate change impacts: flood frequency in England, *Clim. Change*, *92*, 41 – 63, doi:10.1007/s10584-008-9471-4.

Keshavarzi, A., F. Sarmadian, M. Sadeghnejad, and P. Pezeshki (2010), Developing Pedotransfer Functions for Estimating some Soil Properties using Artificial Neural Network and Multivariate Regression Approaches, *ProEnvironment*, *3*, 322 – 330.

Khan, A., B. S. Naz, and L. C. Bowling (2015a), Separating snow, clean and debris covered ice in the Upper Indus Basin, Hindukush-Karakoram-Himalayas, using Landsat images between 1998 and 2002, *J. Hydrol.*, *521*, 46 – 64, doi:10.1016/j.jhydrol.2014.11.048.

Khan, F., J. Pilz, M. Amjad, and D. A. Wiberg (2015b), Climate variability and its impacts on water resources in the Upper Indus Basin under IPCC climate change scenarios, *Int. J. Glob. Warm.*, *8*(1), 46 – 69, doi:10.1504/IJGW.2015.071583.

Khattak, M. S., M. S. Babel, and M. Sharif (2011), Hydro-meteorological trends in the upper Indus River basin in Pakistan, *Clim. Res.*, *46*(2), 103 – 119, doi:10.3354/cr00957.

Khromova, T. E., M. B. Dyurgerov, and R. G. Barry (2003), Late-twentieth century changes in glacier extent in the Ak-shirak Range, Central Asia, determined from historical data and ASTER imagery, *Geophys. Res. Lett.*, *30*(16), 3 – 7, doi:10.1029/2003GL017233.

Khromova, T. E., G. B. Osipova, D. G. Tsvetkov, M. B. Dyurgerov, and R. G. Barry (2006), Changes in glacier extent in the eastern Pamir, Central Asia, determined from historical data and ASTER imagery, *Remote Sens. Environ.*, *102*(1-2), 24 – 32, doi:10.1016/j.rse.2006.01.019.

Kjellström, E., F. Boberg, M. Castro, J. H. Christensen, G. Nikulin, and E. Sánchez (2010), Daily and monthly temperature and precipitation statistics as performance indicators for regional climate models, *Clim. Res.*, *44*, 135 – 150, doi:10.3354/cr00932.

Knutti, R., and J. Sedláček (2012), Robustness and uncertainties in the new CMIP5 climate model projections, *Nat. Clim. Chang.*, *3*, 369 – 373, doi:10.1038/nclimate1716.

Knutti, R., D. Masson, and A. Gettelman (2013), Climate model genealogy: Generation CMIP5 and how we got there, *Geophys. Res. Lett.*, *40*(6), 1194 – 1199, doi:10.1002/grl.50256.

Kokkonen, T., H. Koivusalo, A. Jakeman, and J. Norton (2006), Construction of a Degree-Day Snow Model in the Light of the"Ten Iterative Steps in Model Development", in *Proceedings of the iEMSs Third Biennial Meeting: Summit on Environmental Modelling and Software, Environmental Modelling and Software Society*, Burlington, USA.

Komori, J., T. Koike, T. Yamanokuchi, and P. Tshering (2012), Glacial Lake Outburst Events in the Bhutan Himalayas, *Glob. Environ. Res.*, *16*(October), 59 – 70.

Konz, M., and J. Seibert (2010), On the value of glacier mass balances for hydrological model calibration, *J. Hydrol.*, *385*(1-4), 238 – 246, doi:10.1016/j.jhydrol.2010.02.025.

Konz, M., S. Uhlenbrook, L. Braun, A. Shrestha, and S. Demuth (2007), Implementation of a process-based catchment model in a poorly gauged, highly glacierized Himalayan headwater, *Hydrol. Earth Syst. Sci.*, (1993), 1323 – 1339.

Kraaijenbrink, P. (2013), *Advanced Delta Change method*, De Bilt, The Netherlands.

Krishna Kumar, K., S. K. Patwardhan, A. Kulkarni, K. Kamala, K. Koteswara Rao, and R. Jones (2011), Simulated projections for summer monsoon climate over India by a high-resolution regional climate model (PRECIS), *Curr. Sci.*, *101*(3), 312 – 326.

Kundzewicz, Z. W., and E. Z. Stakhiv (2010), Are climate models "ready for prime time" in water resources management applications, or is more research needed?, *Hydrol. Sci. J.*, *55*(7), 1085 – 1089, doi:10.1080/02626667.2010.513211.

Kustas, W.P., A. Rango, and R. Uijlenhoet (1994), A simple energy budget algorithm for the snowmelt runoff model. *Water Resour. Res.*, *50*(5), 1515 – 1527, doi:10.1029/94WR00152.

Lambrecht, A., and M. Kuhn (2007), Glacier changes in the Austrian Alps during the last three decades, derived from the new Austrian glacier inventory, *Ann. Glaciol.*, *46*(1), 177 – 184, doi:10.3189/172756407782871341.

Leander, R., and T. A. Buishand (2007), Resampling of regional climate model output for the simulation of extreme river flows, *J. Hydrol.*, *332*, 487 – 496, doi:10.1016/j.jhydrol.2006.08.006.

Lehner, B., K. Verdin, and A. Jarvis (2008), New Global Hydrography Derived From Spaceborne Elevation Data, *Eos, Trans. Am. Geophys. Union*, *89*(10), 93 – 104, doi:10.1029/2008EO100001.

Lenaerts, J. T. M., M. R. van den Broeke, S. J. Déry, G. König-Langlo, J. Ettema, and P. K. Munneke (2010), Modelling snowdrift sublimation on an Antarctic ice shelf, *Cryosph.*, *4*(2), 179 – 190, doi:10.5194/tc-4-179-2010.

Lenderink, G., A. Buishand, and W. van Deursen (2007), Estimates of future discharges of the river Rhine using two scenario methodologies: direct versus delta approach, *Hydrol. Earth Syst. Sci.*, *11*(3), 1145 – 1159, doi:10.5194/hess-11-1145-2007.

LIGG, WECS, and NEA (1988), Report on first expedition to glaciers and glacier lakes in the Pumqu (Arun) and Poiqu (Bhote-Sun Kosi) river basins, Xizang (Tibet), China, Science Press, Beijing, China.

Liu, X., and B. Chen (2000), Climatic Warming In The Tibetan Plateau During Recent Decades, *Int. J. Climatol., 20,* 1729 – 1742.

Liu, Z., and E. Todini (2002), Towards a comprehensive physically-based rainfall-runoff model, *Hydrol. Earth Syst. Sci.*, *6*(5), 859 – 881, doi:10.5194/hess-6-859-2002.

Lu, A., S. Kang, Z. Li, and W. H. Theakstone (2010), Altitude effects of climatic variation on Tibetan plateau and its vicinities, *J. Earth Sci.*, *21*(2), 189 – 198, doi:10.1007/s12583-010-0017-0.

Lutz, A. F., W. W. Immerzeel, A. Gobiet, F. Pellicciotti, and M. F. P. Bierkens (2013), Comparison of climate change signals in CMIP3 and CMIP5 multi-model ensembles and implications for Central Asian glaciers, *Hydrol. Earth Syst. Sci.*, *17*(9), 3661 – 3677, doi:10.5194/hess-17-3661-2013.

Lutz, A. F., W. W. Immerzeel, A. B. Shrestha, and M. F. P. Bierkens (2014), Consistent increase in High Asia's runoff due to increasing glacier melt and precipitation, *Nat. Clim. Chang.*, *4*, 587 – 592, doi:10.1038/NCLIMATE2237.

MacDonald, M. K., J. W. Pomeroy, and A. Pietroniro (2010), On the importance of sublimation to an alpine snow mass balance in the Canadian Rocky Mountains, *Hydrol. Earth Syst. Sci.*, *14*(7), 1401 – 1415, doi:10.5194/hess-14-1401-2010.

Maraun, D. et al. (2010), Precipitation downscaling under climate change: recent developments to bridge the gap between dynamical models and the end user, *Rev. Geophys.*, *48*(RG3003), 1 – 34.

Marshak, S., and D. R. Prothero (2008), *Earth: portrait of a planet.*, WW Norton.

Martinec, J., and A. Rango (1986), Parameter values for snowmelt runoff modelling, *J. Hydrol.*, *84*, 197 – 219, doi:10.1016/0022-1694(86)90123-X.

Marzeion, B., A. H. Jarosch, and M. Hofer (2012), Past and future sea-level change from the surface mass balance of glaciers, *Cryosph.*, *6*, 1295–1322, doi:10.5194/tc-6-1295-2012.

Masson, D., and R. Knutti (2011), Climate model genealogy, *Geophys. Res. Lett.*, *38*(8), 1 – 4, doi:10.1029/2011GL046864.

Maurer, E. P., and D. W. Pierce (2014), Bias correction can modify climate model simulated precipitation changes without adverse effect on the ensemble mean, *Hydrol. Earth Syst. Sci.*, *18*(3), 915 – 925, doi:10.5194/hess-18-915-2014.

Maussion, F., D. Scherer, T. Mölg, E. Collier, J. Curio, and R. Finkelnburg (2014), Precipitation Seasonality and Variability over the Tibetan Plateau as Resolved by the High Asia Reanalysis, *J. Clim.*, *27*(5), 1910 – 1927, doi:10.1175/JCLI-D-13-00282.1.

McSweeney, C. F., R. G. Jones, and B. B. B. Booth (2012), Selecting ensemble members to provide regional climate change information, *J. Clim.*, *25*(20), 7100 – 7121, doi:10.1175/JCLI-D-11-00526.1.

Meehl, G. A., C. Covey, T. Delworth, M. Latif, B. Mcavaney, J. F. B. Mitchell, R. J. Stouffer, and K. E. Taylor (2007), The WCRP CMIP3 multimodel dataset: A New Era in Climate Change Research, *Bull. Am. Meteorol. Soc.*, *88*(September), 1382 – 1394.

Meinshausen, M. et al. (2011), The RCP greenhouse gas concentrations and their extensions from 1765 to 2300, *Clim. Change*, *109*(1), 213 – 241, doi:10.1007/s10584-011-0156-z.

Ménégoz, M., H. Gallée, and H. W. Jacobi (2013), Precipitation and snow cover in the Himalaya: from reanalysis to regional climate simulations, *Hydrol. Earth Syst. Sci.*, *17*, 3921 – 3936, doi:10.5194/hessd-10-7651-2013.

Mihalcea, C., C. Mayer, G. Diolaiuti, A. Lambrecht, C. Smiraglia, and G. Tartari (2006), Ice ablation and meteorological conditions on the debris-covered area of Baltoro glacier, Karakoram, Pakistan, *Ann. Glaciol.*, (1894), *292* – 300.

Miller, J. D., W. W. Immerzeel, and G. Rees (2012), Climate Change Impacts on Glacier Hydrology and River Discharge in the Hindu Kush – Himalayas A Synthesis of the Scientific Basis, *Mt. Res. Dev.*, *32*(4), 461 – 467.

Minville, M., F. Brissette, and R. Leconte (2008), Uncertainty of the impact of climate change on the hydrology of a nordic watershed, *J. Hydrol.*, *358*(1-2), 70 – 83, doi:10.1016/j.jhydrol.2008.05.033.

Mir, R. A., S. K. Jain, A. K. Saraf, and A. Goswami (2015), Accuracy assessment and trend analysis of MODIS-derived data on snow-covered areas in the Sutlej basin, Western Himalayas, *Int. J. Remote Sens.*, *36*(15), 3837 – 3858, doi:10.1080/01431161.2015.1070320.

Mirza, U. K., N. Ahmad, T. Majeed, and K. Harijan (2008), Hydropower use in Pakistan: Past, present and future, *Renew. Sustain. Energy Rev.*, *12*(6), 1641 – 1651, doi:10.1016/j.rser.2007.01.028.

Mishra, V. (2015), Climatic uncertainty in Himalayan Water Towers, *J. Geophys. Res. Atmos.*, *120*, 2689 – 2705, doi:10.1002/2014JD022650.

Molden, D. J., R. A. Vaidya, A. B. Shrestha, G. Rasul, and M. S. Shrestha (2014), Water infrastructure for the Hindu Kush Himalayas, *Int. J. Water Resour. Dev.*, *30*(1), 60 – 77, doi:10.1080/07900627.2013.859044.

Mölg, T., F. Maussion, and D. Scherer (2013), Mid-latitude westerlies as a driver of glacier variability in monsoonal High Asia, *Nat. Clim. Chang.*, *4*, 68 – 73, doi:10.1038/nclimate2055.

Möller, M., and C. Schneider (2010), Calibration of glacier volume – area relations from surface extent fluctuations and application to future glacier change, *J. Glaciol.*, *56*(195), 33 – 40.

Moss, R. H. et al. (2010), The next generation of scenarios for climate change research and assessment., *Nature*, *463*(7282), 747 – 56, doi:10.1038/nature08823.

Mukhopadhyay, B., and A. Khan (2014a), A quantitative assessment of the genetic sources of the hydrologic flow regimes in Upper Indus Basin and its significance in a changing climate, *J. Hydrol.*, *509*, 549 – 572, doi:10.1016/j.jhydrol.2013.11.059.

Mukhopadhyay, B., and A. Khan (2014b), Rising river flows and glacial mass balance in central Karakoram, *J. Hydrol.*, *513*, 192 – 203, doi:10.1016/j.jhydrol.2014.03.042.

Mukhopadhyay, B., and A. Khan (2015a), A reevaluation of the snowmelt and glacial melt in river flows within Upper Indus Basin and its significance in a changing climate, *J. Hydrol.*, *527*, 119 – 132, doi:10.1016/j.jhydrol.2013.11.059.

Mukhopadhyay, B., and A. Khan (2015b), Boltzmann – Shannon entropy and river flow stability within Upper Indus Basin in a changing climate, *Int. J. River Basin*, *13*(1), 87 – 95, doi:10.1016/j.jhydrol.2013.11.059.

Narama, C., A. Kääb, M. Duishonakunov, and K. Abdrakhmatov (2010), Spatial variability of recent glacier area changes in the Tien Shan Mountains, Central Asia, using Corona (~1970), Landsat (~2000), and ALOS (~2007) satellite data, *Glob. Planet. Change*, *71*(1-2), 42 – 54, doi:10.1016/j.gloplacha.2009.08.002.

Nash, J. E., and J. V. Sutcliffe (1970), River flow forecasting through conceptual models part I – A discussion of principles, *J. Hydrol.*, *10*(3), 282 – 290.

Neitsch, S. L., J. G. Arnold, J. R. Kiniry, and J. R. Williams (2011), *Soil & Water Assessment Tool Theoretical Documentation Version 2009*.

Nepal, S., and A. B. Shrestha (2015), Impact of climate change on the hydrological regime of the Indus, Ganges and Brahmaputra river basins: a review of the literature, *Int. J. Water Resour. Dev.*, (May 2015), 1 – 18, doi:10.1080/07900627.2015.1030494.

Nicholson, L., and D. I. Benn (2006), Calculating ice melt beneath a debris layer using meteorological data, *J. Glaciol.*, *52*(178), 463 – 470, doi:10.3189/172756506781828584.

Nohara, D., A. Kitoh, M. Hosaka, and T. Oki (2006), Impact of Climate Change on River Discharge Projected by Multimodel Ensemble, *J. Hydrometeorol.*, *7*, 1076 – 1089.

Nuimura, T. et al. (2015), The GAMDAM glacier inventory: a quality-controlled inventory of Asian glaciers, *Cryosph.*, *9*(3), 849 – 864, doi:10.5194/tc-9-849-2015.

Oki, T., and K. Shinjiro (2006), Global Hydrological Cycles and World Water Resources, *Science*, *313*.

Östrem, G. (1959), Ice Melting under a Thin Layer of Moraine, and the Existence of Ice Cores in Moraine Ridges, *Geogr. Ann.*, *41*(4), 228 – 230.

Palazzi, E., J. Von Hardenberg, and A. Provenzale (2013), Precipitation in the Hindu-Kush Karakoram Himalaya: Observations and future scenarios, *J. Geophys. Res. Atmos.*, *118*, 85 – 100, doi:10.1029/2012JD018697.

Palazzi, E., J. von Hardenberg, S. Terzago, and A. Provenzale (2014), Precipitation in the Karakoram-Himalaya: a CMIP5 view, *Clim. Dyn.*, 21 – 45, doi:10.1007/s00382-014-2341-z.

Patzelt, G. (1978), The Austrian glacier inventory: status and first results, in *Proceedings of the Riederalp Workshop*, pp. 181 – 184.

Paul, F., and A. Linsbauer (2012), Modeling of glacier bed topography from glacier outlines, central branch lines, and a DEM, *Int. J. Geogr. Inf. Sci.*, *26*(7), 1 – 18, doi:10.1080/13658816.2011.627859.

Paul, F., C. Huggel, and A. Kääb (2004), Combining satellite multispectral image data and a digital elevation model for mapping debris-covered glaciers, *Remote Sens. Environ.*, *89*(4), 510 – 518, doi:10.1016/j.rse.2003.11.007.

Pellicciotti, F., B. Brock, U. Strasser, P. Burlando, M. Funk, and J. Corripio (2005), An enhanced temperature-index glacier melt model including the shortwave radiation balance: development and testing for Haut Glacier d'Arolla, Switzerland, *J. Glaciol.*, *51*(175), 573 – 587.

Pellicciotti, F., C. Buergi, W. W. Immerzeel, M. Konz, and A. B. Shrestha (2012), Challenges and Uncertainties in Hydrological Modeling of Remote Hindu Kush – Karakoram – Himalayan (HKH) Basins: Suggestions for Calibration Strategies, *Mt. Res. Dev.*, *32*(1), 39 – 50, doi:10.1659/MRD-JOURNAL-D-11-00092.1.

van Pelt, S. C., J. J. Beersma, T. A. Buishand, B. J. J. M. van den Hurk, and P. Kabat (2012), Future changes in extreme precipitation in the Rhine basin based on global and regional climate model simulations, *Hydrol. Earth Syst. Sci.*, *16*(12), 4517 – 4530, doi:10.5194/hess-16-4517-2012.

Pepin, N. et al. (2015), Elevation-dependent warming in mountain regions of the world, *Nat. Clim. Chang.*, *5*, 424 – 430, doi:10.1038/nclimate2563.

Perkins, S. E., A. J. Pitman, N. J. Holbrook, and J. McAneney (2007), Evaluation of the AR4 climate models' simulated daily maximum temperature, minimum temperature, and precipitation over Australia using probability density functions, *J. Clim.*, *20*, 4356 – 4376, doi:10.1175/JCLI4253.1.

Peterson, T. C. (2005), Climate change indices, *WMO Bull.*, *54*(2), 83 – 86.

Pfeffer, W. et al. (2014), The Randolph Glacier Inventory: a globally complete inventory of glaciers, *J. Glaciol.*, *60*(221), 537 – 552, doi:10.3189/2014JoG13J176.

Piani, C., G. P. Weedon, M. Best, S. M. Gomes, P. Viterbo, S. Hagemann, and J. O. Haerter (2010), Statistical bias correction of global simulated daily precipitation and temperature for the application of hydrological models, *J. Hydrol.*, *395*(3-4), 199 – 215, doi:10.1016/j.jhydrol.2010.10.024.

Pielke, R. A., and R. L. Wilby (2012), Regional Climate Downscaling: What's the Point?, *Eos (Washington. DC).*, *93*(5), 52 – 53, doi:10.1002/wea543.Wilby.

Pierce, D. W., T. P. Barnett, B. D. Santer, and P. J. Gleckler (2009), Selecting global climate models for regional climate change studies., *Proc. Natl. Acad. Sci. U. S. A.*, *106*(21), 8441 – 8446, doi:10.1073/pnas.0900094106.

Pomeroy, J. W., and R. L. H. Essery (1999), Turbulent fluxes during blowing snow: field tests of model sublimation predictions, *Hydrol. Process.*, *13*, 2963 – 2975, doi:10.1002/(SICI)1099-1085(19991230)13:18<2963::AID-HYP11>3.0.CO;2-9.

Prasch, M. (2010), Distributed Process Oriented Modelling of the Future Impact of Glacier Melt Water on Runoff in the Lhasa River Basin in Tibet. PhD thesis, Ludwig-Maximillians-University of Munich.

Prasch, M., W. Mauser, and M. Weber (2013), Quantifying present and future glacier melt-water contribution to runoff in a central Himalayan river basin, *Cryosph.*, *7*(3), 889 – 904, doi:10.5194/tc-7-889-2013.

Prudhomme, C., N. Reynard, and S. Crooks (2002), Downscaling of global climate models for flood frequency analysis: where are we now?, *Hydrol. Process.*, *16*(6), 1137 – 1150, doi:10.1002/hyp.1054.

Quincey, D. J., L. Copland, C. Mayer, M. Bishop, A. Luckman, and M. Belò (2009), Ice velocity and climate variations for Baltoro Glacier, Pakistan, *J. Glaciol.*, *55*(194), 1061 – 1071, doi:10.3189/002214309790794913.

Quincey, D. J., M. Braun, N. F. Glasser, M. P. Bishop, K. Hewitt, and A. Luckman (2011), Karakoram glacier surge dynamics, *Geophys. Res. Lett.*, *38*(L18504), doi:10.1029/2011GL049004.

Quincey, D. J., N. F. Glasser, S. J. Cook, and A. Luckman (2015), Heterogeneity in Karakoram glacier surges, *J. Geophys. Res. Earth Surf.*, *accepted a*, doi:10.1002/2015JF003515.

Qureshi, A. S. (2011), Water Management in the Indus Basin in Pakistan: Challenges and Opportunities, *Mt. Res. Dev.*, *31*(3), 252 – 260, doi:10.1659/MRD-JOURNAL-D-11-00019.1.

Racoviteanu, A. E., R. Armstrong, and M. W. Williams (2013), Evaluation of an ice ablation model to estimate the contribution of melting glacier ice to annual discharge in the Nepal Himalaya, *Water Resour. Res.*, *49*(9), 5117 – 5133, doi:10.1002/wrcr.20370.

Radić, V., and G. K. C. Clarke (2011), Evaluation of IPCC Models' Performance in Simulating Late-Twentieth-Century Climatologies and Weather Patterns over North America, *J. Clim.*, *24*(20), 5257 – 5274, doi:10.1175/JCLI-D-11-00011.1.

Radić, V., and R. Hock (2010), Regional and global volumes of glaciers derived from statistical upscaling of glacier inventory data, *J. Geophys. Res.*, *115*(F01010), 1 – 10, doi:10.1029/2009JF001373.

Radić, V., and R. Hock (2011), Regionally differentiated contribution of mountain glaciers and ice caps to future sea-level rise, *Nat. Geosci.*, *4*(2), 91 – 94, doi:10.1038/ngeo1052.

Radić, V., and R. Hock (2013), Glaciers in the Earth's Hydrological Cycle: Assessments of Glacier Mass and Runoff Changes on Global and Regional Scales, *Surv. Geophys.*, doi:10.1007/s10712-013-9262-y.

Radić, V., A. Bliss, A. C. Beedlow, R. Hock, E. Miles, and J. G. Cogley (2014), Regional and global projections of twenty-first century glacier mass changes in response to climate scenarios from global climate models, *Clim. Dyn.*, 37 – 58, doi:10.1007/s00382-013-1719-7.

Ragettli, S., and F. Pellicciotti (2012), Calibration of a physically based, spatially distributed hydrological model in a glacierized basin: On the use of knowledge from glaciometeorological processes to constrain model parameters, *Water Resour. Res.*, *48*, W03509, doi:10.1029/2011WR010559.

Ragettli, S., F. Pellicciotti, R. Bordoy, and W. W. Immerzeel (2013), Sources of uncertainty in modeling the glacio-hydrological response of a Karakoram watershed to climate change, *Water Resour. Res.*, *49*, 1 – 19, doi:10.1002/wrcr.20450.

Ragettli, S., F. Pellicciotti, W. W. Immerzeel, E. Miles, L. Petersen, M. Heynen, J. M. Shea, D. Stumm, S. Joshi, and A. B. Shrestha (2015), Unraveling the hydrology of a Himalayan watershed through integration of high resolution in- situ data and remote sensing with an advanced simulation model, *Adv. Water Resour.*, *78*, 94 – 111, doi:10.1016/j.advwatres.2015.01.013.

Rajbhandari, R., A. B. Shrestha, A. Kulkarni, S. K. Patwardhan, and S. R. Bajracharya (2014), Projected changes in climate over the Indus river basin using a high resolution regional climate model (PRECIS), *Clim. Dyn.*, doi:10.1007/s00382-014-2183-8.

Ramesh, K. V, and P. Goswami (2014), Assessing reliability of regional climate projections: the case of Indian monsoon., *Nat. Sci. reports*, *4*, 4071, doi:10.1038/srep04071.

Rangwala, I., and J. R. Miller (2012), Climate change in mountains: A review of elevation-dependent warming and its possible causes, *Clim. Change*, *114*, 527 – 547, doi:10.1007/s10584-012-0419-3.

Rees, H. G., and D. N. Collins (2006), Regional differences in response of flow in glacier-fed Himalayan rivers to climatic warming, *Hydrol. Process.*, *20*, 2157 – 2169, doi:10.1002/hyp.

Reggiani, P., and T. H. M. Rientjes (2014), A reflection on the long-term water balance of the Upper Indus Basin, *Hydrol. Res.*, 1 – 17, doi:10.2166/nh.2014.060.

Reid, T. D., M. Carenzo, F. Pellicciotti, and B. W. Brock (2012), Including debris cover effects in a distributed model of glacier ablation, *J. Geophys. Res.*, *117*(D18105), doi:10.1029/2012JD017795.

Richey, A. S., B. F. Thomas, M.-H. Lo, J. T. Reager, J. S. Famiglietti, K. Voss, S. Swenson, and M. Rodell (2015), Quantifying renewable groundwater stress with GRACE, *Water Resour. Res.*, *51*, 5219 – 5238, doi:10.1002/2015WR017349.

Sanchez, E., R. Romera, M. A. Gaertner, C. Gallardo, and M. Castro (2009), A weighting proposal for an ensemble of regional climate models over Europe driven by 1961 – 2000 ERA40 based on monthly precipitation probability density functions, *Atmos. Sci. Lett.*, *10*, 249 – 254, doi:10.1002/asl.

Sanderson, B. M., R. Knutti, and P. Caldwell (2015a), A Representative Democracy to Reduce Interdependency in a Multimodel Ensemble, *J. Clim.*, *28*(13), 5171 – 5194, doi:10.1175/JCLI-D-14-00362.1.

Sanderson, B. M., R. Knutti, and P. Caldwell (2015b), Addressing Interdependency in a Multimodel Ensemble by Interpolation of Model Properties, *J. Clim.*, *28*(13), 5150 – 5170, doi:10.1175/JCLI-D-14-00361.1.

Schaefli, B., B. Hingray, M. Niggli, and A. Musy (2005), A conceptual glacio-hydrological model for high mountainous catchments, *Hydrol. Earth Syst. Sci.*, *2*(1), 73 – 117, doi:10.5194/hessd-2-73-2005.

Schaner, N., N. Voisin, B. Nijssen, and D. P. Lettenmaier (2012), The contribution of glacier melt to streamflow, *Environ. Res. Lett.*, *7*, 034029, doi:10.1088/1748-9326/7/3/034029.

Scherler, D., B. Bookhagen, and M. R. Strecker (2011), Spatially variable response of Himalayan glaciers to climate change affected by debris cover, *Nat. Geosci.*, *4*(3), 156 – 159, doi:10.1038/ngeo1068.

Schneider, U., A. Becker, P. Finger, A. Meyer-Christoffer, M. Ziese, and B. Rudolf (2013), GPCC's new land surface precipitation climatology based on quality-controlled in situ data and its role in quantifying the global water cycle, *Theor. Appl. Climatol.*, 26, doi:10.1007/s00704-013-0860-x.

Sevestre, H., and D. I. Benn (2015), Climatic and geometric controls on the global distribution of surge-type glaciers: implications for a unifying model of surging, *J. Glaciol.*, *61*(228), 646 – 662, doi:10.3189/2015JoG14J136.

Shabalova, M., W. P. A. van Deursen, and T. A. Buishand (2003), Assessing future discharge of the river Rhine using regional climate model integrations and a hydrological model, *Clim. Res.*, *23*(3), 233–246, doi: 10.3354/cr023233

Sharif, M., D. R. Archer, H. J. Fowler, and N. Forsythe (2013), Trends in timing and magnitude of flow in the Upper Indus Basin, *Hydrol. Earth Syst. Sci.*, *17*(4), 1503 – 1516, doi:10.5194/hess-17-1503-2013.

Sharma, M., and R. Kumar (2008), GIS-based landslide hazard zonation: A case study from the Parwanoo area, Lesser and Outer Himalaya, H.P., India, *Bull. Eng. Geol. Environ.*, *67*(1), 129 – 137, doi:10.1007/s10064-007-0113-2.

Sharmila, S., S. Joseph, A. K. Sahai, S. Abhilash, and R. Chattopadhyay (2015), Future projection of Indian summer monsoon variability under climate change scenario: An assessment from CMIP5 climate models, *Glob. Planet. Change*, *124*, 62 – 78, doi:10.1016/j.gloplacha.2014.11.004.

Sheffield, J., G. Goteti, and E. F. Wood (2006), Development of a 50-Year High-Resolution Global Dataset of Meteorological Forcings for Land Surface Modeling, *J. Clim.*, *19*(13), 3088 – 3111, doi:10.1175/JCLI3790.1.

Shrestha, A. B., C. P. Wake, P. A. Mayewski, and J. E. Dibb (1999), Maximum Temperature Trends in the Himalaya and Its Vicinity: An Analysis Based on Temperature Records from Nepal for the Period 1971–94, *J. Clim.*, *12*, 2775 – 2786.

Shrestha, A. B., C. P. Wake, J. E. Dibb, and P. A. Mayewski (2000), Precipitation Fluctuations in the Nepal Himalaya and Its Vicinity and Relationship With Some Large Scale Climatological Parameters, *Int. J. Climatol.*, *20*, 317–327

Shrestha, A. B., N. Agrawal, B. Alfthan, S. Bajracharya, J. Maréchal, and B. van Oort (2015), *The Himalayan Climate and Water Atlas: Impact of climate change on water resources in five of Asia's major river basins.*, ICIMOD, GRID-Arendal, CICERO.

Siddiqi, A., J. L. Wescoat, S. Humair, and K. Afridi (2012), An empirical analysis of the hydropower portfolio in Pakistan, *Energy Policy*, *50*, 228 – 241, doi:10.1016/j.enpol.2012.06.063.

Siderius, C., H. Biemans, A. Wiltshire, S. Rao, W. H. P. Franssen, P. Kumar, A K. Gosain, M. T. H. van Vliet, and D. N. Collins (2013), Snowmelt contributions to discharge of the Ganges., *Sci. Total Environ.*, *468-469*, S93 – S101, doi:10.1016/j.scitotenv.2013.05.084.

Siegfried, T., T. Bernauer, R. Guiennet, S. Sellars, A. W. Robertson, J. Mankin, P. Bauer-Gottwein, and A. Yakovlev (2012), Will climate change exacerbate water stress in Central Asia?, *Clim. Change*, *112*, 881 – 899, doi:10.1007/s10584-011-0253-z.

Sillmann, J., V. V. Kharin, X. Zhang, F. W. Zwiers, and D. Bronaugh (2013a), Climate extremes indices in the CMIP5 multimodel ensemble: Part 1. Model evaluation in the present climate, *J. Geophys. Res. Atmos.*, *118*(4), 1716 – 1733, doi:10.1002/jgrd.50203.

Sillmann, J., V. V. Kharin, F. W. Zwiers, X. Zhang, and D. Bronaugh (2013b), Climate extremes indices in the CMIP5 multimodel ensemble: Part 2. Future climate projections, *J. Geophys. Res. Atmos.*, *118*(6), 2473 – 2493, doi:10.1002/jgrd.50188.

Singh, P., and L. Bengtsson (2004), Hydrological sensitivity of a large Himalayan basin to climate change, *Hydrol. Process.*, *18*, 2363 – 2385, doi:10.1002/hyp.1468.

Singh, P., and S. K. Jain (2002), Snow and glacier melt in the Satluj River at Bhakra Dam in the western Himalayan region, *Hydrol. Sci. J.*, *47*(1), 93 – 106, doi:10.1080/02626660209492910.

Singh, P., M. Arora, and N. K. Goel (2006), Effect of climate change on runoff of a glacierized Himalayan basin, *Hydrol. Process.*, *20*(9), 1979 – 1992, doi:10.1002/hyp.5991.

Soncini, A., D. Bocchiola, G. Confortola, A. Bianchi, R. Rosso, C. Mayer, A. Lambrecht, E. Palazzi, C. Smiraglia, and G. Diolaiuti (2015), Future Hydrological Regimes in the Upper Indus Basin: A Case Study from a High-Altitude Glacierized Catchment, *J. Hydrometeorol.*, *16*(1), 306 – 326, doi:10.1175/JHM-D-14-0043.1.

Sorg, A., T. Bolch, M. Stoffel, O. Solomina, and M. Beniston (2012), Climate change impacts on glaciers and runoff in Tien Shan (Central Asia), *Nat. Clim. Chang.*, *2*(10), 725 – 731, doi:10.1038/nclimate1592.

Sorg, A., M. Huss, M. Rohrer, and M. Stoffel (2014), The days of plenty might soon be over in glacierized Central Asian catchments, *Environ. Res. Lett.*, *9*(104018), 8, doi:10.1088/1748-9326/9/10/104018.

De Souza, K., E. Kituyi, B. Harvey, M. Leone, K. S. Murali, and J. D. Ford (2015), Vulnerability to climate change in three hot spots in Africa and Asia: key issues for policy-relevant adaptation and resilience-building research, *Reg. Environ. Chang.*, *15*, 747 – 753, doi:10.1007/s10113-015-0755-8.

Sperber, K. R., and H. Annamalai (2014), The use of fractional accumulated precipitation for the evaluation of the annual cycle of monsoons, *Clim. Dyn.*, *43*(12), 3219 – 3244, doi:10.1007/s00382-014-2099-3.

Sperber, K. R., H. Annamalai, I. S. Kang, A. Kitoh, A. Moise, A. Turner, B. Wang, and T. Zhou (2013), The Asian summer monsoon: An intercomparison of CMIP5 vs. CMIP3 simulations of the late 20th century, *Clim. Dyn.*, *41*(9-10), 2711 – 2744, doi:10.1007/s00382-012-1607-6.

Stahl, K., R. D. Moore, J. M. Shea, D. Hutchinson, and A. J. Cannon (2008), Coupled modelling of glacier and streamflow response to future climate scenarios, *Water Resour. Res.*, *44*(W02422), 1 – 13, doi:10.1029/2007WR005956.

Strasser, U., M. Bernhardt, M. Weber, G. E. Liston, and W. Mauser (2008), Is snow sublimation important in the alpine water balance?, *Cryosph.*, *2*, 53 – 66.

Surendra, K. C., S. K. Khanal, P. Shrestha, and B. Lamsal (2011), Current status of renewable energy in Nepal: Opportunities and challenges, *Renew. Sustain. Energy Rev.*, *15*(8), 4107 – 4117, doi:10.1016/j.rser.2011.07.022.

Tachikawa, T., M. Hato, M. Kaku, and A. Iwasaki (2011), Characteristics of ASTER GDEM version 2, in *Geoscience and Remote Sensing Symposium (IGARSS), IEEE International*, pp. 3657 – 3660.

Tahir, A. A., P. Chevallier, Y. Arnaud, L. Neppel, and B. Ahmad (2011a), Modeling snowmelt-runoff under climate scenarios in the Hunza River basin, Karakoram Range, Northern Pakistan, *J. Hydrol.*, *409*(1-2), 104 – 117, doi:10.1016/j.jhydrol.2011.08.035.

Tahir, A. A., P. Chevallier, Y. Arnaud, and B. Ahmad (2011b), Snow cover dynamics and hydrological regime of the Hunza River basin, Karakoram Range, Northern Pakistan, *Hydrol. Earth Syst. Sci.*, *15*(7), 2275 – 2290, doi:10.5194/hess-15-2275-2011.

Tahir, A. A., P. Chevallier, Y. Arnaud, M. Ashraf, and M. T. Bhatti (2015), Snow cover trend and hydrological characteristics of the Astore River basin (Western Himalayas) and its comparison to the Hunza basin (Karakoram region), *Sci. Total Environ.*, *505*, 748 – 761, doi:10.1016/j.scitotenv.2014.10.065.

Taylor, K. E., R. J. Stouffer, and G. A. Meehl (2012), An Overview of CMIP5 and the Experiment Design, *Bull. Am. Meteorol. Soc.*, *93*(4), 485 – 498, doi:10.1175/BAMS-D-11-00094.1.

Terink, W., R. T. W. L. Hurkmans, P. J. J. F. Torfs, and R. Uijlenhoet (2010), Bias correction of downscaled precipitation and temperature reanalysis data for the Rhine Basin, *Hydrol. Earth Syst. Sci., 14*, 687 – 703.

Terink, W., A. F. Lutz, G. W. H. Simons, W. W. Immerzeel, and P. Droogers (2015), SPHY v2.0: Spatial Processes in HYdrology, *Geosci. Model Dev.*, *8*, 2009 – 2034, doi:10.5194/gmd-8-2009-2015.

Themeßl, M. J., A. Gobiet, and A. Leuprecht (2011a), Empirical-statistical downscaling and error correction of daily precipitation from regional climate models, *Int. J. Climatol.*, *31*(10), 1530 – 1544, doi:10.1002/joc.2168.

Themeßl, M. J., A. Gobiet, and G. Heinrich (2011b), Empirical-statistical downscaling and error correction of regional climate models and its impact on the climate change signal, *Clim. Change*, *112*(2), 449 – 468, doi:10.1007/s10584-011-0224-4.

Turner, A. G., and H. Annamalai (2012), Climate change and the South Asian summer monsoon, *Nat. Clim. Chang.*, *2*, 587 – 595, doi:10.1038/nclimate1495.

UN (2015), *World Population Prospects, 2015 Revision*, New York.

Unger-Shayesteh, K., S. Vorogushyn, D. Farinotti, A. Gafurov, D. Duethmann, A. Mandychev, and B. Merz (2013), What do we know about past changes in the water cycle of Central Asian headwaters? A review, *Glob. Planet. Change*, *in press*, doi:10.1016/j.gloplacha.2013.02.004.

Viste, E., and A. Sorteberg (2015), Snowfall in the Himalayas: an uncertain future from a little-known past, *Cryosph.*, *9*(3), 1147 – 1167, doi:10.5194/tc-9-1147-2015.

Viviroli, D., R. Weingartner, and B. Messerli (2003), Assessing the Hydrological Significance of the World's Mountains, *Mt. Res. Dev.*, *23*(1), 32 – 40, doi:10.1659/0276-4741(2003)023[0032:ATHSOT]2.0.CO;2.

van Vuuren, D. P., E. Stehfest, M. G. J. den Elzen, J. van Vliet, and M. Isaac (2010), Exploring IMAGE model scenarios that keep greenhouse gas radiative forcing below 3W/m2 in 2100, *Energy Econ.*, *32*(5), 1105 – 1120, doi:10.1016/j.eneco.2010.03.001.

van Vuuren, D. P. et al. (2011a), RCP2.6: exploring the possibility to keep global mean temperature increase below 2°C, *Clim. Change*, *109*, 95 – 116, doi:10.1007/s10584-011-0152-3.

van Vuuren, D. P. et al. (2011b), The representative concentration pathways: an overview, *Clim. Change*, *109*(1-2), 5 – 31, doi:10.1007/s10584-011-0148-z.

Wada, Y., L. P. H. van Beek, C. M. van Kempen, J. W. T. M. Reckman, S. Vasak, and M. F. P. Bierkens (2010), Global depletion of groundwater resources, *Geophys. Res. Lett.*, *37*(L20402), 1 – 5, doi:10.1029/2010GL044571.

Wada, Y., L. P. H. van Beek, and M. F. P. Bierkens (2011), Modelling global water stress of the recent past: on the relative importance of trends in water demand and climate variability, *Hydrol. Earth Syst. Sci.*, *15*(12), 3785 – 3808, doi:10.5194/hess-15-3785-2011.

Wagnon, P. et al. (2013), Seasonal and annual mass balances of Mera and Pokalde glaciers (Nepal Himalaya) since 2007, *Cryosph.*, *7*(6), 1769 – 1786, doi:10.5194/tc-7-1769-2013.

van de Wal, R. S. W., and M. Wild (2001), Modelling the response of glaciers to climate change by applying volume-area scaling in combination with a high resolution GCM, *Clim. Dyn.*, *18*, 359 – 366.

Wanders, N., and Y. Wada (2014), Human and climate impacts on the 21st century hydrological drought, *J. Hydrol.*, doi:10.1016/j.jhydrol.2014.10.047.

Wang, L., Z. Li, and F. Wang (2011), Spatial distribution of the debris layer on glaciers of the Tuomuer Peak, western Tian Shan, *J. Earth Sci.*, *22*(4), 528 – 538, doi:10.1007/s12583-011-0205-6.

Wang, W., Y. Xiang, Y. Gao, A. Lu, and T. Yao (2015), Rapid expansion of glacial lakes caused by climate and glacier retreat in the Central Himalayas, *Hydrol. Process.*, *29*(6), 859 – 874, doi:10.1002/hyp.10199.

Warszawski, L., K. Frieler, V. Huber, F. Piontek, O. Serdeczny, and J. Schewe (2014), The Inter-Sectoral Impact Model Intercomparison Project (ISI-MIP): project framework., *Proc. Natl. Acad. Sci. U. S. A.*, *111*(9), 3228 – 32, doi:10.1073/pnas.1312330110.

Weber, M., L. Braun, W. Mauser, and M. Prasch (2010), Contribution of rain, snow- and icemelt in the Upper Danube discharge today and in the future, *Geogr. Fis. Dinam. Quat*, *33*, 221 – 230.

Weedon, G. P., S. Gomes, P. Viterbo, W. J. Shuttleworth, E. Blyth, H. Österle, J. C. Adam, N. Bellouin, O. Boucher, and M. Best (2011), Creation of the WATCH Forcing Data and Its Use to Assess Global and Regional Reference Crop Evaporation over Land during the Twentieth Century, *J. Hydrometeorol.*, *12*(5), 823 – 848, doi:10.1175/2011JHM1369.1.

Weedon, G. P., G. Balsamo, N. Bellouin, S. Gomes, M. J. Best, and P. Viterbo (2014), The WFDEI meteorological forcing data set:WATCH Forcing Data methodology applied to ERA-Interim reanalysis data, *Water Resour. Res.*, 7505 – 7514, doi:10.1002/2014WR015638.Received.

Weertman, J. (1957), On the sliding of glaciers, *J. Glaciol.*, *3*, 33 – 38.

Widmann, M., and C. S. Bretherton (2003), Statistical Precipitation Downscaling over the Northwestern United States Using Numerically Simulated Precipitation as a Predictor, *J. Clim.*, *16*, 799 – 816.

Wilby, R. L., and T. M. L. Wigley (1997), Downscaling general circulation model output: a review of methods and limitations, *Prog. Phys. Geogr.*, *21*(4), 530 – 548, doi:10.1177/030913339702100403.

Winiger, M., M. Gumpert, and H. Yamout (2005), Karakorum-Hindukush-western Himalaya: assessing high-altitude water resources, *Hydrol. Process.*, *19*(12), 2329 – 2338, doi:10.1002/hyp.5887.

Yao, T. et al. (2012), Different glacier status with atmospheric circulations in Tibetan Plateau and surroundings, *Nat. Clim. Chang.*, *2*(9), 663 – 667, doi:10.1038/nclimate1580.

Yatagai, A., K. Kamiguchi, O. Arakawa, A. Hamada, N. Yasutomi, and A. Kitoh (2012), APHRODITE: Constructing a Long-Term Daily Gridded Precipitation Dataset for Asia Based on a Dense Network of Rain Gauges, *Bull. Am. Meteorol. Soc.*, *93*(9), 1401 – 1415, doi:10.1175/BAMS-D-11-00122.1.

Zemp, M., S. U. Nussbaumer, I. Gärtner-Roer, M. Hoelzle, F. Paul, and W. Haeberli (2011), *WGMS (2011): Glacier Mass Balance Bulletin No. 11 (2008-2009)*, Zurich, Zwitserland.

Zhang, H., G. H. Huang, D. Wang, and X. Zhang (2011), Uncertainty assessment of climate change impacts on the hydrology of small prairie wetlands, *J. Hydrol.*, *396*(1-2), 94 – 103, doi:10.1016/j.jhydrol.2010.10.037.

Zhang, Y., S. Liu, and Y. Ding (2006), Observed degree-day factors and their spatial variation on glaciers in western China, *Ann. Glaciol.*, *43*(1), 301 – 306, doi:10.3189/172756406781811952.

Zhao, L., R. Ding, and J. C. Moore (2014), Glacier volume and area change by 2050 in high mountain Asia, *Glob. Planet. Change*, *122*, 197 – 207, doi:10.1016/j.gloplacha.2014.08.006.

Table A1: Complete pool of RCP4.5 model runs considered in study described in Chapter 2 (continued on next pages)

GCM run	ΔT (°C)	ΔP (%)	Daily time step available	Normalised ΔT	Normalised ΔP	D to warm, dry corner	D to warm, wet corner	D to cold, wet corner	D to cold, dry corner	Selected for step 2
ACCESS1-0_r1i1p1	3.05	5.92	Yes	0.68	0.19	0.24	0.74	0.91	0.58	No
ACCESS1-3_r1i1p1	2.76	11.90	Yes	0.47	0.70	0.73	0.47	0.42	0.70	No
bcc-csm1-1_r1i1p1	2.22	14.46	Yes	0.22	0.87	1.03	0.69	0.12	0.78	Cold, Wet
bcc-csm1-1-m_r1i1p1	2.27	5.77	Yes	0.24	0.18	0.67	0.98	0.73	0.16	Cold, Dry
BNU-ESM_r1i1p1	2.54	12.75	Yes	0.42	0.75	0.81	0.50	0.35	0.73	Cold, Wet
CanESM2_r1i1p1	3.37	16.96	Yes	0.84	0.97	0.87	0.09	0.74	1.14	Warm, Wet
CanESM2_r2i1p1	3.34	17.26	Yes	0.81	0.98	0.88	0.12	0.71	1.13	No
CanESM2_r3i1p1	3.44	19.41	Yes	0.89	1.00	0.90	0.10	0.80	1.20	No
CanESM2_r4i1p1	3.32	15.86	Yes	0.80	0.95	0.85	0.11	0.70	1.09	No
CanESM2_r5i1p1	3.30	18.26	Yes	0.75	0.99	0.90	0.17	0.66	1.10	No
CCSM4_r1i1p1	2.28	6.41	Yes	0.25	0.26	0.67	0.92	0.66	0.22	No
CCSM4_r2i1p1	2.03	9.69	Yes	0.02	0.57	1.00	0.94	0.34	0.48	Cold, Wet
CCSM4_r6i1p1	2.20	4.46	Yes	0.20	0.14	0.70	1.03	0.77	0.11	Cold, Dry
CESM1-BGC_r1i1p1	2.09	6.10	Yes	0.11	0.20	0.80	1.06	0.70	0.10	Cold, Dry
CESM1-CAM5_r1i1p1	3.16	9.07	Yes	0.69	0.52	0.47	0.44	0.70	0.72	No
CMCC-CM_r1i1p1	3.28	4.22	Yes	0.73	0.13	0.17	0.79	1.00	0.63	Warm, Dry
CMCC-CMS_r1i1p1	3.47	-2.94	Yes	0.92	0.05	0.05	0.85	1.18	0.83	Warm, Dry
CNRM-CM5_r1i1p1	2.33	11.87	Yes	0.31	0.69	0.83	0.63	0.30	0.62	Cold, Wet
CSIRO-Mk3-6-0_r1i1p1	3.42	9.67	Yes	0.87	0.56	0.46	0.34	0.84	0.90	No
CSIRO-Mk3-6-0_r2i1p1	3.38	9.07	Yes	0.86	0.51	0.41	0.40	0.86	0.86	No
CSIRO-Mk3-6-0_r3i1p1	3.44	13.32	Yes	0.88	0.82	0.72	0.09	0.79	1.06	Warm, Wet
CSIRO-Mk3-6-0_r4i1p1	3.52	15.57	Yes	0.96	0.94	0.84	0.07	0.86	1.20	Warm, Wet
CSIRO-Mk3-6-0_r5i1p1	3.51	14.84	Yes	0.95	0.90	0.80	0.05	0.85	1.17	Warm, Wet
CSIRO-Mk3-6-0_r6i1p1	3.48	13.52	Yes	0.94	0.83	0.73	0.08	0.84	1.11	Warm, Wet
CSIRO-Mk3-6-0_r7i1p1	3.57	10.19	Yes	0.99	0.61	0.52	0.30	0.93	1.03	No
CSIRO-Mk3-6-0_r8i1p1	3.32	15.26	Yes	0.76	0.91	0.82	0.14	0.66	1.05	No
CSIRO-Mk3-6-0_r9i1p1	3.47	8.01	Yes	0.91	0.37	0.27	0.54	0.97	0.86	No
CSIRO-Mk3-6-0_r10i1p1	3.63	11.48	Yes	1.00	0.67	0.57	0.25	0.93	1.06	No
GISS-E2-R_r6i1p1	2.16	4.12	Yes	0.17	0.12	0.73	1.07	0.79	0.07	Cold, Dry

GCM run	ΔT (°C)	ΔP (%)	Daily time step available	Normalised ΔT	Normalised ΔP	D to warm, dry corner	D to warm, wet corner	D to cold, wet corner	D to cold, dry corner	Selected for step 2
GISS-E2-R_r6i1p3	2.49	10.59	Yes	0.40	0.63	0.73	0.57	0.40	0.61	No
HadGEM2-AO_r1i1p1	3.36	7.59	Yes	0.83	0.33	0.24	0.57	0.92	0.76	No
HadGEM2-CC_r1i1p1	2.88	9.07	Yes	0.58	0.53	0.53	0.49	0.61	0.64	No
HadGEM2-ES_r1i1p1	3.26	8.95	Yes	0.72	0.48	0.42	0.45	0.75	0.73	No
HadGEM2-ES_r2i1p1	3.32	8.15	Yes	0.78	0.39	0.31	0.53	0.86	0.74	No
HadGEM2-ES_r3i1p1	2.99	8.66	Yes	0.66	0.43	0.41	0.53	0.73	0.65	No
HadGEM2-ES_r4i1p1	3.03	8.15	Yes	0.67	0.38	0.36	0.57	0.77	0.63	No
inmcm4_r1i1p1	1.68	2.69	Yes	0.00	0.06	0.90	1.23	0.84	0.11	Cold, Dry
IPSL-CM5A-LR_r1i1p1	3.52	9.91	Yes	0.97	0.58	0.48	0.33	0.92	0.99	No
IPSL-CM5A-LR_r2i1p1	3.45	3.08	Yes	0.90	0.09	0.01	0.81	1.14	0.80	Warm, Dry
IPSL-CM5A-LR_r3i1p1	3.32	6.24	Yes	0.77	0.23	0.18	0.69	0.95	0.69	Warm, Dry
IPSL-CM5A-LR_r4i1p1	3.38	8.47	Yes	0.85	0.42	0.32	0.48	0.89	0.81	No
IPSL-CM5A-MR_r1i1p1	3.54	6.19	Yes	0.98	0.22	0.14	0.69	1.11	0.89	Warm, Dry
IPSL-CM5B-LR_r1i1p1	2.08	12.91	Yes	0.09	0.77	1.06	0.82	0.13	0.67	Cold, Wet
MIROC5_r1i1p1	2.82	12.59	Yes	0.55	0.74	0.73	0.39	0.48	0.78	No
MIROC5_r2i1p1	2.72	16.21	Yes	0.46	0.96	0.96	0.44	0.37	0.93	No
MIROC5_r3i1p1	2.77	14.18	Yes	0.51	0.86	0.86	0.40	0.41	0.86	No
MIROC-ESM_r1i1p1	3.20	8.92	Yes	0.70	0.46	0.41	0.48	0.74	0.70	No
MIROC-ESM-CHEM_r1i1p1	3.35	9.14	Yes	0.82	0.54	0.44	0.37	0.80	0.84	No
MPI-ESM-LR_r1i1p1	2.78	-3.96	Yes	0.52	0.04	0.39	0.94	0.95	0.42	No
MPI-ESM-LR_r2i1p1	2.97	-5.63	Yes	0.65	0.01	0.27	0.93	1.04	0.55	No
MPI-ESM-LR_r3i1p1	2.91	-4.65	Yes	0.61	0.03	0.30	0.91	1.01	0.52	No
MPI-ESM-MR_r1i1p1	2.67	4.02	Yes	0.45	0.11	0.45	0.91	0.87	0.35	No
MPI-ESM-MR_r2i1p1	2.84	-5.33	Yes	0.56	0.02	0.35	0.94	0.99	0.47	No
MPI-ESM-MR_r3i1p1	2.78	-5.75	Yes	0.53	0.00	0.39	0.97	1.00	0.44	No
MRI-CGCM3_r1i1p1	2.33	8.35	Yes	0.30	0.41	0.67	0.78	0.53	0.37	No
NorESM1-M_r1i1p1	2.16	8.91	Yes	0.16	0.45	0.82	0.86	0.45	0.36	No
CCSM4_r3i1p1	2.06	8.22	No	0.04	0.40	0.91	0.99	0.51	0.30	No
CCSM4_r4i1p1	2.06	6.65	No	0.03	0.28	0.89	1.07	0.62	0.19	No
CCSM4_r5i1p1	2.07	3.91	No	0.05	0.10	0.85	1.17	0.81	0.05	No
CESM1-CAM5_r2i1p1	3.21	10.14	No	0.71	0.59	0.53	0.36	0.68	0.78	No
CESM1-CAM5_r3i1p1	3.30	6.79	No	0.74	0.29	0.25	0.63	0.88	0.67	No

GCM run	ΔT (°C)	ΔP (%)	Daily time step available	Normalised ΔT	Normalised ΔP	D to warm, dry corner	D to warm, wet corner	D to cold, wet corner	D to cold, dry corner	Selected for step 2
GISS-E2-H_r1i1p1	2.37	13.14	No	0.34	0.81	0.90	0.56	0.26	0.75	No
GISS-E2-H_r2i1p1	2.34	10.39	No	0.33	0.62	0.77	0.63	0.36	0.57	No
GISS-E2-H_r3i1p1	2.47	12.89	No	0.38	0.76	0.85	0.54	0.31	0.72	No
GISS-E2-H_r4i1p1	2.30	7.79	No	0.27	0.34	0.68	0.84	0.58	0.30	No
GISS-E2-H_r5i1p1	2.44	8.94	No	0.35	0.47	0.66	0.69	0.50	0.45	No
GISS-E2-H_r1i1p2	2.47	12.13	No	0.37	0.72	0.82	0.56	0.32	0.67	No
GISS-E2-H_r2i1p2	2.50	11.07	No	0.41	0.65	0.73	0.55	0.40	0.63	No
GISS-E2-H_r3i1p2	2.32	14.76	No	0.28	0.88	1.00	0.62	0.18	0.80	No
GISS-E2-H_r4i1p2	2.47	6.34	No	0.39	0.25	0.53	0.83	0.71	0.32	No
GISS-E2-H_r5i1p2	2.25	9.03	No	0.23	0.49	0.78	0.79	0.42	0.41	No
GISS-E2-H_r1i1p3	2.96	13.12	No	0.63	0.80	0.74	0.29	0.54	0.88	No
GISS-E2-H_r2i1p3	2.94	15.28	No	0.62	0.92	0.87	0.28	0.52	0.98	No
GISS-E2-H_r3i1p3	2.89	14.12	No	0.59	0.85	0.81	0.31	0.49	0.90	No
GISS-E2-H_r4i1p3	2.90	12.47	No	0.60	0.73	0.70	0.34	0.53	0.81	No
GISS-E2-H_r5i1p3	2.76	13.55	No	0.49	0.84	0.84	0.41	0.40	0.84	No
GISS-E2-H-CC_r1i1p1	2.32	5.49	No	0.29	0.17	0.61	0.95	0.75	0.20	No
GISS-E2-R_r1i1p1	2.10	7.87	No	0.12	0.35	0.82	0.95	0.55	0.25	No
GISS-E2-R_r2i1p1	2.19	7.31	No	0.19	0.32	0.74	0.91	0.59	0.24	No
GISS-E2-R_r3i1p1	2.08	4.90	No	0.08	0.16	0.83	1.11	0.74	0.07	No
GISS-E2-R_r4i1p1	2.02	10.18	No	0.01	0.60	1.02	0.94	0.31	0.51	No
GISS-E2-R_r5i1p1	2.07	2.95	No	0.06	0.08	0.84	1.17	0.83	0.04	No
GISS-E2-R_r1i1p2	2.15	7.30	No	0.14	0.31	0.79	0.96	0.59	0.21	No
GISS-E2-R_r2i1p2	2.09	8.77	No	0.10	0.44	0.87	0.93	0.46	0.34	No
GISS-E2-R_r3i1p2	2.18	4.62	No	0.18	0.15	0.72	1.04	0.75	0.10	No
GISS-E2-R_r4i1p2	2.29	6.25	No	0.26	0.24	0.66	0.92	0.68	0.21	No
GISS-E2-R_r5i1p2	2.15	6.43	No	0.15	0.27	0.77	0.98	0.63	0.18	No
GISS-E2-R_r1i1p3	2.63	13.05	No	0.44	0.78	0.82	0.47	0.36	0.76	No
GISS-E2-R_r2i1p3	2.57	11.69	No	0.43	0.68	0.74	0.52	0.40	0.66	No
GISS-E2-R_r3i1p3	2.85	12.09	No	0.57	0.71	0.69	0.38	0.51	0.77	No
GISS-E2-R_r4i1p3	2.79	14.81	No	0.54	0.89	0.87	0.36	0.44	0.90	No
GISS-E2-R_r5i1p3	2.76	11.09	No	0.48	0.66	0.69	0.48	0.45	0.67	No
GISS-E2-R-CC_r1i1p1	2.12	6.83	No	0.13	0.30	0.80	0.98	0.60	0.20	No

Table A2: Complete pool of RCP8.5 model runs considered in study described in Chapter 2 (continued on next pages)

GCM run	ΔT (°C)	ΔP (%)	Daily time step available	Normalised ΔT	Normalised ΔP	D to warm, dry corner	D to warm, wet corner	D to cold, wet corner	D to cold, dry corner	Selected for step 2
ACCESS1-0_r1i1p1	4.76	10.93	Yes	0.46	0.28	0.48	0.76	0.72	0.40	No
ACCESS1-3_r1i1p1	4.38	16.88	Yes	0.32	0.57	0.75	0.66	0.40	0.52	No
bcc-csm1-1_r1i1p1	4.40	29.65	Yes	0.35	0.94	1.00	0.55	0.26	0.88	Cold, Wet
BNU-ESM_r1i1p1	4.91	9.84	Yes	0.51	0.24	0.41	0.77	0.78	0.44	No
CanESM2_r1i1p1	5.99	28.94	Yes	0.85	0.91	0.81	0.05	0.75	1.11	Warm, Wet
CanESM2_r2i1p1	6.05	36.86	Yes	0.88	0.97	0.87	0.07	0.79	1.17	Warm, Wet
CanESM2_r3i1p1	6.06	37.39	Yes	0.90	1.00	0.90	0.10	0.80	1.20	Warm, Wet
CanESM2_r4i1p1	5.98	29.37	Yes	0.84	0.93	0.83	0.07	0.74	1.11	Warm, Wet
CanESM2_r5i1p1	6.01	37.02	Yes	0.87	0.99	0.89	0.09	0.77	1.17	Warm, Wet
CCSM4_r1i1p1	4.29	10.98	Yes	0.24	0.29	0.69	0.90	0.62	0.24	Cold, Dry
CCSM4_r2i1p1	4.07	13.39	Yes	0.12	0.43	0.85	0.92	0.47	0.33	No
CCSM4_r6i1p1	4.24	11.40	Yes	0.19	0.32	0.74	0.91	0.58	0.24	Cold, Dry
CESM1-BGC_r1i1p1	4.09	13.03	Yes	0.13	0.40	0.82	0.92	0.50	0.30	No
CESM1-CAM5_r1i1p1	4.89	17.71	Yes	0.50	0.63	0.67	0.48	0.48	0.67	No
CMCC-CM_r1i1p1	5.78	11.79	Yes	0.81	0.35	0.27	0.56	0.90	0.75	No
CMCC-CMS_r1i1p1	6.30	-3.11	Yes	0.93	0.04	0.06	0.86	1.19	0.83	Warm, Dry
CNRM-CM5_r1i1p1	3.89	17.44	Yes	0.07	0.59	0.96	0.88	0.31	0.49	Cold, Wet
CSIRO-Mk3-6-0_r1i1p1	5.28	25.03	Yes	0.65	0.82	0.77	0.26	0.55	0.91	No
CSIRO-Mk3-6-0_r2i1p1	5.22	23.41	Yes	0.56	0.79	0.77	0.36	0.47	0.83	No
CSIRO-Mk3-6-0_r3i1p1	5.27	26.92	Yes	0.63	0.88	0.83	0.27	0.53	0.95	No
CSIRO-Mk3-6-0_r4i1p1	5.56	29.93	Yes	0.76	0.96	0.87	0.15	0.67	1.08	No
CSIRO-Mk3-6-0_r5i1p1	5.39	24.51	Yes	0.69	0.81	0.74	0.23	0.60	0.92	No
CSIRO-Mk3-6-0_r6i1p1	5.46	19.05	Yes	0.71	0.69	0.62	0.29	0.64	0.85	No
CSIRO-Mk3-6-0_r7i1p1	5.30	25.13	Yes	0.66	0.84	0.78	0.25	0.56	0.93	No
CSIRO-Mk3-6-0_r8i1p1	5.25	28.89	Yes	0.62	0.90	0.85	0.28	0.52	0.95	No
CSIRO-Mk3-6-0_r9i1p1	5.32	26.41	Yes	0.68	0.87	0.80	0.23	0.58	0.96	No
CSIRO-Mk3-6-0_r10i1p1	5.50	25.23	Yes	0.74	0.85	0.77	0.17	0.64	0.98	No
EC-EARTH_r2i1p1	4.43	6.79	Yes	0.37	0.15	0.54	0.92	0.80	0.27	Cold, Dry
EC-EARTH_r8i1p1	4.44	5.97	Yes	0.40	0.13	0.50	0.92	0.82	0.30	No

GCM run	ΔT (°C)	ΔP (%)	Daily time step available	Normalised ΔT	Normalised ΔP	D to warm, dry corner	D to warm, wet corner	D to cold, wet corner	D to cold, dry corner	Selected for step 2
EC-EARTH_r9i1p1	4.28	7.43	Yes	0.22	0.18	0.68	0.99	0.73	0.14	Cold, Dry
HadGEM2-AO_r1i1p1	4.79	21.32	Yes	0.47	0.74	0.77	0.46	0.41	0.73	No
HadGEM2-CC_r1i1p1	5.08	17.55	Yes	0.53	0.60	0.62	0.48	0.52	0.66	No
HadGEM2-ES_r1i1p1	5.24	15.06	Yes	0.60	0.51	0.51	0.49	0.63	0.65	No
HadGEM2-ES_r2i1p1	5.47	13.86	Yes	0.72	0.46	0.40	0.48	0.76	0.71	No
HadGEM2-ES_r3i1p1	5.23	11.84	Yes	0.59	0.37	0.41	0.62	0.72	0.56	No
HadGEM2-ES_r4i1p1	5.13	14.70	Yes	0.54	0.50	0.54	0.54	0.60	0.60	No
inmcm4_r1i1p1	3.61	5.38	Yes	0.00	0.12	0.90	1.19	0.79	0.10	Cold, Dry
IPSL-CM5A-LR_r1i1p1	6.48	3.51	Yes	1.00	0.07	0.10	0.83	1.22	0.90	Warm, Dry
IPSL-CM5A-LR_r2i1p1	6.46	4.10	Yes	0.99	0.10	0.09	0.80	1.19	0.89	Warm, Dry
IPSL-CM5A-LR_r3i1p1	6.41	6.95	Yes	0.96	0.16	0.08	0.74	1.13	0.86	Warm, Dry
IPSL-CM5A-LR_r4i1p1	6.44	3.59	Yes	0.97	0.09	0.07	0.82	1.19	0.87	Warm, Dry
IPSL-CM5A-MR_r1i1p1	6.21	10.55	Yes	0.91	0.25	0.15	0.65	1.04	0.82	No
IPSL-CM5B-LR_r1i1p1	4.25	23.41	Yes	0.21	0.78	0.97	0.71	0.16	0.69	Cold, Wet
MIROC5_r1i1p1	4.29	17.73	Yes	0.25	0.65	0.85	0.70	0.29	0.57	Cold, Wet
MIROC5_r2i1p1	4.50	23.31	Yes	0.41	0.76	0.82	0.51	0.34	0.73	No
MIROC5_r3i1p1	4.57	20.03	Yes	0.43	0.72	0.78	0.51	0.37	0.70	No
MIROC-ESM_r1i1p1	5.89	8.73	Yes	0.82	0.22	0.14	0.68	0.99	0.73	No
MIROC-ESM-CHEM_r1i1p1	6.35	8.36	Yes	0.94	0.21	0.11	0.70	1.09	0.85	No
MPI-ESM-LR_r1i1p1	5.53	-6.02	Yes	0.75	0.01	0.17	0.90	1.10	0.66	No
MPI-ESM-LR_r2i1p1	5.64	-8.51	Yes	0.78	0.00	0.16	0.91	1.13	0.69	No
MPI-ESM-LR_r3i1p1	5.66	-5.70	Yes	0.79	0.03	0.13	0.88	1.11	0.70	No
MPI-ESM-MR_r1i1p1	5.22	-1.40	Yes	0.57	0.06	0.33	0.90	0.97	0.47	No
MRI-CGCM3_r1i1p1	4.36	22.08	Yes	0.29	0.75	0.89	0.62	0.25	0.68	Cold, Wet
NorESM1-M_r1i1p1	4.34	11.72	Yes	0.28	0.34	0.67	0.84	0.59	0.30	No
CCSM4_r3i1p1	4.24	14.32	No	0.18	0.49	0.82	0.83	0.42	0.39	No
CCSM4_r4i1p1	4.39	7.82	No	0.34	0.19	0.57	0.90	0.75	0.25	No
CCSM4_r5i1p1	4.16	10.58	No	0.16	0.26	0.76	0.97	0.64	0.17	No
CESM1-CAM5_r2i1p1	4.87	18.39	No	0.49	0.68	0.71	0.47	0.45	0.69	No
CNRM-CM5_r2i1p1	3.85	13.42	No	0.03	0.44	0.94	0.98	0.46	0.35	No
CNRM-CM5_r4i1p1	3.87	15.10	No	0.04	0.53	0.96	0.93	0.38	0.43	No
CNRM-CM5_r6i1p1	3.93	18.01	No	0.10	0.66	0.98	0.83	0.24	0.56	No

GCM run	ΔT (°C)	ΔP (%)	Daily time step available	Normalised ΔT	Normalised ΔP	D to warm, dry corner	D to warm, wet corner	D to cold, wet corner	D to cold, dry corner	Selected for step 2
CNRM-CM5_r10i1p1	3.89	17.58	No	0.06	0.62	0.99	0.89	0.29	0.52	No
GISS-E2-H_r1i1p1	4.38	11.05	No	0.31	0.31	0.63	0.84	0.63	0.29	No
GISS-E2-H_r1i1p2	4.33	15.44	No	0.26	0.54	0.78	0.73	0.39	0.47	No
GISS-E2-H_r1i1p3	4.65	15.55	No	0.44	0.56	0.65	0.57	0.48	0.57	No
GISS-E2-R_r1i1p1	3.74	14.12	No	0.01	0.47	0.96	0.98	0.44	0.38	No
GISS-E2-R_r1i1p2	3.90	12.94	No	0.09	0.38	0.86	0.96	0.52	0.28	No
GISS-E2-R_r1i1p3	4.43	19.37	No	0.38	0.71	0.80	0.55	0.34	0.67	No
NorESM1-ME_r1i1p1	4.15	13.14	No	0.15	0.41	0.81	0.90	0.49	0.31	No

Summary

The hydrological cycle can be considered as the most important recycling system of matter on Earth, since water is an essential and widely used substance in every living organism. Water is used for food production, production of raw materials and goods, energy generation, consumption, and sanitation. Mountains play a special role in the hydrological cycle, acting as water towers, storing water as snow and ice and supplying water to downstream areas. In Asia, water resources largely depend on water generated in the mountainous upstream parts of several large river basins and hundreds of millions of people depend on their waters downstream. The large-scale impacts of climate change for the water resources in High Mountain Asia are poorly understood, because the area has a complex climate, which is poorly monitored. Climate change may have large consequences for water availability, seasonal changes in runoff generation and the frequency and magnitude of hydrological extremes. Climate change impact assessments in this region are lacking, covering only small catchments, or based on crude assumptions and simple approaches. In the research described in this thesis robust climate change impact assessments for water resources in High Mountain Asia have been made. To achieve this, novel approaches have been developed to improve the understanding of the impacts future climate change may have in this region.

Climate change impact studies depend on projections of future climate provided by climate models. The number of climate models is large and increasing, yet limitations in computational capacity make it necessary to compromise the number of climate models that can be included in a climate change impact study. The selection of climate models is not straightforward and can be done following different methods. Usually the selection is either based on the entire range of changes in climatic variables as projected by the total ensemble of available climate models, or on the skill of climate models to simulate past climate. In the research presented in this thesis, these approaches are combined in a novel selection procedure that aims at defining an ensemble of climate models that covers the full range of possible futures in terms of changes in mean temperature and precipitation, and changes in temperature and precipitation extremes, while at the same time only including climate models that have sufficient skill in simulating historical climate. The selected ensembles indicate that climate projections in High Mountain Asia are highly uncertain, especially for precipitation, but that changes are imminent.

To bridge the scale gap between climate models and hydrological models for river basin scale assessments, empirical-statistical downscaling and bias-correction methods are used. In this study two existing downscaling techniques are implemented. Using the delta change method, climate change projections are generated, and then used to force a cryospheric-hydrological model to assess climate change impact for hydrology in the upstream basins of the Indus, Ganges, Brahmaputra, Salween and Mekong rivers until 2050. This downscaling method allows for the assessment of changes in overall water availability. For the upper Indus basin, which has the largest glacier and snow melt dependency, and is Asia's climate change hotspot, the Advanced Delta Change method is used to generate climate change scenarios up to 2100 which allow for the simulation of changes in hydrological extremes.

A novel regionalized glacier mass balance model, which is suitable to estimate future changes in glacier extent at river basin scale is presented. This glacier mass balance model is specifically developed for implementation in large-scale hydrological models, where the spatial resolution does not allow for simulating individual glaciers and data-scarcity is an issue. Forcing this model with

downscaled climate change projections shows that glacier extent in High Mountain Asia will be reduced strongly during the 21st century.

The downscaled climate change scenarios and associated projections of future glacier extent are used to force a new high-resolution, fully distributed cryospheric-hydrological model to assess changes in future hydrology. In a first impact assessment, future water availability in the upstream basins of the Indus, Ganges, Brahmaputra, Salween and Mekong rivers until 2050 is assessed. Water availability is expected to increase in each of the five basins, despite the large differences in hydrological regimes between basins and between rivers and tributaries within basins. For the upper Ganges, Brahmaputra, Salween and Mekong river basins this is due to increased precipitation, whereas for the upper Indus basin the main driver is accelerated melt. A second impact assessment is done for the upper Indus basin. For this basin, hydrological projections until 2100 are generated and the analysis focuses on seasonal shifts and changes in extreme discharges. Besides, the cryospheric-hydrological is calibrated using as three-step calibration approach, integrating data of geodetic glacier mass balances, remotely sensed snow cover, and observed discharge. The analysis reveals that the upper Indus basin faces a very uncertain future in terms of water availability in the long run. Projections of changes in water availability at the end of the 21st century range from -15% to +60% with respect to the reference. This uncertainty mainly stems from the large spread in the precipitation projections throughout the 21st century. Despite the large uncertainties in future climate and water availability, basin-wide patterns and trends of intra-annual shifts in water availability are consistent across climate change scenarios. For the near future (2021-2050), these trends mainly consist of minor increases in summer flows combined with increased flows during other seasons. For the far future (2071-2100) the trends show decreases in summer flows combined with stronger increasing flows during the other seasons. Furthermore, increases in intensity and frequency of extreme discharges are found for most of the upper Indus basin and for most scenarios and models considered, implying increases in flooding events during the 21st century.

Since a consistent increase in water availability and increase in extreme discharges is projected for the upstream river basins in High Mountain Asia at least until 2050, a change of focus in adaptation strategies to coping with extreme events and intra-annual shifts in water availability is desirable. The approaches described in this thesis stand out from previous research in the region and generated robust projections, new insights and understanding. Limitations and possibilities for further improvement have been identified, which provide new challenges for future research.

Samenvatting

De hydrologische kringloop kan worden beschouwd als het belangrijkste natuurlijke recycling-mechanisme op Aarde. Water is immers een essentieel en veel gebruikte stof in ieder levend organisme. De mens gebruikt water voor de productie van voedsel, grondstoffen en goederen, voor het genereren van energie, voor consumptie en voor sanitatie. Gebergten spelen een speciale rol in de hydrologische kringloop, waarin ze functioneren als watertorens die water in de vorm van sneeuw en ijs opslaan en benedenstroomse gebieden van water voorzien. In Azië is de watervoorziening voor een groot deel afhankelijk van water dat wordt gegenereerd in de bergachtige bovenstroomse stroomgebieden van een aantal grote rivieren. Benedenstrooms zijn honderden miljoenen mensen afhankelijk van dit water. De grootschalige effecten van klimaatverandering op de watervoorraden in de hooggebergten van Azië zijn nog slecht begrepen, omdat het gebied een complex klimaat heeft en er weinig metingen worden gedaan. Klimaatverandering zou echter grote consequenties kunnen hebben voor de waterbeschikbaarheid, seizoenale veranderingen in afvoer, en de frequentie en grootte van hydrologische extremen. Studies naar de effecten van klimaatverandering in deze regio ontbreken, beslaan slechts kleine stroomgebieden, of zijn gebaseerd op grove aannames en eenvoudige benaderingen. Voor het onderzoek dat in dit proefschrift wordt beschreven zijn gedegen studies naar de effecten van klimaatverandering op de watervoorraden in de hooggebergten van Azië uitgevoerd. Om dit te bereiken zijn vernieuwende methoden ontwikkeld om het begrip van de effecten die klimaatverandering op deze regio heeft te vergroten.

Studies naar de effecten van klimaatverandering zijn afhankelijk van projecties van het toekomstige klimaat die door klimaatmodellen worden geleverd. Het aantal beschikbare klimaatmodellen is groot en neemt toe. Vanwege de gelimiteerde rekenkracht van computers is het noodzakelijk om het aantal klimaatmodellen, dat in een studie naar de effecten van klimaatverandering kan worden meegenomen, te beperken. De selectie van klimaatmodellen is niet eenvoudig en kan op verschillende manieren worden gedaan. Meestal is het selectieproces óf gebaseerd op de bandbreedte van voorspelde veranderingen in het volledige ensemble van klimaatmodellen, óf op de kwaliteit van klimaatmodellen om historisch klimaat correct te simuleren. In het onderzoek dat in dit proefschrift wordt gepresenteerd zijn deze twee benaderingen gecombineerd in een nieuwe selectieprocedure. Het doel van deze procedure is om een ensemble van klimaatmodellen te selecteren dat de volledige bandbreedte van mogelijke toekomsten voor wat betreft veranderingen in gemiddelden van temperatuur en neerslag en veranderingen in extremen van temperatuur en neerslag beslaat. Daarnaast worden in deze selectieprocedure alleen klimaatmodellen gekozen die het historische klimaat met voldoende nauwkeurigheid kunnen simuleren. De geselecteerde ensembles van klimaatmodellen wijzen er op dat klimaatprojecties voor de hooggebergten in Azië zeer onzeker zijn, met name voor neerslag, maar dat veranderingen ophanden zijn.

Om het gat in ruimtelijke schaal tussen klimaatmodellen en hydrologische modellen te overbruggen worden methoden voor empirisch-statistische neerschaling en afwijkingscorrectie gebruikt. In deze studie worden twee verschillende neerschalingstechnieken geïmplementeerd. Met behulp van de "delta change" methode worden klimaatprojecties gegenereerd die gebruikt worden om een cryosferisch-hydrologisch model aan te sturen. Met dit model worden de effecten van klimaatverandering op de hydrologie van de bovenstroomse stroomgebieden van

de Indus, Ganges, Brahmaputra, Salween en Mekong tot en met het jaar 2050 geanalyseerd. De gebruikte neerschalingsmethode maakt het mogelijk om veranderingen in algehele waterbeschikbaarheid te analyseren. Voor het bovenstroomse deel van het Indus-stroomgebied, dat de grootste afhankelijkheid van gletsjer- en sneeuwsmelt heeft, is de "Advanced Delta Change" neerschalingsmethode gebruikt om klimaatprojecties tot en met het jaar 2100 te genereren. Deze methode biedt de mogelijkheid om veranderingen in hydrologische extremen te simuleren.

In dit proefschrift wordt een nieuw regionaal massabalansmodel voor gletsjers gepresenteerd, dat geschikt is om toekomstige veranderingen in gletsjer-areaal op rivierstroomgebiedsschaal te schatten. Dit massabalansmodel is specifiek ontwikkeld voor implementatie in hydrologische modellen met een grote ruimtelijke schaal, waarin het vanwege de beperkte ruimtelijke resolutie niet mogelijk is om individuele gletsjers te simuleren en waar gedetailleerde gegevens schaars zijn. Het aansturen van dit model met neergeschaalde klimaatprojecties toont aan dat het areaal van gletsjers in de hooggebergten van Azië waarschijnlijk sterk zal afnemen gedurende de 21e eeuw.

De neergeschaalde klimaatscenarios en bijbehorende projecties van toekomstige gletsjer-areaal zijn gebruikt om een nieuw, ruimtelijk gedistribueerd cryosferisch-hydrologisch model met een hoge resolutie aan te sturen om toekomstige veranderingen in de hydrologie te analyseren. In een eerste studie naar de effecten van klimaatverandering, is de toekomstige waterbeschikbaarheid in de bovenstroomse stroomgebieden van de Indus, Ganges, Brahmaputra, Salween en Mekong geanalyseerd tot en met het jaar 2050. Verwacht wordt dat de waterbeschikbaarheid in elk van de vijf stroomgebieden toeneemt ondanks de grote verschillen in hydrologische eigenschappen tussen de stroomgebieden onderling, en tussen de hoofdrivieren en zijrivieren binnen de stroomgebieden. Voor de bovenstroomse Ganges, Brahmaputra, Salween en Mekong komt deze toename door toenemende neerslag, terwijl de toename in de bovenstroomse Indus voornamelijk door versnelde gletsjersmelt komt. Een tweede studie naar de effecten van klimaatverandering is uitgevoerd voor het bovenstroomse deel van het Indus-stroomgebied. Voor dit stroomgebied zijn hydrologische projecties tot en met het jaar 2100 gegenereerd, waarbij de analyse zich richt op seizoenale verschuivingen en veranderingen in extreme afvoeren. Daarnaast is in deze studie het cryosferisch-hydrologische model gecalibreerd met een calibratieprocedure in drie stappen, waarbij gegevens van geodetische gletsjermassabalansen, sneeuwbedekking afgeleid van satellietwaarnemingen, en in de rivier gemeten afvoergegevens, zijn geïntegreerd. De analyse toont aan dat de bovenstroomse Indus voor wat betreft de waterbeschikbaarheid op lange termijn een zeer onzekere toekomst tegemoet gaat. Projecties van veranderingen in waterbeschikbaarheid aan het einde van de 21e eeuw variëren van -15% tot +60% in vergelijking met de referentieperiode (1971-2000). Deze onzekerheid komt voornamelijk door de grote spreiding in neerslagprojecties voor de 21e eeuw. Ondanks de grote onzekerheden in het toekomstige klimaat en de toekomstige waterbeschikbaarheid, zijn patronen en trends van seizoenale verschuivingen in waterbeschikbaarheid voor alle klimaatscenarios consistent. Deze trends bestaan voor de nabije toekomst (2021-2050) voornamelijk uit kleine toenamen in zomerafvoeren en toenemende afvoeren in andere seizoenen. Voor de verre toekomst (2071-2100) bestaan de trends uit afnames in zomerafvoeren gecombineerd met sterker toenemende afvoeren in andere seizoenen. Bovendien zijn toenamen in de frequentie en grootte van extreme afvoeren gevonden voor het grootste deel van de bovenstroomse Indus en voor de meeste scenarios en klimaatmodellen, wat impliceert dat overstromingen waarschijnlijk toe zullen nemen gedurende de 21e eeuw.

Omdat tenminste tot en met het jaar 2050 een consistente toename van waterbeschikbaarheid die gepaard gaat met een toename van extreme afvoeren wordt verwacht voor de bovenstroomse stroomgebieden van rivieren die in de hooggebergten van Azië ontspringen, is het wenselijk dat

bij het bepalen van klimaatadaptatiestrategieën de aandacht verschuift naar het aanpassen aan seizoenale verschuivingen in waterbeschikbaarheid en toenames in extreme gebeurtenissen. De methodes die in dit proefschrift worden beschreven onderscheiden zich van eerder onderzoek in de regio en hebben geleid tot gedegen projecties en nieuwe inzichten en kennis. Beperkingen in de gebruikte methoden en mogelijkheden voor toekomstige verbeteringen zijn beschreven en bieden nieuwe uitdagingen voor toekomstig onderzoek.

Curriculum Vitae

Arthur Lutz, Dutch and Austrian citizen, was born on 1 March 1985 in Stuttgart, Germany. In 1989 he moved to the Netherlands where he grew up in Ter Aar. Numerous visits to family in the Austrian Alps incited his interest for the natural processes at the Earth's surface and in mountains in particular. From 2003 to 2009 he studied at Utrecht University, where he gained his BSc. in Earth Sciences and MSc. in Physical Geography (both completed 'with distinction'). He particularly focused on the cryospheric environment by attending specialization courses in glaciology and permafrost at the University Centre in Svalbard and completing an internship in the cryospheric research group at the University of Zürich, Switzerland. After completion of his studies Arthur worked as a consultant and GIS-specialist in archaeology and in 2011 he joined FutureWater, a Wageningen-based research and advisory company that works throughout the world to combine scientific research with practical solutions for water management. At FutureWater he works in projects with focus on water resources in relation to climate change, energy and food security. Between 2012 and 2016 Arthur extended his activities at FutureWater in a combined PhD project with the Department of Physical Geography at Utrecht University, quantifying the impacts of climate change for water resources in High Mountain Asia. Arthur has a solid background in hydrology, hydrological modeling, GIS, remote sensing and cryospheric sciences. His expertises include hydrological modeling at various scales and with a variety of modeling tools, climate change impacts for future water resources, data analysis, hydro-meteorological monitoring in the field, and training. He has a broad international working experience, in countries including China, Colombia, India, Kyrgyzstan, Mozambique, Nepal and Pakistan.

List of peer reviewed publications

Lutz, A.F., W.W. Immerzeel, P.D.A. Kraaijenbrink, A.B. Shrestha. (under review) Climate change impacts on the upper Indus hydrology: sources, shifts and extremes. *PLOS ONE*.

Lutz, A.F., H.W. ter Maat, H. Biemans, A.B. Shrestha, P. Wester, W.W. Immerzeel. (in press) Selecting representative climate models for climate change impact studies: an advanced envelope-based selection approach. *International Journal of Climatology*.

Immerzeel, W. W., N. Wanders, A.F. Lutz, J.M. Shea, M.F.P. Bierkens. (2015) Reconciling high altitude precipitation with glacier mass balances and runoff. *Hydrology and Earth System Sciences*, 19, 4673-4687, doi:10.5194/hess-19-4673-2015

Terink, W., A.F. Lutz, G.W.H. Simons, W.W. Immerzeel, P. Droogers. (2015) SPHY v2.0: Spatial Processes in HYdrology. *Geoscientific Model Development*, 8, 2009-2034, doi:10.5194/gmd-8-2009-2015.

Lutz, A.F., W.W. Immerzeel, A.B. Shrestha, M.F.P. Bierkens. (2014) Consistent increase in High Asia's runoff due to increasing glacier melt and precipitation, *Nature Climate Change*, 4, 587-592

Lutz, A.F., W. W. Immerzeel, A. Gobiet, F. Pellicciotti, M. F. P. Bierkens. (2013) Comparison of climate change signals in CMIP3 and CMIP5 multi-model ensembles and implications for Central Asian glaciers, *Hydrology and Earth System Sciences*, 17, 3661 – 3677

Asch, N. van, A.F. Lutz, M.C.H. Duijkers, O. Heiri, S.J. Brooks, W.Z. Hoek. (2011) Rapid climate change during the Weichselian Lateglacial in Ireland: chironomid-inferred summer temperatures from Fiddaun, Co. Galway. *Palaeogeography, Palaeoclimatology, Palaeoecology*, 315–316, pp. 1-11.

Financial support

The work presented in this thesis was financially supported by a number of organisations and funding agencies through different projects and research programmes:

FutureWater, Wageningen, The Netherlands.

Ministry of Foreign Affairs, Norway and Swedish International Development Agency (Sida) through the Himalayan Climate Change Adaptation Programme (HICAP).

United Kingdom Government's Department for International Development (DFID) and International Development Research Centre (IDRC), Canada, through the Himalayan Adaptation, Water and Resilience (HI-AWARE) consortium under the Collaborative Adaptation Research Initiative in Africa and Asia (CARIAA).

Asian Development Bank through the project titled Water and Adaptation Interventions in Central and West Asia (TA-7532).

United Kingdom's Department for International Development (DFID), through the Indus Basin Programme.

ICIMOD core funds contributed by the governments of Afghanistan, Australia, Austria, Bangladesh, Bhutan, China, India, Myanmar, Nepal, Norway, Pakistan, Switzerland, and the United Kingdom.

Netherlands Organization for Scientific Research (NWO), through the VENI grant of W.W. Immerzeel.

European Research Council (ERC) under the European Union's Horizon 2020 research and innovation programme (grant agreement 676819 W.W. Immerzeel).